Theory and application of quasi-elastic equations in terrain-following coordinates based on the full pressure field

by
Francois Alwyn Engelbrecht

Submitted in partial fulfilment of the requirements
for the degree of

PHILISOPHIAE DOCTOR

in the
Faculty of Natural and Agricultural Sciences
University of Pretoria

May 2006

Theory and application of quasi-elastic equations in terrain-following coordinates based on the full pressure field

Francois Alwyn Engelbrecht

Promoter: Prof. C.J. deW. Rautenbach
Co-promoter: Dr. J.L. McGregor
Department: Department of Geography, Geoinformatics and Meteorology
Faculty: Faculty of Natural and Agricultural Sciences
University: University of Pretoria
Degree: Philosophiae Doctor

Summary

The thesis reports on the development of a new quasi-elastic nonhydrostatic model, cast in a terrain-following coordinate based on the full pressure field. The equations used are the σ coordinate analogue of the nonhydrostatic pressure coordinate equations formulated by White (1989). The equations are filtered of vertically propagating acoustic waves. However, since Lamb waves are present, the equations may be termed quasi-elastic. In contrast to similar quasi-elastic pressure-based models, the equations and the numerical solution procedure presented here are formulated independent of the use of a reference state thermodynamic profile. Thus, it is possible that the equations may be used to simulate atmospheric motion at spatial scales larger than the meso-scale.

A novel split semi-Lagrangian procedure is formulated to solve the quasi-elastic equations on a grid that is nonstaggered in both the horizontal and vertical. A nonstaggered grid is appealing to use in semi-Lagrangian discretizations of the atmospheric equations, since only one set of trajectories needs to be calculated during each advection time step. However, it is well known that the nonstaggered grid has poor gravity wave dispersion properties. In this study, this problem is alleviated by using high-order centered spatial differencing, and by applying a spatial filter to remove two-grid-interval waves from the grid. It is shown that large time steps (large Courant numbers) are allowed during the semi-Lagrangian advection step. This makes the method computationally attractive compared to explicit or split-explicit procedures that use an Eulerian approach to treat the advection terms. For situations where the fast moving gravity waves carry a non-negligible amount of the energy, the split semi-Lagrangian approach may even be computationally more efficient than the widely used semi-implicit semi-Lagrangian solution procedures. The thesis reports on a large set of bubble convection tests performed with the new kernel. It is concluded that the new model is worth developing further.

Teorie en toepassing van kwasi-elastiese vergelykings in terrein-volgende koordinate gebasseer op die volle drukveld

Francois Alwyn Engelbrecht

Promotor: Prof. C.J. deW. Rautenbach
Mede-promotor: Dr. J.L. McGregor
Departement: Departement Geografie, Geoinformatika en Meteorologie
Fakulteit: Fakulteit Natuur - en Landbouwetenskappe
Universiteit: Universiteit van Pretoria
Graad: Philosophiae Doctor

Samevatting

Die proefskrif handel oor die ontwikkelling van 'n nuwe kwasi-elastiese nie-hidrostatiese model, in 'n terrein-volgende koordinaat gebasseer op die volle drukveld. Die vergelykings wat gebruik word is die σ-koordinaat analoog van die nie-hidrostatiese drukkoordinaat vergelykings geformuleer deur White (1989). Die vergelykings is gefilter van vertikaal voortplantende klankgolwe. Lamb-golwe is egter teenwoordig en daarom kan die vergelykings kwasi-elasties genoem word. In kontras met soortgelyke kwasi-elastiese drukgebasseerde modelle, is die vergelykings wat hier gebruik word onafhanklik van die gebruik van 'n termodinamiese verwysingsprofiel. Dit is dus moontlik dat die vergelykings gebruik kan word om atmosferiese sirkulasie op ruimtelike skale groter as die meso-skaal te simuleer.

'n Oorspronklike split semi-Lagrange prosedure is geformuleer om die kwasi-elastiese vergelykings op te los op 'n rooster wat in die horisontaal en vertikaal nie-verspringend is. So 'n rooster is aanloklik om te gebruik in die semi-Lagrangian diskretisering van die atmosferiese vergelykings, aangesien dit nodig is om net 'n enkele stel trajekte te bereken gedurende elke adveksie tydstap. Dit is egter welbekend dat die nie-verspringende rooster swak gravitasiegolf dispersie eienskappe het. In die studie word hierdie probleem hanteer deur hoe orde differensiasie te gebruik en deur 'n ruimtelike filter toe te pas wat twee-rooster-interval golwe van die rooster verwyder. Dit word aangetoon dat groot tydstape (groot Courant getalle) toegelaat word gedurende die semi-Lagrange adveksie stap. Dit maak die metode berekeningsgewys aantreklik in vergelyking met eksplisiete en split-eksplisiete prosedures wat 'n Euler benadering gebruik vir die adveksie terme. Vir situasies waar die vinnigbewegende gravitasie golwe 'n nie-weglaatbare hoeveelheid van die energie dra, kan die split semi-Lagrange benadering selfs meer berekeningseffektief wees as die gewilde semi-implisiete semi-Lagrange prosedures. 'n Groot reeks borrel konveksie eksperimente is uitgevoer met die nuwe kern en dit blyk die moeite werd te wees om die nuwe model verder te ontwikkel.

Acknowledgements

The author wishes to express his appreciation to the following persons and organisations for their assistance and contribution to make this dissertation possible:

- *Prof. C.J. deW. Rautenbach* (Head of the Department of Geography, Geoinformatics and Meteorology at the University of Pretora) for his appreciation of my interest in numerical atmospheric modelling, and for supporting this theoretical study during times where research becomes increasingly application-driven.
- *Dr. J.L. McGregor* (Specialist Scientist) from the Commonwealth Scientific and Industrial Research Organisation (CSIRO), section Marine and Atmospheric Research in Australia, for his continuous encouragement, guidance and expert advice during the course of the study.
- *Dr. G. Green* (retired director of the Water Research Commission (WRC) in South Africa) for the interest that he took in the research and my career as an atmospheric scientist.
- *Dr. JD. Gertenbach* (South African Weather Service), *Me. H. Riphagen* (retired), *Mr Gusti van Zyl* (Univeristy of Pretoria) and *Me C.J. Potgieter* (Agricultural Research Council) for many helpful discussions during the course of the study.
- Two external examiners, whose comments helped to improve the thesis.
- *CSIRO Marine and Atmospheric Research* in Australia for inviting me to visit Dr. J.L. McGregor in January 2002 and 2004, for the purpose of collaborative research into nonhydrostatic atmospheric model development.
- The *WRC* for financially supporting the research into atmospheric model development in South Africa.
- The friendly librarians of the South African Weather Service, Karin and Anastasia, for assisting me with finding most of the references listed at the end of this thesis.
- My colleges in the Department of Geography, Geoinformatics and Meteorology for their encouragement and interest in my research.
- My family, dear friends and Duimpie, for their encouragement and support.
- My girlfriend Christien, who became my wife during the course of the study despite of all the hours I spent behind a computer.
- Most of all, I would like to thank God for giving me the strength to undertake this study, and for the privilege of being able to study the atmosphere.

Contents

List of Symbols

$\hat{a}_{\hat{u}}$	x component of the estimated acceleration
$\hat{a}_{\hat{v}}$	y component of the estimated acceleration
$\hat{a}_{\hat{\dot{\sigma}}}$	σ component of the estimated acceleration
c	phase speed
c_s	speed of sound
c_p	specific heat at constant air pressure
c_v	specific heat at constant air volume
f	Coriolis parameter
g	acceleration of gravity
h	surface elevation
	depth of fluid in the shallow-water equations (section 4.3.3)
H	mean depth of fluid in the shallow-water equations
$\tilde{H}$	vertical length scale
$H^{'}$	scale of the height perturbation
H_0	RT_0/g
k	wave number in x direction
K_s	horizontal diffusion coefficient applied to wind field
K_{Ts}	horizontal diffusion coefficient applied to temperature field
K_σ	vertical diffusion coefficient applied to wind field
$K_{T\sigma}$	vertical diffusion coefficient applied to temperature field
l	wave number in y direction
L	horizontal length scale
L_x	wave length in x direction
L_y	wave length in y direction
L_z	wave length in z direction
m	wave number in z direction
N	$\equiv \sqrt{g\kappa/H_0}$

p	pressure
p_{surf}	surface presure
p_{surf_ref}	reference surface pressure
p_{surf_ave}	mean sea-level pressure
p_0	$\equiv p_{surf\_ref} - p_T$
p_T	constant pressure at top of model
p_s	$\equiv p_{surf} - p_T$
$\hat{p}_s$	amplitude of wave-like solution for p_s
$p_0(\mathbf{x})$	pressure at lower boundary that is independent of time but may depend on horizontal position
p_{sr}	$\equiv p_0(\mathbf{x}) - p_T$
p_{STAN}	standard pressure level
P	pressure scale
r	$\equiv gp/RT$
r_{ref}	$\equiv gp/RT_{ref}$
r_l	relaxation coefficient
$\mathbf{r}$	vector moving with fluid
R	gas constant
R_A	relative phase speed
s	$\equiv (p/p_s)(g/RT)$
S_{ref}	$\equiv -dT_{ref}/dp + \kappa T_{ref}/p$, reference state static stability function
t	time
τ	time
T	temperature
T'	temperature perturbation
$\hat{T}'$	amplitude of wave-like solution for the temperature perturbation
T_0	temperature of isothermal atmosphere
T_{ref}	reference state temperature

T_{ref_ave}	mean reference state temperature
u	wind speed in x direction
$\hat{u}$	amplitude of wave-like solution for u (Chapter 3);
	estimated wind speed in x direction at time-level $\tau + \Delta t/2$ (Chapter 4)
$\tilde{u}$	horizontal velocity scale
U	constant wind speed in x direction
$\mathbf{u}$	three-dimensional velocity vector
$\hat{\mathbf{u}}$	estimated velocity at time-level $\tau + \Delta t/2$
v	wind speed in y direction
$\hat{v}$	estimated wind speed in y direction at time-level $\tau + \Delta t/2$
V	constant wind speed in y direction
$\mathbf{v}$	$\equiv (u, v)$, horizontal velocity.
w	wind speed in z direction
$\tilde{w}_{ref}$	$\equiv -R\omega T_{ref}/gp$, approximated vertical velocity
$\hat{w}$	$\equiv -R\omega T/gp$, approximated vertical velocity
x^*	x coordinate of departure point
y^*	y coordinate of departure point
z	geometric height
$z^{'}$	geometric height perturbation
z_{ref}	reference state geometric height
Δx	constant grid increment along x axis
Δy	constant grid increment along y axis
Δt	constant time-step
Δt_s	advection time-step
Δt_a	adjustment time-step
$\Delta\sigma$	constant grid increment along σ axis
α	specific volume (Chapter 1);

	$\equiv u\Delta t/\Delta x$ (Chapter 4 and 5)
α^*	$\equiv -\left(p_0/\theta_{ref}\right) d\theta_{ref}/dp$
β	$\equiv v\Delta t/\Delta y$
γ	c_p/c_v
ϵ	$\equiv (1/g)\, DW/Dt$, measure of the vertical acceleration
ζ	vertical component of the vorticity
θ	potential temperature
$\theta^{'}$	potential temperature perturbation
θ_0	homogeneous reference state potential temperature
θ_{ref}	reference state potential temperature
ϑ	numerical value of the local frequency
ϑ_T	analytic local frequency
κ	$\equiv R/c_p$, ratio of gas constant to specific heat at constant pressure
λ	latitude (Chapter 1);
	amplification factor (Chapter 5)
μ	wave number in z direction
ν	frequency of oscillation
π	hydrostatic pressure (Chapter 2);
	$\equiv \arccos(-1)$ (Chapter 3 to 5)
π_{surf}	hydrostatic pressure at the surface
π_T	hydrostatic pressure at model top
$\hat{\pi}$	$\equiv \hat{p}_s/p_0$
ρ	density
ρ_0	constant basic state density
ρ_{ref}	reference state density
σ	pressure-scaled vertical coordinate
σ^*	σ coordinate of departure point
$\dot{\sigma}$	$\equiv D\sigma/Dt$, vertical velocity in σ coordinates

$\hat{\dot{\sigma}}$	amplitude of wave-like solution for $\dot{\sigma}$ (Chapter 3);
	estimated vertical velocity in σ coordinates at time-level $\tau + \Delta t/2$ (Chapter 4)
ϕ	geopotential
ϕ'	geopotential perturbation
$\hat{\phi}'$	amplitude of wave-like solution for geopotential perturbation
ϕ_{ref}	reference state geopotential
χ	$\equiv [(p/RT)\,(\partial\phi/\partial p)]^{-1}$
ω	$\equiv Dp/Dt$, vertical velocity in isobaric coordinates
$\tilde{\omega}$	ω scale
ω_T	gravity wave frequency
Ω	ω/p
Ω_T	true frequency
Ω_N	frequency of waves in the numerical solution

List of Figures

List of Tables

List of Abbreviations

AGCM	Atmospheric general circulation model
ALADIN	Aire Limitee Adaptation Dynamique Dyveloppement International
CAT	Clear air turbulence
C-CAM	Conformal-cubic atmospheric model
CFL	Courant-Friedrichs-Lewy
CSIR	Center for Scientific and Industrial Research
CSIRO	Commonwealth Scientific and Industrial Research Organisation
DARLAM	Division of Atmospheric Research Limited Area Model
HC	Horizontal advection Courant number
VC	Verical advection Courant number
MM5	Fith-generation Pennsylvania State University-National Center for Atmospheric Research Meso-scale Model
MP	Miller-Pearce
NCAR	National Center for Atmospheric Research
NCEP	National Centers for Environmental Prediction
NWP	Numerical weather prediction
PC	Personal Computer
RAMS	Regional Atmospheric Modelling System
SAWB	South African Weather Bureau
SAWS	South African Weather Service
SAST	South African Standard Time
SOR	Successive Over-Relaxation
UKMO	United Kingdom Meteorological Office
UCT	University of Cape Town
UP	University of Pretoria
WITS	University of the Witwatersrand
WRC	Water Research Commission

Chapter 1

Introduction

1.1 Background to the research

1.1.1 Hydrostatic and nonhydrostatic atmospheric models

1.1.1.1 Unapproximated and fully-elastic equations

It is believed that the equations of momentum, mass and energy conservation for a perfect gas (e.g. Kasahara, 1974; Haltiner and Williams, 1980; Burger and Riphagen, 1990) govern atmospheric motion over a wide range of spatial scales: from small turbulent eddies of a few millimeters in diameter, to synoptic and planetary waves stretching over thousands of kilometers (e.g. Haltiner and Williams, 1980; Holton, 1992). In fact, this set of nonlinear partial differential equations, applied in unapproximated form over the full depth of the atmosphere, is thought to offer the only possibility for the development of a universal atmospheric model (Laprise 1992, Caya and Laprise, 1999; Davies et al. 2003, White et al., 2005). That is, these equations may be used to describe atmospheric motion over the full range of spatial scales it occurs, over any portion of the atmosphere. Based on the fundamental laws of physics, they remain equally applicable in an unknown stellar atmosphere. The unapproximated atmospheric equations are too complicated to be solved analytically. However, these equations may be simplified until qualitative interpretation of physical and dynamical processes is feasible, or until analytic solutions are obtainable. This has become an important study field, called "Dynamic Meteorology". The approximations introduced are normally only valid for atmospheric circulations that occur at a specific spatial scale. For example, the quasi-geostrophic equation set (e.g. Hoskins and Pearce, 1983; Holton, 1992) is widely applied to qualitatively describe atmospheric circulation over the mid-latitudes of Earth. Numerical solutions of the unapproximated equations or an approximated set may also be obtained. This has become another important study field in Meteorology, called "Numerical Atmospheric Modelling".

The universal applicability of the unapproximated equations apparently renders them ideal for the numerical simulation of atmospheric circulation. However, there are currently only a few models that use these equations. An important reason for this, is that acoustic waves form part of the solution set of the unapproximated equations (e.g. Haltiner and Williams, 1980; Room, 1998). Consider, for example, the case of motion that occurs in the $x-z$ plane only. If uniformity is assumed in the lateral direction (y), and if the Coriolis, friction and diabatic terms are neglected, the unapproximated equations reduce to (Miller and White, 1984):

$$\frac{Du}{Dt} + \frac{1}{\rho}\frac{\partial p}{\partial x} = 0 \tag{1.1}$$

$$\frac{Dw}{Dt} + \frac{1}{\rho}\frac{\partial p}{\partial z} + g = 0 \tag{1.2}$$

$$\frac{D\ln\rho}{Dt} + \frac{\partial u}{\partial x} + \frac{\partial w}{\partial z} = 0 \tag{1.3}$$

$$\frac{D\ln T}{Dt} - \kappa\frac{D\ln p}{Dt} = 0. \tag{1.4}$$

Equations (1.1) and (1.2) are the horizontal and vertical components of the momentum equation, and (1.3) and (1.4) are the mass continuity and thermodynamic equations, respectively; u and w are the wind components in the x and z directions, respectively. The density ρ, pressure p and temperature T are related by the perfect gas law $p = \rho RT$; R is the gas constant, and $\kappa = R/c_p$ with c_p the specific heat at constant pressure. The total derivative is $D/Dt \equiv \partial/\partial t + u\partial/\partial x + \partial + w\partial/\partial z$; all partial derivatives with respect to x and t are carried out at constant z. If (1.1)-(1.4) are linearized around an isothermal basic state of no motion in hydrostatic balance , it may be shown that waves travelling at speed

$$c_s = \sqrt{\frac{c_p}{c_v}RT_0} \tag{1.5}$$

are part of the solution set of the linearized equations (e.g. Haltiner and Williams, 1980). Here c_v is the specific heat at constant volume, T_0 is the temperature of the isothermal reference state and (1.5) is the famous formula for the speed of sound.

An equation set that contains sound waves as part of its solution set is termed "fully-elastic" or "fully-compressible". Acoustic waves, however, are believed to have no significant influence on the atmospheric processes that determine weather and climate (e.g. Haltiner and Williams, 1980). The presence of these fast travelling waves implies computational penalties during the numerical solution of the fully-elastic equations (e.g. Room, 1998; Davies et al., 2003). Until

fairly recently, these computational constraints have rendered fully-elastic equation sets impractical for general use. However, with the advent of ever faster computers, in combination with the development of economical semi-implicit time integration schemes (e.g. Robert, 1969; Tanguay et al., 1990), the unapproximated equations have become practical and increasingly popular over the last few years. This popularity is linked to a general trend to develop universal models that may be applied at all spatial and time scales (e.g. Laprise, 1992; Wood and Staniforth, 2003; Davies et al., 2005; White et al., 2005). It might well be that the unapproximated equations are the only option for the eventual development of a truly universal model (Davies et al., 2003). The use of various approximated equation sets, however, remains relevant for theoretical and modelling studies, as well as for operational use. The main classes of approximated equations are discussed in the following sections.

1.1.1.2 The hydrostatic approximation and hydrostatic models

With the advent of computers in the late 1940s, the operational use of atmospheric equations for the purpose of numerical weather prediction (NWP) became computationally feasible. When applied to obtain regional or global predictions, these models were restricted by computational constraints to horizontal spatial resolutions that varied from a few hundred kilometers in the early 1950s, to a few tens of kilometers at present. At these resolutions, many atmospheric circulation patterns can not be fully resolved. For example, individual thunderstorms occur at spatial scales ranging from a few hundred meters to a few kilometers (the micro and small scales). Gravity waves and sea-breezes, which occur at the meso (a few tens of kilometers) or smaller scales, are other important circulation systems that can not be properly resolved when the model resolution is in the order of a few tens of kilometers or coarser. Untill the early 1990's, computational constraints did not allow for the operational use of the fully-elastic equations in NWP and climate simulation models. Approximated equation sets were derived from the fully-elastic unapproximated equations in order to specifically describe the scales of motion that could be resolved at the model resolutions used operationally. Although the resulting equation sets do not possess the property of universal applicability, they are computationally much less expensive to solve numerically.

Probably the single most fundamental simplification introduced to the fully-elastic equations, has been the "hydrostatic approximation". A basic scale analysis of the unapproximated equations (e.g. Holton, 1992) indicates that the vertical acceleration term in the vertical momentum equation is of fundamental importance to describe small and micro-scale circulations, such as the updrafts and downdrafts in individual thunderstorms. However, for systems occurring at scales of a few tens of kilometers (meso-scale) to the synoptic-scale and larger, the vertical acceleration term is of negligible importance. At these scales, there exists an almost perfect balance between the downward gravity force and upward pressure gradient force in the atmosphere. This balance is referred to as

"hydrostatic balance". Neglecting the vertical acceleration term from the vertical momentum equation is called the "hydrostatic approximation". An equation set that employs the hydrostatic approximation, in combination with associated simplifications introduced to the remaining equations, is called a "hydrostatic" equation set. For example, on making the hydrostatic approximation, the vertical momentum equation in the two-dimensional fully elastic equations (1.1)-(1.4) for an inviscid, nonrotating adiabatic atmosphere reduces to:

$$\frac{\partial p}{\partial z} = -\rho g. \tag{1.6}$$

Equation (1.6) is the well-known "hydrostatic equation". The majority of atmospheric models applied operationally since the 1950s until the early 1990s solved hydrostatic equation sets, and have evolved into highly sophisticated "hydrostatic primitive equation models". These models describe both nearly-geostrophic and gravity wave motion, and apart from the hydrostatic approximation, also include the spherical geopotential and shallow atmosphere approximations (see the recent discussion by White et al., 2005). Acoustic waves may usually be filtered from a given hydrostatic equation set, by means of applying appropriate lower and upper boundary conditions (e.g. Miller and White, 1984). This implies a significant computational advantage over the fully-elastic equations during the time-integration of a hydrostatic model.

At the typical horizontal resolutions employed by hydrostatic models, circulation with nonhydrostatic features (primarily convection and gravity waves) can not be resolved explicitly. The hydrostatic approximation is therefore valid, but the contribution of nonhydrostatic processes to the momentum, mass and energy budgets of the atmosphere needs to be incorporated into the models statistically. Examples of these statistical representations are cumulus or convective and gravity-wave-drag parameterization schemes. Intensive development and use of hydrostatic models at meteorological centers world wide for more than five decades have caused these models to become highly evolved and sophisticated.

1.1.1.3 The anelastic approximation and nonhydrostatic models

"Nonhydrostatic" equation sets span the fully-elastic equations and all approximated sets in which the vertical acceleration term is retained. Nonhydrostatic models have been used for research purposes since the 1960s (e.g. Ogura and Charney, 1962; Dutton and Fichtl, 1969). The majority of these models made use of the anelastic approximation, which filters sound waves from the resulting equation set, whilst retaining the vertical acceleration term. In its most extreme form (the so called Boussinesq approximation), the anelastic assumption consists of the incompressibility assumption and the assumption that the basic state density field is independent of height (e.g. Mahrt, 1986; Tritton, 1988). The two-dimensional Boussinesq equations for an inviscid nonrotational and adiabatic atmosphere are:

$$\frac{Du}{Dt} + \frac{1}{\rho_0}\frac{\partial p}{\partial x} = 0 \tag{1.7}$$

$$\frac{Dw}{Dt} + \frac{1}{\rho_0}\frac{\partial p}{\partial z} - \frac{\theta^{'}}{\theta_0}g = 0 \tag{1.8}$$

$$\frac{\partial u}{\partial x} + \frac{\partial w}{\partial z} = 0 \tag{1.9}$$

$$\frac{D\theta^{'}}{Dt} + w\frac{d\theta_0}{dz} = 0. \tag{1.10}$$

Here $\theta^{'}$ is the deviation of the potential temperature from a reference state $\theta_0(z)$. The constant basic state density ρ_0 has replaced ρ in the horizontal momentum equation. The vertical momentum equation (1.8) is nonhydrostatic in nature and (1.10) is a form of (1.4) in terms of the potential temperature deviation. Note that the incompressibility assumption results in the simplified continuity equation (1.9), compared to the continuity equation (1.3) of the fully-elastic equations. A linear analysis indicates that the Boussinesq equations are filtered of sound waves. Equation sets with this property are called "anelastic".

Various anelastic equation sets have been derived in which the Boussinesq approximation is relaxed to some extent (Ogura and Phillips, 1962; Wilhelmson and Ogura, 1972; Clark and Peltier, 1977). The absence of sound waves in the solution set of the anelastic equations implies a significant computational advantage over the fully-elastic equations during numerical integration (e.g. Davies et al., 2003). The anelastic approximation, however, at least when applied in height-based coordinates, is not deemed appropriate to simulate flow at large spatial scales. A primary reason for this, is that anelastic equation sets in height-based coordinates significantly misrepresent the internal Rossby modes, at wavelengths typically encountered in NWP and climate simulation models (Davies et al., 2003). Studies with anelastic nonhydrosatic models were therefore mostly concerned with the circulation characteristics of micro to meso-scale circulation systems such as thunderstorms and mountain waves. A closely related group of equations that are filtered of vertically propagating acoustic modes, but retain the Lamb waves, have also been developed (Miller, 1974; Miler and White, 1984; White, 1989; Durran, 1989). Some of these quasi-elastic equation sets seem to be more widely aplicable than the anelastic equations (White, 1989; Davies et al., 2003, also see Chapters 2 and 3).

The approximations introduced to obtain anelastic or quasi-elastic equation sets require that a diagnostic elliptic equation (often in the pressure or geopotential perturbation) needs to be solved at each time step during numerical solution (see Chapter 3). Solving a three-dimensional elliptic equation is computationally very intense (see Chapter 4). It may be noted that the computational

advantage gained by the bigger time steps allowed during numerical solution of anelastic and quasi-elastic equation sets, is partially cancelled by solving the computationally expensive elliptic equation. It may even be argued that an efficient time-splitting scheme for the fully-elastic equations, that avoids solving an elliptic equation, may be computationally just as efficient as using a filtered equation set. However, for the case where the vertical resolution is higher than the horizontal resolution, vertically propagating sound waves are very restrictive on the time-step used in explicit or split-explicit solutions of the fully-elastic equations. Here filtered equations sets offer a clear computational advantage (e.g. Davies et al., 2003; also see Chapter 5). Also, solving an elliptic equation may allow better coupling between the dynamics of a model and physical parameterizations, than would be possible in time-splitting procedure where the use of an elliptic equation is avoided. Thus, solving an elliptic equation may be advantageous during the numerical solution of the fully-elastic equations, which would again render the use of filtered equation sets advantageous from a computational perspective. In the case of global modelling at resolutions where the hydrostatic approximation is valid, the semi-implicit solution of the fully-elastic equations, which allow the use of large time steps and also require the solution of an elliptic equation, is at present regarded as the most efficient solution procedure (e.g. Tapp and White, 1976; Tanguay et al., 1990; Davies et al., 2005; also see Chapter 5).

With the advent of ever faster computers in the 1990s, it became possible to integrate numerical atmospheric models operationally at resolutions where the hydrostatic assumption is not valid (horizontal resolutions finer than 10 km, approximately). However, even present computational constraints limit operational simulations at such fine resolutions to be performed over only relatively small model domains. At most of the large meteorological centers of the world, intensive research was initiated to convert the highly sophisticated and evolved hydrostatic NWP models into nonhydrostatic models (Janjic et al., 2001). This is generally thought to be the best way to proceed in order to obtain a nonhydrostatic model suitable for operational NWP. The well developed framework (physical parameterization schemes, data assimilation procedures, etc.) of the hydrostatic model is retained, but the hydrostatic equation set is replaced with nonhydrostatic (usually the fully-elastic) equations (Gallus and Rancic, 1996; Janjic et al., 2001; Davies et al., 2005). The main alternatives are to develop an existing anelastic model until it is suitable for integration of a wider range of spatial scales and for relatively long integration periods (White, 1989), or to develop a completely new model based on the fully-elastic equations (Tanguay et al., 1990).

Against the background of the worldwide research on nonhydrostatic models, this thesis reports on the development of a dynamic kernel (an equation set and the numerical procedure to solve it) for a new nonhydrostatic atmospheric model. The equation set used has never been applied before in atmospheric

modelling, although closely related equation sets have been used. The unique characteristics and advantages of the equation set are discussed. A numerical solution procedure was developed which allows for efficient numerical solution of the equation set. The suitability of the dynamic kernel to simulate nonhydrostatic circulation in the atmosphere is illustrated by means of a large set of numerical tests. In the following sections, the status quo of atmospheric modelling in South Africa is discussed, and it is motivated why the research effort to develop a new atmospheric model was made.

1.1.2 Numerical atmospheric modelling in South Africa

In the 1960s, a small group of scientists from the Center for Scientific and Industrial Research (CSIR) and the South African Weather Bureau (SAWB) became the first South Africans to develop a three-dimensional NWP model. This grid-point model was applied over the southern hemisphere and formulated in terms of the quasi-geostrophic barotropic equations. When the model was first used operationally in the 1970s, it was integrated over only two or three levels in the vertical because of computational constraints (Riphagen, personal communication). The research group was headed by Burger of the CSIR. In later years, he and Riphagen of the CSIR (and later SAWB), were to write a number of telling papers on how to obtain energy-consistent approximations of the atmospheric equations (Burger, 1991; Burger and Riphagen, 1979, 1981, 1990, 1999). In a study of the equations of motion expressed in an arbitrary vertical coordinate sytem, Burger and Riphagen (1990) retained in the components of the momentum equation the Coriolis terms that vary with the cosine of the latitude (the $\cos\lambda$ terms) (see the recent discussion by White et al., 2005) and other terms not included in the hydrostatic primitive equations. The omission of the $\cos\lambda$ terms has been called the "traditional approximation" (Eckart, 1960). The paper by Burger and Riphagen (1990) preceded a recent international trend in global atmospheric modelling, in which the hydrostatic primitive equations (that contain the traditional approximation) are replaced by more complete quasi-hydrostatic (White et al., 1995) or fully elastic nonhydrostatic (Dudhia and Bresch, 2002; Davies et al. 2005; White et al., 2005) equation sets that contain the full Coriolis force.

In South Africa, the earlier theoretical investigations of Riphagen and Burger led to the the development of a new filtered quasi-geostrophic model based on energy conservation principles (Burger and Riphagen, 1978, 1979; Riphagen and Burger, 1978). The model ran operationally at the SAWB, as a backup model for a hydrostatic primitive equation model that was obtained from an international institution. In the early 1980s, a five-level, split-explicit, hydrostatic primitive equation model for hemispheric prediction was developed at the CSIR (Riphagen, 1984). The performance of the model was evaluated over an 18 month semi-operational run at the SAWB, and it was found to be comparable to that of the international model used at the time. A theoretical investigation

of the computational stability of the model was carried out, which resulted in a longer time step being allowed (Riphagen and Burger, 1986).

The development of the hydrostatic primitive equation model by Riphagen (Riphagen, 1984; Riphagen and Burger, 1986) provided an excellent foundation for future model development in South Africa. Unfortunately, a change in philosophy at the CSIR in the mid-1980s caused the organisation to become more commercially driven, and research into NWP became a low priority. Riphagen joined the SAWB in 1986, however, here it was decided to obtain model codes from international institutions, rather than to maintain and improve a locally developed code. This decision was based on the believe that the NWP research group at SAWB, which was small in comparison to international modelling groups, would not be able to keep up with all the development in NWP taking place at the time. Today, with the vision of hindsight, this decision was probably not the correct one to make. Relatively small research groups that were active at the same time in countries such as Australia, have managed to develop atmospheric models that are today state-of the art in atmospheric modelling. The SAWB, however, has become dependent on Northern Hemisphere organisations for obtaining numerical models. To apply these model codes locally has proven to be a labour intensive task in itself. Expensive license fees also became a reality. To obtain the supercomputers that are required to run the computing-intensive model codes of Northern Hemisphere countries in South Africa, has placed an additional financial burden on the SAWB.

Since the majority of meteorologists in South Africa were employed by the SAWB (and today by the South African Weather Service (SAWS)), only a few further studies in the field of numerical meteorology took place in the country. These were mostly concerned with the numerical schemes and data assimilation systems applied in some of the international models that became operational at the SAWB (e.g. Riphagen, 1989, 1999; Tennant et al., 1997; Riphagen et al., 2002). Today South Africa lacks meteorologists skilled in the field of numerical atmospheric modelling.

Since the late 1980s, a number of international atmospheric models has been run in-house at the SAWB, to obtain numerical predictions on the short to seasonal time scales (e.g. Riphagen, 1993, 2005). Probably the most important of these models is the ETA-model from the National Centers for Environmental Prediction (NCEP), which was first used in 1992. The ETA model became the base model for the daily weather forecasts issued by the SAWB and the later SAWS. The fifth generation Pennsylvania State University-National Center for Atmospheric Research (NCAR) Meso-scale Model (MM5) also runs operationally at the SAWS at present, where it is is mainly used for the generation of aviation forecasting products. In 2004 changes at NCEP persuaded the SAWS to obtain a new model for operational runs, this time from the United Kingdom Meteorological Office (UKMO). The UKMO model (Davies et al., 2005) still needs to

be operationally implemented at the SAWS.

Some universities in South Africa have also managed to obtain and implement model codes from international institutions. At the University of the Witwatersrand (WITS) sensitivity experiments with the Regional Atmospheric Modelling System (RAMS) were performed in the 1980s and 1990s (Crimp et al., 1998). The regional climate model DARLAM (Division of Atmospheric Research Limited Area Model) was also applied to perform climate simulations over southern Africa (Joubert et al., 1999). Since then the climatology group at WITS has found different focus areas. The University of Cape Town (UCT) has become more active in the field, and has been performing climate simulations with MM5 since the 1990s. Recently, five-year MM5 simulations of present and future climate over Southern Africa was performed and described by the UCT group (Hewitson et al., 2005). Computational constraints associated with the expensive-to-integrate MM5 have so far prevented the UCT group from performing longer simulations. Regarding research into numerical atmospheric modelling, the meteorology group at the University of Pretoria (UP) is probably the most active South African university.

1.1.3 Atmospheric modelling activities at the University of Pretoria

Atmospheric modelling research at UP was initiated in the early 1990s when the CSIRO4 atmospheric general circulation model (AGCM) was obtained through a license agreement between UP and the Commonwealth Scientific and Industrial Research Organisation (CSIRO) in Australia. The model was installed on a local super computer (CONVEX C-120). A number of model simulations were performed, including a 20-year control run, as well as selected experiments describing the interaction between the ocean surface and atmosphere over the Indian and Atlantic Oceans (Van Heerden et al., 1995).

In 1995, with the assistance of CSIRO researchers, the CSIRO Mark 2 AGCM with an R21 spectral resolution was installed on a CRAY-EL94 super computer located at the SAWB by Rautenbach. A number of experiments were performed in order to investigate ocean-atmosphere interaction (Jury et al., 1996; Jury et al., 2000). The model's ability to simulate present day climate over southern Africa was also investigated. The AGCM became a useful tool to produce experimental seasonal forecasts of rainfall over the southern African region (Rautenbach, 2003). In his PhD-thesis Rautenbach, with the assistance of Gordan from the CSIRO, introduced a hybrid (sigma/pressure) vertical co-ordinate to the dynamic formulation of the CSIRO9 Mark II AGCM (Rautenbach, 1999). In this study it was indicated that the hybrid vertical co-ordinate system contributes to improved climate simulation in the upper levels of the atmosphere.

Regional climate modelling has numerous unexplored applications over the southern African region (Engelbrecht and Rautenbach, 2000). Seen against this background an agreement was reached in 1999 between UP and the CSIRO to install the regional model DARLAM on a suitable computer at UP. With this prospect in mind the author (Engelbrecht) visited the CSIRO Atmospheric Research during January 2000. With assistance from CSIRO scientists McGregor and Katzfey, DARLAM was installed on a computer at UP. The first climate simulations performed with DARLAM at UP are described by Engelbrecht (2000) and Engelbrecht et al. (2002).

In 2002, intensive research on atmospheric model development commenced at the University of Pretoria, as part of a project sponsored by the South African Water Research Commission (WRC). During the course of the project, the hydrostatic Conformal-Cubic Atmospheric Model (C-CAM) of CSIRO was implemented on computers at UP. Various sensitivity studies were performed in order to improve the model's ability to simulate rainfall over southern Africa (Rautenbach et al., 2005). With the assistance of CSIRO scientists McGregor and Thatcher, the research group at UP managed to run C-CAM operationally for routine NWP over southern Africa (Rautenbach et al., 2005). UP is the first institution in South Africa, other than the SAWS, to accomplish this. An important aspect of the WRC project, was the development of a nonhydrostatic kernel for a new atmospheric model, which contributed to the development of an a nonhydrostatic kernel for C-CAM. The present thesis contributed largely to this research aspect of the WRC project (Rautenbach et al., 2005). In a subsequent WRC project concerned with the hydrological impact of global warming on South Africa, C-CAM was also used to perform two 30-year simulations of climate and climate change over Southern Africa (Engelbrecht, 2005).

1.2 Motivation for the research

1.2.1 Recent developments in nonhydrostatic atmospheric modelling

The development of nonhydrostatic models has been ongoing for about four decades. It started with different mesoscale investigations (e.g. Ogura and Charney, 1962; Dutton and Fichtl, 1969; Miller and Pearce, 1974; Tapp and White, 1976; Klemp and Wilhelmson, 1978; Pielke, 1984). The resolution of operational NWP models, however, has until fairly recently been limited by computing power and time constraints of the operational environment to resolutions where the hydrostatic approximation is almost perfectly valid. Operational forecasts therefore mostly relied on hydrostatic models until recently. With computer systems becoming faster and more affordable over the past decade, a corresponding increase in the resolution of both NWP and climate simulation models occurred. This, as well as the growing requirements of model precision, has brought the transition of the highly developed existing hydrostatic models

to nonhydrostatic models into the limelight. Over the past decade many atmospheric research institutions have started to replace operational hydrostatic models with nonhydrostatic versions (Gallus and Rancic, 1996; Davies et al., 2005). Model upgrading is much easier if connections with the existing hydrostatic model is preserved during the development of the nonhydrostatic model (Janjic et al., 2001). In this regard, preserving the vertical coordinate of the hydrostatic model (usually some type of pressure coordinate) is essential.

With operational model resolutions now beyond the hydrostatic limit (less than about 10 km in the horizontal) over relatively small domains, convection is at least partially resolved (and partially explicitly simulated) by the nonhydrostatic models. Convection can probably only be fully resolved at model resolution of about two orders of magnitude higher - that is, about 100 m in the horizontal. It is therefore likely that for many years to come, operational nonhydrostatic models will function at resolutions where convection can only be partially resolved. The use of convection parameterization schemes at these resolutions is a relatively unexplored study field in atmospheric modelling. In fact, the parameterization schemes applied in hydrostatic models have generally been designed to function at resolutions where convection cannot be resolved at all. These parameterization schemes need to be reviewed and probably modified in order to function well beyond the hydrostatic limit. Theoretical studies of the explicit simulation of moist convection is another growing study field and nonhydrostatic models are a primary tool for these investigations. Explicit simulations of moist convection will benefit the design of convection parameterization schemes for application at model resolutions where convection can not be fully resolved.

Meteorological research in South Africa would greatly benefit by having easy access to a nonhydrostatic model. Setting up high-resolution simulations requires thorough knowledge of the nonhydrostatic model's code. Since the codes of international models are extensive and highly evolved, using such models correctly requires thorough research in itself. These models are usually formulated in terms of certain map projections of Earth, which complicates the design of numerical experiments by users not fully familiar with the model equations and the projection used. As an alternative to studying the code from an international model, a new nonhydrostatic model may be developed from scratch. Such a research effort might simultaneously contribute to the development of an international model, for example, from hydrostatic to nonhydrostatic dynamics.

To summarize, the development of a new nonhydrostatic model, and/or thorough knowledge of an existing nonhydrostatic model code, will make it possible for meteorologists in South Africa to contribute to four important, interlinked and growing fields in numerical atmospheric modelling:

- The development of nonhydrostatic models in general (equation sets, vertical coordinates, numerical solution procedures, etc.).
- Conversion of existing hydrostatic (mostly pressure-based) hydrostatic models into nonhydrostatic models.
- The study of moist convection by means of explicit numerical simulations with a nonhydrostatic model.
- The development of convection parameterization schemes for nonhydrostatic models that are applied at resolutions where convection is only partially resolved.

1.2.2 Nonhydrostatic circulation systems over South Africa

Atmospheric circulation systems exhibiting nonhydrostatic features frequently occur over southern Africa. In particular, severe thunderstorms often occur over the Highveld and eastern escarpment of South Africa (Garstang et al., 1987), whilst mountain waves are regularly observed over the Lesotho Drakensberg (De Villiers, 1998) and the mountains of the southwestern Cape (see Fig. 1.2). The characteristics of these systems have never been studied by means of high-resolution, nonhydostatic model simulations. The reasons for this deficiency in meteorological studies over South Africa are clear: the non-existence of a locally developed nonhydrostatic model, and a shortage of local meteorologists skilled in the use of an international nonhydrostatic model. In this subsection of the thesis, the most important nonhydrostatic circulation systems occuring over South Africa are reviewed, and it is illustrated that there is a need for nonhydrostatic model simulations to aid the study of the characteristics of these systems.

1.2.2.1 Convective rainfall over South Africa

The Summer rainfall region of South Africa receives most of its precipitation in the form of convective rainfall. Quite often the convection occurs east of upper air troughs that pass over the country from west to east. In fact, 80% of the rainfall over the summer rainfall region occurs when tropical-temperate troughs (a westerly trough in combination with an easterly wave) moves over southern Africa (Harrison, 1984, 1986). During these events tropical air enters the country, mostly from Botswana or Namibia. The thunderstorms that occur under these circumstances are organised in a north-west to south-east alignment, extending from Namibia to the east coast of South Africa. However, convective thunderstorms also occur frequently over the Highveld and eastern escarpment regions purely in response to surface heating and low-level convergence. Thus, convection over South Africa may occur under a wide range of circumstances. However, surprisingly little research has been performed up to date on the climatological properties of South African thunderstorms. In particular, the dynamical characteristics of thunderstorms occurring in South Africa are not well understood.

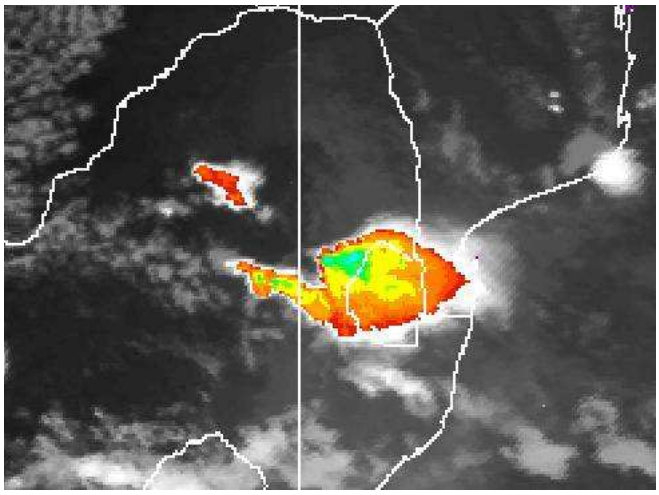

Figure 1.1: A Meteosat 7 colour enhanced infrared satellite image showing a severe thunderstorm over Swaziland and the Lowveld of South Africa. Storm splitting may have occured, since two overshooting tops are indicated by the light blue regions (coldest cloud top temperatures).

1.2.2.2 Thunderstorms in South Africa

There have been few investigations that attempted to quantify the typical frequencies and intensity of thunderstorms over South Africa, and no proper thunderstorm climatology is available. Most studies have been concerned with the frequency of occurrence of hail-producing thunderstorms. These studies largely relied on the use of radar data (Carte and Held, 1987; Held, 1978; Held, 1982). The radar-based and earlier studies (Schulze, 1972), indicate that there are typically more than 80 rain days over the high plateau of KwaZulu-Natal, about 70 over Gauteng, and between 20 and 30 over the KwaZulu-Natal coastal areas. Hail-producing thunderstorms annually destroy about 1% of South Africa's crops (Visser, 2000) and a single hail event may cause damage of millions of rands to buildings and cars (Visser, 2000). There are no formal studies on the dynamics of severe thunderstorms over South Africa available in the literature. The little that is known about the dynamics of these storms, was derived from general thunderstorm circulation theory (e.g. Klemp, 1987; Doswell, 1991; Holton, 1992) applied to the southern hemisphere (Doswell, 1991; De Coning et al., 2000) and from radar-based case studies of individual storms (Visser, 2000; De Coning et al., 2000). Figure 1.1 shows an outbreak of wedged-shaped (possibly severe) thunderstorms over the Drakensberg mountains in South Africa.

A wind that turns counter clockwise with height (backs) is typical of the development of rotating thunderstorms in the southern hemisphere (e.g. Doswell, 1991; Holton, 1992). This type of wind profile commonly occurs over eastern

South Africa in the austral summer. Ridging high-pressure systems would typically induce a north-easterly low-level flow over eastern South Africa, with an upper air trough simultaneously causing north-westerly flow at 700 and 500 hPa. Often a jet stream, or at least very strong westerly winds, are to be found at the same time at about 200 hPa. Thus, the development of rotation in thunderstorms occurring over eastern South Africa, and the associated storm splitting (e.g. Holton, 1992) should be fairly common. Unfortunately, the absence of Doppler radar systems in the country hampers the identification and study of these events. However, with high-resolution Meteosat Second Generation (MSG) (Meteosat 8) satellite images recently becoming available in South Africa, the identification of the occurrence of at least storm-splitting is possible. The long record of ordinary radar data that is available for the Highveld and eastern Free State is also a valuable source of information to gain more insight into the dynamics of South African thunderstorms. However, the development of rotating storms is less easily identified using ordinary radar data, and the ideal solution for the study and real-time forecasting of rotating thunderstorms would be use of Doppler radar in the country (De Coning et al., 2000). A high-resolution nonhydrosatic numerical atmospheric model may be used to aid the study of the dynamics of rotating and severe thunderstorms occurring over South Africa, in combination with the radar and satellite data.

Supercell thunderstorms in South Africa

Supercell thunderstorms (rotating storms associated with heavy rainfall, severe hail and sometimes tornadoes) rarely occur in South Africa (De Coning et al., 2000; Admirat et al., 1985). This statement is supported by studies concerned with the nature of hail producing thunderstorms over South Africa (Held, 1978; Held, 1982; Carte and Held, 1978). However, the typical wind profile associated with the development of the severe cyclonic (clockwise) rotating supercell thunderstorms in the southern hemisphere (Doswell, 1991; De Coning et al., 2000), occurs fairly often over eastern South Africa (see the previous paragraph). Other environmental conditions apparently prevent rotating thunderstorms from developing into severe supercell storms on a regular basis. However, Visser (2000) argues that the frequency of occurrence of supercell thunderstorms over South Africa may be underestimated due to the poor observational network in the country. These aspects require further study, and environmental conditions favourable for supercell formation over South Africa need to be quantified. A high-resolution nonhydrostatic model may be of great help in such investigations.

Tornadoes

A tornado is defined as a violently rotating column of air with small diameter extending from a thunderstorm to the ground (Goliger et al., 1997). Tornadoes are often accompanied with damaging winds, heavy rainfall and hail. The CSIR

data base of tornadic activity (Goliger et al., 1997) contains 200 reports of tornadic events over South Africa, dating from 1905 to 1996. Most tornadoes have been observed over the eastern escarpment areas and over Gauteng (probably as a result of the high population density in the latter area). Most of these tornadoes occurred between November and March, typically between 16:00 and 19:00 South African Standard Time (SAST) (Goliger et al., 1997). They varied in intensity from F0 to F3 (see Fujita, 1973a,b for a discussion of the Fujita-Pearson scale to evaluate tornado intensity). The classification of tornadoes in the above data base was mostly based on assesessment of the damage caused. Many of the severe storms that occur in the country are never surveyed for damage or evidence of tornadoes. In fact, the mere identification of tornadic events occuring in South Africa is challenging (De Coning and Adam, 2000) and their frequency of occurrence is most probably underestimated.

During the 1998/99 summer season, several severe thunderstorms occurred over the eastern escarpment. At least three of these severe storm events were accompanied by tornadoes (De Coning and Adam, 2000). The circulation properties of two of the tornadic events, occurring at Harismith and Mount Aliff, were studied in some detail by De Coning and Adam (2000) and Visser (2000). The study of the Harismith tornado utilized the hydrostatic ETA model at 48 km horizontal resolution over South Africa. The model was only found to be helpful in identifying the area where thunderstorms occurred on the specific day. The radar data were more illuminating, and showed evidence that storm splitting (a feature associated with rotation in severe thunderstorms, Klemp, 1987; Holton, 1992) occurred. The surface observation network, in combination with model data, showed evidence that the wind was backing with height (which is inducive to the formation of clockwise rotation in thunderstorms in the southern hemisphere). For the Mount Aliff tornado, De Coning and Adam (2000) found that typical stability and wind shear indices, as simulated by the ETA model, correctly identified the area where the tornado occurred as one favourable for severe thunderstorms and/or tornadoes. The severe thunderstorm that spawned the tornado was too far away from the nearest radar station for thorough analysis by means of radar data.

The occurrence of an intense tornadic event may cause wide-spread damage and loss of life. The Harismith tornado, for example, was estimated to have caused damage of between between 3 and 4 million rands; 21 people died and 350 were injured by the Mount Aliff tornado (De Coning and Adam, 2000). More research is needed in order to identify the atmospheric characteristics that are inducive of tornadic events over South Africa. A nonhydrostatic model may be invaluable in such investigations.

1.2.2.3 Mountain waves

When the prevailing wind over the Lesotho Drakensberg mountains is northwesterly, mountain wave clouds are often observed in the lee of the mountains.

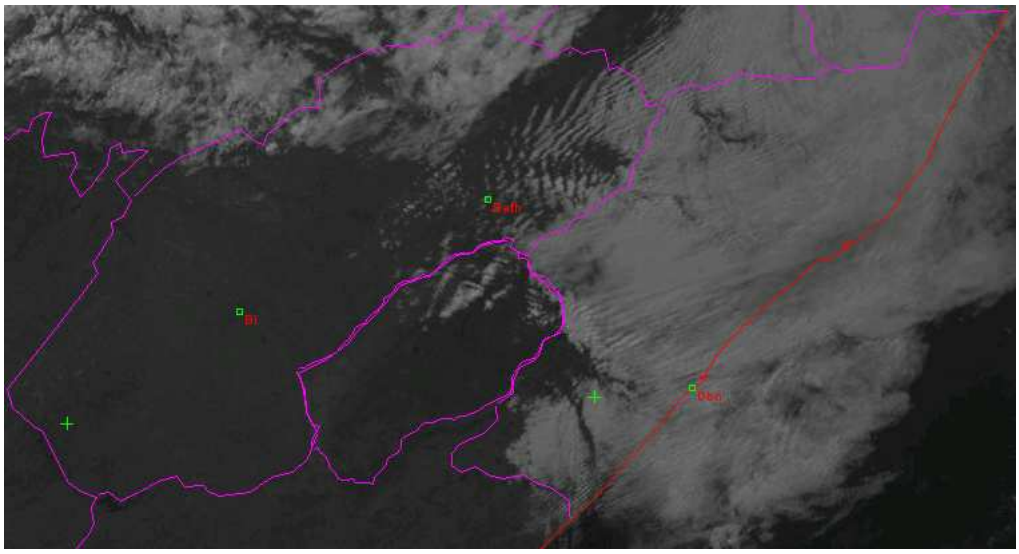

Figure 1.2: A Meteosat 8 visible satellite image showing the formation of mountain waves downstream of the Drakensberg region of South Africa and Lesotho.

These clouds form when the air mass present over the mountain is stably stratified. As air is forced to rise over the mountain barrier, a series of oscillations is induced as the air decelerates and accelerates in the stable environment. If the air is sufficiently moist, condensation takes place where the air is rising, in this way forming the mountain wave clouds. If the air is not sufficiently moist (as is often the case with north-westerly flow over the Lesotho Drakensberg) mountain waves may still develop, without the mountain wave clouds being present. Aircraft flying over the area under such conditions may experience clear air turbulence (CAT) in the rising and descending portions of the mountain waves. The occurrence of CAT over the Lesotho Drakensberg has caused injuries to passengers in aircrafts flying over the area on a number of occasions (De Villiers, 1998, 2001). The synoptic-scale conditions favourable for the occurrence of mountain waves over the Lesotho Drakensberg have been studied by De Villiers (1998; 2001). Except for these studies, no attempt has been made to quantify the stability and wind shear conditions conducive to the occurrence of mountain waves over the Lesotho Drakensberg. A nonhydrostatic model is essential to the study the dynamics of these waves in some detail.

It may also be noted that mountain waves occur frequently over the mountains of the southwestern Cape, in the north-westerly flow ahead of an approaching cold front. Such an event is depicted in Fig. 2, an infrared MSG satellite image which shows the occurrence of mountain waves over a region of more than 100 km^2 over the south western Cape. Although weather forecasters in the country are well aware of the potential aviation hazards implied by events like this (De

Villiers, 1998, 2001), the dynamics of the south-western Cape mountain waves, as for the Lesotho mountain waves, remain to be the studied.

1.2.2.4 Modelling nonhydrostatic circulation systems occurring over South Africa

Running a NWP model operationally at resolutions beyond the hydrostatic limit over a typical nested model domain including South Africa, is not feasible within the bounds of present computing resources available in the country. However, for research purposes, studies at these resolution are possible, at least over limited areas of the country (the Highveld, for example). It should be possible to apply some of the nonhydrostatic atmospheric models used in South Africa for studies of this kind, in particular, the MM5 model may be used. To set up a nonhydrostatic model at high resolution over a specific area, however, is fairly challenging. Multiple nesting is required, and to initialize the atmospheric state for a specific experiment, careful consideration is needed to prevent the generation of spurious gravity and sound waves (Mendez-Nunez and Carroll, 1994). There is currently a lack of expertise in the country to design experiments of this kind. Still, there is a clear need for research on the application of an existing or a newly developed nonhydrostatic model in order to study the characteristics of thunderstorms and mountain waves that occur over South Africa. This study is an attempt to develop modelling capacity for future investigations into the characteristics of nonhydrostatic circulation systems occurring over South Africa.

It may finally be noted that studies into air quality standards over South Africa may benefit from the application of a high-resolution nonhydrostatic model. At present the input of air pollution dispersion models in South Africa consists largely of surface observations, since upper air balloon soundings and vertical wind profile observations by sodar are only available at a small number of locations in the country. The input from the ETA model, which runs operationally at the SAWS at a horizontal resolution of 32 km over the country, is used as aditional input. However, high-resolution (horizontal resolutions of about 1 km or finer over the Higveld, for example) simulations of the three-dimensional wind field in the boundary layer may be used as input for a Lagrangian dispersion model, in this way improving simulations of pollution advection and dispersion. This provides further motivation for a research effort aimed at developing nonhydrostatic modelling capacity in the country.

1.3 Objectives of the research

Taking into account the status of numerical atmospheric modelling in South Africa, the research links between UP and CSIRO Atmospheric Research, the current worldwide research into the development of nonhydrostatic models, and

the potential applications of nonhydrostatic models over southern Africa, the research outlined in this thesis has two main objectives:

To identify a nonhydrostatic equation set in terrain-following pressure-based (σ) coordinates suitable for implementation in an existing hydrostatic σ coordinate model, and to study the characteristics of the equation set.

This was attained through a literature study of the large variety of nonhydrostatic equation sets developed over the last four decades. Three groups of nonhydrostatic equation sets were considered: fully-elastic, quasi-elastic and anelastic. Most existing hydrostatic NWP and climate simulation models employ pressure-based vertical coordinates. The most convenient way of obtaining nonhydrostatic versions of these models is by the use of a formulation of nonhydrostatic equations cast in pressure-based coordinates. In particular, the development of a nonhydrostatic equation set in pressure-based terrain-following coordinates, may facilitate the conversion of the hydrostatic CSIRO model C-CAM to nonhydrostatic dynamics. Therefore the literature studied focussed on the different nonhydrostatic equation sets formulated in pressure-based coordinates. The research led to the formulation of a quasi-elastic equation set in σ-coordinates that has not been used before. The unique characteristics of this equation set were studied, largely by the use of linear perturbation analysis and numerical experiments.

To develop a dynamic kernel for a new nonhydrostatic atmospheric model based on the quasi-elastic equation set.

A time-split semi-Lagrangian method was developed to solve the quasi-elastic equation set, in two or three spatial dimensions. The method is shown to be more efficient than the explicit methods used previously to solve similar nonhydrostatic equation sets. The three-dimensional model code that was developed opens the door for further model development and capacity building in the field of numerical atmospheric modelling, at UP and in South Africa.

1.4 Organisation of the report

The present Chapter sets the scene for the thesis and motivates why the research effort to develop a nonhydrostatic kernel for a new atmospheric model was made. In Chapter 2 the different types of vertical coordinates that may be used to formulate nonhydrostatic equation sets are reviewed. The use of pressure-based coordinates is discussed in particular, since a pressure-based nonhydrostatic model is formulated and applied in the thesis. The fully-elastic (unapproximated) equations in pressure and σ coordinates are stated, and it is motivated why these equation sets are not regarded suitable for numerical atmospheric modelling. The fully-elastic equations based on the hydrostatic pressure field

are then stated, and it is explained why this equation set has become a popular choice for the development of universal models. Different approximated non-hydrostatic pressure-based equation sets, which may be termed anelastic and quasi-elastic, are reviewed. These equation sets employ vertical coordinates that are based on the full pressure field. They offer computational advantages over the fully-elastic equations, but seemingly at the cost of a loss in universal applicability. The scales of motion that the different approximated sets apply to are stated, and the computational advantages offered by each set are mentioned.

In Chapter 3 nonhydrostatic models employing vertical coordinates based on the full (nonhydrostatic) pressure field as vertical coordinate are studied. The first model of this kind, formulated in p coordinates, was developed by Miller (1974) and Miller and Pearce (1974). The characteristics of the Miller-Pearce (MP) model, which is limited for application at the meso-scale, are reviewed. The MP model in p coordinates was extended by White (1989) for application at larger-scales. This equation set of White (1989) is transformed to σ coordinates in Chapter 3. An elliptic equation that is used to diagnose the geopotential distribution is also derived. The characteristics of the σ coordinate equation set are studied, largely by means of linear stability analysis. It is shown that the equation set implies an energy equation similar to that of the hydrostatic equations, with the additional representation of vertical kinetic energy. The equations are shown to be filtered of vertically propagating acoustic waves and it is illustrated that the Lamb waves in the model are significantly retarded. This implies that the derived equation set offers computational advantages over other nonhydrostatic equation sets based on the fully-elastic equations.

A time-split, semi-Lagrangian procedure to solve the quasi-elastic equations in two or three spatial dimensions on a nonstaggered grid is developed in Chapter 4. The semi-Lagrangian method used to calculate the departure points of air parcels is discussed, as well as the associated interpolation schemes applied in two or three spatial dimensions. A forward-backward scheme that handles the fast travelling waves during the adjustment step is described. It is shown that it is essential to apply a spatial filter at the smallest resolvable scales, in order to avoid problems with stationary two-grid-interval waves. An iterative procedure is formulated which efficiently solves the elliptic equation in the geopotential, in two or three spatial dimensions. In Chapter 5 the accuracy and stability properties of the split semi-Lagrangian solution procedure applied to the quasi-elastic equations in σ coordinates is demonstrated with a series of convective bubble experiments in two and three spatial dimensions. The experiments also function to illustrate that the dynamic core functions well at resolutions far beyond the hydrostatic limit. A new numerical test was designed, in which the development of rotation in an environments with wind shear is simulated. The results obtained for this test comform well with the linear theory of storm splitting. Conclusions on the research are drawn in Chapter 6.

1.5 New aspects of the research

The most important novel aspects of the research may be summarized as follows:

- The formulation of a nonhydrostatic equation set in terrain-following coordinates based on the full (nonhydrostatic) pressure field - an equation set which has not been used before in atmospheric modelling.
- A theoretical analysis of the derived equation set, showing its unique characteristics and advantages. The analysis indicates the equation set may be termed quasi-elastic.
- The development of a novel time-split semi-Lagrangian solution procedure which efficiently solves the quasi-elastic equations on a nonstaggered grid.
- The first numerical simulations of bubble convection in three spatial dimensions. A new numerical test was designed, in which nonhydrostatic splitting flow is simulated in an environment with vertical wind shear.

Thus, a novel dynamic kernel has been developed, providing the framework for a new locally-developed meso-scale atmospheric circulation model.

Chapter 2

Nonhydrostatic models in pressure-based coordinates

2.1 Introduction

Many different types of vertical coordinate systems have been applied successfully in atmospheric modelling (see, for example, Haltiner and Williams, 1980). Pressure-based vertical coordinates have been the most popular choice, for operational weather prediction and climate simulation, over the last four decades. By pressure-based coordinates are meant "pure" pressure coordinates (Eliassen, 1949), and terrain-following pressure-scaled (σ) coordinates (Phillips, 1957). Pressure-based vertical coordinates offer some unique advantages over other vertical coordinate systems. Firstly, atmospheric measurements are taken at constant pressure levels during balloon soundings. Interpolation of the observed variables at constant pressure levels to model levels in the vertical is most accurately and conveniently achieved if the model is using pressure-based coordinates. More importantly though, is that the atmospheric equations in pressure coordinates assume a simpler form than in most other coordinate systems (e.g. Miller and White, 1984; Room et al., 2001). This is true in particular for hydrostatic primitive equation models cast in pressure coordinates. In this framework, the atmosphere is non-divergent and the continuity equation reduces to a diagnostic equation (see, for example, Haltiner and Williams, 1980; Holton, 1992). In pressure-based coordinates, density is also eliminated from the prognostic equations, which is advantageous since density is not readily measured in the atmosphere. With the elimination of density, the momentum equations and thermodanamic energy equation simplify in addition to the simplifications to the continuity equation. Finally, many conceptual models used in weather forecasting have been developed in terms of the distribution of certain variables at constant pressure levels.

The popularity of the hydrostatic primitive equation models for operational weather prediction and climate simulation during the last four decades has been strongly linked to computational constraints of the operational environment (see the discussion in Chapter 1). These constraints implied that models could only be integrated operationally at resolutions where the hydrostatic approximation is valid (resolutions coarser than approximately 10 km, e.g. Daley, 1988). Therefore, until recently, all operational models were hydrostatic models. As discussed in the previous paragraph, pressure-based vertical coordinates are the most popular choice for application in operational hydrostatic primitive equation models. Thus, the constraints of the operational environment, and the advantages offered by pressure-based coordinates to hydrostatic modelling, have made hydrostatic primitive equation models in pressure-based coordinates the natural choice for operational atmospheric modelling. Only in the 1990s did faster computers start to allow simulations beyond the hydrostatic limit, although only over limited areas of Earth. Even at the large meteorological centers of the world, global (nonhydrostatic and hydrostatic) weather forecasting models are at present still integrated at resolutions where the hydrostatic assumption is valid.

Despite the computational constraints on obtaining operational simulations beyond the hydrostatic limit, the development of nonhydrostatic models has been ongoing for more than four decades. Most of these models were developed purely for research purposes, to study the properties of meso-scale circulation systems exibiting nonhydrostatic circulation features (e.g. Ogura and Charney, 1962; Dutton and Fichtl, 1969; Miller and Pearce, 1974; Tapp and White, 1976; Klemp and Wilhelmson, 1978; Pielke, 1984). The majority of nonhydrostatic models developed employed vertical coordinate systems based on the geometric height (z-based coordinate systems) (e.g. Ogura and Charney, 1962; Ogura and Phillips, 1962; Lipps and Hemler, 1982; Shutts and Gray, 1994; Smolarkiewicz et al., 2001). A recent review of the various types of z-based coordinate models, from the perspective of a normal mode analysis, is given by Davies et al. (2003). An important conclusion from this study is that only the fully-elastic z-based equations are suitable for modelling at spatial scales ranging from the micro-scale to the large-scale. All approximate sets, including anelastic, quasi-elastic and hydrostatic z-based equations, appear to have limitations to the spatial scales for which they may be applied (Davies et al., 2003).

In 1974 Miller developed the first nonhydrostatic model employing a pressure-based vertical coordinate. The model was used to study cumulonimbus convection by Miller and Pearce (1974) and became known as the Miller-Pearce (MP) Model. An important property of the MP model is its anelastic nature in pressure coordinates. The filtering of sound waves is achieved by introducing approximations to the fully-elastic pressure coordinate equations from the basis of a scale analysis (Miller, 1974; also see section 2.3.1). Miller and White (1984) derived the MP model from the basis of a formal power series expansion,

and also stated the quasi-elastic σ coordinate equivalent of the model. The MP model in presure coordinates and also in σ coordinates was used in numerous studies of the numerical simulation of convection and airflow over mountains (e.g. Miller and Pearce, 1974; Xue and Thorpe, 1991; Miranda and James, 1992).

In the early 1990s it was realized that the operational use of models beyond the hydrostatic limit would soon become computationally feasible (e.g. Tanguay et al., 1990). It was envisaged that the new generation of models would be able to simulate atmospheric proceses ranging from the micro- to the large-scale. By this time the hydrostatic primitive equation models, all cast in pressure-based vertical coordinates, were highly evolved and sophisticated (Janjic et al., 2001). It was realized that the most convenient way of obtaining nonhydrostatic models suitable for operational use, would be to convert existing hydrostatic pressure-based models to nonhydrostatic models (Laprise, 1992; Bubnova et al., 1995). The only pressure-based nonhydrostatic model developed at the time was the MP model. However, originally designed to obtain simulations of nonhydrostatic micro- and meso-scale processes (Miller, 1974), the MP model is not deemed for appropriate for simulations at larger scales (White, 1989; see also section 2.3.1 and Chapter 3). In fact, it is believed that for a model to be able to simulate atmospheric motion at spatial scales ranging from the micro- to the large-scale, it needs to be be fully-elastic (Laprise, 1998; Davies et al., 2003; Davies et al., 2005). However, the suspicion that the full pressure field may be singular in the case of severe vertical acceleration (Laprise, 1992, 1998), has prevented the development of a fully-elastic model based on the full pressure field as vertical coordinate. Instead, Laprise (1992) suggested the use of hydrostatic pressure as vertical coordinate for the fully-elastic equations. This novel idea soon became popular, and a number of fully-elastic pressure-based vertical coordinate models were developed (e.g. Bubnova et al., 1995; Gallus and Rancic 1996; Janjic et al., 2001). It was even suggested that the fully-elastic equations based on the hydrostatic pressure is the only manageable option for operational nonhydrostatic NWP (Bubnova et al., 1995). However, a fully-elastic global model empoying a z-based vertical coordinate, suitable for both operatonal NWP and climate simulation, has recently been developed at the UKMO (Davies et al., 2005).

The purpose of the present chapter is to introduce the different nonhydrostatic equation sets cast in pressure-based vertical coordinates. These include the fully-elastic equations based on the hydrostatic pressure field, and the MP model that is based on the full pressure field. Other variants discussed include the equations used in the MM5 model (Dudhia, 1993; Dudhia and Bresch, 2002), and an anelastic σ coordinate equation set that was developed from the MP model (Room et al., 2001). Most importantly, however, is an extension of the MP model in pressure coordinates by White (1989), that is presented in section 2.3.3. This equation set is discussed in much more detail in Chapter 3, and its

σ coordinate equivalent forms the basis of the new numerical model developed in Chapter 4. Against the background of the various types of pressure-based vertical coordinates that have been developed, the particular choice of vertical coordinate and associated equation set applied in the present study is motivated in section 2.4.

2.2 Fully elastic equations in pressure-based vertical coordinates

In this and the following sections, the various nonhydrostatic equation sets employing pressure-based coordinates are stated. The emphasis is on showing how the MP model and its extension by White (1989) are related to other nonhydrostatic pressure-based equation sets. For the sake of simplicity, the Coriolis, friction and diabatic terms are neglegted, and the motion is taken to be independent of the transverse coordinate y. In practical modelling applications, the Coriolis, friction and diabatic terms must be included and the motion generally also depends on y. Extension to these more general cases is straightforward and will not be described here. However, with meso-scale applications in mind, a more general three-dimensional quasi-elastic equation set including Coriolis terms is formulated in Chapter 3, for the specific choice of vertical coordinate used in the thesis.

2.2.1 The fully-elastic equations with the full pressure field as vertical coordinate

The fully-elastic equations (1.1) to (1.4) with geometric height as vertical coordinate, for a nonrotating, frictionless and adiabatic atmosphere, have been stated in chapter 1. These equations may be transformed to full pressure coordinates to obtain (Miller and White, 1984):

$$\frac{Du}{Dt} + (1+\epsilon)\left(\frac{\partial \phi}{\partial x}\right) = 0, \tag{2.1}$$

$$\frac{RT}{p} + (1+\epsilon)\left(\frac{\partial \phi}{\partial p}\right) = 0, \tag{2.2}$$

$$\frac{\partial u}{\partial x} + \frac{\partial \omega}{\partial p} - \frac{D\ln(1+\epsilon)}{Dt} = 0, \tag{2.3}$$

$$\frac{DT}{Dt} - \kappa\frac{T}{p} = 0. \tag{2.4}$$

Here p denotes the full (true) pressure field, which may be nonydrostatic. $\omega = Dp/Dt$; $\phi = gz$ (the geopotential); $D/Dt = \partial/\partial t + u\partial/\partial x + \omega\partial/\partial p$; all partial differentiations with respect to x and t are carried out at constant p, whilst ϵ is a measure of the vertical acceleration defined as

$$\epsilon \equiv \frac{1}{g}\frac{Dw}{Dt} = \frac{1}{g^2}\frac{D\phi}{Dt}. \tag{2.5}$$

2.2.2 The fully-elastic equations in σ coordinates based on the full pressure field

The σ coordinate based on the full pressure field may be defined as

$$\sigma = \frac{p}{p_{surf}}, \tag{2.6}$$

whith p the full (possibly nonhydrostatic) pressure and p_{surf} the corresponding surface pressure. Following Miller and White (1984), (2.1) to (2.4), or alternatively (1.1) to (1.4), may be transformed to σ coordinates defined by (2.6) to obtain:

$$\frac{Du}{Dt} + (1+\epsilon)\left(\frac{\partial\phi}{\partial x}\right) + RT\left(\frac{\partial \ln p_{surf}}{\partial x}\right) = 0, \tag{2.7}$$

$$\frac{RT}{\sigma} + (1+\epsilon)\left(\frac{\partial\phi}{\partial\sigma}\right) = 0, \tag{2.8}$$

$$\frac{\partial u}{\partial x} + \frac{\partial\dot{\sigma}}{\partial\sigma} + \frac{D\ln p_{surf}}{Dt} - \frac{D\ln(1+\epsilon)}{Dt} = 0, \tag{2.9}$$

$$\frac{DT}{Dt} - \kappa T\left(\frac{\dot{\sigma}}{\sigma} + \frac{D\ln p_{surf}}{DT}\right) = 0. \tag{2.10}$$

Here

$$\frac{D}{Dt} = \frac{\partial}{\partial t} + u\frac{\partial}{\partial x} + \dot{\sigma}\frac{\partial}{\partial\sigma}; \tag{2.11}$$

all partial derivatives with respect to t and x are carried out at constant σ and $\dot{\sigma} = D\sigma/Dt$, whilst $\phi = gz$ is the geopotential; ϵ is defined by (2.5).

It would be possible to develop a fully-elastic nonhydrostatic model that uses the full pressure field, or a terrain following coordinate based on the full pressure field, as vertical coordinate. However, such a coordinate runs the risk of becoming singular in cases of severe vertical accelerations (Laprise, 1992; Bubnova et al., 1995; Laprise, 1998). Therefore, a fully-elastic numerical model using a vertical coordinate based on the full pressure field has never been realized.

2.2.3 The fully-elastic equations in σ coordinates based on the hydrostatic pressure field

The use of the hydrostatic pressure as vertical coordinate for fully elastic models was first suggested by Laprise (1992). Using the hydrostatic pressure as vertical coordinate avoids the potential singularity of coordinates based on the full pressure field. This coordinate system has the additional advantage that it leads to a formulation of the fully elastic equations that closely parallels that of the hydrostatic primitive equation models using pressure based coordinates (Laprise, 1992). Thus, by the choice of hydrostatic pressure as vertical coordinate, the conversion of a hydrostatic model formulated in terms of the pressure field to a nonhydrostatic model can be conveniently achieved (Laprise, 1992; Bubnova et al., 1995; Gallus and Rancic, 1996).

Laprise (1992) and Bubnova et al. (1995) stated a form of the fully elastic equations in a generalized vertical coordinate that is monotonically linked to the pressure that would have occurred, should the atmosphere have been in hydrostatic equilibrium. An alternative formulation, directly based on the hydrostatic pressure as vertical coordinate, is given by Janjic et al. (2001). In the latter formulation, the σ coordinate is defined by

$$\sigma = \frac{\pi - \pi_T}{\pi_{surf} - \pi_T}. \tag{2.12}$$

Here π represents the "actual" hydrostatic pressure that would have occurred, should the atmosphere have been in hydrostatic equilibrium. Thus, π is a function of space and time, whilst π_{surf} and π_T are the hydrostatic pressures at the surface and at the top of the model atmosphere. In terms of the vertical coordinate defined by (2.12) the formulation of the fully-elastic, two-dimensional equations for an adiabatic, frictionless, nonrotational atmosphere is (see Janjic et al., 2001):

$$\frac{Du}{Dt} = -(1+\epsilon)\frac{\partial \phi}{\partial x} - \alpha \frac{\partial p}{\partial x}, \tag{2.13}$$

$$\frac{Dw}{Dt} = g\left(\frac{\partial p}{\partial \pi} - 1\right), \tag{2.14}$$

$$\frac{D\mu}{Dt} + \mu\left(\frac{\partial u}{\partial x} + \frac{\partial \dot{\sigma}}{\partial \sigma}\right) = 0, \tag{2.15}$$

$$c_p \frac{DT}{Dt} = \alpha \frac{Dp}{Dt}. \tag{2.16}$$

Here (2.13) is the horizontal momentum equation, (2.14) the vertical momentum equation, (2.15) is the continuity equation and (2.16) the thermodynamic energy equation. As before, ϵ is defined by (2.5). The symbols for the full (nonhydrostatic) and hydrostatic pressures are p and π, respectively. The total

derivative is defined by (2.11) , but with σ defined by (2.12). The vertical velocity may be written as $w \equiv (1/g)\, D\phi/Dt$. All other variables have their usual meaning.

The fully elastic equations based on the hydrostatic pressure field have been successfully implemented in the limited-area models Aire Limitee Adaptation Dynamique Dyveloppement International (ALADIN) in France (Bubnova et al., 1995) and ETA in the USA (Gallus and Rancic, 1996). A new model based on these equations was developed by Janjic et al. (2001). The even more recently developed Weather Research and Forecasting model (WRF) also employs the fully elastic equations cast in the σcoordinate based on the hydrostatic pressure (Skamarock et al., 2005).

The form of the vertical coordinate used in the fully-elastic MM5 model may finally be noted. Here a σ coordinate based on a constant in time, hydrostatic mean background pressure field is used (Dudhia, 1993). The regional MM5 model has primarily been used for short-range NWP and meso-scale studies (Dudhia, 1993). Bubnova et al. (1995) have stated that the choice of vertical coordinate used in the MM5 model may limit the application of the model to relatively short time scales over relatively small domains. This limitation is due to the constant in time σ coordinate, that depends on a mean temperature profile through the link between the mean reference hydrostatic surface presure and the terrain height (Bubnova et al., 1995). Long integration periods over large areas may involve a great change of air masses, for which a coordinate system depending on a mean temperature profile is not suitable (Bubnova et al., 1995). However, it should be noted that a global version of the MM5 model has been developed (Dudhia and Bresch, 2002). Employing the same vertical coordinate based on a hydrostatic mean background pressure as the regional version of the model, the global model has been used for real-time medium range forecasting (Dudhia and Bresch, 2002). In these experiments the model used a horizontal resolution of about 128 km, which is well within the limits of validity of the hydrostatic approximation. It remains to be clarified whether using the σ coordinate based on the hydrostatic mean background pressure limits the spatial and time scales for which the model may be applied.

2.3 Approximated nonhydrostatic equation sets based on the full pressure field

The suspicion that the relationship between the full pressure field and height may not always be monotone, has prevented the development of a numerical model that employes the fully-elastic equations based on the full pressure field. However, a group of approximated nonhydrostatic equation sets based on the full pressure field have been under development since the 1970s, and have been applied successfully in meso-scale numerical models. For these approximated

equation sets, the potential singularity of a vertical coordinate based on the full pressure field is apparently not reached. In this section, these equation sets are briefly reviewed in stated. For the purpose of introducing the various approximated equation sets, it is sufficient to work in two spatial dimensions as before. The new (three-dimensional) numerical model that is developed in Chapters 3 to 5, is based on an equation set that is closely related to the equation sets introduced in this section.

2.3.1 The Miller-Pearce model

Miller (1974) developed the first nonhydrostatic atmospheric model that employed a pressure-based vertical coordinate. This model uses the full pressure field as vertical coordinate, and was initially derived from a scale analysis of the fully-elastic equations based on the full pressure field.

Following the analysis of Miller (1974), a reference state which is a function of pressure only and is in hydrostatic balance may be defined:

$$\frac{d\phi_{ref}}{dp} = -\frac{RT_{ref}}{p}. \tag{2.17}$$

The thermodynamic variables may be expressed as deviations from a reference state as follows

$$\phi = \phi_{ref} + \phi^{'}(x,\, p,\, t)\,, \tag{2.18}$$

$$T = T_{ref} + T^{'}(x,\, p,\, t)\,. \tag{2.19}$$

Writing

$$\phi = gz \tag{2.20}$$

as before, it follows that

$$z = z_{ref} + z^{'}. \tag{2.21}$$

As before, z represents the geometric height above sea level of a certain pressure level.

Expanding the fully-elastic equations (2.1) to (2.4) without approximation around the reference state gives (Miller and White, 1984):

$$\frac{Du}{Dt} = -(1+\epsilon)\frac{\partial \phi^{'}}{\partial x}, \tag{2.22}$$

$$-\frac{RT^{'}}{p} = \frac{\partial \phi^{'}}{\partial p} + \epsilon\left(\frac{-RT_{ref}}{p} + \frac{\partial \phi^{'}}{\partial p}\right), \tag{2.23}$$

Table 2.1: Scale analysis of the horizontal momentum equation

Du/Dt	$=$	$-\partial\phi^{'}/\partial x$	$-\epsilon\partial\phi^{'}/\partial x$
$\tilde{u}^2/L$		$gH^{'}/L$	$\left(gH^{'}/L\right)\left(\tilde{H}\tilde{u}^2/L^2g\right)$

$$\frac{\partial u}{\partial x}+\frac{\partial \omega}{\partial p}=D\left[\ln\left(1+\epsilon\right)\right]/Dt, \tag{2.24}$$

$$\frac{DT^{'}}{Dt}=\omega S_{ref}+\kappa\omega T^{'}/p. \tag{2.25}$$

Note that u, w and ω keep their original definitions since the reference state is defined as a state of no motion. $S_{ref}=S_{ref}\left(p\right)$ is the reference state static stability function and is defined as

$$S_{ref}=-\frac{dT_{ref}}{dp}+\kappa\frac{T_{ref}}{p}. \tag{2.26}$$

In his scale analysis, Miller (1974) considered the case where the vertical length scale $\tilde{H}$ and horizontal length scale L in the dynamical system are similar. That is,

$$\tilde{H}\sim L. \tag{2.27}$$

Let $\tilde{u}$, $\tilde{\omega}$ and $H^{'}$ be the characteristic values of u, ω and $z^{'}$. The pressure scale is denoted by P. It follows that

$$\frac{D}{Dt}\sim\frac{\tilde{u}}{L} \tag{2.28}$$

and

$$\epsilon\sim\frac{\tilde{H}}{g}\left(\frac{\tilde{u}}{L}\right)^2. \tag{2.29}$$

A scale analysis of the horizontal momentum equation (Table 2.1) and continuity equation (Table 2.2) gives

$$\tilde{u}^2\sim gH^{'} \tag{2.30}$$

and

$$\frac{\tilde{u}}{L}\sim\frac{\tilde{\omega}}{P}, \tag{2.31}$$

provided that the length scale of the system is much less in magnitude than the horizontal velocity scale.

Table 2.2: Scale analysis of the continuity equation

$\partial u/\partial x$	$+\epsilon\partial u/\partial x$	$+\partial\omega/\partial p$	$+\epsilon\partial\omega/\partial p$	$=$	$D\epsilon/Dt$
$\tilde{u}/L$	$(\tilde{u}/L)\left(\tilde{H}\tilde{u}^2/L^2g\right)$	$\tilde{\omega}/P$	$\left(\tilde{H}\tilde{u}^2/L^2g\right)(\tilde{\omega}/P)$		$(\tilde{u}/L)\left(\tilde{H}\tilde{u}^2/L^2g\right)$

Table 2.3: Scale analysis of the vertical momentum equation

$(1/g^2)\frac{D}{Dt}\left(D\phi^{'}/DT\right)$	$(1/g^2)\,\omega^2\partial^2\phi_{ref}/\partial p^2$	$+\left(\partial\phi^{'}_{ref}/\partial p\right)D\omega/Dt$	$=$	$\chi-1$
$\left(H^{'}/L\right)^2$	$\left(H^{'}/L\right)\left(\tilde{H}/L\right)$	$\left(H^{'}/L\right)\left(\tilde{H}/L\right)$		$H^{'}/\tilde{H}$

In order to perform a scale analysis of the vertical momentum equation, it is convenient to rewrite (2.23) in the form

$$\frac{1}{g^2}\frac{D}{Dt}\left(\frac{D\phi^{'}}{Dt}\right)+\frac{1}{g^2}\omega^2\frac{\partial^2\phi_{ref}}{\partial p^2}+\frac{1}{g^2}\frac{\partial\phi_{ref}}{\partial p}\frac{D\omega}{Dt}=\chi-1, \tag{2.32}$$

where

$$\chi=-\left(\frac{p}{RT}\frac{\partial\phi}{\partial p}\right)^{-1}. \tag{2.33}$$

The scale analysis of the vertical momentum equation presented in Table 2.3 makes use of (2.30) and (2.31), with the additional assumption that

$$H^{'}\ll\tilde{H}. \tag{2.34}$$

It follows that the first term in (2.32) may be neglected in comparison with the remaining terms.

From the scale analysis in (2.1) to (2.3) a consistent approximated equation set based on the full pressure field is is obtained:

$$\frac{Du}{Dt}=-\frac{\partial\phi^{'}}{\partial x}, \tag{2.35}$$

$$\frac{R}{g}\frac{D}{Dt}\left(\omega T_{ref}/p\right)=-\left(gp/RT_{ref}\right)\frac{\partial\phi^{'}}{\partial p}-g\frac{T^{'}}{T_{ref}}, \tag{2.36}$$

$$\frac{\partial u}{\partial x}+\frac{\partial\omega}{\partial p}=0, \tag{2.37}$$

$$\frac{DT^{'}}{Dt} = \omega S_{ref} + \kappa \omega T^{'}/p. \tag{2.38}$$

Note that the unapproximated form of the thermodynamic energy equation is used, but that approximations have been introduced to the continuity and momentum equations. Note that (2.35) to (2.38) are formulated in terms of a reference temperature profile. An important property of (2.35) to (2.38) is that the equations are filtered of vertically propagating acoustic waves, whilst Lamb waves may be filtered by an appropriate choice of lower and upper boundary conditions (Miller, 1974). The equations may therefore be termed anelastic. During the explicit numerical solution of these equations, the complete absence of sound waves greatly alleviates the the restriction on the time step as imposed by the Courant-Friedrichs-Lewy (CFL) condition. The equation set is the p coordinate counterpart of the anelastic height-based equations of Ogura and Phillips (1962), although there is no precise mathematical equivalence (Miller and White, 1984). Miller and Pearce (1974) used (2.35) to (2.38) to study cumulonimbus convection, and the equations became known as the Miller-Pearce (MP) model.

Miller and White (1984) extended the work of Miller (1974) by deriving (2.35) to (2.38) from a formal power series expansion. They also derived the corresponding σ coordinate equations:

$$\frac{Du}{DT} + \frac{\partial \phi^{'}}{\partial x} - \sigma \left(\frac{\partial \phi^{'}}{\partial \sigma} \right) \frac{\partial \ln p_{surf}}{\partial x} = 0 \tag{2.39}$$

$$\frac{R}{g} \frac{D}{Dt} \left[T_{ref} \left(\frac{D \ln p_{surf}}{Dt} + \frac{\dot{\sigma}}{\sigma} \right) \right] + g \frac{T^{'}}{T_{ref}} + \frac{\sigma g}{R T_{ref}} \frac{\partial \phi^{'}}{\partial \sigma} = 0 \tag{2.40}$$

$$\frac{\partial u}{\partial x} + \frac{\partial \dot{\sigma}}{\partial \sigma} + \frac{D \ln p_{surf}}{Dt} = 0 \tag{2.41}$$

$$\frac{DT^{'}}{Dt} - \left(\frac{D \ln p_{surf}}{Dt} + \frac{\dot{\sigma}}{\sigma} \right) \left(p_{surf} \sigma S_{ref} + \kappa T^{'} \right) = 0. \tag{2.42}$$

Here σ is defined by (2.6) in terms of the full pressure field; the material derivative is as stated for the fully-elastic σ coordinate equations based on the full pressure field. Lamb waves are present in the solution set of (2.39) to (2.42) but vertically propagating sound waves are absent (Miller and White, 1984), rendering the equations quasi-elastic. The absence of vertically propagating sound waves alleviates the CFL stability restriction on time steps, especially when high vertical resolution is used (Xue and Thorpe, 1991). Equation set (2.39) to (2.42) is similar to the formulation of the anelastic equations in normalized height coordinates (Gal-Chen and Somerville, 1975), although no precise mathematical

equivalence exists beteen the two sets (Miller and White, 1984). The MP model in p and σ coordinates has been used in numerous studies of the numerical simulation of convection and airflow over mountains (e.g. Miller and Pearce, 1974; Xue and Thorpe, 1991; Miranda and James, 1992). The formulation of the MP model in terms of a reference temperature profile may limit its application to the meso-scale, and more specifically to regions where the horizontal gradient on constant pressure levels is rather weak (White, 1989). More details on the applications, characteristics and limits of applicability of the MP model can be found in Chapter 3.

2.3.2 Anelastic terrain-following equations

The presence of Lamb waves in the σ coordinate form of the MP model implies computational penalties compared to the corresponding anelastic p coordinate equations (Miller and White, 1984). Room et al. (2001) have modified the MP model in σ coordinates in order to filter the Lamb waves in addition to the filtered vertically propagating acoustic waves. The main feature of the anelastic model formulated by Room et al. (2001) is that the lower boundary is given by a fixed pressure distribution $p_0(\mathbf{x})$ that is independent of time. This implies that the domain of the model is fixed in pressure coordinates:

$$p_T \leq p \leq p_0(\mathbf{x}). \tag{2.43}$$

Here p_T is the model top, which may be chosen as $p_T = 0$. The pressure p_0 is the mean background pressure at the surface, which may be calculated from the barometric formula (Room et al., 2001):

$$p_0(\mathbf{x}) = p_{surf\_ave} \exp^{(-g/R)\int_0^{h(\mathbf{x})}\left(1/T_{ref\_ave}(z)\right)dz}. \tag{2.44}$$

Here p_{surf_ave} is the mean sea-level pressure, R is the gas constant for dry air, g is the gravitational acceleration, T_{ref_ave} is the mean background temperature and $h(\mathbf{x})$ is the surface elevation.

The σ coordinate used is defined as

$$\sigma = \frac{p - p_T}{p_{sr}}, \tag{2.45}$$

where $p_{sr}(\mathbf{x}) = p_0(\mathbf{x}) - p_T$.

When the MP model in pressure coordinates (2.35) to (2.38) is tranformed to σ coordinates defined by (2.45), the equations of motion obtained are, with the exception of the continuity equation, the same as the MP model in σ coordinates. (Note, however, that the σ coordinate in the MP model is based on the full surface pressure field, which is a prognostic variable in the MP model). The

total derivative of the surface pressure in σ coordinates defined by (2.45) reduces to

$$\frac{D \ln p_{sr}}{Dt} = u \frac{\partial \ln p_{sr}}{\partial x}, \tag{2.46}$$

and the continuity equation transforms to

$$\frac{\partial u}{\partial x} + \frac{\partial \dot{\sigma}}{\partial \sigma} + u \frac{\partial \ln p_{sr}}{\partial x} = 0. \tag{2.47}$$

Writing (2.47) in flux form and integrating from the model top to the model surface gives

$$\nabla \cdot \left(p_{sr} \int_0^1 u d\sigma \right) = 0. \tag{2.48}$$

Equation (2.48) replaces the surface pressure tendency equation that arises in the MP model in σ coordinates (see Chapter 3). Room et al. (2001) have shown that the Lamb waves are filtered by the application of (2.48) in combination with fixing the lower boundary p_0. The complete removal of acoustic modes implies a significant computational advantage over the σ coordinate MP model, especially when an explicit procedure is used to solve the equations (Room et al., 2001). The set of anelastic σ coordinate equations has been termed the nonhydrostatic adjusted dynamics (NHAD) model (Room et al., 2001).

A potential disadvantage of the NHAD model may result from its main feature, the fixed surface pressure profile. Some meso-scale and synoptic scale weather systems may cause large variations in surface pressure from the mean barometric state (2.44). For example, in cases such as these, the pressure $p_0(\mathbf{x})$ may be greater than the actual surface pressure. This implies that calculations at the lowest model level will be carried out below the actual terrain height, which is an unphysical situation. In order to perform calculations at the model level(s) below the actual terrain height, assumptions on certain variables need to be introduced. For example, a temperature and geopotential profile "below ground level" will need to be introduced. In the case where $p_0(x)$ is less than the actual surface pressure, the atmospheric layer below $p_0(x)$ will not be represented in the model. Thus, the use of the $p_0(x)$ profile may limit the application of the NHAD model to meso-scale circulation systems where variations in the surface pressure from the mean barometric state are small.

In the hydrostatic σ coordinate models and nonhydrostatic models based on the full pressure field (such as the MP model) the σ coordinate used is based on the actual surface pressure simulated by the model. The surface $\sigma = 1$ therefore always follow model terrain height precisely. It is interesting to note that this is not the case for the fully-elastic models based on the actual hydrostatic pressure field. Here nonhydrostatic effects may cause the actual surface pressure simulated to be less or greater than the simulated hydrostatic surface

pressure. However, these variations of the actual surface pressure from the hydrostatic surface pressure are likely to be less than variations from the average barometric pressure. Thus, a problem similar to that described above for the NHAD model, although probably of much smaller significance, may occur in the fully-elastic models based on the actual hydrostatic presure. However, for fully-elastic models such as the MM5, where the vertical coordinate is based on the mean background hydrostatic pressure, problems at the lower boundary similar to that described for the NHAD model may be expected (see also Bubnova et al., 1995 and section 2.2.3).

2.3.3 White's extension of the MP Model

Both the MP model and Room's anelastic σ coordinate equations are formulated in terms of a reference temperature and geopotential profile. This may limit the application of these models to situations where the temperature profile is rather homogeneous (White, 1989). An extended p coordinate equation set based on the MP model, but formulated independently from a reference profile, was developed by White (1989):

$$\frac{Du}{Dt} + \frac{\partial \phi}{\partial x} = 0, \tag{2.49}$$

$$\frac{R}{g}\frac{D}{Dt}(\frac{\omega T}{p}) + g + \frac{gp}{RT}\frac{\partial \phi}{\partial p} = 0, \tag{2.50}$$

$$\frac{\partial u}{\partial x} + \frac{\partial \omega}{\partial p} = 0, \tag{2.51}$$

$$\frac{DT}{Dt} - \kappa\frac{\omega T}{p} = 0. \tag{2.52}$$

Here p represents the full pressure field as in the MP model, and all the other symbols have their usual meaning. White's equation set is discussed in more detail in Chapter 3. The equation set appears to be more suitable than the MP and NHAD models for application in regions such as frontal zones, where the horizontal temperature gradient is steep. It may possibly also be applied in large-scale modelling (White, 1989) (as opposed to meso-scale modelling). White's equations appear not to have been used before in a numerical atmospheric model. In Chapter 3 the p coordinate equations of White are transformed to σ coordinates. It is shown that the resulting equation set is closely linked to the MP model in σ coordinates, in the sense that it is also quasi-elastic. In Chapter 4, a new meso-scale numerical model based on the σ coordinate equations of White is formulated.

2.4 Discussion

In this chapter the various pressure-based nonhydrostatic equation sets developed have been discussed. The numerical models based on these equation sets may be divided into the following four groups (Room et al., 2001):

1. The MP model that employs the full (nonhydrostatic) pressure as the vertical coordinate (Miller, 1974; Miller and Pearce, 1974; Miller and White, 1984). The MP model contains approximations that make it anelastic in pressure coordinates and quasi-elastic in σ coordinates. There have been numerous applications of the MP model to the numerical simulation of convection and airflow over mountains (e.g. Miller and Pearce, 1974; Xue and Thorpe, 1991; Miranda and James, 1992). The formulation of the MP model in terms of a reference thermodynamic profile, that depends on pressure alone, may limit its application to cases where the horizontal temperature gradient on pressure surfaces is weak (White, 1989). The properties of the MP model are discussed in more detail in Chapter 3.

2. Fully-elastic models that employ the hydrostatic component of the pressure field as the vertical coordinate (Laprise 1992). These equations and coordinate system have been implemented in the Meteo-France operational limited-area model, ALADIN (Bubnova et al., 1995), the nonhydrostatic version of the ETA model (Gallus and Rancic, 1996), the model developed by Janjic and Gerrity (2001) and the WRF model (Skamarock et al., 2005).

3. Models which use the hydrostatic mean background field as the vertical coordinate. This coordinate frame is employed in the nonhydrostatic extension of the Penn-State National Center for Atmospheric Research model (Dudhia 1993, Dudhia and Bresch, 2002).

4. Models that may be regarded as hybrids of the three groups described. Most noteworthy is the model of Room et al. (2001), which makes use of the actual pressure field and a mean background field of surface pressure to define a terrain-following vertical coordinate. This model is unique in the sense that it is the only anelastic σ coordinate model that has been developed so far. However, its formulation in terms of a constant-in-time surface pressure distribution and a reference thermodynamic profile is likely to limit its application to the meso-scale.

There has been no realization of a numerical model using the fully-elastic equations based on the full pressure field. This is due to the suspicion that such a coordinate might become singular in the presence of severe vertical advection (Laprise, 1992, 1998; Bubnova et al., 1995). It appears also as if White's (1989) extension of the MP model in pressure coordinates has not been realized as a numerical model. This equation set is likely to be more generally applicable

than the MP model (see section 2.3.3 and Chapter 3). In Chapter 3, this equation set is transformed to σ coordinates, and a new numerical model based on the σ coordinate equations is formulated in Chapter 4.

Chapter 3

Derivation and properties of the quasi-elastic equations in terrain-following coordinates based on the full pressure field

3.1 Introduction

As mentioned in Chapter 2, the first nonhydrostatic atmospheric flow model in pressure-based coordinates was formulated by Miller (1974) and Miller and Pearce (1974). This model employed the full pressure field as vertical coordinate. The approximations introduced by Miller (1974) to the fully elastic equations in p coordinates ensured the absence of vertically propagating sound waves from the equation set. Buoyancy modes remain undistorted by the simplifications, and horizontally propagating sound waves (Lamb waves) may be removed by applying the lower boundary condition $\omega = 0$ at $p = p_0$ where p_0 is a constant. The complete removal of sound waves yields the equation set to be anelastic. A sound theoretical basis for these equations (hereafter called the Miller-Pearce equations, MP equations or MP model) is provided by Miller and White (1984), and they also transformed the equations to σ coordinates. Lamb waves (Lamb, 1932) are present in the σ coordinate formulation, where the lower boundary condition is $\dot{\sigma} = 0$ at $\sigma = 1$ and the upper boundary is defined as $p = 0$. The presence of Lamb waves implies a computational penalty compared to the pressure coordinate formulation (Miller and White, 1984; Room et al., 2001). Because the MP equations in σ coordinates are filtered of vertically propagating sound waves, but do allow the propagation of sound waves in the horizontal, the equation set may be called quasi-elastic (or pseudo-anelastic (Room et al., 2001) .

The MP model has been applied successfully in pressure coordinates in numerous studies of systems where the initial state is fairly uniform. These include studies of cumulonimbus and other convective systems (Miller and Pearce, 1974; Moncrieff and Miller, 1976; Miller and Betts, 1977; Thorpe and Miller, 1978; Thorpe et al., 1982; Brugge and Moncrief, 1985). The MP model in σ coordinates was used in two spatial dimensions to simulate mountain waves (Xue and Thorpe, 1991) and for studying gravity wave drag and critical level resonance in three-spatial dimensions (Miranda and James, 1992; Miranda and Valente, 1997). Room et al. (2001) modified the MP model in σ coordinates by filtering out the Lamb waves. The filtering was achieved by choosing the lower boundary of the model domain to have a fixed pressure distribution in space and time, and deducing proper vertical boundary conditions for the nonhydrostatic geopotential height-equation (Room et al., 2001; also see Chapter 2). The anelastic σ coordinate equations allow the use of significantly larger time-steps during numerical integration compared to the corresponding MP equations (Room et al., 2001). A potential disadvantage of the anelastic equations derived by Room et al. (2001) is that the surface pressure fluctuation is calculated by assuming hydrostatic balance at the lowest model level, and by approximating the latter with the hydrostatic balance in terms of a reference state temperature profile. If the actual surface pressure is lower then the fixed background pressure, calculations in the model are performed below the actual terrain geometric height (see Chapter 2). Still, in a set of numerical experiments involving airflow over orographic obstacles, the surface pressure fields obtained from using the MP equations applied by Miranda and James (1992) and from applying the anelastic equations showed close correspondence (Room et al., 2001). The anelastic σ coordinate equations are called the NHAD model (nonhydrostatic adjusted dynamics, Room et al. (2001)).

Both the MP and NHAD models are restrictive in the sense that they are formulated in terms of a reference state that is in hydrostatic equilibrium and is a function of pressure only. A single reference state may not be typical everywhere in a given computational domain. In particular, this may be true if the model is applied in large-scale modelling or in mesoscale simulations of features such as frontal zones (White, 1989). White (1989) extended the MP model to be able to represent large temperature variations on pressure surfaces, by avoiding the explicit use of a reference state. The extended equations imply a p coordinate analogue of Ertel's potential vorticity conservation law and conserves energy (White, 1989). Salmon and Smith (1994) showed that White's equations have a Hamiltonian structure and that the conservation properties follow from the symmetry properties of the relevant Hamiltonian.

This Chapter commences with an overview of the MP model and White's equations in pressure coordinates, whereafter the σ coordinate analogue of the pressure coordinate equations of White (1989) is derived. In fact, the work in this chapter represents the first formulation of White's extended pressure coordinate

equations in σ coordinates. The σ coordinate used is based on the full (non-hydrostatic) pressure field, just as the pressure and σ coordinates used in the MP-model and by White (1989) are based on the full pressure field. Recently formulated terrain-following nonhydrostatic models mostly make use (as discussed in Chapter 2) of vertical coordinates based on the hydrostatic pressure (Laprise, 1992; Juang, 1992; Gallus and Rancic, 1996; Janjic et al., 2001) or on a hydrostatic reference-pressure field (Dudhia, 1993; Hsu and Sun, 2001; Dudhia and Bresch, 2002). The σ coordinate used by Room et al. (2001) is a type of hybrid, since it is defined in terms of the full pressure field and a reference surface pressure distribution. The σ coordinate used in the present chapter makes use of the actual surface pressure, such as in the MP model and the equations of White (1989), and employs a prognostic equation for the surface pressure. Lamb waves may therefore be expected to form part of the solution set of these equations, and they are indeed shown to be quasi-elastic.

Numerical solutions of the NHAD and MP equations in p or σ coordinates all make use of an elliptic equation in the geopotential. A similar elliptic equation is derived for the σ coordinate quasi-elastic equations presented in this chapter. It is shown that the equation may be obtained from a coordinate transformation of the corresponding pressure coordinate equation derived by White (1989), or alternatively, directly from the quasi-elastic equations in σ coordinates. An energy equation for the quasi-elastic equations is also derived. Finally, the characteristics of the gravity and sound waves in the quasi-elastic σ coordinate equation system are discussed. It is shown how the phase speed of these fast travelling waves depends on the choice of the model top.

3.2 The Miller-Pearce model

3.2.1 Basic concepts

In pressure coordinates, the vertical velocity w may be expressed as:

$$\frac{Dw}{Dt} = \frac{\partial z}{\partial t} + u\frac{\partial z}{\partial x} + v\frac{\partial z}{\partial y} + \omega\frac{\partial z}{\partial p}. \tag{3.1}$$

Here

$$\frac{D}{Dt} \equiv \frac{\partial}{\partial t} + u\frac{\partial}{\partial x} + v\frac{\partial}{\partial y} + \omega\frac{\partial}{\partial p} \tag{3.2}$$

is the material derivative; all partial derivatives with respect to t, x and y are carried out at constant p. The horizontal components of the wind are denoted by u and v. Note that p represents the full pressure field, and $\omega \equiv Dp/Dt$.

In the free atmosphere, that is, away from boundaries which may impose constraints on w, the last term on the right-hand side of (3.1) is dominant (Miller, 1974). It is common practice to ignore the contributions of the first two terms in

(3.1), and to use the hydrostatic aproximation (1.6) to approximate w as $-\omega/g\rho$ (e.g. Miller, 1974; Holton, 1992). It is less obvious that this approximation is valid when differentiated (Miller, 1974), that is, as

$$\frac{Dw}{Dt} \simeq \frac{D}{Dt}\left(\frac{\omega}{g\rho}\right). \tag{3.3}$$

It is also not immediately clear to what extent the properties of a given equation set are changed by the use of approximation (3.3). However, by scale analysis of the fully-elastic equations based on the full pressure field as vertical coordinate, it may be shown that (3.3) may be applied to find an approximated form of the vertical momentum equation that is consistent with other approximations made to the horizontal momentum and continuity equations (Miller, 1974, also see Chapter 2). Indeed, the first nonhydrostatic flow model in pressure coordinates as formulated by Miller (1974) and Miller and Pearce (1974) was based on approximation (3.3). In the MP-model the true vertical acceleration Dw/Dt is replaced in the vertical momentum equation by $D\tilde{w}_{ref}/Dt$, where

$$\tilde{w}_{ref} = \frac{-\omega}{g\rho_{ref}} = -\frac{R}{g}\frac{\omega T_{ref}}{p}. \tag{3.4}$$

Here g is the gravitational acceleration and R is the gas constant for a unit mass of air. $T_{ref} = T_{ref}(p)$ and $\rho = \rho_{ref}(p)$ are reference profiles of temperature T and density ρ. In conjunction with approximations made in the continuity and horizontal momentum equations, this replacement of Dw/Dt by $D\tilde{w}_{ref}/Dt$ ensures the absence of vertically propagating acoustic modes from the solution set of the MP equations, whilst buoyancy modes remain undistorted (and no spurious modes are introduced) (Miller, 1974; Miller and White, 1984). Horizontally propagating acoustic modes (the Lamb modes) may be removed from the pressure coordinate MP equations by applying the lower boundary condition $\omega = 0$ at $p = p_0$, where p_0 is a constant (Miller, 1974; Miller and White, 1984).

3.2.2 The Miller-Pearce model in pressure coordinates

For an adiabatic, frictionless atmosphere the three-dimensional MP model with pressure as the vertical coordinate consists of the following approximate forms of the horizontal and vertical momentum equations (3.5) to (3.7), continuity equation (3.8) and the exact thermodynamic equation for a perfect gas (3.9):

$$\frac{Du}{Dt} - fv + \frac{\partial \phi^{'}}{\partial x} = 0, \tag{3.5}$$

$$\frac{Dv}{Dt} + fu + \frac{\partial \phi^{'}}{\partial y} = 0, \tag{3.6}$$

$$\frac{R}{g}\frac{D}{Dt}\left(\frac{\omega T_{ref}}{p}\right) + g\frac{T^{'}}{T_{ref}} + \frac{gp}{RT_{ref}}\frac{\partial \phi^{'}}{\partial p}, = 0 \tag{3.7}$$

$$\frac{\partial u}{\partial x} + \frac{\partial v}{\partial y} + \frac{\partial \omega}{\partial p}, = 0 \tag{3.8}$$

$$\frac{DT}{Dt} - \kappa \frac{\omega T}{p} = 0. \tag{3.9}$$

Note that Coriolis terms are included in the horizontal component equations; f is the Coriolis parameter. The material derivative is defined by (3.2). In equations (3.5) to (3.9) all differentiations with respect to time and the horizontal coordinates are carried out at constant pressure; u and v are the velocity components in the x and y directions; $\kappa = R/c_p$ with c_p the specific heat at constant pressure and ϕ is the geopotential, gz, z being geometric height. $\phi^{'}$ and $T^{'}$ are the departures of ϕ and T from the reference profiles $\phi_{ref}(p)$ and $T_{ref}(p)$:

$$\phi = \phi_{ref}(p) + \phi^{'};\ T = T_{ref}(p) + T^{'}. \tag{3.10}$$

The reference state is chosen to be in hydrostatic balance, so that:

$$\frac{d\phi_{ref}}{dp} + \frac{RT_{ref}}{p} = 0. \tag{3.11}$$

Time integration of the MP equations makes use of an elliptic diagnostic equation for $\phi^{'}$ which results when (3.8) is applied to differentiated forms of equations (3.5) to (3.7) (Johnson, 1978; Miller and White (1984); Brugge and Moncrieff (1985):

$$\frac{\partial^2 \phi^{'}}{\partial x^2} + \frac{\partial^2 \phi^{'}}{\partial y^2} + \frac{\partial}{\partial p}\left(r_s^2 \frac{\partial \phi^{'}}{\partial p}\right) = 2J_3 - \frac{\partial}{\partial p}\left(g r_{ref} \frac{T^{'}}{T_{ref}} - \frac{\omega^2}{r_{ref}} \frac{dr_{ref}}{dp}\right) \tag{3.12}$$

in which

$$J_3 = \left(\frac{\partial u}{\partial x}\frac{\partial v}{\partial y} - \frac{\partial v}{\partial x}\frac{\partial u}{\partial y}\right) + \left(\frac{\partial v}{\partial y}\frac{\partial \omega}{\partial p} - \frac{\partial \omega}{\partial y}\frac{\partial v}{\partial p}\right) + \left(\frac{\partial \omega}{\partial p}\frac{\partial u}{\partial x} - \frac{\partial u}{\partial p}\frac{\partial \omega}{\partial x}\right) \tag{3.13}$$

and

$$r_{ref} = \frac{gp}{RT_{ref}}. \tag{3.14}$$

Boundary conditions on the solution of (3.12) are obtained using equations (3.5) to (3.7) and (3.9) together with appropriate specifications of u, v, ω and $T^{'}$ at the boundaries (Miller and White, 1984).

Miller (1974) derived the MP equations for flow independent of one horizontal coordinate by transforming the geometric-height coordinate equations to pressure coordinates and then neglecting various small terms (also see Chapter 2). By using a scaling and power series expansion method, Miller and White (1984) gave a formal justification of the MP equations for flow independent of one horizontal coordinate. Their derivation assumed that the departures of $\phi^{'}$ and $T^{'}$ from the reference state profiles were due solely to processes occurring on the convective scale (White, 1989). They identified the quantity

$$\alpha^{*} \equiv -\frac{p_0}{\theta_{ref}}\frac{d\theta_{ref}}{dp} \tag{3.15}$$

as the key parameter whose smallness ($\alpha \ll 1$) validates the approximations made by Miller (1974). In (3.15), $\theta_{ref} = \theta_{ref}(p)$ is the potential temperature profile corresponding to $T_{ref}(p)$, that is, $\theta_{ref} = T_{ref}\,(p_0/p)^{\kappa}$ with p_0 a reference pressure level. Condition (3.15) is satisfied everywhere in the troposphere. Even in the extreme case of the Antarctica surface layer $\alpha \leq 0.3$ (Miranda and James, 1992).

Equations (3.5) - (3.9) imply an energy equation of the form

$$\frac{D}{Dt}(\frac{1}{2}u^2 + \frac{1}{2}v^2 + \frac{1}{2}\tilde{w}_{ref}^2 + c_pT) = -\bar{\nabla}_p \cdot (\phi\mathbf{v}) - \frac{\partial}{\partial p}(\omega\phi) \tag{3.16}$$

in which $\bar{\nabla} = (\partial/\partial x, \partial/\partial y)$ and $\mathbf{v} = (u\,, v)$ is the horizontal velocity (White, 1989). Equation (3.16) is an extension of the familiar energy equation for the hydrostatic equations, to include the contribution of the approximate vertical velocity $\tilde{w}_{ref}$ to the specific kinetic energy (White, 1989). Miller and White (1984) noted a 2-dimensional case of (3.16). Johnson (1978) carried out a detailed study of the vorticity properties of the MP model, and established the existence of an anologue of Ertel's potential vorticity theorem.

The MP model has been applied successfully in pressure coordinates in numerous studies of systems where the initial state is fairly uniform. These were mostly studies of cumulonimbus and other convective systems (Moncrieff and Miller, 1976; Miller and Bets, 1977; Thorpe and Miller, 1978; Thorpe et al., 1982; Brugge and Moncrieff, 1985). The appearence of the reference temperature $T_{ref}(p)$ in the definition of $\tilde{w}$ (and elsewhere in the vertical momentum equation) was not a hampering feature in these studies, since each was concerned with situations in which the initial state is horizontally homogeneous. Variations of the temperature on pressure surfaces is thus due solely to convection itself, and these turn out to be small. Should the MP model be used in mesoscale simulations - or, as speculatively suggested by Miller and White (1984), in larger scale modelling - the use of $T_{ref}(p)$ instead of the true local temperature, T, would be less sound. In frontal zones, for example, considerable variations of temperature may occur on pressure surfaces, and a single reference

state might not be typical of different parts of the computational domain (White, 1989). However, it should be noted that similar height-based equation sets (e.g. Ogura and Phillips, 1962; Gal-Chen and Somerville, 1975) have been used to successfully simulate fronts. The tropopause may be a more problematic region to apply the MP model to. The tropopause slopes in the horizontal, so that there will be relatively larger departures in temperature from a reference state that depends on pressure, on a pressure surface that intersects the tropopause. A modification of the MP model to represent large temperature variations on pressure surfaces, and that is independent of the use of a thermodynamic reference profile, was stated by White (1989). This equation set is described in section 3.2.4. A normal-mode analysis of the MP and White (1989) equations (in pressure and σ coordinates), following recent work performed in height-based coordinates (Thuburn et al., 2002a; Thuburn et al., 2002b; Davies et al., 2003), may provide more clearity on the validity of these equation sets as a function of different flow regimes.

3.2.3 The Miller-Pearce model in sigma coordinates

The σ coordinate version of the MP equations was derived by Miller and White (1984) by means of a coordinate transformation of the equations in pressure coordinates. Here the σ coordinate form of the equations is defined by (2.6) in terms of the full pressure field. The σ coordinate equations, here stated in three spatial dimensions, are:

$$\frac{Du}{DT} - fv + \left(\frac{\partial \phi^{'}}{\partial x}\right) - \sigma\left(\frac{\partial \phi^{'}}{\partial \sigma}\right)\frac{\partial \ln p_{surf}}{\partial x} = 0, \tag{3.17}$$

$$\frac{Dv}{DT} + fu + \left(\frac{\partial \phi^{'}}{\partial y}\right) - \sigma\left(\frac{\partial \phi^{'}}{\partial \sigma}\right)\frac{\partial \ln p_{surf}}{\partial y} = 0, \tag{3.18}$$

$$\frac{R}{g}\frac{D}{Dt}\left[T_{ref}\left(\frac{D \ln p_s}{Dt} + \frac{\dot{\sigma}}{\sigma}\right)\right] + g\frac{T^{'}}{T_{ref}} + \frac{\sigma g}{RT_{ref}}\frac{\partial \phi^{'}}{\partial \sigma} = 0, \tag{3.19}$$

$$\frac{\partial u}{\partial x} + \frac{\partial v}{\partial y} + \frac{\partial \dot{\sigma}}{\partial \sigma} + \frac{D \ln p_{surf}}{Dt} = 0, \tag{3.20}$$

$$\frac{DT^{'}}{Dt} - \left(\frac{D \ln p_{surf}}{Dt} + \frac{\dot{\sigma}}{\sigma}\right)\left(p_{surf}\sigma s_{ref} + \kappa T^{'}\right) = 0. \tag{3.21}$$

In these equations partial differentiations with respect to x and y are carried out at constant σ. Note that s_{ref} denotes $-\left(T_{ref}/\theta_{ref}\right)\left(d\theta_{ref}/dp\right)$, the mean static stability function (Miller and White, 1984). As stated before in (3.10), $T^{'}$ and $\phi^{'}$ denotes departures from a hydrostatic reference state (2.25) that is a function of pressure only. The surface pressure is denoted by p_{surf} as in Chapter 2, and all the other variables and constants are defined as before.

The MP model in σ coordinates was used in two spatial dimensions to simulate mountain waves (Xue and Thorpe, 1991) and for studying gravity wave drag and critical level resonance in three spatial dimensions (Miranda and James, 1992; Miranda and Valente, 1997). The MP model in σ coordinates was also successfully applied in the "cold bubble test" (see Straka, 1993 and Chapter 5) to simulate a descending cold bubble in an isentropic environment (Xue, 1989; see also Gallus and Rancic, 1994). Note the use of a reference profile that depends on pressure in the equations, which may restrict the application of the model to situations where the atmospheric state is fairly uniform on isobaric levels (White, 1989).

3.3 White's extension of the MP model in pressure coordinates

3.3.1 The momentum, continuity and thermodynamic energy equations

Choosing to avoid the formulation in terms of a reference state used in the MP model, White (1989) stated the following set of pressure coordinate equations:

$$\frac{Du}{Dt} - fv + \frac{\partial \phi^{'}}{\partial x} = 0, \tag{3.22}$$

$$\frac{Dv}{Dt} + fu + \frac{\partial \phi^{'}}{\partial y} = 0, \tag{3.23}$$

$$\frac{R}{g}\frac{D}{Dt}(\frac{\omega T}{p}) + g\frac{T^{'}}{T} + \frac{gp}{RT}\frac{\partial \phi^{'}}{\partial p} = 0, \tag{3.24}$$

$$\frac{\partial u}{\partial x} + \frac{\partial v}{\partial y} + \frac{\partial \omega}{\partial p} = 0, \tag{3.25}$$

$$\frac{DT}{Dt} - \kappa\frac{\omega T}{p} = 0. \tag{3.26}$$

Here (3.22) and (3.23) are the horizontal momentum equations, (3.24) is the vertical momentum equation, (3.25) is the continuity equation and (3.26) the thermodynamic energy equation. These equations are independent of the choice of hydrostatic reference state (3.16) (White, 1989). They could be written with $\phi^{'}$ and $T^{'}$ replaced by ϕ and T, but White (1989) argued that the subtraction of reference profiles $\phi_{ref}\,(p)$ and $T_{ref}\,(p)$ is desirable in computational practice. Thus, equations (3.22) to (3.26) differs from the MP model in pressure cooridinates (3.5) to (3.9) only in the replacement of the reference state temperature $T_{ref}\,(p)$ by the true temperature T. This appears not to be a trivial extension: The vorticity and potential vorticity dynamics of the extended set (3.22)

to (3.26) are algebraicly different from the MP equations (3.5) to (3.9) (White, 1989). Equations (3.22) to (3.26) imply the energy equation

$$\frac{D}{Dt}(\frac{1}{2}u^2 + \frac{1}{2}v^2 + \frac{1}{2}\hat{w^2} + c_pT) = -\bar{\nabla}_p \cdot (\phi\mathbf{v}) - \frac{\partial}{\partial p}(\omega\phi), \tag{3.27}$$

where

$$\hat{w} = \frac{-\omega RT}{gp}. \tag{3.28}$$

Equation (3.27) is a generalization of (3.16) of the MP equations. White (1989) also showed that (3.22) to (3.26), as the MP equations, imply a pressure coordinate analogue of Ertel's potential vorticity conservation law.

In this study it is preferred not to make use of the reference profile (3.16) in White's equations (3.22) to (3.24). This decision is based on the belief that the use of perturbation quantities in (3.22) to (3.24) instead of the full fields does not imply significant advantages in computational practice (McGregor, personnel communicaton). In fact, the elliptic equations that are eventually derived for White's equations (see sections 3.3.2 and 3.4.7), can be most conveniently solved numerically if they are formulated in terms of the full geopotential field (see Chapter 4). Formulating the elliptic equation in terms of perturbation quantities of the hydrostatic reference profile (3.16) requires a more complicated specification of the lower boundary conditions needed during the numercial solution of the elliptic equation (see Xue, 1989; also see Chapter 4). Using (3.10) to write the perturbation quantities $\phi^{'}$ and $T^{'}$ in terms of the full fields ϕ and T, and substituting into (3.22) to (3.24), a statement of the momentum equations in terms of the full ϕ and T fields is obtained:

$$\frac{Du}{Dt} - fv + \frac{\partial\phi}{\partial x} = 0, \tag{3.29}$$

$$\frac{Dv}{Dt} + fu + \frac{\partial\phi}{\partial y} = 0, \tag{3.30}$$

$$\frac{R}{g}\frac{D}{Dt}(\frac{\omega T}{p}) + g + \frac{gp}{RT}\frac{\partial\phi}{\partial p} = 0. \tag{3.31}$$

Equations (3.29) to (3.31) is the form of the momentum equations of White (1989) that is used in the present study. It may be noted that White's equations (3.29) to (3.31), (3.25) and (3.26) were derived from a Hamiltonian perspective by Salmon and Smith (1994).

3.3.2 A diagnostic equation for ϕ in pressure coordinates

Following the procedure suggested by Miller and White (1984) for the two-dimensional MP-equations, a diagnostic equation for ϕ may be derived from equations (3.22) to (3.26).

Differentiating (3.22) with respect to x and (3.23) with respect to y, and forming $D\left(\partial u/\partial x\right)/Dt$ and $D\left(\partial v/\partial y\right)/Dt$ from the resulting two equations, gives

$$\frac{D}{Dt}\left(\frac{\partial u}{\partial x}\right)+\left(\frac{\partial u}{\partial x}\right)^{2}+\frac{\partial v}{\partial x}\frac{\partial u}{\partial y}+\frac{\partial \omega}{\partial x}\frac{\partial u}{\partial p}-f\frac{\partial v}{\partial x}+\frac{\partial^{2}\phi}{\partial x^{2}}=0 \tag{3.32}$$

and

$$\frac{D}{Dt}\left(\frac{\partial v}{\partial y}\right)+\frac{\partial u}{\partial y}\frac{\partial v}{\partial x}+\left(\frac{\partial v}{\partial y}\right)^{2}+\frac{\partial \omega}{\partial y}\frac{\partial v}{\partial p}+f\frac{\partial u}{\partial y}+u\frac{df}{dy}+\frac{\partial^{2}\phi}{\partial y^{2}}=0. \tag{3.33}$$

It may be noted that

$$\frac{D}{Dt}(\frac{\omega T}{p})=\frac{T}{p}\frac{D\omega}{Dt}+\frac{\omega}{p}\frac{DT}{Dt}-\frac{\omega^{2}T}{p^{2}}=\frac{T}{p}\frac{D\omega}{Dt}-\frac{1}{\gamma}\frac{\omega^{2}T}{p^{2}}, \tag{3.34}$$

by the use of (3.26). Here $\gamma=c_{p}/c_{v}$. After substituting (3.34) in (3.24) and differentiating to p it follows, by forming $D\left(\partial\omega/\partial p\right)/Dt$ from the resulting equation, that

$$\frac{D}{Dt}(\frac{\partial \omega}{\partial p})+\frac{\partial u}{\partial p}\frac{\partial \omega}{\partial x}+\frac{\partial v}{\partial p}\frac{\partial \omega}{\partial y}+(\frac{\partial \omega}{\partial p})^{2}$$

$$+\frac{\partial}{\partial p}(rg-\frac{\omega^{2}}{\gamma p}+r^{2}\frac{\partial \phi}{\partial p})=0. \tag{3.35}$$

Here $r=gp/RT$. Adding the terms $D\left(\partial u/\partial x\right)/Dt$, $D\left(\partial v/\partial y\right)/Dt$, and $D\left(\partial\omega/\partial p\right)/Dt$, and applying (3.25) leads to the required diagnostic equation for ϕ:

$$\frac{\partial^{2}\phi}{\partial x^{2}}+\frac{\partial^{2}\phi}{\partial y^{2}}+\frac{\partial}{\partial p}(r^{2}\frac{\partial \phi}{\partial p})=$$

$$2J_{3}+f(\frac{\partial v}{\partial x}-\frac{\partial u}{\partial y})-u\frac{df}{dy}-\frac{\partial}{\partial p}(rg-\frac{\omega^{2}}{\gamma p}) \tag{3.36}$$

in which J_3 is given by (3.13). Equation (3.36) is mathematically equivalent to the elliptic equation stated by White (1989) in terms of perturbation quantities $\phi^{'}$ and $T^{'}$.

3.3.3 Two-dimensional equations in pressure coordinates

The two-dimensional version of White's equations in pressure coordinates (neglecting the Coriolis effect) is:

$$\frac{Du}{Dt}+\frac{\partial \phi}{\partial x}=0, \tag{3.37}$$

$$\frac{R}{g}\frac{D}{Dt}\left(\frac{\omega T}{p}\right)+g+\frac{gp}{RT}\frac{\partial\phi}{\partial p}=0, \tag{3.38}$$

$$\frac{\partial u}{\partial x}+\frac{\partial\omega}{\partial p}=0, \tag{3.39}$$

$$\frac{DT}{Dt}-\kappa\frac{\omega T}{p}=0. \tag{3.40}$$

These equations may be compared to (2.35) to (2.38), the two-dimensional MP equations in presure coordinates. In two spatial dimensions, the elliptic equation assumes the form:

$$\frac{\partial^2\phi}{\partial x^2}+\frac{\partial}{\partial p}\left(r^2\frac{\partial\phi}{\partial p}\right)=$$

$$2\left(\frac{\partial\omega}{\partial p}\frac{\partial u}{\partial x}-\frac{\partial u}{\partial p}\frac{\partial\omega}{\partial x}\right)-\frac{\partial}{\partial p}\left(rg-\frac{\omega^2}{\gamma p}\right). \tag{3.41}$$

3.4 Derivation of White's equations in σ coordinates by a coordinate transformation

3.4.1 Transformation relations

In the following sections the equations derived by White (1989) in pressure coordinates are transformed to σ coordinates, with

$$\sigma=\frac{p-p_T}{p_{surf}-p_T}=\frac{p-p_T}{p_s} \tag{3.42}$$

Here p represents the full (nonhydrostatic) pressure field, p_T is the prescribed pressure at the model top (a constant), p_{surf} is the actual surface pressure and $p_s=p_{surf}-p_T$. Note that $p_{surf}=p_{surf}(x,y,t)$ and $p_s=p_s(x,y,t)$.

Let A be any scalar (or vector) dependent variable. The required transformation relationships btween σ and pressure coordinates (Phillips, 1957; Kasahara, 1974; Haltiner and Williams, 1980) are:

$$\left(\frac{\partial A}{\partial q}\right)_\sigma=\left(\frac{\partial A}{\partial q}\right)_p+\frac{\partial A}{\partial p}\left(\frac{\partial p}{\partial q}\right)_\sigma \tag{3.43}$$

with $q=x$, y or t, and

$$\frac{\partial A}{\partial\sigma}=\frac{\partial A}{\partial p}\frac{\partial p}{\partial\sigma}. \tag{3.44}$$

Alternatively,

$$\frac{\partial A}{\partial p} = \frac{\partial A}{\partial \sigma}\frac{\partial \sigma}{\partial p}. \tag{3.45}$$

If equation (3.45) is substituted into equation (3.43), the result is

$$(\frac{\partial A}{\partial q})_\sigma = (\frac{\partial A}{\partial q})_p + \frac{\partial A}{\partial \sigma}\frac{\partial \sigma}{\partial p}(\frac{\partial p}{\partial q})_\sigma. \tag{3.46}$$

It is worthwhile to note that

$$\frac{\partial \sigma}{\partial p} = \frac{\partial}{\partial p}(\frac{p - p_T}{p_{surf} - p_T}) = \frac{1}{p_{surf} - p_T}\frac{\partial p}{\partial p} = \frac{1}{p_s} \tag{3.47}$$

or, alternatively,

$$\frac{\partial p}{\partial \sigma} = p_s \tag{3.48}$$

and

$$(\frac{\partial p}{\partial q})_\sigma = \frac{\partial}{\partial q}(\sigma p_s + p_T)_\sigma = \sigma(\frac{\partial p_s}{\partial q})_\sigma. \tag{3.49}$$

Equations (3.47) and (3.49) can now be substituted into equation (3.46) to obtain the transformation relationship

$$\left(\frac{\partial A}{\partial q}\right)_\sigma = \left(\frac{\partial A}{\partial q}\right)_p + \frac{\partial A}{\partial \sigma}\frac{\sigma}{p_s}\left(\frac{\partial p_s}{\partial q}\right)_\sigma = \left(\frac{\partial A}{\partial q}\right)_p + \frac{\partial A}{\partial \sigma}\sigma\left(\frac{\partial \ln p_s}{\partial q}\right)_\sigma, \tag{3.50}$$

whilst substituting equation (3.47) in (3.45) gives

$$\frac{\partial A}{\partial p} = \frac{1}{p_s}\frac{\partial A}{\partial \sigma}. \tag{3.51}$$

3.4.2 The horizontal momentum equations

From equations (3.50) it follows that

$$\left(\frac{\partial \phi}{\partial x}\right)_p = \left(\frac{\partial \phi}{\partial x}\right)_\sigma - \sigma\frac{\partial \phi}{\partial \sigma}\left(\frac{\partial \ln p_s}{\partial x}\right)_\sigma. \tag{3.52}$$

The equation for momentum conservation in the x direction in pressure coordinates (3.29) therefore transforms to σ coordinates as

$$\frac{Du}{Dt} - fv + \frac{\partial \phi}{\partial x} - \sigma\frac{\partial \phi}{\partial \sigma}\frac{\partial \ln p_s}{\partial x} = 0. \tag{3.53}$$

Similarly, the pressure coordinate equation for momentum conservation in the y-direction (3.30) may be tranformed to σcoordinates to obtain

$$\frac{Dv}{Dt} + fu + \frac{\partial \phi}{\partial y} - \sigma \frac{\partial \phi}{\partial \sigma} \frac{\partial \ln p_s}{\partial y} = 0. \tag{3.54}$$

3.4.3 The vertical momentum equation

From equations (3.51) it follows that

$$\frac{\partial \phi}{\partial p} = \frac{\partial \phi}{\partial \sigma} \frac{\partial \sigma}{\partial p} = \frac{1}{p_s} \frac{\partial \phi}{\partial \sigma}. \tag{3.55}$$

From this, the vertical momentum equation in pressure coordinates (3.31) transforms to

$$\frac{R}{g} \frac{D}{Dt} \left(\frac{\omega T}{p} \right) + g + \frac{p}{p_s} \frac{g}{RT} \frac{\partial \phi}{\partial \sigma} = 0. \tag{3.56}$$

3.4.4 The continuity equation

From the transformation relationship (3.50) it follows that

$$\left(\frac{\partial u}{\partial x} \right)_p = \left(\frac{\partial u}{\partial x} \right)_\sigma - \sigma \frac{\partial u}{\partial \sigma} \left(\frac{\partial \ln p_s}{\partial x} \right)_\sigma \tag{3.57}$$

and

$$\left(\frac{\partial v}{\partial y} \right)_p = \left(\frac{\partial v}{\partial y} \right)_\sigma - \sigma \frac{\partial v}{\partial \sigma} \left(\frac{\partial \ln p_s}{\partial y} \right)_\sigma . \tag{3.58}$$

Noting the relationship between $\dot{\sigma}$ and ω

$$\begin{aligned} \omega \equiv \frac{Dp}{Dt} &= \frac{\partial p}{\partial t} + u \frac{\partial p}{\partial x} + v \frac{\partial p}{\partial y} + \dot{\sigma} \frac{\partial p}{\partial \sigma} \\ &= \sigma \frac{\partial p_s}{\partial t} + u\sigma \frac{\partial p_s}{\partial x} + v\sigma \frac{\partial p_s}{\partial y} + \dot{\sigma} p_s, \end{aligned} \tag{3.59}$$

from the use of equations (3.48) and (3.49), it follows from equation (3.51) that

$$\frac{\partial \omega}{\partial p} = \frac{1}{p_s} \frac{\partial \omega}{\partial \sigma}$$

$$= \frac{1}{p_s} \left[\frac{\partial p_s}{\partial t} + u \frac{\partial p_s}{\partial x} + v \frac{\partial p_s}{\partial y} + \sigma \left(\frac{\partial p_s}{\partial x} \frac{\partial u}{\partial \sigma} + \frac{\partial p_s}{\partial y} \frac{\partial v}{\partial \sigma} \right) + \frac{\partial \dot{\sigma}}{\partial \sigma} p_s \right]. \tag{3.60}$$

From the use of equations (3.57), (3.58) and (3.60) the continuity equation (3.25) transforms to σ coordinates as follows:

$$\frac{\partial u}{\partial x}+\frac{\partial v}{\partial y}+\frac{\partial \dot{\sigma}}{\partial \sigma}+\frac{\partial \ln p_s}{\partial t}+u\frac{\partial \ln p_s}{\partial x}+v\frac{\partial \ln p_s}{\partial y} = 0, \tag{3.61}$$

or, in a more compact form:

$$\frac{\partial u}{\partial x}+\frac{\partial v}{\partial y}+\frac{\partial \dot{\sigma}}{\partial \sigma}+\frac{D \ln p_s}{Dt}=0. \tag{3.62}$$

3.4.5 The thermodynamic energy equation

The form of the thermodynamic energy equation in σ coordinates is the same as for the pressure coordinate equation (3.40):

$$\frac{DT}{Dt}-\kappa\frac{\omega T}{p}=0. \tag{3.63}$$

3.4.6 The extended nonhydrostatic equation set

For the sake of convenience and future reference, the set of equations derived in σ coordinates based on the full pressure field is restated and renumbered:

$$\frac{Du}{Dt}-fv+\frac{\partial \phi}{\partial x}-\sigma\frac{\partial \phi}{\partial \sigma}\frac{\partial \ln p_s}{\partial x}=0, \tag{3.64}$$

$$\frac{Dv}{Dt}+fu+\frac{\partial \phi}{\partial y}-\sigma\frac{\partial \phi}{\partial \sigma}\frac{\partial \ln p_s}{\partial y}=0, \tag{3.65}$$

$$\frac{R}{g}\frac{D}{Dt}\left(\frac{\omega T}{p}\right)+g+\frac{p}{p_s}\frac{g}{RT}\frac{\partial \phi}{\partial \sigma}=0, \tag{3.66}$$

$$\frac{\partial u}{\partial x}+\frac{\partial v}{\partial y}+\frac{\partial \dot{\sigma}}{\partial \sigma}+\frac{D \ln p_s}{Dt}=0, \tag{3.67}$$

$$\frac{DT}{Dt}-\kappa\frac{\omega T}{p}=0. \tag{3.68}$$

It is convenient to introduce the quantity Ω by using relation (3.59) between the variables $\dot{\sigma}$ and ω:

$$\Omega=\frac{\omega}{p}=\frac{p_s}{\sigma p_s+p_T}\left(\sigma\frac{D \ln p_s}{Dt}+\dot{\sigma}\right). \tag{3.69}$$

3.4.7 A diagnostic equation for ϕ in σ coordinates

Note that from this point in the text and onwards, partial derivatives with respect to x, y and t are taken on constant σ levels, unless when stated otherwise. From the transformation relationships (3.50) and (3.51) it follows that:

$$\left(\frac{\partial \phi^2}{\partial x^2}\right)_p = \left(\frac{\partial \phi^2}{\partial x^2}\right) - \sigma \frac{\partial \ln p_s}{\partial x}\frac{\partial^2 \phi}{\partial x \partial \sigma} - \sigma \frac{\partial \phi}{\partial \sigma}\frac{\partial}{\partial x}\left(\frac{\partial \ln p_s}{\partial x}\right) - \sigma \frac{\partial \ln p_s}{\partial x}\frac{\partial^2 \phi}{\partial x \partial \sigma}$$

$$+\frac{\partial}{\partial \sigma}\left(\frac{\partial \phi}{\partial \sigma}\frac{\sigma}{p_s}\frac{\partial p_s}{\partial x}\right)\frac{\sigma}{p_s}\frac{\partial p_s}{\partial x}$$

$$= \left(\frac{\partial^2 \phi}{\partial x^2}\right)_\sigma - 2\sigma \frac{\partial \ln p_s}{\partial x}\frac{\partial^2 \phi}{\partial x \partial \sigma} + \sigma \frac{\partial}{\partial \sigma}\left(\sigma \frac{\partial \phi}{\partial \sigma}\right)\left(\frac{\partial \ln p_s}{\partial x}\right)^2 - \sigma \frac{\partial \phi}{\partial \sigma}\frac{\partial^2 \ln p_s}{\partial x^2}. \quad (3.70)$$

The last two terms in equation (3.70) can be written in alternative forms:

$$\sigma \frac{\partial}{\partial \sigma}\left(\sigma \frac{\partial \phi}{\partial \sigma}\right)\left(\frac{\partial \ln p_s}{\partial x}\right)^2 = \frac{\partial}{\partial \sigma}\left(\sigma^2 \frac{\partial \phi}{\partial \sigma}\right)\left(\frac{\partial \ln p_s}{\partial x}\right)^2 - \sigma \frac{\partial \phi}{\partial \sigma}\left(\frac{\partial \ln p_s}{\partial x}\right)^2 \quad (3.71)$$

and

$$-\sigma \frac{\partial \phi}{\partial \sigma}\frac{\partial^2 \ln p_s}{\partial x^2} = -\sigma \frac{\partial \phi}{\partial \sigma}\frac{1}{p_s}\frac{\partial^2 p_s}{\partial x^2} + \sigma \frac{\partial \phi}{\partial \sigma}(\frac{\partial \ln p_s}{\partial})^2. \quad (3.72)$$

Substituting (3.71) and (3.72) into (3.70) gives the required coordinate transformation for the term $\left(\partial^2 \phi / \partial x^2\right)_p$:

$$(\frac{\partial^2 \phi}{\partial x^2})_p = (\frac{\partial^2 \phi}{\partial x^2})_\sigma - 2\sigma \frac{\partial \ln p_s}{\partial x}\frac{\partial^2 \phi}{\partial x \partial \sigma} + \frac{\partial}{\partial \sigma}(\sigma^2 \frac{\partial \phi}{\partial \sigma})(\frac{\partial \ln p_s}{\partial x})^2 - \sigma \frac{\partial \phi}{\partial \sigma}\frac{1}{p_s}\frac{\partial^2 p_s}{\partial x^2}. \quad (3.73)$$

Similarly, it can be shown that

$$(\frac{\partial^2 \phi}{\partial y^2})_p = (\frac{\partial^2 \phi}{\partial y^2})_\sigma - 2\sigma \frac{\partial \ln p_s}{\partial y}\frac{\partial^2 \phi}{\partial y \partial \sigma} + \frac{\partial}{\partial \sigma}(\sigma^2 \frac{\partial \phi}{\partial \sigma})(\frac{\partial \ln p_s}{\partial y})^2 - \sigma \frac{\partial \phi}{\partial \sigma}\frac{1}{p_s}\frac{\partial^2 p_s}{\partial y^2}. \quad (3.74)$$

To complete the tranformation of terms on the left-hand side of (3.36), transformation relationship (3.51) can be used to show that

$$\frac{\partial}{\partial p}(r^2 \frac{\partial \phi}{\partial p}) = \frac{\partial}{\partial \sigma}(s^2 \frac{\partial \phi}{\partial \sigma}). \quad (3.75)$$

Here $r = gp/RT$ as before and $s = (\sigma + p_T/p_s)\,(g/RT) = (p/p_s)\,(g/RT)$.

The Jacobian terms (3.13) on the right-hand side of (3.36) transforms to σ coordinates using transformation relationships (3.50) and (3.51) as follows:

$$\frac{\partial \omega}{\partial p}\frac{\partial u}{\partial x} - \frac{\partial u}{\partial p}\frac{\partial \omega}{\partial x} = \frac{1}{p_s}\frac{\partial \omega}{\partial \sigma}\left(\frac{\partial u}{\partial x} - \frac{\partial u}{\partial \sigma}\sigma\frac{\partial \ln p_s}{\partial x}\right) - \frac{1}{p_s}\frac{\partial u}{\partial \sigma}\left(\frac{\partial \omega}{\partial x} - \frac{\partial \omega}{\partial \sigma}\sigma\frac{\partial \ln p_s}{\partial x}\right)$$

$$= \frac{\partial u}{\partial x}\frac{\partial}{\partial \sigma}\left(\Omega\frac{p}{p_s}\right) - \frac{1}{p_s}\frac{\partial u}{\partial \sigma}\frac{\partial}{\partial x}\left(\Omega p\right) \tag{3.76}$$

and similarly,

$$\frac{\partial \omega}{\partial p}\frac{\partial v}{\partial y} - \frac{\partial v}{\partial p}\frac{\partial \omega}{\partial y} = \frac{\partial v}{\partial y}\frac{\partial}{\partial \sigma}\left(\Omega\frac{p}{p_s}\right) - \frac{1}{p_s}\frac{\partial v}{\partial \sigma}\frac{\partial}{\partial y}\left(\Omega p\right). \tag{3.77}$$

The remaining terms in the Jacobian transform to:

$$\left(\frac{\partial u}{\partial x}\frac{\partial v}{\partial y} - \frac{\partial v}{\partial x}\frac{\partial u}{\partial y}\right)_p = \frac{\partial u}{\partial x}\frac{\partial v}{\partial y} - \frac{\partial v}{\partial x}\frac{\partial u}{\partial y}$$

$$+\sigma\left[\frac{\partial \ln p_s}{\partial x}\left(\frac{\partial u}{\partial y}\frac{\partial v}{\partial \sigma} - \frac{\partial v}{\partial y}\frac{\partial u}{\partial \sigma}\right) + \frac{\partial \ln p_s}{\partial y}\left(\frac{\partial v}{\partial x}\frac{\partial u}{\partial \sigma} - \frac{\partial u}{\partial x}\frac{\partial v}{\partial \sigma}\right)\right]. \tag{3.78}$$

The Coriolis terms transform as follows:

$$f\left(\frac{\partial v}{\partial x} - \frac{\partial u}{\partial y}\right)_p = f\left(\frac{\partial v}{\partial x} - \frac{\partial u}{\partial y}\right) + f\sigma\left[\frac{\partial u}{\partial \sigma}\left(\frac{\partial \ln p_s}{\partial y}\right) - \frac{\partial v}{\partial \sigma}\left(\frac{\partial \ln p_s}{\partial x}\right)\right], \tag{3.79}$$

whilst the term $-udf/dy$ remains unchanged by the coordinate transformation.

The remaining two terms on the right-hand side of (3.36) transform as follows:

$$-\frac{\partial}{\partial p}\left(rg - \frac{\omega^2}{\gamma p}\right) = -\frac{\partial}{\partial \sigma}\left(sg - \frac{1}{\gamma}\Omega^2\frac{p}{p_s}\right). \tag{3.80}$$

Combining the above transformation relationships (3.73 to 3.80) yields an elliptic equation for ϕ in σ coordinates:

$$\frac{\partial^2 \phi}{\partial x^2} + \frac{\partial^2 \phi}{\partial y^2} + \frac{\partial}{\partial \sigma}\left(s^2\frac{\partial \phi}{\partial \sigma}\right) - 2\sigma\left(\frac{\partial \ln p_s}{\partial x}\frac{\partial^2 \phi}{\partial x \partial \sigma} + \frac{\partial \ln p_s}{\partial y}\frac{\partial^2 \phi}{\partial y \partial \sigma}\right) +$$

$$\left[\left(\frac{\partial \ln p_s}{\partial x}\right)^2 + \left(\frac{\partial \ln p_s}{\partial y}\right)^2\right]\left[\frac{\partial}{\partial \sigma}\left(\sigma^2\frac{\partial \phi}{\partial \sigma}\right)\right] - \frac{\sigma}{p_s}\left(\frac{\partial^2 p_s}{\partial x^2} + \frac{\partial^2 p_s}{\partial y^2}\right)\frac{\partial \phi}{\partial \sigma} =$$

$$2\{\left\{\left(\frac{\partial u}{\partial x}+\frac{\partial v}{\partial y}\right)\frac{\partial}{\partial\sigma}\left(\Omega\frac{p}{p_s}\right)\right.$$

$$-\frac{1}{p_s}\left[\frac{\partial}{\partial x}(\Omega p)\frac{\partial u}{\partial\sigma}+\frac{\partial}{\partial y}(\Omega p)\frac{\partial v}{\partial\sigma}\right]+\frac{\partial u}{\partial x}\frac{\partial v}{\partial y}-\frac{\partial v}{\partial x}\frac{\partial u}{\partial y}+$$

$$\left.\sigma\left[\frac{\partial \ln p_s}{\partial x}\left(\frac{\partial u}{\partial y}\frac{\partial v}{\partial\sigma}-\frac{\partial v}{\partial y}\frac{\partial u}{\partial\sigma}\right)+\frac{\partial \ln p_s}{\partial y}\left(\frac{\partial v}{\partial x}\frac{\partial u}{\partial\sigma}-\frac{\partial u}{\partial x}\frac{\partial v}{\partial\sigma}\right)\right]\right\}$$

$$+f\left[\frac{\partial v}{\partial x}-\frac{\partial u}{\partial y}+\sigma\left(\frac{\partial u}{\partial\sigma}\frac{\partial \ln p_s}{\partial y}-\frac{\partial v}{\partial\sigma}\frac{\partial \ln p_s}{\partial x}\right)\right]-u\frac{df}{dy}-\frac{\partial}{\partial\sigma}\left(sg-\frac{p}{p_s}\Omega^2\frac{1}{\gamma}\right). \tag{3.81}$$

Equation (3.81) may also be derived directly from equations (3.64) to (3.69). This tedious derivation can be found in Appendix A.

3.4.8 Two-dimensional version of White's equations in σ coordinates

In two spatial dimensions, the pressure coordinate momentum, continuity and thermodynamic energy equations of White (1989) transform to the following σ coordinate equations:

$$\frac{Du}{Dt}+\left(\frac{\partial\phi}{\partial x}\right)-\sigma\left(\frac{\partial\phi}{\partial\sigma}\right)\frac{\partial \ln p_s}{\partial x}=0, \tag{3.82}$$

$$\frac{R}{g}\frac{D}{Dt}\left(\frac{\omega T}{p}\right)+g+\frac{p}{p_s}\frac{g}{RT}\frac{\partial\phi}{\partial\sigma}=0, \tag{3.83}$$

$$\frac{\partial u}{\partial x}+\frac{\partial\dot{\sigma}}{\partial\sigma}+\frac{D \ln p_s}{Dt}=0, \tag{3.84}$$

$$\frac{DT}{Dt}-\kappa\frac{\omega T}{p}=0. \tag{3.85}$$

The two-dimensional diagnostic equation for ϕ in σ coordinates is:

$$\frac{\partial^2\phi}{\partial x^2}+\frac{\partial}{\partial\sigma}\left(s^2\frac{\partial\phi}{\partial\sigma}\right)-2\sigma\frac{\partial \ln p_s}{\partial x}\frac{\partial^2\phi}{\partial x\partial\sigma}+\left(\frac{\partial \ln p_s}{\partial x}\right)^2\frac{\partial}{\partial\sigma}\left(\sigma^2\frac{\partial\phi}{\partial\sigma}\right)-\frac{\sigma}{p_s}\left(\frac{\partial^2 p_s}{\partial x^2}\right)\frac{\partial\phi}{\partial\sigma}=$$

$$2\left[\frac{\partial u}{\partial x}\frac{\partial}{\partial\sigma}\left(\Omega\frac{p}{p_s}\right)-\frac{1}{p_s}\frac{\partial}{\partial x}(\Omega p)\frac{\partial u}{\partial\sigma}\right]-\frac{\partial}{\partial\sigma}\left[(sg)-\frac{1}{\gamma}\frac{p}{p_s}\Omega^2\right]. \tag{3.86}$$

3.5 Properties of the nonhydrostatic σ coordinate equations based on the full pressure field

In the following sections, the properties of the derived σ coordinate formulation of the equations of White (1989) are studied. Links and differences with respect to the MP equations in σ coordinates are pointed out.

3.5.1 Physical implications of the approximated vertical momentum equation

The unapproximated vertical momentum equation, for motion on an f plane, is

$$\frac{Dw}{Dt} + g + \frac{1}{\rho}\frac{\partial p}{\partial z} = 0. \tag{3.87}$$

Here w is the Cartesian vertical velocity Dz/Dt. Following the discussion of White (1989) for the extended pressure coordinate equations, (3.87) may be written as

$$\frac{1}{g}\frac{\partial \phi}{\partial \sigma}\frac{Dw}{Dt} + \frac{\partial \phi}{\partial \sigma} + RT\frac{p_s}{p} = 0. \tag{3.88}$$

Note that the reference state relation (3.11) transforms to σ coordinates as

$$\frac{\partial \phi_{ref}}{\partial \sigma} + \frac{p_s}{p}RT_{ref} = 0 \tag{3.89}$$

on the use of (3.51). Subtracting the reference state relation from equation (3.88), and rearranging the terms, gives

$$\frac{Dw}{Dt} + g\frac{\partial \sigma}{\partial \phi}\left(\frac{\partial \phi'}{\partial \sigma} + \frac{p_s}{p}RT'\right) = 0. \tag{3.90}$$

Substituting for $\partial\sigma/\partial\phi$ from equation (3.88) leads to

$$\frac{Dw}{Dt} + g\frac{\partial \sigma}{\partial \phi}\left(\frac{\partial \phi'}{\partial \sigma} + \frac{p_s}{p}RT'\right) = 0. \tag{3.91}$$

From considering (3.91) possible approximations become apparent. Upon introducing the approximations

$$Dw/Dt \ll g \tag{3.92}$$

and

$$w \simeq \hat{w} \equiv -\omega/\rho g = -\omega RT/gp, \tag{3.93}$$

(3.91) reduces to (3.67), the σ coordinate form of the extended MP vertical momentum equation. It does not contain the further replacement of T by T_{ref}, from which the MP vertical momentum equation is obtained.

3.5.2 Energetics of the σ coordinate equations

In order to obtain an equation for the energy budget of the σ coordinate equations (3.64) to (3.68), multiplying (3.64) by u, (3.65) by v, (3.66) by $\hat{w}$, (3.68) by c_p and adding the equations give:

$$\frac{D}{Dt}\left(\frac{1}{2}u^2+\frac{1}{2}v^2+\frac{1}{2}\hat{w^2}+c_pT\right)=-u\frac{\partial\phi}{\partial x}-v\frac{\partial\phi}{\partial y}+\sigma\frac{\partial\phi}{\partial\sigma}\left(u\frac{\partial\ln p_s}{\partial x}+v\frac{\partial\ln p_s}{\partial y}\right)$$
$$+\hat{w}\left(g+\frac{p}{p_s}\frac{g}{RT}\frac{\partial\phi}{\partial\sigma}\right)+R\frac{\omega T}{p}. \tag{3.94}$$

From multiplying (3.94) by p_s, it follows that

$$p_s\frac{D}{Dt}\left(\frac{1}{2}u^2+\frac{1}{2}v^2+\frac{1}{2}\hat{w^2}+c_pT\right)=-p_s\left(u\frac{\partial\phi}{\partial x}+v\frac{\partial\phi}{\partial y}\right)+\sigma\frac{\partial\phi}{\partial\sigma}\left(u\frac{\partial p_s}{\partial x}+v\frac{\partial p_s}{\partial y}\right)$$
$$+\hat{w}p_s\left(g+\frac{p}{p_s}\frac{g}{RT}\frac{\partial\phi}{\partial\sigma}\right)+p_sR\frac{\omega T}{p}. \tag{3.95}$$

By using (3.93) it can be shown that (3.95) reduces to:

$$p_s\frac{D}{Dt}\left(\frac{1}{2}u^2+\frac{1}{2}v^2+\frac{1}{2}\hat{w^2}+c_pT\right)=\sigma\frac{\partial\phi}{\partial\sigma}\left(u\frac{\partial p_s}{\partial x}+v\frac{\partial p_s}{\partial y}\right)$$
$$-\left[\frac{\partial\left(p_su\phi\right)}{\partial x}-\phi\frac{\partial\left(up_s\right)}{\partial x}+\frac{\partial\left(p_sv\phi\right)}{\partial y}-\phi\frac{\partial\left(vp_s\right)}{\partial y}\right]-\omega\frac{\partial\phi}{\partial\sigma}$$

$$=-\frac{\partial\left(p_su\phi\right)}{\partial x}-\frac{\partial\left(p_sv\phi\right)}{\partial y}+\phi\left(u\frac{\partial p_s}{\partial x}+v\frac{\partial p_s}{\partial y}\right)+\phi p_s\left(\frac{\partial u}{\partial x}+\frac{\partial v}{\partial y}\right)$$
$$-\omega\frac{\partial\phi}{\partial\sigma}+\sigma\frac{\partial\phi}{\partial\sigma}\left(u\frac{\partial p_s}{\partial x}+v\frac{\partial p_s}{\partial y}\right). \tag{3.96}$$

From the use of the continuity equation (3.67) and relationship (3.69) it is finally obtained that:

$$p_s\frac{D}{Dt}\left(\frac{1}{2}u^2+\frac{1}{2}v^2+\frac{1}{2}\hat{w^2}+c_pT\right)=-\frac{\partial\left(p_su\phi\right)}{\partial x}-\frac{\partial\left(p_sv\phi\right)}{\partial y}-\frac{\partial}{\partial\sigma}\left(p_s\dot{\sigma}\phi\right)$$
$$-\frac{\partial}{\partial\sigma}\left(\phi\sigma\right)\frac{\partial p_s}{\partial t}. \tag{3.97}$$

Equation (3.97) corresponds to the energy equation found by Miller and White (1984) for the two-dimensional MP equations in σ coordinates, with the difference that the aproximated "vertical" specific kinectic energy per unit mass is evaluated in terms of a reference temperature in the MP equations, by using (3.4). As pointed out by Miller and White (1984) for the energy equation corresponding to the MP equations, (3.97) is similar to the total energy equation implied by the usual hydrostatic σ coordinate equations (e.g. Haltiner, 1971). The main difference with respect to the energy equation of the hydrostatic σ coordinate equations, is that the contribution of vertical velocity to the specific kinetic energy is present in approximated form in (3.97), whilst it is neglected in the hydrostatic form of the equation.

3.5.3 Linearized equations

Knowledge of the types of motion described by a given equation set is essential not only for understanding the dynamical properties of the system, but also for practical purposes when numerical computations are carried out and a suitable algorithm is to be chosen (Miller, 1974).

The linear analysis presented in this section closely follows that of Miller and White (1984). However, the use of the modified σ coordinate (3.42) with $p_T > 0$ requires a more complicated treatment than the case of $p_T = 0$ (as used by Miller and White, 1984). The two-dimensional σ coordinate equations (3.82) to (3.85) are studied in order to keep the analysis compact, but the extension to three dimensions is obvious. Equations (3.82) to (3.85) are linearized around a reference state of no motion, that is $u_{ref} = 0$ and $\dot{\sigma}_{ref} = 0$. The reference state is chosen to be isothermal and in hydrostatic balance:

$$\frac{d\phi_{ref}}{dp} = -\frac{RT_0}{p}, \tag{3.98}$$

which by the use of transformation relation (3.51) translates to

$$\frac{\partial\phi_{ref}}{\partial\sigma} = \frac{-p_s}{p} RT_0. \tag{3.99}$$

Here T_0 is the temperature of the reference state and $\phi_{ref} = \phi_{ref}(p)$. The reference surface pressure p_{surf_ref} is constant. Note that the reference state is a function of pressure only, which implies that the reference state geopotential depends on the horizontal position at levels of constant σ. In fact it is useful to note that, from the transformation relation (3.50),

$$\begin{aligned}\left(\frac{\partial\phi_{ref}}{\partial x}\right)_\sigma &= \left(\frac{\partial\phi_{ref}}{\partial x}\right)_p + \frac{\partial\phi_{ref}}{\partial\sigma}\frac{\sigma}{p_s}\left(\frac{\partial p_s}{\partial x}\right)_\sigma \\ &= \sigma\frac{\partial\phi_{ref}}{\partial\sigma}\left(\frac{\partial \ln p_s}{\partial x}\right)_\sigma = -\sigma\frac{p_s}{p}RT_0\left(\frac{\partial \ln p_s}{\partial x}\right)_\sigma,\end{aligned} \tag{3.100}$$

since ϕ_{ref} is a function of pressure only.

The perturbation fields $\alpha^{'}$ are defined by

$$\alpha = \alpha_{ref} + \alpha^{'} \tag{3.101}$$

for a particular field variable α. Following the usual linearization procedure, all variables in (3.82) to (3.86) are written in terms of reference and perturbation parts. By neglecting the products of perturbations, and by making use of (3.99) and (3.100), the linearized equations may be shown to be:

$$\frac{\partial u}{\partial t} + \frac{\partial \phi^{'}}{\partial x} = 0, \tag{3.102}$$

$$H_0 \frac{\partial}{\partial t}\left[\frac{p_0}{\sigma p_0 + p_T}\left(\frac{\sigma}{p_0}\frac{\partial p_s}{\partial t} + \dot{\sigma}\right)\right] + \frac{T^{'}}{T_0}g + \left(\frac{\sigma p_0 + p_T}{p_0}\right)\frac{1}{H_0}\frac{\partial \phi^{'}}{\partial \sigma} = 0, \tag{3.103}$$

$$\frac{\partial u}{\partial x} + \frac{\partial \dot{\sigma}}{\partial \sigma} + \frac{1}{p_0}\frac{\partial p_s}{\partial t} = 0, \tag{3.104}$$

$$\frac{\partial T^{'}}{\partial t} - \kappa\left[\frac{p_0}{\sigma p_0 + p_T}\left(\frac{\sigma}{p_0}\frac{\partial p_s}{\partial t} + \dot{\sigma}\right)\right] T_0 = 0. \tag{3.105}$$

Here $H_0 = RT_0/g$ and $p_0 = p_{surf\_ref} - p_T$. Note that in deriving the linearized equations, the assumptions $\left|T^{'}\right| \ll T_0$ and $\left|p_s^{'}\right| \ll p_0$ are made explicitly.

3.5.4 Towards wave-like solutions of the linearized equations

In order to investigate the presence and characteristics of sound and gravity waves that form part of the solution set of (3.82) to (3.85), wave-like solutions of the form

$$Q\left(x,\, t\right) = \hat{Q}\exp^{ik(x-ct)} \tag{3.106}$$

are posed for (3.82) to (3.85), for each field variable Q (with the field variables being u, $\dot{\sigma}$, $\phi^{'}$, $T^{'}$ and p_s) . Here $\hat{Q}$ is a function of σ at most. It is convenient to write $\hat{p_s}$ in terms of p_0, as $\hat{p_s} = p_0\hat{\pi}$. Note that $kc = \nu$, where ν is the frequency of oscillation, $k = 2\pi/L_x$ is the wave number and L_x is the wave length. For propagating waves the phase speed is constant for an observer moving at the phase speed c. The following equations relating the amplitudes of the posed solutions are obtained from substituting (3.106) into (3.102) to (3.105):

$$-c\hat{u} + \hat{\phi}' = 0, \tag{3.107}$$

$$H_0\left\{\frac{p_0}{\sigma p_0+p_T}\left[-ikc\hat{\dot{\sigma}}+(ikc)^2\sigma\hat{\pi}\right]\right\}+g\frac{\hat{T}'}{T_0}+\left(\frac{\sigma p_0+p_T}{p_0}\right)\frac{1}{H_0}\frac{d\hat{\phi}'}{d\sigma}=0, \tag{3.108}$$

$$ik\hat{u}+\frac{d\hat{\dot{\sigma}}}{d\sigma}-ikc\hat{\pi}=0, \tag{3.109}$$

$$(-ikc)\,\hat{T}'-\kappa\left[\frac{p_0}{\sigma p_0+p_T}\left(\hat{\dot{\sigma}}-ikc\sigma\hat{\pi}\right)\right]T_0=0. \tag{3.110}$$

Eliminating $\hat{u}$ and $\hat{T}'$ from (3.107) to (3.110) gives

$$\frac{d\hat{\dot{\sigma}}}{d\sigma}-ikc\hat{\pi}+i\frac{k}{c}\hat{\phi}'=0, \tag{3.111}$$

$$icH_0^2\left(k^2-\frac{N^2}{c^2}\right)\left(\hat{\dot{\sigma}}-ikc\sigma\hat{\pi}\right)-\left(\frac{\sigma p_0+p_T}{p_0}\right)^2 k\frac{d\hat{\phi}'}{d\sigma}=0, \tag{3.112}$$

where $N^2=g\kappa/H_0$.

Following Miller and White (1984) the best way to proceed is to eliminate $\hat{\dot{\sigma}}$ from equations (3.111 and 3.112) to obtain a second-order differential equation for $\hat{\phi}'$:

$$\frac{d}{d\sigma}[(\frac{\sigma p_0+p_T}{p_0})^2\frac{d\hat{\phi}'}{d\sigma}]+H_0^2(\frac{N^2}{c^2}-k^2)\hat{\phi}'=0. \tag{3.113}$$

Equation (3.113) may alternatively be derived from the linearized version of the elliptic equation (3.81). This approach is useful in the eventual analysis of numerical schemes used to solve the system (3.64) to (3.68) (see Chapter 4), and is presented in Appendix B.

Under the transformations

$$Z=-H_0\ln(\frac{\sigma p_0+p_T}{p_0}), \tag{3.114}$$

$$F=\hat{\phi}'\exp^{-Z/2H_0}, \tag{3.115}$$

(3.113) becomes

$$\frac{D^2F}{DZ^2}+(\frac{N^2}{c^2}-k^2-\frac{1}{4H_0^2})F=0. \tag{3.116}$$

The algebra involved in deriving (3.116) is discussed in Appendix C.

For later application, it is useful to find a the relation between $\hat{\pi}$ and $\hat{\phi}'$. This is achieved by integrating (3.111) over $\sigma = [0, 1]$ and by applying $\hat{\dot{\sigma}} = 0$ (that is, $\dot{\sigma} = 0$) at $\sigma = 0$ and 1

$$\hat{\pi} = \frac{1}{c^2} \int_0^1 \hat{\phi}' d\sigma. \tag{3.117}$$

3.5.5 Solutions of (3.116) with exponential variation in height

3.5.5.1 Form of the sound wave solutions

Solutions of (3.116) with exponential height variation (if they exist) have

$$\mu^2 = \frac{1}{4H_0^2} - \left(\frac{N^2}{c^2} - k^2 \right) > 0, \tag{3.118}$$

so that

$$\hat{\phi}' = \left[A \exp^{-\mu Z} + B \exp^{\mu Z} \right] \exp^{\frac{Z}{2H_0}} \tag{3.119}$$

and one may define $\mu > 0$. Equation (3.118) is the frequency equation for Lamb-waves described by (3.82) to (3.85) (see the analysis by Miller (1974) and Miller and White (1984) for the MP equations, also see the following sections 3.5.5.5 and 3.5.5.6).

It may be noted that relationship (3.118) may consistently be obtained by considering the upper and lower boundary conditions that apply to $\dot{\sigma}$, $\hat{\phi}'$, and $d\hat{\phi}'/d\sigma$. The details of this derivation are given in Appendix D and make use of results obtained in sections 3.5.5.3 and 3.5.5.4. A second equation relating μ and c needs to be obtained, in order to find an expression for c in terms of the reference state parameters and physical constants. To this end, it is useful to linearize the term $D\phi/Dt$ at $\sigma = 1$. Note that

$$\frac{D\phi}{Dt} = \frac{\partial \phi}{\partial t} + u \frac{\partial \phi}{\partial x} \tag{3.120}$$

at $\sigma = 1$. Using (3.50) and (3.51), this may be written as:

$$\frac{D\phi}{Dt} = \frac{\partial \phi'}{\partial t} + \sigma \frac{d\phi_{ref}}{dp} \left(\frac{\partial p_s}{\partial t} + u \frac{\partial p_s}{\partial x} \right) + u \frac{\partial \phi'}{\partial x}$$

$$= \frac{\partial \phi'}{\partial t} + \sigma \left(\frac{-RT_0}{\sigma p_s + p_T} \right) \left(\frac{\partial p_s}{\partial t} + u \frac{\partial p_s}{\partial x} \right) + u \frac{\partial \phi'}{\partial x}. \tag{3.121}$$

Linearizing (3.121) and requiring that $w = 0$ at $\sigma = 1$ (where $\dot{\sigma} = 0$ by definition) gives (at $\sigma = 1$):

$$\frac{\partial \phi^{'}}{\partial t} = \frac{RT_0}{p_0}\frac{\partial p_s}{\partial t} = \frac{gH_0}{p_0}\frac{\partial p_s}{\partial t}. \tag{3.122}$$

Note that by requiring $w = 0$ at $\sigma = 1$ (that is $Z = 0$), specifies $\sigma = 1$ as a level surface. Equation (3.122) reduces to

$$\hat{\phi'} = gH_0\hat{\pi} \tag{3.123}$$

at $\sigma = 1$, on the substitution of (3.106). The required second equation relating μ and c may be obtained by substituting appropriate expressions for $\hat{\phi'}$ and $\hat{\pi}$ in (3.123).

3.5.5.2 Finding an expression for $\hat{\phi'}$ at $\sigma = 1$

Recalling the definition $Z = -H_0 \ln[\frac{\sigma p_0 + p_T}{p_0}]$, it follows from (3.119) that

$$\hat{\phi'} = A(\frac{\sigma p_0 + p_T}{p_0})^{H_0(\mu - \frac{1}{2H_0})} + B(\frac{\sigma p_0 + p_T}{p_0})^{H_0(-\mu - \frac{1}{2H_0})}. \tag{3.124}$$

From (3.124) it follows that

$$\hat{\phi'}\,(\sigma = 1)) = A\left(\frac{p_0 + p_T}{p_0}\right)^{H_0(\mu - 1/2H_0)} + B\left(\frac{p_0 + p_T}{p_0}\right)^{H_0(-\mu - 1/2H_0)}. \tag{3.125}$$

3.5.5.3 Applying the linearized continuity equation

From substituting (3.124) in (3.117) it is obtained that:

$$\hat{\pi} = \frac{1}{c^2}\left\{A\left[\frac{1}{H_0\,(\mu + 1/2H_0)}\right]\left[\left(\frac{p_0 + p_T}{p_0}\right)^{H_0(\mu + 1/2H_0)} - \left(\frac{p_T}{p_0}\right)^{H_0(\mu + 1/2H_0)}\right]\right.$$

$$\left. + B\left[\frac{1}{H_0\,(-\mu + 1/2H_0)}\right]\left[\left(\frac{p_0 + p_T}{p_0}\right)^{H_0(-\mu + 1/2H_0)} - \left(\frac{p_T}{p_0}\right)^{H_0(-\mu + 1/2H_0)}\right]\right\}. \tag{3.126}$$

Equations (3.126) and (3.125) may now be substituted into (3.123), in order to find the required second relationship between c and μ. However, in order to eliminate constants A and B from the resulting equation, it is necessary to find the relationship between the constants. This relationship is derived in the next subsection.

3.5.5.4 Utilizing the upper boundary condition on $d\hat{\phi}'/d\sigma$

From differentiating equation (3.124) with respect to σ it follows that

$$\frac{d\hat{\phi}'}{d\sigma} = AH_0\left(\mu - 1/2H_0\right)\left(\frac{\sigma p_0 + p_T}{p_0}\right)^{H_0(\mu-\frac{3}{2H_0})} + BH_0\left(-\mu - 1/2H_0\right)\left(\frac{\sigma p_0 + p_T}{p_0}\right)^{H_0(-\mu-\frac{3}{2H_0})} \tag{3.127}$$

Equation (3.112) yields, for the case $p_T > 0$, that $d\hat{\phi}'/d\sigma = 0$ at the upper boundary $\sigma = 0$ (from noting that $\dot{\sigma} = 0$ at $\sigma = 0$ per definition). From this result an equation relating A and B may be obtained by the use of (3.127):

$$A\left[H_0\left(\mu - \frac{1}{2H_0}\right)\left(\frac{p_T}{p_0}\right)^{H_0(\mu-\frac{3}{2H_0})}\right] + B\left[H_0\left(-\mu - \frac{1}{2H_0}\right)\left(\frac{p_T}{p_0}\right)^{H_0(-\mu-\frac{3}{2H_0})}\right] = 0, \tag{3.128}$$

which reduces to

$$B = A\frac{\left(\mu - \frac{1}{2H_0}\right)}{\left(\mu + \frac{1}{2H_0}\right)}\left(\frac{p_T}{p_0}\right)^{2H_0\mu}. \tag{3.129}$$

3.5.5.5 A second relationship between μ and c

From substituting (3.125) and (3.126) into (3.123) and applying (3.129) we obtain that:

$$\left(\frac{p_0 + p_T}{p_0}\right)^{H_0(\mu-\frac{1}{2H_0})} + \left(\frac{\mu - \frac{1}{2H_0}}{\mu + \frac{1}{2H_0}}\right)\left(\frac{p_T}{p_0}\right)^{2H_0\mu}\left(\frac{p_0 + p_T}{p_0}\right)^{H_0(-\mu-\frac{1}{2H_0})} = \frac{g}{c^2}\left\{\left(\frac{1}{\mu + \frac{1}{2H_0}}\right)\left[\left(\frac{p_0 + p_T}{p_0}\right)^{H_0(\mu+\frac{1}{2H_0})} - \left(\frac{p_T}{p_0}\right)^{H_0(\mu+\frac{1}{2H_0})}\right] + \left(\frac{\mu - \frac{1}{2H_0}}{\mu + \frac{1}{2H_0}}\right)\left(\frac{p_T}{p_0}\right)^{2H_0\mu}\left(\frac{1}{-\mu + \frac{1}{2H_0}}\right)\left[\left(\frac{p_0 + p_T}{p_0}\right)^{H_0(-\mu+\frac{1}{2H_0})} - \left(\frac{p_T}{p_0}\right)^{H_0(-\mu+\frac{1}{2H_0})}\right]\right\}, \tag{3.130}$$

which reduces to

$$\left(\mu + \frac{1}{2H_0}\right)\left(\frac{p_0 + p_T}{p_0}\right)^{H_0(\mu-\frac{1}{2H_0})} + \left(\mu - \frac{1}{2H_0}\right)\left(\frac{p_T}{p_0}\right)^{2H_0\mu}\left(\frac{p_0 + p_T}{p_0}\right)^{H_0(-\mu-\frac{1}{2H_0})} = \frac{g}{c^2}\left[\left(\frac{p_0 + p_T}{p_0}\right)^{H_0(\mu+\frac{1}{2H_0})} - \left(\frac{p_T}{p_0}\right)^{2H_0\mu}\left(\frac{p_0 + p_T}{p_0}\right)^{H_0(-\mu+\frac{1}{2H_0})}\right]. \tag{3.131}$$

It may be noted that in the limit, when p_T approaches 0, (3.131) reduces to

$$\mu + \frac{1}{2H_0} = \frac{g}{c^2}. \tag{3.132}$$

This corresponds exactly to the result obtained by Miller and White (1984), for the MP equations, as formulated originally with $p_T = 0$. It is not clear how the simultaneous equations (3.118) and (3.131) may solved for the general case of $p_T > 0$, in order to obtain an expression for c in terms of the reference state parameters and physical constants. However, an approximated relationship may be obtained by making use of a Taylor series expansion for c^2 in (3.131). To this end, note that from (3.131) it follows that

$$c^2 = g \left\{ \left[\left(p_0 + p_T \right) / p_0 \right]^{H_0(\mu + 1/2H_0)} - \left(p_T / p_0 \right)^{2H_0\mu} \left[\left(p_0 + p_T \right) / p_0 \right]^{H_0(-\mu + 1/2H_0)} \right\} /$$

$$\left\{ \left(\mu + 1/2H_0 \right) \left[\left(p_0 + p_T \right) / p_0 \right]^{H_0(\mu - 1/2H_0)} \right.$$

$$\left. + \left(\mu - 1/2H_0 \right) \left(p_T / p_0 \right)^{2H_0\mu} \left[\left(p_0 + p_T \right) / p_0 \right]^{H_0(-\mu - 1/2H_0)} \right\}. \tag{3.133}$$

From (3.133) the function $\partial c^2 / \partial p_T$ may be calculated, and c^2 may be approximated with a Taylor series expansion around $p_T = 0$ as

$$c^2 \left(\mu, \, p_T \right) = c^2 \left(\mu, \, 0 \right) + \left(\frac{\partial c^2}{\partial p_T} \left(\mu, \, 0 \right) \right) \left(p_T \right) + O \left(p_T^2 \right) \tag{3.134}$$

Evaluating c^2 and $\partial c^2 / \partial p_T$ at $p_T = 0$ and substituting in (3.134) leads to the approximated relationship

$$c^2 \approx \frac{g}{\mu + 1/2H_0} + \left(\frac{gH_0}{p_0} \right) \left(1 - \frac{\mu - 1/2H_0}{\mu + 1/2H_0} \right) p_T. \tag{3.135}$$

3.5.5.6 The influence of the height of the model top on the phase speed of the Lamb waves

Equations (3.118) and (3.135) may be used to obtain an approximated expression for c in terms of the reference state parameters and physical constants. To this end, note that c^2 may be eliminated from (3.135) by the use of (3.118), to give

$$\frac{N^2}{1/4H_0^2 + k^2 - \mu^2} = \frac{g}{\mu + 1/2H_0} + \left(\frac{gH_0}{p_0} \right) \left(1 - \frac{\mu - 1/2H_0}{\mu + 1/2H_0} \right) p_T. \tag{3.136}$$

Rearranging the terms in (3.136) gives

$$g \left(1 + p_T / p_0 \right) \mu^2 + N^2 \mu - \left(1/4H_0^2 + k^2 \right) g \left(1 + p_T / p_0 \right) + N^2 / 2H_0, \tag{3.137}$$

which has solutions

$$\mu = \frac{-N^2 \pm \sqrt{N^4 + 4g\,(1 + p_T/p_0)\,[(1/4H_0^2 + k^2)\,g\,(1 + p_T/p_0) - N^2/2H_0]}}{2g\,(1 + p_T/p_0)}. \tag{3.138}$$

Equation (3.138) gives the relationship between μ and the reference state parameters and physical constants. It may be noted that only the positive root represents a physical solution, since $\mu > 0$ by definition. From (3.118) it follows that

$$c = \pm N/\sqrt{(1/4H_0^2 + k^2 - \mu^2)}. \tag{3.139}$$

Equation (3.138) may be used to eliminate μ from (3.139) to give a relationship between c and the reference state parameters and physical constants. The dependency of c on wave number and the height of the model top is depicted in Fig. 3.1, by the use of (3.138) and (3.139), for the choice of $p_T = 0\,hPa$ (yellow line), $p_T = 135\,hPa$ (green line) and $p_T = 442\,hPa$ (black line). The true sound wave speed is depicted by the red line. Formulas (3.138) and (3.139) were applied for $T_0 = 300\,K$; all the other constants have been defined earlier.

It is clear from Fig. 3.1 that for the choice $p_T = 0$ the Lamb wave phase speed is retarded at all wave lengths. The retardation is the strongest at the shortest resolvable scales, whilst the Lamb wave phase speed approaches the true sound wave speed in the long wave length limit. For the case $p_T = 135\,hPa$ and $p_T = 442\,hPa$, the Lamb waves are also retarded at the shortest resolvable scales. However, at lower wave numbers the Lamb waves are accelerated, reaching almost 400 m/s in the long wave length limit for the case $p_T = 442\,hPa$.

In boundary layer modelling, air pollution studies and numerical tests designed to test the performance of numerical schemes, it is common practice to choose the model top well below 0 hPa. With these and meso-scale applications in mind, more insight into the Lamb wave behaviour may be obtained from considering Fig. 3.2. Here the Lamb wave phase speed is displayed as a function of horizontal wave length, for $0.2\,km \leq L_x \leq 200.2\,km$. Note that $Lx = 0.2\,km$ represents the shortest resolvable wave for the choice $2\Delta x = 200\,m$. The colour code used is as stated for Fig. 3.1. Close to the limit of the shortest resolvable waves, the retardation of the Lamb waves are considerable for all the choices of p_T, being about 50 % for wavelengths of about 20 km. Thus, for micro- and meso-scale applications over relatively small domains, the equations (3.82)-(3.85) offer significant computational advantages over the fully-elastic equations. It may be noted that for the choice of $p_T = 442\,hPa$, Lamb waves travelling faster than the true sound wave speed are only present for wave lengths longer than about $140\,km$.

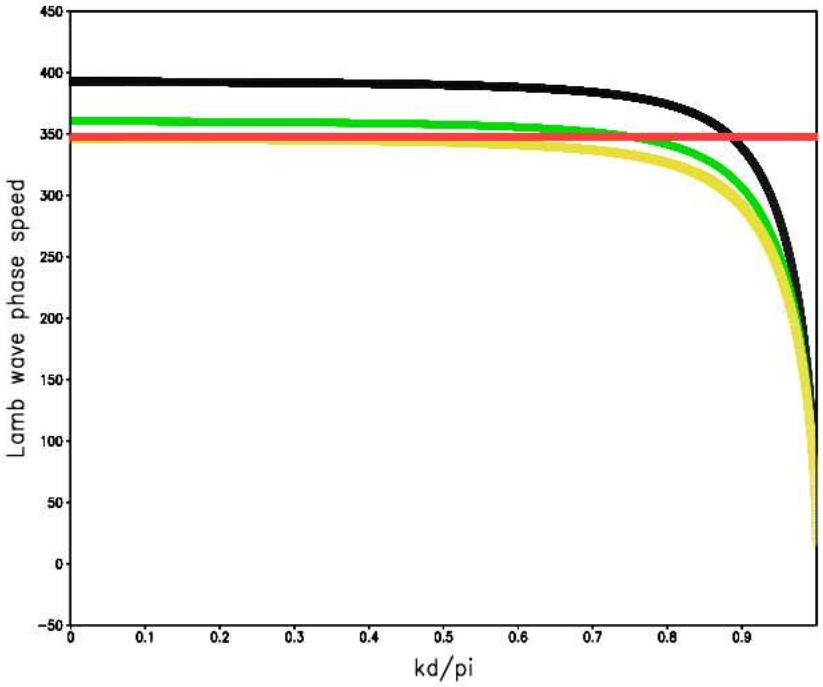

Figure 3.1: Lamb wave phase speed as a function of the normalised wave number, for various choices of the height of the model top: $p_T = 0\,hPa$ (yellow line); $p_T = 135\,hPa$ (green line); $p_T = 442\,hPa$ (black line). The true sound wave speed is depicted by the red line.

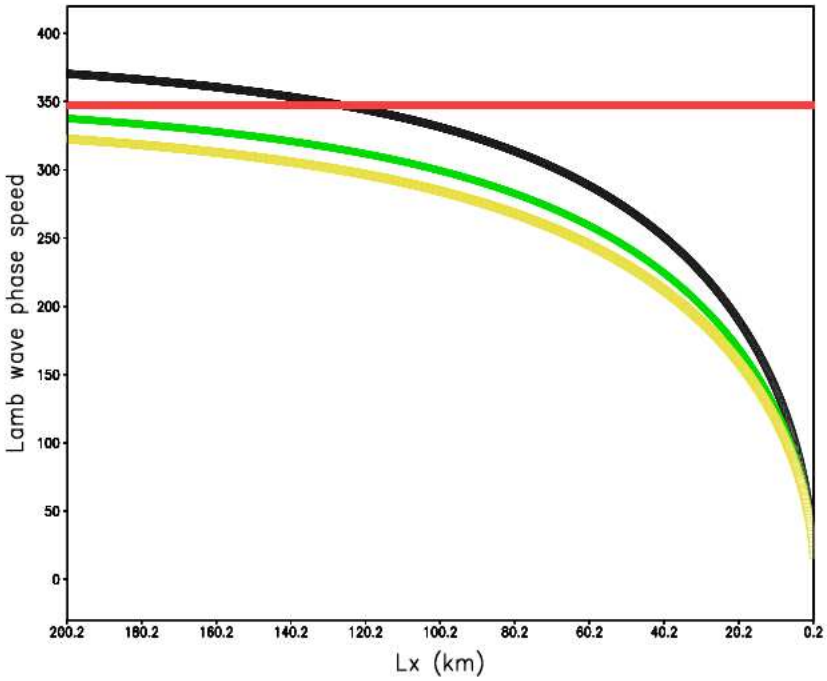

Figure 3.2: Lamb wave phase speed as a function of horizontal wave length, for various choices of the height of the model top: $p_T = 0\,hPa$ (yellow line); $p_T = 135\,hPa$ (green line); $p_T = 442\,hPa$ (black line). The true sound wave speed is depicted by the red line.

3.5.6 Solutions with sinusoidal variation in height

3.5.6.1 Form of the gravity wave solutions

Solutions of (3.116) with sinusoidal height variation (if they exist) have

$$m^2 = -\frac{1}{4H_0^2} + (\frac{N^2}{c^2} - k^2) > 0 \tag{3.140}$$

so that

$$\hat{\phi}' = [A \exp^{-imZ} + B \exp^{imZ}] \exp^{\frac{Z}{2H_0}} \tag{3.141}$$

and one may define $m > 0$. Equation (3.140) corrresponds to the frequency equation obained for gravity waves in the fully-elastic equations (see, for example, Eckart, 1960; Miller, 1974). The fully-elastic equations additionally describe horizontally and vertically propagating acoustic modes (e.g. Eckart, 1960; Miller, 1974), which are not present in (3.82) to (3.85), except for the Lamb waves described in section 3.5.5.

For later application (in Chapter 4) , it is useful to write (3.140) alternatively as

$$-\omega_T^2 \left(k^2 + m^2 + \frac{1}{4H_0^2}\right) c^2 + k^2 c^2 N^2 = 0, \tag{3.142}$$

with $\omega_T = kc$ the true frequency of the gravity waves.

3.5.6.2 Finding an expression for $\hat{\phi}'$ at $\sigma = 1$

From noting that by definition $Z = -H_0 \ln\left[(\sigma p_0 + p_T)/p_0\right]$, it follows that

$$\hat{\phi}' = \left(A \exp^{imH_0 ln[(\sigma p_0 + p_T)/p_0]} + B \exp^{-imH_0 ln[(\sigma p_0 + p_T)/p_0]}\right) \left(\frac{p_0}{\sigma p_0 + p_T}\right)^{1/2}. \tag{3.143}$$

From (3.143) it follows that

$$\hat{\phi}'(\sigma = 1) = \left(A \exp^{imH_0 ln[(p_0 + p_T)/p_0]} + B \exp^{-imH_0 ln[(p_0 + p_T)/p_0]}\right) \left(\frac{p_0}{p_0 + p_T}\right)^{1/2}. \tag{3.144}$$

3.5.6.3 Applying the linearized continuity equation

From substituting (3.143) in (3.117) and integrating it may be shown that

$$\hat{\pi} = \frac{1}{c^2 \left(1 + 4m^2 H_0^2\right)} \times$$

$$\left\{A\left(2-4mH_0i\right)\left[\left(\frac{p_0+p_T}{p_0}\right)^{1/2}\exp^{imH_0\ln[(p_0+p_T)/p_0]}-\left(\frac{p_T}{p_0}\right)^{1/2}\exp^{imH_0\ln(p_T/p_0)}\right]+\right.$$

$$\left.B\left(2+4mH_0i\right)\left[\left(\frac{p_0+p_T}{p_0}\right)^{1/2}\exp^{-imH_0\ln[(p_0+p_T)/p_0]}-\left(\frac{p_T}{p_0}\right)^{1/2}\exp^{-imH_0\ln(p_T/p_0)}\right]\right\}. \tag{3.145}$$

The details of the derivation may be found in Appendix E. Similar to the approach used to analyse the sound waves in the linearized equations, equations (3.144) and (3.145) may be substituted into equation (3.123), in order to find the required second relationship between c and m. In order to eliminate constants A and B from the resulting equation, it is necessary to find the relationship between the constants. This relationship is derived in the next subsection.

3.5.6.4 Utilizing the upper boundary condition on $d\hat{\phi}'/d\sigma$

From differentiating (3.143) with respect to σ it follows that

$$\frac{d\hat{\phi}'}{d\sigma}=\left(\frac{p_0}{\sigma p_0+p_T}\right)\left[A\left(-\frac{1}{2}+imH_0\right)\exp^{imH_0\ln[(\sigma p_0+p_T)/p_0]}\right.$$
$$\left.+B\left(-\frac{1}{2}-imH_0\right)\exp^{-imH_0\ln[(\sigma p_0+p_T)/p_0]}\right] \tag{3.146}$$

Recalling that for the case $p_T>0$, $d\hat{\phi}'/d\sigma=0$ at $\sigma=0$ (see section 3.5.5.4), an equation relating A and B may be obtained by the use of (3.146):

$$A\left(-\frac{1}{2}+imH_0\right)\exp^{imH_0\ln(p_T/p_0)}+B\left(-\frac{1}{2}-imH_0\right)\exp^{-imH_0\ln(p_T/p_0)}=0 \tag{3.147}$$

which may be written as

$$B=A\frac{(-2+4imH_0)}{(2+4imH_0)}\exp^{i2mH_0\ln(p_T/p_0)}. \tag{3.148}$$

3.5.6.5 A second relationship between m and c

From substituting (3.144) and (3.145) into (3.123) and applying (3.148) it is obtained that:

$$\left[\exp^{imH_0\ln[(p_0+p_T)/p_0]}+\left(\frac{-2+4imH_0}{2+4imH_0}\right)\exp^{imH_0\{2\ln(p_T/p_0)-\ln[(p_0+p_T)/p_0]\}}\right]\left(\frac{p_0}{p_0+p_T}\right)^2=$$

$$\frac{gH_0}{c^2\left(1+4m^2H_0^2\right)}\times$$

$$\left\{(2-4mH_0i)\left[\left(\frac{p_0+p_T}{p_0}\right)^{1/2}\exp^{imH_0\ln[(p_0+p_T)/p_0]}-\left(\frac{p_T}{p_0}\right)^{1/2}\exp^{imH_0\ln(p_T/p_0)}\right]+\right.$$

$$\left(\frac{-2+4imH_0}{2+4imH_0}\right)(2+4imH_0)\times$$

$$\left.\left[\left(\frac{p_0+p_T}{p_0}\right)^{1/2}\exp^{imH_0\{2\ln(p_T/p_0)-\ln[(p_0+p_T)/p_0]\}}-\left(\frac{p_T}{p_0}\right)^{1/2}\exp^{imH_0\ln(p_T/p_0)}\right]\right\} \tag{3.149}$$

which reduces to

$$(2+4imH_0)\exp^{imH_0\ln[(p_0+p_T)/p_0]}+(-2+4imH_0)\exp^{imH_0\{2\ln(p_T/p_0)-\ln[(p_0+p_T)/p_0]\}}$$

$$=\frac{4gH_0}{c^2}\left(\exp^{imH_0\ln[(p_0+p_T)/p_0]}-\exp^{imH_0\{2\ln(p_T/p_0)-\ln[(p_0+p_T)/p_0]\}}\right). \tag{3.150}$$

It is not clear how (3.150) and (3.140) may be combined to find an expression which explicitly describes the phase speed c of the gravity waves as a function of the reference state parameters and physical constants. However, equation (3.150) implies the approximated relationship

$$c^2\left|2+4imH_0\right|\leq 4gH_0, \tag{3.151}$$

which may be written as

$$c^2\leq\frac{gH_0}{1+4m^2H_0^2}. \tag{3.152}$$

In the limit, where m approaches zero (the long vertical wave length limit), it holds that

$$c\leq\sqrt{gH_0}. \tag{3.153}$$

Equation (3.153) indicates an upper limit of the phase speed of the gravity waves in the quasi-elastic equations. Note that (3.153) is reminiscent of the phase speed $c = \sqrt{gH}$ of gravity waves in the shallow-water equations, with H the mean depth of the fluid (see Chapter 4). Equations (3.140) and (3.150) may possibly be solved numerically in order to describe the relationship between the gravity wave phase speed c and the reference state parameters more exactly (similar to the result obtained for the Lamb wave phase speed in section 3.5.5). Most importantly though, is that the form of the gravity wave solutions (3.140) correspond to that of the fully elastic equations (e.g. Eckart, 1960; Miller, 1974). This illustrates that buoyancy modes are left undistorted by the approximations introduced to obtain the MP equations and the equations of White (1989).

3.6 Discussion

The main objective of the present chapter was to derive the σ coordinate equivalent of the extended pressure coordinate equations of White (1989). This was achieved by a direct transformation of the pressure coordinate equations to σ coordinates (section 3.4). The numerical solution of the σ coordinate equations, as in the case of the pressure coordinate equations of White (1989) and the MP model, makes use of an elliptic equation in the geopotential. The σ coordinate version of this equation may be derived by means of a coordinate transformation of the associated pressure coordinate equation (section 3.4) or directly from the σ coordinate equations (Appendix A). Equations (3.64) to (3.68) and elliptic equation (3.81) represent the first formulation of White's pressure coordinate equations in σ coordinates. The equations derived make possible the construction of a numerical model based on the σ coordinate equivalent of White's pressure coordinate equations. This numerical model is realized in Chapter 4.

When the derived σ coordinate equations are linearized around an isothermal reference state of no motion, the resulting equations correspond exactly to the linearized MP equations in σ coordinates. The equations of White therefore offers the same advantages as the MP equations with respect to the properties of fast-travelling waves that form part of the solution set of the equations. Equation (3.140) obtained for the phase speed of gravity waves in the σ coordinate equations, is the same as that obtained for the fully-elastic equations. It illustrates that the buoyancy modes in the equations remain undistorted by the simplifications introduced to the unapproximated equations. The linear analysis of the sound waves present in the system, indicates that vertically travelling sound waves are filtered from the equations. The phase speed of Lamb waves that are present in the σ coordinate equations are significantly retarded at short wavelengths (Fig. 3.1), although this advantage is reduced when the model top is chosen to be below $0\,hPa$ (Fig. 3.1). The filtering of the sound waves propagating in the vertical, in combination with the retardation of the Lamb waves, yields the equation set to be "quasi-elastic".

The advantage offered by the extended σ coordinate equations, compared to the MP equations in σ coordinates, is that they are formulated independent of the use of a reference profile. Even the elliptic equation (3.81) is non-linear and may be numerically solved without applying linearization of any kind (see Chapter 4). The extended σ coordinate equations are therefore likely to remain applicable to situations where the basic state is not horizontally homogeneous. The corresponding MP model is likely to be a less accurate description of the flow in such a situation, because of its formulation in terms of a reference profile that depends on pressure only.

Chapter 4

The split semi-Lagrangian solution procedure

4.1 Introduction

In Chapter 3 the pressure coordinate equation set of White (1989) is transformed to σ coordinates, and the properties of the equation set are discussed. The equation set (3.64) to (3.68) (or (3.82) to (3.85) in two spatial dimensions) will from now on be refered to as the "quasi-elastic σ coordinate equations", or just as the "quasi-elastic equations". In this Chapter, an adiabatic kernel for a new mesoscale numerical model based on these equations is described. The main and novel feature of the new dynamic kernel, is that it uses a split semi-Lagrangian procedure to solve the quasi-elastic equations on a nonstaggered grid. The numerical formulation is able to deal with nonzero topography. In fact, the dynamic kernel is developed with the aim to closely parallel the formalism of existing operational hydrostatic σ coordinate models. In this way, the convenient conversion of existing hydrostatic σ coordinate models to non-hydrostatic models based on the quasi-elastic equations is facilitated.

Numerical solutions of the σ coordinate MP and NHAD models all utilised explicit leapfrog solution procedures (e.g. Xue and Thorpe, 1991; Miranda and James, 1992; Room et al., 2001). In these numerical solutions, the maximum size of time step allowed is limited by the well-known CFL condition. The absence of sound waves propagating in the vertical greatly alleviates the restriction on the time step in the MP model, especially when high vertical resolution is required (Xue and Thorpe, 1991). However, in the σ coordinate applications of the MP model, the presence of Lamb waves still places a significant restriction on the maximum size of time-step allowed (Room et al., 2001). In the NHAD model the additional filtering of Lamb waves results in additional alleviation of the restriction placed on the maximum size of time step by the CFL condition (Room et al., 2001). However, the maximum size of time step used remains

restricted to some extent by the by the presence of fast travelling gravity waves. Also, the σ coordinate employed in the NHAD model in order to achieve the filtering of Lamb waves (see Chapter 2; Room et al., 2001), is likely to restrict the application of the model to relatively small domains and short spatial scales (see Chapter 2).

The solution procedure presented in this Chapter employs a split semi-Lagrangian approach to solve the quasi-elastic σ coordinate equations. That is, for numerical solution the equations are split into an advective and non-advective part. The slow advection process is treated during a semi-Lagrangian advection step that may employ a large time step. Indeed, it is shown that the split semi-Lagrangian scheme can be used to obtain stable integrations at large Courant numbers present during the advection step. Hereafter the remaining terms, which describe fast moving waves, are treated explicitly during an adjustment phase that employs a smaller time step. It may be noted that the numerical modelling of cloud microphysics and condensation can potentially be incorporated in another adjustment phase, that may also require a small time step for the adequate modelling of cloud thermodynamics and precipitation formation. The numerical procedure presented does not require linearization of any kind. It may be noted that although a number of split semi-Lagrangian models solving the hydrostatic equations have been developed (Bates and McDonald, 1982; Bates, 1984; McGregor, 1986; Leslie and Purser, 1991), there have been only a few applications of split semi-Lagrangian procedures in the context of nonhydrostatic equation sets.

An important feature of the new numerical scheme is that it is formulated on a nonstaggered grid, also referred to as an A-grid (e.g. Mesinger and Arakawa, 1976; Arakawa and Lamb, 1977). A nonstaggered grid is appealing to use in semi-Lagrange discretizations, since one set of trajectories can be used to provide common departure points for all variables (McGregor, 2005). On a staggered grid, at least one more set of trajectories is needed to calculate the departure points of variables at staggered positions. Also, the wind components need to be obtained by averaging procedures at the staggered grid points where they are not calculated explicitly, in order to facilitate the calculation of departure points associated with these staggered grid points. This may possibly impact negatively on numerical consistency and accuracy. Once the different sets of trajectories have been calculated on the staggered grid, different sets of grid point interpolations are needed to calculate the values of variables at the different sets of departure points. Only a single set of interpolations is required on the nonstaggered grid for the single set of departure points (Leslie and Purser, 1991). Thus, from the viewpoint of numerical accuracy and computational economy, there exist strong motivation for the use of nonstaggered grids in semi-Lagrange discretizations of the atmospheric equations. However, there are only a few atmospheric models that employ a nonstaggered grid (e.g. Kaplan et al., 1982; Kalnay-Rivas and Hoitsma, 1979; Purser and Leslie, 1988; Leslie and Purser,

1991). The main reason for the unpopularity of the A-grid, is that the spatial discretization of the shallow water equations reveals that the nonstaggered grid has poor dispersion properties compared to the usual staggered grids (e.g. Winninghoff 1968; Mesinger and Arakawa, 1976; Arakawa and Lamb, 1977; Schoenstadt, 1978).

Conversely, the staggered C-grid has become very popular for use in atmospheric models, because it has good dispersion behaviour for large Rossby radius of deformation (defined relative to the grid spacing) (McGregor, 2005). However, as discussed in the previous paragraph, the C-grid and other staggered grids are somewhat problematic to use for semi-Lagrangian solution procedures. Recently, a reversible staggering arrangement of variables has been proposed to obtain improved gravity wave dispersion characteristics while still using a formulation of the primitive equations on the A-grid (McGregor, 1995). The basic idea is to perform a transformation from the A-grid to a C-grid for the calculation of the gravity wave terms, using a new reversible interpolation scheme based on the generalized Vandermonde method. The so called R-grid scheme ensures consistent transformation of variables between staggered and nonstaggered positions, and has excellent dispersion characteristics for the geostrophic adjustment of the shallow-water equations (McGregor, 2005). The reversible staggering approach is most accurately performed in a cyclic domain (McGregor, 2005). For the limited-area, meso-scale applications of the model developed in this study, the reversible staggering approach is certainly an option in order to improve on the poor gravity wave dispersion properties of the nonstaggered grid. However, the method will need modification for the non-cyclic boundary conditions commonly encountered in in limited-area modelling. Instead, an alternative approach has been selected in this study, and that is to improve the gravity wave dispersion properties of the A-grid by means of high-order spatial differencing and filtering. It should also be noted that the focus in this study is on the development of a new meso-scale model. Although the accurate treatment of gravity waves is of fundamental importance for such a model, the geostrophic adjustment process does not play an important role at the spatial and time scales that the model will be applied to (see Chapter 5).

Thus, the distinguishing feature of the new numerical scheme developed is the split semi-Lagrangian approach that is used on a nonstaggered grid. This approach ensures numerical accuracy and computational economy during the calculation of departure points, and the corresponding interpolations. High-order spatial filtering is used to filter the smallest resolvable gravity waves on the nonstaggered grid, whilst the waves that are resolved may be treated accurately by employing high order spatial differencing. The three main building blocks used to construct the split semi-Lagrangian scheme are discussed in the next three sections. Firstly the semi-Lagrangian scheme applied in the model to numerically represent the advection process, is discussed in section 4.2. In particular, the method developed by McGregor (1993) to evaluate the departure

points of fluid parcels is presented. The phase and amplitude accuracy properties resulting from the bicubic interpolation scheme that is used to evaluate the values of variables at departure points (McDonald, 1984) are also analysed. Secondly, high-order spatial differencing formulas for use on the nonstaggered grid are presented in section 4.3, following Purser and Leslie (1988). Thirdly, the high-order spatial filtering used to filter the shortest resolvable gravity waves from the nonstaggered grid (Shapiro, 1975), are discussed in section 4.4. The split semi-Lagrangian solution procedure is outlined in section 4.5. The procedure involves the solution of an elliptic equation for the geopotential at each adjustment time-step; the iterative technique used is discussed in section 4.6. In section 4.7 the frequency response of the forward-backward scheme used in the adjustment step is analysed. The gravity wave response to discretization on the nonstaggered grid is evaluated in section 4.8. The effect of high-order spatial differencing on improving the frequency (or phase speed) accuracy of the discretized waves is discussed in particular. Lateral and vertical boundary conditions for the model are formulated in section 4.9. In section 4.10, the properties of the newly developed scheme are compared to those of the numerical schemes used in the MP and NHAD models. A discussion of the results obtained and some conclusions can be found in section 4.11.

4.2 The semi-Lagrangian advection scheme

During the last 20 years, semi-Lagrangian schemes for treating horizontal and (or) vertical advection in NWP and climate simulation models have become increasingly popular (e.g. Robert, 1981, 1982; Bates and McDonald, 1982; McDonald, 1986; McGregor, 1987; Ritchie, 1987; Tanguay et al., 1989; McGregor, 1993; Bates et al., 1995; Davies et al., 2005). This popularity stems from the large advection time-steps permitted by semi-Lagrangian advection schemes compared to Eulerian schemes, without compromising numerical stability. The semi-Lagrangian approach for solving the advection terms consists of two steps: The calculation of the departure point of each grid point in the model, and secondly, the evaluation of variables at the departure point by means of spatial interpolation. In this study, an efficient procedure developed by McGregor (1993) is applied to calculate the departure points, whilst bicubic spatial interpolation (McDonald, 1984) is used to evaluate the values of variables at the departure points. These two procedures are discussed in the following two sections.

4.2.1 McGregor's method for the calulation of the departure points

An Eulerian procedure that avoids both interpolation and iteration for determining the departure points of trajectories was proposed by McGregor (1993). The technique can achieve a high degree of accuracy, is somewhat simpler and more economical than other schemes, and can be applied to semi-Lagrangian models on the plane or on the sphere. The procedure has been applied sucess-

fully to the simulation of horizontal advection in the hydrostatic semi-implicit semi-Lagrangian regional models DARLAM and the variable resolution global model C-CAM (McGregor, 1993, 1996; McGregor and Dix, 2001; McGregor et al., 2002). In this section, the method of McGregor (1993) is formulated for application in the split semi-Lagrangian procedure used to solve the nonhydrostatic quasi-elastic equations (see section 4.5). The procedure is used to treat both horizontal and vertical advection in the new model.

Following the discussion by McGregor (1993), let $\mathbf{r}(t)$ denote a member of a set of vectors moving with the fluid. With each grid point, a different vector $\mathbf{r}(t)$ will be associated at time t. Thus, the grid points are the prescribed arrival locations of the vectors move with the fluid. To advance the model integration from time τ to $\tau + \Delta t$, a vector $\mathbf{r}(\tau + \Delta t)$ is set up at the position of each arrival grid point. It is required to find the starting position of the vector at the preceding time step, namely $\mathbf{r}(\tau)$. This may be expressed in terms of the Taylor series

$$\mathbf{r}(\tau) = \mathbf{r}(\tau + \Delta t) + \Sigma_{n=1}^{\infty} \frac{(-\Delta t)^n}{n!} \frac{d^n \mathbf{r}}{dt^n}(\tau + \Delta t), \tag{4.1}$$

where

$$\frac{d^n \mathbf{r}(t)}{dt^n} = \frac{d}{dt}\left[\frac{d^{n-1}\mathbf{r}(t)}{dt^{n-1}}\right] \quad n = 2, 3, ... \tag{4.2}$$

and the total derivative has the usual definition of a time derivative following the motion of a parcel,

$$\frac{d}{dt} = \frac{\partial}{\partial t} + \mathbf{u} \cdot \bar{\nabla}. \tag{4.3}$$

Here $\mathbf{u} = d\mathbf{r}/dt$ is the velocity of the fluid at position $\mathbf{r}(t)$ and $\bar{\nabla}$ is the spatial gradient operator. In (4.3) the time derivative on the left-hand side is naturally viewed in a Lagrangian sense. The right-hand side allows its instantaneous evaluation at the same point in time and space via Eulerian derivatives (McGregor, 1993). However, if the Eulerian velocities change with time, it may be very cumbersome to evaluate the partial time derivatives for the higher order terms in (4.1) (McGregor, 1993). The scheme proposed by McGregor (1993) replaces the total time derivative (4.3) for use in (4.1) and (4.2) by the approximate formula

$$\frac{d}{dt} \approx \hat{\mathbf{u}} \cdot \bar{\nabla}. \tag{4.4}$$

Here $\hat{\mathbf{u}}$ represents the (Eulerian) velocity at the point in space corresponding to $\mathbf{r}(\tau + \Delta t)$, but evaluated at the intermediate time $\tau + \Delta t/2$. The above scheme using (4.1), (4.2) and (4.4), and retaining terms up to the Nth total time derivative is called a D_N scheme (McGregor, 1993). The velocity $\hat{\mathbf{u}}$ may be conveniently determinded by means of extrapolation in time from the known

velocities at previous time steps; a formula with third-order accuracy in time is given by Temperton and Staniforth (1987):

$$\mathbf{u} = \frac{1}{8}\left[15\mathbf{u}\left(\tau\right) - 10\mathbf{u}\left(\tau - \Delta t\right) + 3\mathbf{u}\left(\tau - 2\Delta t\right)\right] + O\left(\Delta t^3\right). \tag{4.5}$$

The idea behind the approximation (4.4) is that for advection purposes the velocities are considered to remain constant in an Eulerian sense over the time interval $(\tau, \tau + \Delta t)$ at their centered in time value (McGregor, 1993). A slight disavantage of the application of formula (4.5), is the need to store values of the wind field at three time-levels, although the scheme is formulated here for two time-level applications. The number of terms that should be retained in practice in the Taylor series (4.1) depends on the smoothness of the velocity field (McGregor, 1993). McGregor (1993) found only slight benefit in going beyond the D_3 scheme. The D_3 scheme has been implemented and used successfully in the hydrostatic regional model DARLAM (McGregor, 1993) and is also used in the more recently developed hydrostatic variable resolution global model C-CAM (McGregor, 1996; McGregor and Dix, 2001; McGregor et al., 2002). In Chapter 5, the D_N schemes for choices of N up to 3 are tested for cases of highly nonhydrostatic flow, and a recommendation of the most appropriate choice of N is made.

The calculation formulas for the three-dimensional departure points as determined by the D_1, D_2 and D_3 schemes are respectively:

$\mathbf{D_1}$ scheme:

$$\begin{bmatrix} x^* \\ y^* \\ \sigma^* \end{bmatrix} = \begin{bmatrix} x \\ y \\ \sigma \end{bmatrix} - \Delta t \begin{bmatrix} \hat{u} \\ \hat{v} \\ \hat{\dot{\sigma}} \end{bmatrix} \tag{4.6}$$

$\mathbf{D_2}$ scheme:

$$\begin{bmatrix} x^* \\ y^* \\ \sigma^* \end{bmatrix} = \begin{bmatrix} x \\ y \\ \sigma \end{bmatrix} - \Delta t \begin{bmatrix} \hat{u} \\ \hat{v} \\ \hat{\dot{\sigma}} \end{bmatrix} + \frac{\Delta t^2}{2!} \begin{bmatrix} \hat{u}\frac{\partial \hat{u}}{\partial x} + \hat{v}\frac{\partial \hat{u}}{\partial y} + \hat{\dot{\sigma}}\frac{\partial \hat{u}}{\partial \sigma} \\ \hat{u}\frac{\partial \hat{v}}{\partial x} + \hat{v}\frac{\partial \hat{v}}{\partial y} + \hat{\dot{\sigma}}\frac{\partial \hat{v}}{\partial \sigma} \\ \hat{u}\frac{\partial \hat{\dot{\sigma}}}{\partial x} + \hat{v}\frac{\partial \hat{\dot{\sigma}}}{\partial y} + \hat{\dot{\sigma}}\frac{\partial \hat{\dot{\sigma}}}{\partial \sigma} \end{bmatrix}$$

or, by introducing notation for the estimated acceleration along the trajectory,

$$\begin{bmatrix} x^* \\ y^* \\ \sigma^* \end{bmatrix} = \begin{bmatrix} x \\ y \\ \sigma \end{bmatrix} - \Delta t \begin{bmatrix} \hat{u} \\ \hat{v} \\ \hat{\dot{\sigma}} \end{bmatrix} + \frac{\Delta t^2}{2!} \begin{bmatrix} \hat{a}_{\hat{u}} \\ \hat{a}_{\hat{v}} \\ \hat{a}_{\hat{\dot{\sigma}}} \end{bmatrix} \tag{4.7}$$

D_3 scheme:

$$\begin{bmatrix} x^* \\ y^* \\ \sigma^* \end{bmatrix} = \begin{bmatrix} x \\ y \\ \sigma \end{bmatrix} - \Delta t \begin{bmatrix} \hat{u} \\ \hat{v} \\ \hat{\dot{\sigma}} \end{bmatrix} + \frac{\Delta t^2}{2!} \begin{bmatrix} \hat{a}_{\hat{u}} \\ \hat{a}_{\hat{v}} \\ \hat{a}_{\hat{\dot{\sigma}}} \end{bmatrix} - \frac{\Delta t^3}{3!} \begin{bmatrix} \hat{u}\frac{\partial \hat{a}_{\hat{u}}}{\partial x} + \hat{v}\frac{\partial \hat{a}_{\hat{u}}}{\partial y} + \hat{\dot{\sigma}}\frac{\partial \hat{a}_{\hat{u}}}{\partial \sigma} \\ \hat{u}\frac{\partial \hat{a}_{\hat{v}}}{\partial x} + \hat{v}\frac{\partial \hat{a}_{\hat{v}}}{\partial y} + \hat{\dot{\sigma}}\frac{\partial \hat{a}_{\hat{v}}}{\partial \sigma} \\ \hat{u}\frac{\partial \hat{a}_{\hat{\dot{\sigma}}}}{\partial x} + \hat{v}\frac{\partial \hat{a}_{\hat{\dot{\sigma}}}}{\partial y} + \hat{\dot{\sigma}}\frac{\partial \hat{a}_{\hat{\dot{\sigma}}}}{\partial \sigma} \end{bmatrix} \tag{4.8}$$

Here $\mathbf{u} = (u, v, \sigma)$ is determined from (4.5). For evaluating the derivatives in (4.7) and (4.8), second order accurate centered finite differencing on the nonstaggered grid (see section 4.3) is used. The modification of calculation formulas (4.6) to (4.8) for two-dimensional applications is obvious.

4.2.2 Bicubic Lagrange spatial interpolation

Once the departure point has been calculated by the use of a particular D_N scheme for each arrival grid point, the values of variables at the departure points need to be evaluated by means of spatial interpolation from the surrounding grid points. In the present study, bicubic Lagrangian interpolation (e.g. McDonald, 1984) is used for this purpose. Perhaps the most important alternative to bicubic Lagrangian interpolation is cubic spline interpolation. However, semi-Lagrange schemes using cubic spline interpolation is known to be less diffusive at the smallest resolvable scales than schemes using bicubic Lagrangian interpolation (Purnell 1976; Pudykiewicz and Staniforth, 1984; Riishogaard et al., 1998; also see the following discussion for bicubic interpolation). This may lead to the generation of spurious small-scale features. Although the problem may be alleviated by the use of high-order explicit diffusion (Pudykiewicz and Staniforth, 1984; Riishogaard et al., 1998), bicubic Lagrangian interpolation appears to be a safer choice for the interpolation scheme in this study.

In what follows, bicubic Lagrange spatial interpolation is discussed in two spatial dimensions. The main purpose of the discussion is to illuminate the amplitude and phase characteristics of bicubic spatial interpolations. The discussion below can easily be modified to cubic or tricubic interpolation for respective application in one or three spatial dimensions.

The equation describing the two-dimensional advection of a scalar ψ is

$$\frac{D\psi}{Dt} = \frac{\partial \psi}{\partial t} + u\frac{\partial \psi}{\partial x} + v\frac{\partial \psi}{\partial y} = 0, \tag{4.9}$$

where u and v are the horizontal wind components. In a two-dimensional Cartesian coordinate system, let $x = I\Delta x$, $y = J\Delta y$ and $t = n\Delta t$. The semi-Lagrangian discretization of equation (4.9) for the evaluation of ψ at grid point (x, y) is:

$$\psi\left[I\Delta x,\, J\Delta y,\, (n+1)\,\Delta t\right] = \psi\left(x^*,\, y^*,\, n\Delta t\right), \tag{4.10}$$

where (x^*, y^*) is the departure point associated with grid point (x, y). The departure point is calculated with one of the D_N schemes in the present study. In the case of bicubic Lagrange interpolation, the function $\psi(x^*, y^*, t)$ is approximated by a cubic Lagrange interpolating polynomial (Carnahan et al. 1969) using values of ψ at the points nearest to x^* and y^*:

$$\psi(x^*, y^*, t) = \Sigma_\mu \Sigma_\nu W_{\mu\nu} \psi^n_{\mu\nu}. \tag{4.11}$$

Here the notation $\psi^n_{i,j} = \psi(i\Delta x, j\Delta y, n\Delta t)$ was introduced and

$$W_{rs} = \prod_{\mu \neq r} \frac{(x^* - x_\mu)}{(x_r - x_\mu)} \prod_{\nu \neq s} \frac{(y^* - y_\nu)}{(y_s - y_\nu)}. \tag{4.12}$$

The subscripts μ and ν range over the points

$$\mu : i-2, i-1, i, i+1 \qquad \nu : j-2, j-1, j, j+1 \tag{4.13}$$

for the bicubic interpolation scheme. McDonald (1984) showed that if the points (i, j) are chosen such that

$$(i-1)\Delta x < x^* \leq i\Delta x \qquad (j-1)\Delta x < \sigma^* \leq j\Delta\sigma \tag{4.14}$$

the semi-Lagrangian method with bicubic spatial interpolation is unconditionally stable for advection at constant velocity.

Amplitude accuracy

From (4.9), the two-dimensional linear advection equation of a scalar ψ is

$$\frac{D\psi}{Dt} = \frac{\partial\psi}{\partial t} + U\frac{\partial\psi}{\partial x} + V\frac{\partial\psi}{\partial y} = 0, \tag{4.15}$$

where the horizontal wind components U and V are constant in space and time. For the constant velocity field, $D\mathbf{r}^n/Dt = 0$ for $n \geq 2$. From equation (4.1) it follows that all the D_N schemes reduce to the D_1 scheme for a constant velocity field. Applying the D_1 scheme to the case of a constant velocity field, implies that the departure point for each arrival grid point is simply calculated from the formulae:

$$\begin{bmatrix} x^* \\ y^* \end{bmatrix} = \begin{bmatrix} x \\ y \end{bmatrix} - \Delta t \begin{bmatrix} U \\ V \end{bmatrix}. \tag{4.16}$$

The phase and amplitude properties of the semi-Lagrangian method that result when bilinear, biquadratic, bicubic and biquartic interpolation schemes are applied to calculate the value of variables at the departure point calculated by (4.16), have been analysed by McDonald (1984). In order to aid the interpretation of numerical results in Chapter 5, the results of McDonald (1984) are reviewed in this and the following section for the bicubic interpolation scheme. The amplitude accuracy of the semi-Lagrangian method may be analysed by using the von Neumann method (e.g. Richtmeyer and Morton, 1967; Mesinger and Arakawa, 1976). To this end, define α, β, $\hat{\alpha}$ and $\hat{\beta}$ as:

$$\alpha = u\frac{\Delta t}{\Delta x} \qquad \beta = v\frac{\Delta t}{\Delta y} \tag{4.17}$$

$$\hat{\alpha} = \alpha + i - I \qquad \hat{\beta} = \beta + j - J. \tag{4.18}$$

α and β may be termed the x and y direction Courant numbers respectively. The selection of interpolation points i and j according to (4.14) guarantees that

$$0 \leq \hat{\alpha} < 1, \qquad 0 \leq \hat{\beta} < 1. \tag{4.19}$$

These are sufficient conditions to ensure absolute stability of the semi-Lagrangian scheme when applied to the linear advection equation (McDonald, 1984). This may be shown by substituting wave-like solutions of the form

$$\psi^n_{I,\,J} = \psi_0 \lambda^n \exp^{i_c(kI\Delta x + lJ\Delta y)} \tag{4.20}$$

into equation (4.10). Here $i_c^2 = -1$; $k = 2\pi/L_x$and $l = 2\pi/L_y$ with L_x and L_y the wave lengths in the x and y directions respectively. λ is the amplification factor. Using (4.14) to evaluate $\psi\left(x^*,\, y^*,\, n\Delta t\right)$, shows that λ splits into an "x amplification factor" and "y amplification factor" as follows (McDonald, 1984):

$$\lambda = \hat{\Lambda}\left(\hat{\alpha},\, k\right)\hat{\Lambda}\left(\hat{\beta},\, l\right). \tag{4.21}$$

Here

$$\left|\hat{\Lambda}\left(\hat{\alpha},\, k\right)\right|^2 = 1 - \hat{\alpha}\left(2 - \hat{\alpha}\right)\left(1 - \hat{\alpha}^2\right)c^2\left[3 + 2c\hat{\alpha}\left(1 - \hat{\alpha}\right)\right]\frac{1}{9}, \tag{4.22}$$

where $c = 1 - \cos k\Delta x$. The formula for $\left|\hat{\Lambda}\left(\hat{\beta},\, l\right)\right|^2$ is given by (4.22) with $\hat{\alpha}$ replaced by $\hat{\beta}$ and k replaced by l. The lines of constant $\left|\Lambda\left(\hat{\alpha},\, k\right)\right|$ are displayed in Fig.4.1 for $0 \leq k\Delta x/\pi \leq 1$ and $0 \leq \alpha \leq 1$. (Note that the shortest waves that may be reolved on the nonstaggered grid with constant grid interval Δx have wave length $2\Delta x$. Thus, $2\Delta x \leq L_x <\leq \infty$, which implies that $0 < k\Delta x \leq \pi$.)

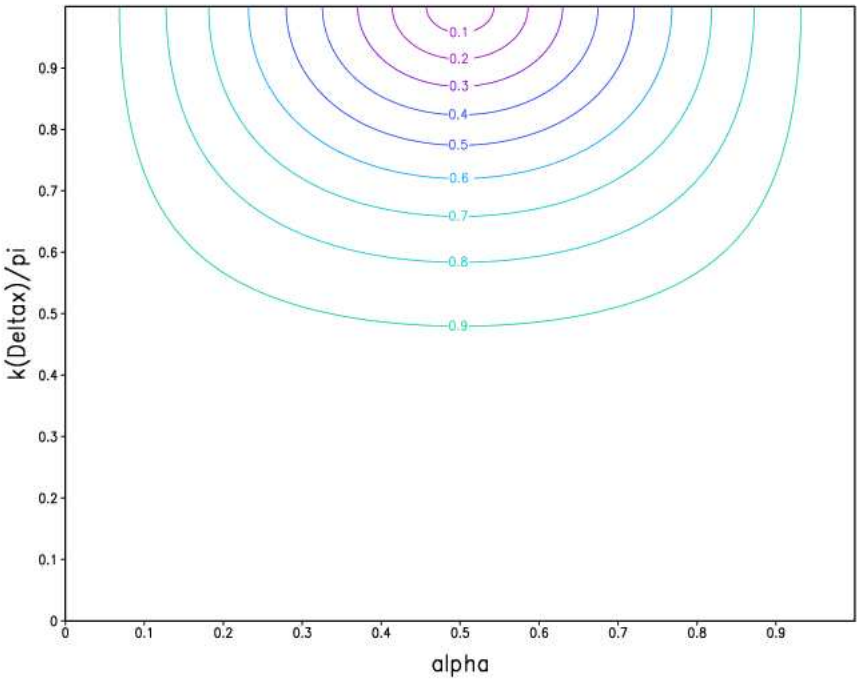

Figure 4.1: Isolines of the amplification factor for bicubic spatial interpolation, as a function of α and $k\Delta x/\pi$ (following McDonald, 1984).

From Fig. 4.1 it can be seen that the bicubic interpolation scheme results in the most severe damping of the scalar ψ when $\alpha = 0.5$. The scheme is undamped for $\alpha = 0$ or 1. The damping is the heaviest for the shortest resolvable wave lengths, and it decreases as the wave length increases (McDonald, 1984). At the shortest resolvable scales, numerical solution of the nonlinear advection equation may result in aliasing errors (where waves of length smaller than two grid intervals are spuriously represented as waves longer than two grid lengths (see Mesinger and Arakawa, 1976). The severe damping of the shortest resolvable wave lengths may be regarded as an advantage of the bicubic Lagrange interpolation scheme, as it funtions to control the numerical "noise" that may be originating at these scales.

Phase accuracy

Another important measure of accuracy of a numerical advection scheme, is how the phase speed of the numerical solution of the advection equation compares to that of the true solution. The phase speed analysis is usually performed in one spatial dimension, since a two-dimensional analysis is cumbersome to perform and the result can not be easily quantitatively interpreted or graphically displayed. Note that for the linear one-dimensional advection equation, the phase speed of the true solution is $\Upsilon = -ku\Delta t$ (Mesinger and Arakawa, 1976), whilst the phase speed of the numerical solution is given by $\tan^{-1}(\lambda_{im}/\lambda_{re})$. Here λ_{im} and λ_{re} are respectively the real and imaginary parts of the amplification factor λ (see Mesinger and Arakawa, 1976). The relative phase speed is therefore defined as

$$R_A = \frac{1}{\Upsilon} \tan^{-1} \frac{\lambda_{im}}{\lambda_{ir}}.$$

The relative phase speed R_A normalised to u of the bicubic Lagrange interpolation scheme, when applied to one dimensional linear advection, is (McDonald, 1984):

$$R_{AL}(\alpha,\, k) = \frac{p}{\alpha} + \frac{\hat{\alpha} \sin k\Delta x \left[1 + a\left(1 - \hat{\alpha^2}\right)/3\right]}{\left(1 - a\hat{\alpha^2} - a^2\alpha\left(1 - \hat{\alpha^2}\right)/3\right)}.$$

The relative phase speed R_A is displayed in Fig. 4.2 as a function of α and k.

It may be seen from Fig. 4.2 that the phase errors decrease as the wave length increases, for all α. Close to $\alpha = 0$ the phase errors is the largest, whereas the error is zero at $\alpha = 1$. Thus, the bicubic interpolation scheme gives a faithful representation of both amplitude and phase of the true solution at large Courant numbers (close to 1). In fact, similar amplitude and phase properties are valid in the region around $\alpha = 2$ (see McDonald, 1984). This implies that a semi-Lagrangian model may be applied at large Courant numbers (large time steps),

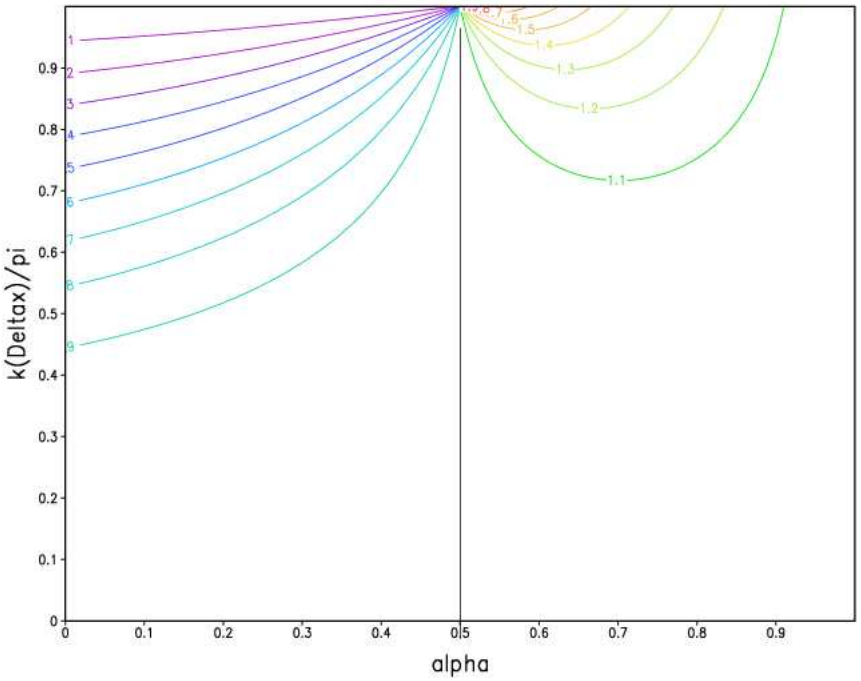

Figure 4.2: Normalised phase speed isolines for bicubic spatial interpolation, as a function of α and $k\Delta x/\pi$ (following McDonald, 1984).

which is advantageous from a computational perspective, without compromising the accuracy of the scheme with respect to amplitude and phase characteristics.

4.3 Finite differencing on the nonstaggered grid

Centered differencing formulae for collinear data were derived by Purser and Leslie (1988), by fitting Lagrange interpolation polynomials appropriate to centered differencing to the relevant number of data points. In this section, these centered differencing formulae of various orders of accuracy are stated for application on the nonstaggered grid. The formulae are then applied to pure gravity wave equations, in order to examine the frequency response of the waves to spatial discretization on the nonstaggered grid. This analysis is of use in section 4.8, where the response of the split semi-Lagrangian scheme to spatial discretization on the nonstaggered grid is examined.

The data are assumed to be positioned at integer multiples of a constant grid space d, that is,

$$a_i = a(id). \tag{4.23}$$

It is convenient to define the binomial envelope function (Purser and Leslie, 1988) $\beta_{M,j}$ as:

$$\beta_{M,j} = \frac{(M!)^2}{(M+j)!\,(M-j)!}. \tag{4.24}$$

4.3.1 Centered differencing for first derivatives

The centered differencing formulae (of even order $2M$) for first derivatives can be expressed as (Purser and Leslie, 1988):

$$\frac{da}{dx}|_{x=id} \approx \frac{1}{d}\Sigma_{j=-M}^{M} D_{M,j} a_{i+j}, \tag{4.25}$$

where

$$D_{M,j} = -D_{M,-j}, \tag{4.26}$$

and

$$D_{M,j} = -\frac{(-1)^j}{j}\beta_{M,j}, \quad j = \pm 1, \ldots \pm M. \tag{4.27}$$

From (4.24) to (4.26) with $M = 1$ the usual centered differencing formula of second order accuracy for first derivatives follows:

$$\frac{da}{dx}|_{x=id} \approx \frac{1}{2d}\left(a_{i+1} - a_{i-1}\right). \tag{4.28}$$

$M = 2$ gives a formula of fourth order accuracy

$$\frac{da}{dx}|_{x=id} = \frac{1}{d}\left(\frac{1}{12}a_{i-2} - \frac{2}{3}a_{i-1} + \frac{2}{3}a_{i+1} - \frac{1}{12}a_{i+2}\right), \tag{4.29}$$

whilst $M = 3$ implies a formula of sixth order accuracy

$$\frac{da}{dx}|_{x=id} = \frac{1}{d}\left(-\frac{1}{60}a_{i-3} + \frac{3}{20}a_{i-2} - \frac{3}{4}a_{i-1} + \frac{3}{4}a_{i+1} - \frac{3}{20}a_{i+2} + \frac{1}{60}a_{i+3}\right). \tag{4.30}$$

4.3.2 Centered differencing for second derivatives

The centered nonstaggered formula for second derivatives from $2M + 1$ points is (Purser and Leslie, 1988):

$$\frac{d^2a}{dx^2}|_{x=id} \approx \frac{1}{d^2}\Sigma_{j=-M}^{j=M} D_{M,j}^{(2)} a_{i+j}, \tag{4.31}$$

where

$$D_{M,j}^{(2)} = D_{M,-j}^{(2)}, \tag{4.32}$$

and

$$D_{M,j}^{(2)} = \frac{-(-1)^j}{j^2} 2\beta_{M,j}, \quad j = \pm 1, \ldots \pm M, \tag{4.33}$$

with

$$D_{M,0}^{(2)} = -\Sigma_{j\neq 0} D_{M,j}^{(2)}. \tag{4.34}$$

From (4.24) and (4.31) to (4.34) with $M = 1$ the usual centered differencing formula of second order accuracy for second derivatives follows:

$$\frac{d^2a}{dx^2} \approx \frac{1}{d^2}\left(a_{i-1} - 2a_i + a_{i+1}\right) \tag{4.35}$$

$M = 2$ gives a formula of fourth order accuracy

$$\frac{d^2a}{dx^2} \approx \frac{1}{d^2}\left(-\frac{1}{12}a_{i-2} + \frac{4}{3}a_{i-1} - \frac{5}{2}a_i + \frac{4}{3}a_{i+1} - \frac{1}{12}a_{i+2}\right), \tag{4.36}$$

whilst $M = 6$ implies a formula of sixth order accuracy

$$\frac{d^2a}{dx^2} \approx \frac{1}{d^2}\left(\frac{1}{90}a_{i-3} - \frac{3}{20}a_{i-2} + \frac{3}{2}a_{i-1} - \frac{49}{18}a_i + \frac{3}{2}a_{i+1} - \frac{3}{20}a_{i+2} + \frac{1}{90}a_{i-3}\right). \tag{4.37}$$

4.3.3 Application to one-dimensional gravity waves

In the equations that govern the simple case of pure gravity waves (see Mesinger and Arakawa, 1976), the dependent variables are functions of one space variable only. The pure gravity wave equations are

$$\frac{\partial u}{\partial t} = -g\frac{\partial h}{\partial x}, \quad \frac{\partial h}{\partial t} = -H\frac{\partial u}{\partial x}; \tag{4.38}$$

with g (gravitational acceleration) and H (the mean depth of the fluid) constants. u is the horizontal wind and h the depth of the fluid. These equations are sometimes referred to as the shallow-water equations (e.g. Holton, 1992), although this terminology has been applied more generally to describe the system of gravity-inertia waves (e.g. McGregor, 2005). Following Mesinger and Arakawa (1976), wave solutions of the form

$$Q\left(x,\, t\right) = \hat{Q}\exp^{i_c(kx-\Omega_T)} \tag{4.39}$$

are substituted in (4.38), which leads to the homogeneous system

$$\Omega_T\hat{u} = gk\hat{h}, \quad \Omega_T\hat{h} = Hk\hat{u}. \tag{4.40}$$

Here $\Omega_T = kc$, where k is the horizontal wave number and c is the phase speed of the gravity waves. Equations (4.40) imply the frequency equation

$$\Omega_T^2 = gHk^2, \tag{4.41}$$

or alternatively,

$$c = \frac{\Omega_T}{k} = \pm\sqrt{gH}. \tag{4.42}$$

Thus, the gravity waves propagate along the x axis in both directions at a constant speed $\sqrt{gH}$, irresepective of the wave length of the waves.

Mesinger and Arakawa (1976) analysed the gravity wave response of (4.38) to second order spatial discretization on the nonstaggered grid. Their discussion is repeated in the the next section, followed by a discussion for higher-order differentiation on the nonstaggered grid in sections 4.3.3.2 and 4.3.3.3.

4.3.3.1 Second order spatial differencing

When the space derivatives in (4.38) are approximated by second order centered differencing, the differential-difference equations

$$\frac{\partial u_i}{\partial t} = -g\frac{h_{i+1}-h_{i-1}}{2\Delta x}, \quad \frac{\partial h_i}{\partial t} = -H\frac{u_{i+1}-u_{i-1}}{2\Delta x} \tag{4.43}$$

are obtained. Here Δx denotes the constant grid space d in (4.23). The solutions (4.39) now assume the form

$$Q_i(t) = \hat{Q} \exp^{i_c(ki\Delta x - \Omega_N t)}, \tag{4.44}$$

where Ω_N denotes the frequency of the gravity waves in the numerical solution. Substitution of (4.44) into (4.43) leads to

$$\Omega_N \hat{u} = g\frac{\sin k\Delta x}{\Delta x}, \quad \Omega_N \hat{h} = H\frac{\sin k\Delta x}{\Delta x}\hat{u}, \tag{4.45}$$

giving the frequency equation

$$\Omega_N^2 = gH\left(\frac{\sin k\Delta x}{\Delta x}\right)^2. \tag{4.46}$$

The relative frequency of gravity waves in the numerical solution (compared to that of the true solution) obtained with second order spatial differencing may be defined as

$$R_2 = \frac{\Omega_T}{\Omega_N} = \frac{\sin k\Delta x}{k\Delta x}. \tag{4.47}$$

Thus, it may be noted that instead of a constant phase speed, the gravity waves now propagate with the phase speed

$$c_2 = \pm\sqrt{gH}\frac{\sin k\Delta x}{k\Delta x}, \tag{4.48}$$

or alternatively,

$$c_2 = cR_2. \tag{4.49}$$

The phase speed of gravity waves c_2 in the numerical solution is not a constant like the true phase speed, but depends on the wave number. Thus, the centered space differencing results in computational dispersion. The relative frequency R_2 is shown in Fig. 4.3 as a function of the normalized wave number $k\Delta x/\pi$ (black line). The $2\Delta x$ wave is stationary. For wave lengths equal to $4\Delta x$, that is, for $k\Delta x/\pi = 1/2$, the relative frequency is about 60%. Thus, there is a significant retardation of the true gravity wave phase speed near the shortest resolvable scales. However, the relative frequency of the waves increases as the wave length increases, and the numerical frequency approach the true frequency in the long wave limit (Fig. 4.3).

4.3.3.2 Fourth order spatial differencing

When the space derivatives in (4.38) are approximated with fourth order centered differences, the differential-difference equations

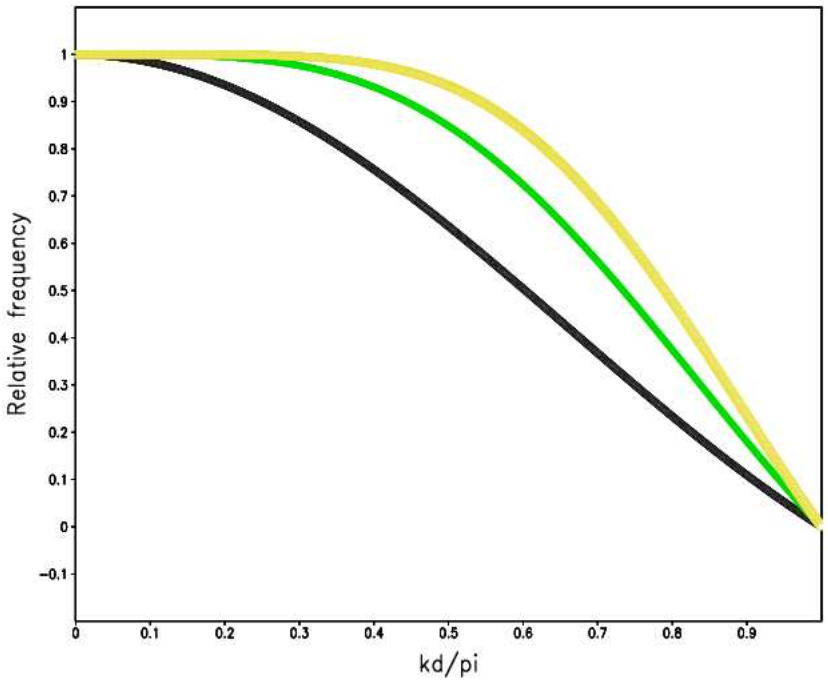

Figure 4.3: The relative frequency of pure gravity waves as a function of wave number, for second order (black line), fourth order (green line) and sixth order (yellow line) spatial differencing on the nonstaggered grid.

$$\frac{\partial u_i}{\partial t} = -\frac{g}{\Delta x}\left(\frac{1}{12}h_{i-2} - \frac{2}{3}h_{i-1} + \frac{2}{3}h_{i+1} - \frac{1}{12}h_{i+2}\right),$$

$$\frac{\partial h_i}{\partial t} = -\frac{H}{\Delta x}\left(\frac{1}{12}u_{i-2} - \frac{2}{3}u_{i-1} + \frac{2}{3}u_{i+1} - \frac{1}{12}u_{i+2}\right). \tag{4.50}$$

are obtained. Substitution of (4.44) into (4.50) leads to

$$\Omega_N \hat{u} = \frac{g}{\Delta x}\left(\frac{4}{3}\sin k\Delta x - \frac{1}{6}\sin 2k\Delta x\right)\hat{h},$$

$$\Omega_N \hat{h} = \frac{H}{\Delta x}\left(\frac{4}{3}\sin k\Delta x - \frac{1}{6}\sin 2k\Delta x\right)\hat{u}, \tag{4.51}$$

giving the frequency equation

$$\Omega_N^2 = \frac{gH}{\Delta x^2}\left(\frac{4}{3}\sin k\Delta x - \frac{1}{6}\sin 2k\Delta x\right)^2. \tag{4.52}$$

The relative frequency of gravity waves in the numerical solution obtained with fourth order spatial differencing therefore is

$$R_4 = \frac{\Omega_T}{\Omega_N} = \frac{1}{k\Delta x}\left(\frac{4}{3}\sin k\Delta x - \frac{1}{6}\sin 2k\Delta x\right). \tag{4.53}$$

Thus, the gravity waves in the numerical solution propagate with the phase speed

$$c_4 = \pm\sqrt{gH}\frac{1}{k\Delta x}\left(\frac{4}{3}\sin k\Delta x - \frac{1}{6}\sin 2k\Delta x\right), \tag{4.54}$$

or alternatively,

$$c_4 = cR_4. \tag{4.55}$$

The relative frequency R_4 is shown in Fig. 4.3 as a function of the normalized wave number $k\Delta x/\pi$ (green line).

4.3.3.3 Sixth order spatial differencing

When the space derivatives in (4.38) are approximated by sixth order centered differences, the differential-difference equations

$$\frac{\partial u_i}{\partial t} = -\frac{g}{\Delta x}\left(-\frac{1}{60}h_{i-3} + \frac{3}{20}h_{i-2} - \frac{3}{4}h_{i-1} + \frac{3}{4}h_{i+1} - \frac{3}{20}h_{i+2} + \frac{1}{60}h_{i+3}\right),$$

$$\frac{\partial h_i}{\partial t} = -\frac{H}{\Delta x}\left(-\frac{1}{60}u_{i-3} + \frac{3}{20}u_{i-2} - \frac{3}{4}u_{i-1} + \frac{3}{4}u_{i+1} - \frac{3}{20}u_{i+2} + \frac{1}{60}u_{i+3}\right), \tag{4.56}$$

result. Substitution of (4.44) into (4.50) leads to

$$\Omega_N \hat{u} = \frac{g}{\Delta x}\left(\frac{3}{2}\sin k\Delta x - \frac{3}{10}\sin 2k\Delta x + \frac{1}{30}\sin 3k\Delta x\right)\hat{h},$$

$$\Omega_N \hat{h} = \frac{H}{\Delta x}\left(\frac{3}{2}\sin k\Delta x - \frac{3}{10}\sin 2k\Delta x + \frac{1}{30}\sin 3k\Delta x\right)\hat{u}. \tag{4.57}$$

giving the frequency equation

$$\Omega_N^2 = \frac{gH}{\Delta x^2}\left(\frac{3}{2}\sin k\Delta x - \frac{3}{10}\sin 2k\Delta x + \frac{1}{30}\sin 3k\Delta x\right)^2. \tag{4.58}$$

The magnitude of relative frequency of gravity waves in the numerical solution obtained with sixth order spatial differencing therefore is

$$R_6 = \frac{\Omega_T}{\Omega_N} = \frac{1}{k\Delta x}\left(\frac{3}{2}\sin k\Delta x - \frac{3}{10}\sin 2k\Delta x + \frac{1}{30}\sin 3k\Delta x\right). \tag{4.59}$$

Thus, the gravity waves in the numerical solution propagate with the phase speed

$$c_6 = \pm\sqrt{gH}\frac{1}{k\Delta x}\left(\frac{3}{2}\sin k\Delta x - \frac{3}{10}\sin 2k\Delta x + \frac{1}{30}\sin 3k\Delta x\right), \tag{4.60}$$

or alternatively,

$$c_6 = cR_6. \tag{4.61}$$

The relative frequency R_6 is shown in Fig. 4.3 as a function of the normalized wave number $k\Delta x/\pi$ (yellow line). Comparing the relative frequency at fourth and sixth-order to the second-order result reveals a great improvement for the scales

$$k\Delta x/\pi < 1/2. \tag{4.62}$$

These are the waves with wave lengths larger than $4\Delta x$. The relative frequency for a wave of length $4\Delta x$ is about 88% at fourth-order, and 92% at the sixth-order, compared to 60% at second-order. Thus, at sixth-order differencing the error in the numerical frequency is less than 10% for the important range (4.62). Similar results were obtained for the shallow-water equations by Purser and Leslie (1988). More insight into the improvement gained in the relative frequency can be obtained by considering Fig. 4.4. Here the relative frequency is plotted for second-order (black), fourth-order (green) and sixth-order (yellow) differencing as a function of the horizontal wave length, for $200\,m \leq L_x \leq 1000\,m$. In the relevant formulas of relative frequency (4.47), (4.53) and (4.59), $\Delta x = 100\,m$ is used, implying that the shortest resolvable wave has wave length $200\,m$. The red line in Fig. 4.4 is obtained from using

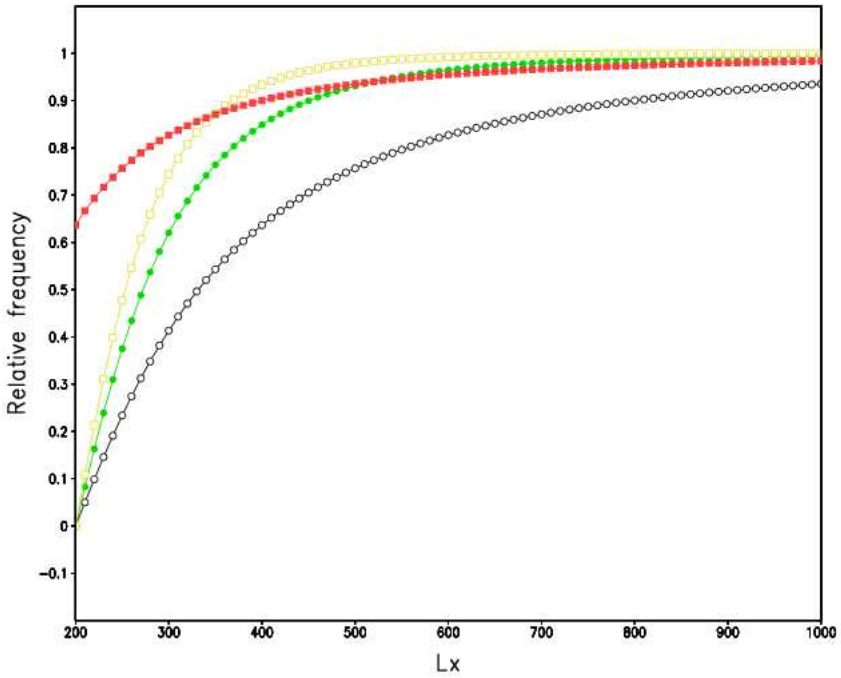

Figure 4.4: The relative frequency of pure gravity waves as a function of wave length, for second order (black line), fourth order (green line) and sixth order (yellow line) spatial differencing on the nonstaggered grid with $\Delta x = 100\,m$. The red line represents the relative frequency of pure gravity waves for second order differencing on the nonstaggered grid with $\Delta x = 50\,m$.

$\Delta x = 50m$ in the relative frequency formula (4.47) obtained with second-order differencing. The doubling of grid resolution results in a far more accurate representation of the frequency of the short wave length gravity waves for second-order differencing (note, however, that the $2\Delta x = 100\,m$ wave is stationary for the case $\Delta x = 50\,m$). It can also be seen in Fig. 4.4 that fourth and sixth-order differencing at a specific grid length produces more accurate results than second-order differencing at double the resolution, for waves lengths larger than about 1.5 and 2.5 grid-lengths respectively. However, despite the advantages to be gained from higher-order differencing at short wave lenghts, the presence of stationary $2\Delta x$ waves remain problematic, irrespective of the degree of the order of differencing.

4.4 Spatial filtering

The unpopularity of the nonstaggered grid in meteorological modelling is largely due to the presence of the spurious stationary two-grid-interval waves, that appear as solutions of the pure gravity wave equations in response to spatial discretization on this grid. When the Coriolis terms are also present, the two-grid-interval waves appear with false low frequencies as pure inertia waves (Mesinger and Arakawa, 1976).

Shapiro (1975) devised a family of stable filters that remove completely the two-grid-interval waves. These filters affect the asymptotically long waves to the least extent possible given the width of each filter's stencil (Purser, 1987).

The one-dimensional filtering operator proposed by Shapiro (1976) for a variable f on a nonstaggered grid is

$$f_i^{p+1} = 1 - \frac{1}{2^{2p+2}} \begin{pmatrix} 2p & +2 \\ p & +1 \end{pmatrix} f_i$$

$$+ \left[\frac{(-1)^p}{2^{2p+2}}\right] \Sigma_{j=0}^{p} (-1)^j \begin{pmatrix} 2p+2 \\ j \end{pmatrix} \left[f_{i+(1+p-j)} + f_{i-(1+p-j)}\right], \qquad (4.63)$$

where $\begin{pmatrix} n \\ m \end{pmatrix} = n!/\left[(n-m)!m!\right]$. The amplitude response function for the operator (4.63) is

$$AR = 1 - \sin^{2p+2}\alpha. \qquad (4.64)$$

Here $\alpha = n\Delta x/2$; $n = 2\pi/\lambda$ with λ the wave length of the component.

In the numerical experiments performed in Chapter 5, $p = 4$ was found to produce satisfactory results. In this case the filtering operator is

$$f_i^5 = \frac{1}{2^{10}}\left[f_{i-5} - 10f_{i-4} + 45f_{i-3} - 120f_{i-2} + 210f_{i-1} + 772f_i\right.$$

$$\left. +210f_{i+1} - 120f_{i+2} + 45f_{i+3} - 10f_{i+4} + f_{i+5}\right] \tag{4.65}$$

For the operator (4.65) the amplitude response of the three-grid, four-grid and six-grid-interval waves are 0.76270, 0.96875 and 0.99902 respectively (Shapiro, 1975). This illustrates the mimimal effect that the filter has at longer wave lengths. Thus, the high-order Shapiro filter is a highly scale-dependent explicit smoothing operator. Its application in the split semi-Lagrangian scheme is discussed in section 4.5.3.

4.5 The split semi-Lagrangian solution procedure

In this section, a two time-level, time-split, semi-Lagrangian scheme is constructed for solving the σ coordinate quasi-elastic equations (3.64) to (3.68). The solution procedure is split into four different phases. The first phase is a semi-Lagrangian advection step with time step Δt_s, followed by an adjustment procedure with N adjustment steps each having time step $\Delta t_a = \Delta t_s/N$. The third and fourth phases consist of the application of a highly scale-dependent spatial filter and explicit diffusion respectively. The horizontal and vertical differencing are carried out on a nonstaggered grid.

4.5.1 Splitting off the advective part

Suppose that the values of all seven variables u, v, $\Omega = \omega/p$, $\dot{\sigma}$, T, ϕ and p_s are known at time level t. The advection process in the horizontal momentum, continuity and thermodynamic energy equations is represented by the following equations:

$$\frac{Du}{Dt} = 0, \tag{4.66}$$

$$\frac{Dv}{Dt} = 0, \tag{4.67}$$

$$\frac{D\ln p_s}{Dt} = 0, \tag{4.68}$$

$$\frac{DT}{Dt} = 0. \tag{4.69}$$

The semi-Lagrangian approach is used to calculate the contribution of advection to the fields u, v, $\ln p_s$ and T at the arrival points . One of the the D_N schemes of McGregor (1993) is applied in three spatial dimensions to calculate the time-level t departure points (x^*, y^*, σ^*) for each time-level $t+\Delta t_s$ arrival grid point. Note that the values of u, v and $\dot{\sigma}$ are required at time levels t, $t-\Delta t$ and $t-2\Delta t$ in order to evaluate (4.5) for application in the D_N scheme. The values of u, v, $\ln p_s$ and T are evaluated at the departure points using a tricubic extension of the bicubic interpolation scheme presented in section 4.2.2 to three spatial dimensions. Note that for application in two spatial dimensions, a D_N scheme is used with bicubic spatial interpolation as discussed in section 4.2.2. Let the departure point values of u, v, $\ln p_s$ and T obtained from the semi-Lagrangian procedure be denoted by u^*, v^*, $\ln p_s^*$ and T^*.

An important feature of the scheme is the use of (4.68) by means of the calculation of the quantity $\ln p_s$ at time level $t+\Delta t_s$ from the semi-Lagrangian procedure, at each arrival grid point. At the end of the advection step, the quantity $A_{p_s} = -u\,(\partial \ln p_s/\partial x) - v\,(\partial \ln p_s/\partial y)$ at time level $t+\Delta t_s$ is diagnosed at each arrival grid point, for use in the adjustment phase of the solution procedure. That is, the the term is effectively calculated from the values of u^*, v^* and $\ln p_s^*$ that correspond to each arrival grid point and it represents the change in the local time tendency of $\ln p_s$ because of advection. Therefore, let this field be denoted by $A_{p_s}^*$. Alternatively, the quantity A_{p_s} may be diagnosed at the beginning of each time step for each grid point and the departure point values ($A_{p_s}^*$) calculated from the semi-Lagrangian procedure for each arrival grid point. The value of $\ln p_s^*$ may then be obtained from $A_{p_s}^*$. The latter approach was followed by McGregor (1986) and Leslie and Purser (1991) to solve hydrostatic equation sets. The numerical experiments performed in Chapter 5 indicate that these two approaches of calculating the advective change to the surface pressure give almost indistinguishable results. Note that a semi-Lagrangian discretization of the vertical momentum equation is not employed in the scheme.

4.5.2 The adjustment step

The values u^*, v^* and T^* calculated during the advection step for each arrival grid point, are used as initial values for the fields of u, v and T during the first step of the adjustment phase of the solution procedure. Initial values required for the fields p_s, ω/p and ϕ, are taken to be effectively at time level t. Forward differences in time are used to update the fields of u, v at time level $t+\Delta t_a$:

$$\frac{u^{t+k\Delta t_a} - u^{t+(k-1)\Delta t_a}}{\Delta t_a} = \left(-\frac{\partial \phi}{\partial x} + \sigma \frac{\partial \phi}{\partial \sigma}\frac{\partial \ln p_s}{\partial x} \right)^{t+(k-1)\Delta t_a} + \frac{f}{2}\left(v^{t+(k-1)\Delta t_a} + v^{t+k\Delta t_a} \right), \tag{4.70}$$

$$\frac{v^{t+k\Delta t_a} - v^{t+(k-1)\Delta t_a}}{\Delta t_a} = \left(-\frac{\partial \phi}{\partial y} + \sigma \frac{\partial \phi}{\partial \sigma}\frac{\partial \ln p_s}{\partial y}\right)^{t+(k-1)\Delta t_a} - \frac{f}{2}\left(u^{t+(k-1)\Delta t} + u^{t+k\Delta t}\right), \tag{4.71}$$

Here k ranges from 1 to N. Note that trapezoidal time stepping (Fisher, 1965; Janjic and Wiin-Nielsen, 1977) is used to treat the Coriolis terms semi-implicitly. The surface pressure tendency $\partial \ln p_s/\partial t$ at time level $t+k\Delta t_a$ is diagnosed using the latest values of u and v, with backward time differencing being applied to update $\ln p_s$ (and thence p_s):

$$\frac{\ln p_s^{t+k\Delta t_a} - \ln p_s^{t+(k-1)\Delta t_a}}{\Delta t_a} = \int_0^1 \left[A^*_{p_s} - \left(\frac{\partial u}{\partial x} + \frac{\partial v}{\partial y}\right)^{t+k\Delta t_a}\right] d\sigma \tag{4.72}$$

Note that (4.72) is obtained from integrating (3.67) over σ, from the model top $\sigma = 0$ to the surface $\sigma = 1$. The field $A^*_{p_s}$ is assumed to remain constant during the adjustment phase. Experiments were performed in which A_{p_s} was updated at the end of each adjustment time step using the latest values of u, v and p_s, but this had an insignificant effect on the simulations. In fact, the contribution of term A_{p_s} to (4.72) and (4.73) was found to be insignificant in the numerical experiments described in the next section. However, these experiments were performed for the case of zero topography; it is likely that the term is more important in regions of steep terrain. The fields of $\dot{\sigma}$ and ω/p are diagnosed consistently with the field $\partial \ln p_s/\partial t$ at time level $t + k\Delta t_a$:

$$\dot{\sigma}^{t+k\Delta t_a} = -\sigma\left(\frac{\partial \ln p_s}{\partial t}\right)^{t+k\Delta t_a} + \int_0^\sigma \left[A^*_{p_s} - \left(\frac{\partial u}{\partial x} + \frac{\partial v}{\partial y}\right)^{t+k\Delta t_a}\right] d\sigma', \tag{4.73}$$

$$\left(\frac{\omega}{p}\right)^{t+k\Delta t_a} = \left\{\frac{p_s^{t+k\Delta t_a}}{\sigma p_s^{t+k\Delta t_a} + p_T}\left\{\sigma\left[\left(\frac{\partial \ln p_s}{\partial t}\right)^{t+k\Delta t_a} - A^*_{p_s}\right] + \dot{\sigma}^{t+k\Delta t_a}\right\}\right\}. \tag{4.74}$$

Here (4.73) has been obtained by integrating (3.67) in the vertical from the model top to level σ and (4.74) follows from relationship (3.69). The temperature field T may now be updated using backward time differencing

$$\frac{T^{t+k\Delta t_a} - T^{t+(k-1)\Delta t_a}}{\Delta t_a} = \kappa\left(\frac{\omega}{p}\right)^{t+k\Delta t_a} T^{t+k\Delta t_a}. \tag{4.75}$$

It is interesting to note that in the semi-implicit solution of the hydrostatic equations used in C-CAM, the right-hand side of the thermodynamic equation (4.75) is handled implicitly with regard to ω. This is necessary because of gravity wave feedback into the ϕ terms of the horizontal momentum equations (McGregor, personal communication). In the present approach this treatment is avoided by diagnosing ϕ from the elliptic equation (see the next paragraph).

Finally, the geopotential field at time-level $t + k\Delta t_a$ is diagnosed from the discretized version of the elliptic equation (3.81). This equation is solved iteratively, using Successive Over-Relaxation (SOR). In most of the numerical experiments performed in Chapter 5, only a few interations are required to obtain suitable convergence of the solution. The iterative solution procedure is outlined in some detail in section 4.6, whilst the computational efficiency of the elliptic solver is discussed in more detail in Chapter 5. It may be noted that the vertical momentum equation is never used explicitly in the solution procedure, but is implicitly present in (3.81).

4.5.3 Spatial filtering

After both the advection step and the N adjustment steps have been performed, spatial filtering is applied to some of the variables calculated. The Shapiro (1975) filter discussed in section 4.4 is applied to perform spatial filtering of the fields u, v, p_s, $\dot{\sigma}$ and ϕ. Since the variable ω/p is diagnosed from the (filtered) fields of $\ln p_s$ and $\dot{\sigma}$ in the adjustment procedure, without any additional centered differencing being performed, there is no need to perform filtering on this field. It is also essential that the spatial filter is not applied to the temperature field. This is due to the fact that no spatial derivatives occur in the adjustment step equation (4.75), which is used to update the temperature field (see section 4.5.2). By the time that the temperature field is updated in the adjustment phase procedure, the right-hand side of (4.75) is effectively already filtered (the spatial filter is applied to p_s and $\dot{\sigma}$ used to diagnose ω/p in (4.75)). It is not meaningful to apply the spatial filter to an already filtered field. Numerical simulations (see Chapter 5) where the temperature field is filtered show excessive numerical noise. Numerical experiments indicated that generally filtering with $p = 4$ produces satisfactory results (see Chapter 5). The horizontal filtering is first performed in the x direction

$$f^5_{i,\,j} = \frac{1}{2^{10}}\left[f_{i-5,\,j,\,k} - 10f_{i-4,\,j,\,k}, +45f_{i-3,\,j,\,k} - 120f_{i-2,\,j,\,k} + 210f_{i-1,\,j,\,k} + \right.$$

$$\left. 772f_{i,\,j,\,k} + 210f_{i+1,\,j,\,k} - 120f_{i+2,\,j,\,k} + 45f_{i+3,\,j,\,k} - 10f_{i+4,\,j,\,k} + f_{i+5,\,j,\,k}\right], \tag{4.76}$$

for each variable u, v, p_s,$\dot{\sigma}$, T and ϕ. This is followed by similar filtering in the y and σ directions.

The spatial filtering effectively removes the two-grid-interval waves from the nonstaggered grid (Shapiro, 1975; also see section 4.4 and Chapter 5), whilst the damping at longer wave lengths is sufficiently small not to impact negatively on the simulations (see section 4.4 and Chapter 5). Thus, the spatial filtering provides highly scale-dependent, explicit filtering in the model. The split semi-Lagrangian scheme with application of the Shapiro filter is stable at large Courant numbers (see Chapter 5).

4.5.4 Explicit diffusion

After application of the Shapiro filter, there is no need to apply explicit diffusion (smoothing) in the split semi-Lagrangian scheme in order to ensure numerical stability, or to control numerical noise originating from the nonstaggered grid. However, the use of explicit diffusion may still be useful in order to obtain a grid-converged solution of a specific flow problem (Straka et al., 1993). In the absence of explicit diffusion, an increase in model resolution will always result in smaller scales of motion to be resolved. However, by applying explicit diffusion, a limit is placed in the resolvable scales, so that numerical solutions of a given flow problem will converge towards a so called "grid converged solution" at increasing resolution. Grid-converged solutions of specific flow problems are most useful for the comparison of different numerical schemes to each other, and to study the characteristics of a specific numerical scheme. In Chapter 5, the simulation of warm and cold convective bubbles by the split semi-Lagrangian scheme are compared to well-known grid-converged solutions of these problems. Thus, after application of the Shapiro filter, explicit filtering is applied in a split manner to the the horizontal wind and temperature fields as follows

$$\frac{u^{t+k\Delta t_s} - u^{t'}}{\Delta t_s} = K_s \left(\frac{\partial^2 u}{\partial x^2} + \frac{\partial^2 u}{\partial y^2} \right)^{t'} + K_\sigma \left(\frac{\partial^2 u}{\partial \sigma^2} \right)^{,t'} \tag{4.77}$$

$$\frac{v^{t+k\Delta t_s} - v^{t'}}{\Delta t_s} = K_s \left(\frac{\partial^2 v}{\partial x^2} + \frac{\partial^2 v}{\partial y^2} \right)^{t'} + K_\sigma \left(\frac{\partial^2 v}{\partial \sigma^2} \right)^{t'}, \tag{4.78}$$

$$\frac{T^{t+k\Delta t_s} - T^{t'}}{\Delta t_s} = K_{Ts} \left(\frac{\partial^2 T}{\partial x^2} + \frac{\partial^2 T}{\partial y^2} \right)^{t'} + K_{T\sigma} \left(\frac{\partial^2 T}{\partial \sigma^2} \right)^{t'}. \tag{4.79}$$

Note that latest available values of the variables u, v, and T, as obtained after application of the adjustment procedure and the Shapiro filter, are used as initial values (denoted by time-level t') in (4.77) to (4.79). K_s and K_{Ts} are the horizontal diffusion coefficients, and K_σ and $K_{T\sigma}$ are the vertical diffusion coefficients. Typical values of the augmented diffusion coefficients $K\Delta t_s/\Delta n^2$ ($n = x$, y, σ) along the x, y and σ axis are respectively 0.0015, 0.0015 and 0.0015 for T and 0.015, 0.015 and 0.015 for u and v. Although the vertical momentum equation is not discretized explicitly, diffusion is applied to the vertical motion

field $\dot{\sigma}$ and p_s indirectly when the diffused horizontal motion field is used in the integration of (4.73) and (4.72).

Note that the dimensionless augmented diffusion coefficient $K\Delta t_s/\Delta n^2$ is convenient to use when the numerical values of the diffusion coefficients need to be specified. Janjic et al. (2001) used the same notation. The explicit diffusion step is the final phase of the split semi-Lagrangian scheme. After this step, all fields have been updated satisfactorily in order for the next semi-Lagrangian advection step to be performed.

4.6 Frequency response of the quasi-elastic equations to the forward-backward time discretization

In this section, the frequency response of the quasi-elastic equations to the forward-backward time discretization is examined using the von Neumann method (e.g. Richtmyer and Morton, 1967; Mesinger and Arakawa, 1976). As in the case of the linear analysis of the quasi-elastic equations performed in Chapter 3, the response analysis in the present section is carried out in two spatial dimensions.

In Chapter 3, the two-dimensional σ coordinate quasi-elastic equations (3.82)-(3.85) were linearized about an isothermal reference state of no motion, for a nonrotating, adiabatic and inviscid atmosphere. A similar linearization may be performed for the form that the two-dimensional equations assume in the adjustment step of the split semi-Lagrangian solution procedure. These linearized equations are:

$$\frac{\partial u}{\partial t} = -\left(\frac{\partial \phi^{'}}{\partial x}\right), \tag{4.80}$$

$$\frac{\partial p_s}{\partial t} = -p_0 \int_0^1 \frac{\partial u}{\partial x} d\sigma, \tag{4.81}$$

$$\dot{\sigma} = -\int_0^\sigma \left(\frac{\partial u}{\partial x}\right) d\sigma - \frac{\sigma}{p_0}\frac{\partial p_s}{\partial t}, \tag{4.82}$$

$$\frac{\partial T^{'}}{\partial t} = \kappa \left(\frac{p_0}{\sigma p_0 + p_T}\right)\left[\frac{\sigma}{p_0}\frac{\partial p_s}{\partial t} + \dot{\sigma}\right] T_0. \tag{4.83}$$

Equations (4.80) to (4.83) correspond to the linearized equations (3.102), (3.104) and (3.105), with the difference that the continuity equation is used in integrated form. That is, (4.81) and (4.82) replace (3.104) in order to obtain the linearized adjustment step equtions (before the time discretization is perfomed). Note once more that the vertical momentum equation is not used explicitly in the split semi-Lagrangian solution procedure. Following the procedure outlined

in Appendix A for the three-dimensional quasi-elastic σ coordinate equations, (3.102)-(3.105) can be shown to imply the linearized elliptic equation:

$$\frac{\partial^2 \phi^{'}}{\partial x^2} + \frac{\partial}{\partial \sigma}\left(s_0^2 \frac{\partial \phi^{'}}{\partial \sigma}\right) + \frac{\partial}{\partial \sigma}\left(s_0 \frac{T^{'}}{T_0} g\right) = 0. \tag{4.84}$$

Here $s_o = (1/H_0)\left(\sigma p_0 + p_T\right)/p_0 = (g/RT_0)\left(\sigma p_0 + p_T\right)/p_0$. Equation (4.84) is the linearized version of the elliptic equation (3.86), which is used in the split semi-Lagrangian discretization of the two-dimensional σ coordinate quasi-elastic equations.

Applying the forward-backward procedure presented in section 4.5 to solve the linearized equations (4.80) to (4.84) results in the following set of difference-differencial equations:

$$\frac{u^t - u^{t-\Delta t}}{\Delta t} = -\frac{\partial \phi^{'t-\Delta t}}{\partial x}, \tag{4.85}$$

$$\frac{p_s^t - p_s^{t-\Delta t}}{\Delta t} = -p_0 \int_0^1 \frac{\partial u^t}{\partial x} d\sigma, \tag{4.86}$$

$$\dot{\sigma}^t = -\int_0^\sigma \left(\frac{\partial u}{\partial x}\right)^t d\sigma - \frac{\sigma}{p_0}\frac{p_s^t - p_s^{t-\Delta t}}{\Delta t}, \tag{4.87}$$

$$\frac{T^{'t} - T^{'t-\Delta t}}{\Delta t} = \kappa\left(\frac{p_0}{\sigma p_0 + p_T}\right)\left[\frac{\sigma}{p_0}\left(\frac{p_s^t - p_s^{t-\Delta t}}{\Delta t}\right) + \dot{\sigma}^t\right] T_0, \tag{4.88}$$

$$\frac{\partial^2 \phi^{'t}}{\partial x^2} + \frac{\partial}{\partial \sigma}\left(s_0^2 \frac{\partial \phi^{'t}}{\partial \sigma}\right) = -\frac{\partial}{\partial \sigma}\left(s_0 \frac{T^{'t}}{T_0} g\right). \tag{4.89}$$

Note that, for the sake of convenience, the time-level notation is slightly different from that used for the advection step in section 4.5. Introducing Fourier decomposition of the form

$$\hat{Q}(\sigma)\exp^{i(kx - \vartheta t)} \tag{4.90}$$

for each variable, a response analysis of the time-discretized equations can be carried out for the corresponding amplitude functions. Note that $\vartheta = kc$ is the Eulerian frequency of the waves. By substituting (4.90) into (4.85)-(4.89) it is obtained that

$$\frac{\hat{u}}{\Delta t}\left(\exp^{-i\vartheta \Delta t} - 1\right) = -ik\hat{\phi^{'}}, \tag{4.91}$$

$$\frac{\hat{\pi}}{\Delta t}\left(1 - \exp^{i\vartheta \Delta t}\right) + ik\int_0^1 \hat{u}\, d\sigma = 0, \tag{4.92}$$

$$\hat{\dot{\sigma}} = -ik\int_0^{\sigma} \hat{u'}\, d\sigma - \frac{\sigma\hat{\pi}}{\Delta t}\left(1-\exp^{i\vartheta\Delta t}\right), \tag{4.93}$$

$$\frac{\hat{T'}}{\Delta t}\left(1-\exp^{i\vartheta\Delta t}\right) = \kappa\left(\frac{p_0}{\sigma p_0 + p_T}\right)\left[\frac{\sigma\hat{\pi}}{\Delta t}\left(1-\exp^{i\vartheta\Delta t}\right) + \hat{\dot{\sigma}}\right]T_0, \tag{4.94}$$

$$\frac{d}{d\sigma}\left[\left(\frac{\sigma p_0 + p_T}{p_0}\right)^2 \frac{d\hat{\phi'}}{d\sigma}\right] - H_0^2 k^2 \hat{\phi'} + H_0^2 \frac{d}{d\sigma}\left(s_0\hat{T}\frac{g}{T_0}\right) = 0. \tag{4.95}$$

Equation (4.95) may be written in terms of $\hat{\phi'}$ by using (4.91), (4.93) and (4.94). To this end, note that (4.94) may be used to show that

$$\frac{d}{d\sigma}\left(s_0\hat{T'}\right) = \frac{\Delta t\kappa}{H_0}\left[\frac{\hat{\pi}}{\Delta t}\left(1-\exp^{i\vartheta\Delta t}\right) + \frac{d\hat{\dot{\sigma}}}{d\sigma}\right]T_0\left(1-\exp^{i\vartheta\Delta t}\right)^{-1}. \tag{4.96}$$

Noting from (4.93) that

$$\frac{d\hat{\dot{\sigma}}}{d\sigma} = -ik\frac{d}{d\sigma}\int_0^{\sigma}\hat{u}\, d\sigma - \frac{\hat{\pi}}{\Delta t}\left(1-\exp^{i\vartheta\Delta t}\right), \tag{4.97}$$

it follows from substituting (4.97) in (4.96) and applying (4.91) that

$$\frac{d}{d\sigma}\left(s_0\hat{T'}\right) = -\frac{\kappa T_0}{H_0}\left[\frac{k^2\Delta t^2}{\left(\exp^{-i\vartheta\Delta t}-1\right)\left(1-\exp^{i\vartheta\Delta t}\right)}\right]\frac{d}{d\sigma}\int_0^{\sigma}\hat{\phi'}\, d\sigma \tag{4.98}$$

Substituting (4.98) in (4.95) leads to

$$\frac{d}{d\sigma}\left[\left(\frac{\sigma p_0 + p_T}{p_0}\right)^2 \frac{d\hat{\phi'}}{d\sigma}\right] - H_0^2 k^2 \hat{\phi'}$$

$$-H_0^2 N^2\left[\frac{k^2\Delta t^2}{\left(\exp^{-i\vartheta\Delta t}-1\right)\left(1-\exp^{i\vartheta\Delta t}\right)}\right]\frac{d}{d\sigma}\int_0^{\sigma}\hat{\phi'}\, d\sigma = 0. \tag{4.99}$$

Equation (4.99) is the vertical structure equation for $\hat{\phi'}$ that results from the forward-backward time discretization. Being of the same form as (3.113), the vertical structure equation of the undiscretized quasi-elastic equations, (4.99) admits solutions of the form (3.143). The corresponding dispersion relation obtained for the gravity waves is

$$m^2 = -\frac{1}{4H_0^2} + \left(\frac{N^2}{c_N^2} - k^2\right) > 0, \tag{4.100}$$

where $m > 0$ by definition and

$$c_N^2 = -\frac{\left(\exp^{-i\vartheta\Delta t} - 1\right)\left(1 - \exp^{i\vartheta\Delta t}\right)}{k^2\Delta t^2} = \frac{2\left(1 - \cos\vartheta\Delta t\right)}{k^2\Delta t^2}. \tag{4.101}$$

Equation (4.100) may be written in the alternative form

$$-k^2c_N^2\left(m^2 + k^2 + 1/4H_0^2\right)c^2 + k^2c^2N^2 = 0. \tag{4.102}$$

The form of (4.102) is identical to (3.142), the dispersion relation for the true frequency ϑ_T, with the substitution

$$\vartheta_T^2 = k^2c_N^2 = \frac{2\left(1 - \cos\vartheta\Delta t\right)}{\Delta t^2}. \tag{4.103}$$

Alternatively, the numerical value of the local frequency ϑ can be compared to its analytic counterpart ϑ_T through the relation

$$\vartheta = \frac{\arccos\left[1 - \left(\vartheta_T\Delta t\right)^2/2\right]}{\Delta t} \tag{4.104}$$

Clearly, (4.104) is defined for

$$-1 \leq 1 - \frac{\left(\vartheta_T\Delta t\right)^2}{2} < 1, \tag{4.105}$$

which may be written as

$$0 < \left|\vartheta_T\right|\Delta t \leq 2, \tag{4.106}$$

or alternatively as

$$0 < \frac{|c|\,\Delta t}{\Delta x} \leq \frac{2}{\pi}. \tag{4.107}$$

Here c denotes the analytic phase speed of the gravity waves. The relative frequency of the gravity waves in the numerical solution is defined as the ratio of the numerical frequency ϑ to the true frequency ϑ_T. That is,

$$R = \frac{\vartheta}{\vartheta_T} = \frac{\arccos\left[1 - \left(\vartheta_T\Delta t\right)^2/2\right]}{\Delta t\vartheta_T}, \tag{4.108}$$

provided that (4.106) is true. Recall the defenition of the Courant number, $\alpha = c\Delta t/\Delta x$. Equation (4.108) may alternatively be written in terms of α as

$$R = \frac{\vartheta}{\vartheta_T} = \frac{\arccos\left[1 - \left(k\Delta x\alpha\right)^2/2\right]}{k\Delta x\alpha}, \tag{4.109}$$

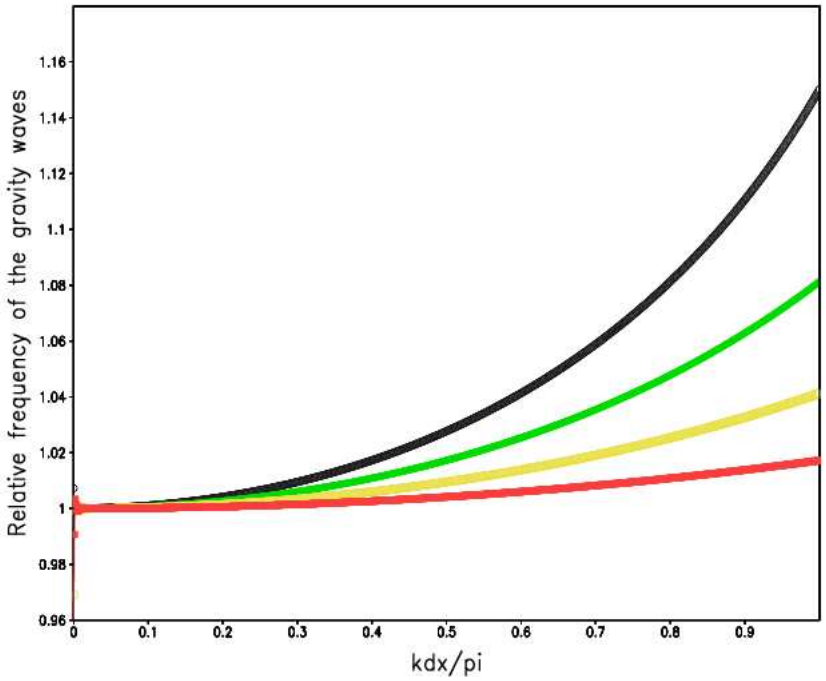

Figure 4.5: Relative frequency of the gravity waves in response to the forward-backward time discretization, as a function of the wave number. The red, yellow, green and black lines represent Courant numbers of 0.2, 0.3, 0.4 and 0.5, respectively.

noting the range of validity (4.107). The relative frequency of the gravity waves in the numerical solution is displayed in Fig. 4.5 for various values of α, as a function of the scaled wave number.

Condition (4.107) suggests that the forward-backward scheme can only be applied for Courant numbers less than or equal to $2/\pi$, else the numerical solution may have unphysical properties. This implies a significant restriction on the maximum size of the time-step that may be used during the adjustment step. From Fig. 4.5 it is evident that the forward-backward scheme accelerates the gravity waves. This artificial acceleration decreases as the wave length decreases, and in the long wave limit the numerical frequency (and phase speed) approaches the true frequency of the gravity waves. The acceleration also increases as the Courant number increases, by as much as 15% for $\alpha = 0.5$ at the shortest resolvable scales.

In practical applications of the split semi-Lagrangian scheme, the accelerating effect of the forward-backward scheme is alleviated by two factors: the damping effect of the bicubic spatial interpolations, particularly at short wave lengths (see section 4.2), and the explicit smoothing of the two-grid-interval wave by the Shapiro time filter (see section 4.4). The impact of these effects on the maximum size of time step that can be used in practical applications of the split semi-Lagrangian procedure, is investigated in Chapter 5 by means of numerical experiments.

4.7 Frequency response to spatial discretization on the nonstaggered grid

In this section, the frequency response to spatial discretization on the nonstaggered grid is examined, again using the von Neumann method (e.g. Rightmyer and Morton, 1967; Mesinger and Arakawa, 1976). As in the previous section, the two-dimensional quasi-elastic equations of the form used in the adjustment step are linearized about an isothermal reference state of no motion, for a non-rotating, adiabatic and inviscid atmosphere. The effect of numerical integration in the vertical (as applied to the continuity equation in order to evaluate p_s and $\dot{\sigma}$, see (4.81) and (4.82)) is not considered here, and in the frequency response analysis that follows, all vertical integrals are evaluated analytically.

4.7.1 Frequency response to horizontal discretization

When the horizontal spatial derivatives in (4.80) to (4.83) are discretized using second-order spatial differencing, and Fourier decomposition of the form (4.90) is performed on the resulting equations, the following amplitude equations result:

$$-i\vartheta\hat{u} = -i\left(\frac{\sin k\Delta x}{\Delta x}\right)\hat{\phi}, \tag{4.110}$$

$$-i\vartheta\hat{\pi} = -i\frac{\sin k\Delta x}{\Delta x}\int_0^1 \hat{u}\, d\sigma, \tag{4.111}$$

$$\hat{\dot{\sigma}} = -i\frac{\sin k\Delta x}{\Delta x}\int_0^\sigma \hat{u}\, d\sigma + i\vartheta\sigma\hat{\pi}, \tag{4.112}$$

$$-i\vartheta\hat{T}' = \kappa\left(\frac{p_0}{\sigma p_0 + p_T}\right)\left[-i\vartheta\sigma\hat{\pi} + \hat{\dot{\sigma}}\right]T_0. \tag{4.113}$$

The second horizontal derivative in (4.84) is left undiscretized, so that (4.95) is obtained after Fourier decomposition. Equation (4.95) is written in the form

$$\frac{d}{d\sigma}\left[\left(\frac{\sigma p_0 + p_T}{p_0}\right)^2\frac{d\hat{\phi}'}{d\sigma}\right] - H_0^2k^2\hat{\phi}' = -H_0^2\frac{d}{d\sigma}\left(s_0\hat{T}'\frac{g}{T_0}\right). \tag{4.114}$$

If the left-hand side of (4.114) is modified to include the effect of horizontal discretization, the frequency equation that results in combination with (4.110) to (4.113) can not be conveniently compared to its analytic counterpart (3.140). Thus, only the effect of horizontal discretization on the right-hand side of (4.114) (the forcing to which the geopotential distribution respond to) will be considered.

The right-hand side of (4.114) can be written in terms of $\hat{\phi}'$ by using (4.110) to (4.113). To this end, note that by using (4.113) it may be shown that

$$\frac{d}{d\sigma}\left(s_0\hat{T}'\right) = \frac{\kappa}{H_0}\left(\hat{\pi} - \frac{1}{i\vartheta}\frac{d\hat{\dot{\sigma}}}{d\sigma}\right)T_0. \tag{4.115}$$

Noting from (4.112) that

$$\frac{d\hat{\dot{\sigma}}}{d\sigma} = -i\frac{\sin k\Delta x}{\Delta x}\frac{d}{d\sigma}\left(\int_0^\sigma \hat{u}d\sigma\right) + i\vartheta\hat{\pi}, \tag{4.116}$$

it follows by applying (4.116) and making use of (4.110) that

$$\frac{d}{d\sigma}\left(s_0\hat{T}\right) = \frac{\kappa}{H_0}\left(\frac{1}{\vartheta^2}\frac{\sin^2 k\Delta x}{\Delta x^2}\right)\left(\frac{d}{d\sigma}\int_0^\sigma \hat{\phi}'\, d\sigma\right)T_0. \tag{4.117}$$

Substituting (4.117) in (4.114) leads to a vertical structure equation for $\hat{\phi}'$,

$$\frac{d}{d\sigma}\left[\left(\frac{\sigma p_0 + p_T}{p_0}\right)^2\frac{d\hat{\phi}'}{d\sigma}\right] - H_0^2k^2\hat{\phi}' + \frac{H_0^2N^2}{\vartheta^2}\left(\frac{\sin^2 k\Delta x}{\Delta x^2}\right)\frac{d}{d\sigma}\int_0^\sigma \hat{\phi}'\, d\sigma = 0. \tag{4.118}$$

Equation (4.118) is of the same form as (3.113), the vertical structure equation for the undiscretized quasi-elastic equations. It therefore admits solutions of the form (3.143). Substituting (3.143) in (4.118) leads to the frequency equation

$$\mu^2 = \frac{1}{4H_0^2} - \left(\frac{N^2}{\vartheta^2} \frac{\sin^2 k\Delta x}{\Delta x^2} - k^2 \right). \tag{4.119}$$

The form of (4.119) is identical to (3.118), the analytic dispersion for the true frequency ϑ_T, with the substitution

$$\frac{1}{\vartheta_T^2} = \frac{1}{\vartheta^2} \frac{\sin^2 k\Delta x}{k^2 \Delta x^2}. \tag{4.120}$$

That is, the numerical value of the local frequency may be compared to its analytic counterpart ϑ_T through the relation

$$\vartheta^2 = \vartheta_T^2 \frac{\sin^2 k\Delta x}{k^2 \Delta x^2}. \tag{4.121}$$

The relative frequency of oscillations in the numerical model using second order spatial differencing may therefore be defined as

$$R_2 = \frac{\vartheta}{\vartheta_T} = \frac{\sin k\Delta x}{k\Delta x}. \tag{4.122}$$

Through a similar derivation process, one may show that the relative frequencies of oscillations in the numerical model for fourth and sixth-order differencing are respectively

$$R_4 = \frac{1}{k\Delta x} \left(\frac{4}{3} \sin k\Delta x - \frac{1}{6} \sin 2k\Delta x \right), \tag{4.123}$$

$$R_6 = \frac{1}{k\Delta x} \left(\frac{3}{2} \sin k\Delta x - \frac{3}{10} \sin 2k\Delta x + \frac{1}{30} \sin 3k\Delta x \right). \tag{4.124}$$

The relative frequencies (4.122) to (4.124) correspond exactly to (4.47), (4.53) and (4.59), the corresponding relative frequency equations for centered differencing as applied to the pure gravity waves on the nonstaggered grid. Fig. 4.3 and the discussion in section 4.3 therefore also apply to the quasi-elastic equations when discretized with centered differences on the nonstaggered grid.

4.7.2 Frequency response to vertical discretization

In order to investigate the frequency response of the quasi-elastic equations on the nonstaggered grid, it may first be noted that the linearized adjustment step equations (4.80) to (4.83) contain no vertical derivatives. Performing Fourier decomposition of the form (4.90) on (4.80) to (4.83) gives the amplitude equations

$$-i\vartheta\hat{u} = -ik\hat{\phi}, \tag{4.125}$$

$$-i\vartheta\hat{\pi} = -ik\int_0^1 \hat{u}\,d\sigma, \tag{4.126}$$

$$\hat{\dot{\sigma}} = -ik\int_0^\sigma \hat{u}\,d\sigma + i\vartheta\sigma\hat{\pi}, \tag{4.127}$$

$$-i\vartheta\hat{T}' = \kappa\left(\frac{p_0}{\sigma p_0 + p_T}\right)\left[-i\vartheta\sigma\hat{\pi} + \hat{\dot{\sigma}}\right]T_0. \tag{4.128}$$

Note once more that the integrals over σ in (4.126) and (4.127) will be treated analytically in the following analysis. By substituting (4.127) in (4.128), and by applying (4.125), the following equation for $\hat{T}'$ in terms of $\hat{\phi}'$ may be obtained:

$$\hat{T}' = \frac{k^2}{\vartheta^2}\kappa T_0\left(\frac{p_0}{\sigma p_0 + p_T}\right)\int_0^\sigma \hat{\phi}'\,d\sigma. \tag{4.129}$$

Substituting (4.129) into the linearized elliptic equation (4.95), gives the following vertical structure equation for $\hat{\phi}'$:

$$\frac{\partial^2\phi'}{\partial x^2} + \frac{\partial}{\partial\sigma}\left(s_0^2\frac{\partial\phi'}{\partial\sigma}\right) = -H_0^2\frac{N^2k^2}{\vartheta^2}\frac{d}{d\sigma}\int_0^\sigma \hat{\phi}'\,d\sigma. \tag{4.130}$$

In order to perform the frequency response analysis to vertical discretization on the nonstaggered grid, (4.130) is written in terms of Z using transformation relationships (3.114) and (C.1). The resulting equation is

$$H_0^2\frac{d^2\hat{\phi}'}{dZ^2} - H_0\frac{d\hat{\phi}'}{dZ} - k^2H_0^2\hat{\phi}' = \underbrace{-H_0^2\frac{N^2k^2}{\vartheta^2}\exp^{Z/H_0}\frac{d}{dZ}\int_{Z|_{\sigma=0}}^{Z|_\sigma}\hat{\phi}'\exp^{-Z/H_0}\,dZ}_{X}\,. \tag{4.131}$$

Equation (4.131) is the vertical structure equation for $\hat{\phi}'$ in terms of Z, it admits solutions of the form

$$\hat{\phi}' = \exp^{(im+1/2H_0)Z} \tag{4.132}$$

(see Chapter 3). The vertical derivatives in (4.131) may now be discretized and wave-like solutions of the form (4.132) substituted in the resulting equation. However, the dispersion relationship that results can not be compared directly to the analytic relationship (3.140) that applies to the undiscretized quasi-elastic equations. A more useful expression is obtained when only the right-hand side of equation (4.131), term X, is discretized. This term represents the main forcing effect to which the geopotential distribution respond.

4.7.2.1 Second order vertical differencing

Substituting wave like solutions of the form (4.132) in (4.131), and using second order differencing to approximate the vertical derivative in term X, gives the dispersion relationship

$$m^2 = -\frac{1}{4H_0^2} + \left[\frac{N^2k^2}{\vartheta^2}\left(\frac{1}{im - 1/2H_0}\right)D_{A2} - k^2\right], \tag{4.133}$$

where

$$D_{A2} = \frac{\exp^{(im-1/2H_0)\Delta Z} - \exp^{-(im-1/2H_0)\Delta Z}}{2\Delta Z}. \tag{4.134}$$

The form of (4.133) is identical to that of the analytic dispersion for the true frequency ϑ_T of the quasi-elastic equations, with the substitution:

$$\frac{1}{\vartheta_T^2} = \frac{1}{\vartheta^2}\left(\frac{1}{im - 1/2H_0}\right)D_{A2}. \tag{4.135}$$

The frequencies of gravity wave oscillations in the numerical model are therefore related to the analytical ones via the relation

$$\vartheta^2 = \vartheta_T^2\left(\frac{1}{im - 1/2H_0}\right)D_{A2}. \tag{4.136}$$

The magnitude of the relative frequency of oscillations in the numerical model using second order spatial differencing may therefore be defined as

$$R_{A2} = \left|\frac{\vartheta}{\vartheta_T}\right| = \left|\left(\frac{D_{A2}}{im - 1/2H_0}\right)^{1/2}\right|. \tag{4.137}$$

Note that D_{A2} may be written as

$$D_{A2} = \frac{\cos m\Delta Z\left(\exp^{-\Delta Z/2H_0} - \exp^{\Delta Z/2H_0}\right)}{2\Delta Z} +$$

$$\frac{i\sin m\Delta Z\left(\exp^{-\Delta Z/2H_0} + \exp^{\Delta Z/2H_0}\right)}{2\Delta Z}. \tag{4.138}$$

The magnitude of the relative frequency R_{A2} for second order differencing is displayed in Fig. 4.6 for $\Delta Z = 100\,m$ and $0 < m\Delta Z/\pi \leq 1$ (black line). It may be noted that the retardation of wave frequencies due to discretization on the nontstaggered grid is the highest for large wave numbers (shorter wave lengths). The $2\Delta Z$ wave is almost stationary. In the long wave limit, the numerical frequency of waves approaches the analytical frequency.

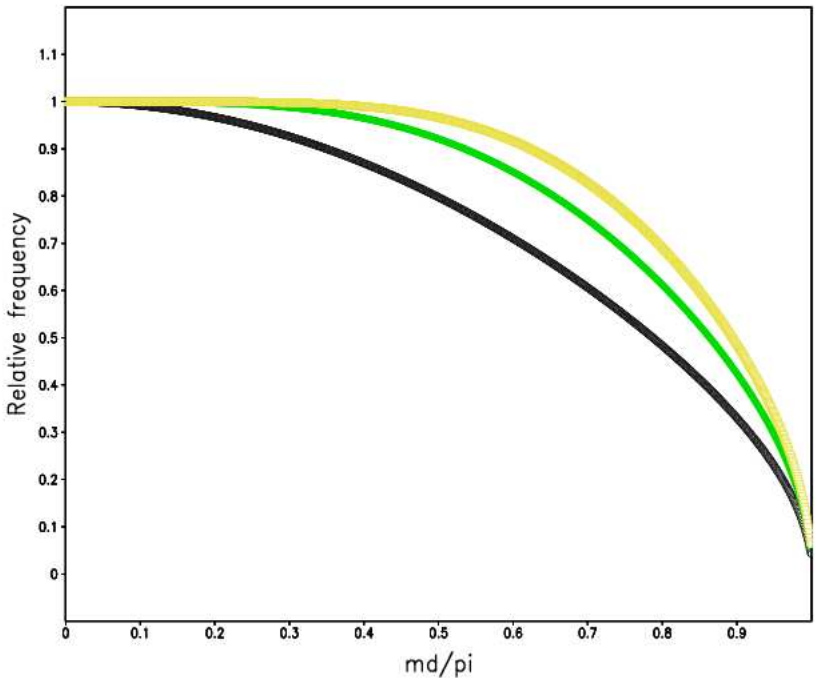

Figure 4.6: Relative frequency of the gravity waves described by the quasi-elastic equations, in response to centered finite diferencing in the vertical on the nonstaggered grid, as a function of the vertical wave number. The black, green and yellow lines represent second, fourth and sixth order differencing, respectively.

4.7.2.2 Fourth order vertical differencing

When fourth order differencing is used to approximate the vertical derivative in term X of (4.131), the resulting dispersion relationship is:

$$m^2 = -\frac{1}{4H_0^2} + \left[\frac{N^2k^2}{\Omega^2}\left(\frac{1}{im - 1/2H_0}\right) D_{A4} - k^2\right], \tag{4.139}$$

where

$$D_{A4} = \frac{1}{12}\left[\frac{\exp^{-(im-1/2H_0)2\Delta Z} - \exp^{(im-1/2H_0)2\Delta Z}}{\Delta Z}\right] +$$

$$\frac{2}{3}\left[\frac{\exp^{(im-1/2H_0)\Delta Z} - \exp^{-(im-1/2H_0)\Delta Z}}{\Delta Z}\right]. \tag{4.140}$$

The form of (4.139) is identical to that of the analytic dispersion (3.140) for the true frequency ϑ_T of the quasi-elastic equations, with the substitution:

$$\frac{1}{\vartheta_T^2} = \frac{1}{\vartheta^2}\left(\frac{1}{im - 1/2H_0}\right) D_{A4}. \tag{4.141}$$

The frequencies of gravity wave oscillations in the numerical model with fourth order spatial differencing are therefore related to the analytical ones via the relation

$$\vartheta^2 = \vartheta_T^2\left(\frac{1}{im - 1/2H_0}\right) D_{A4}. \tag{4.142}$$

The magnitude of the relative frequency of oscillations in the numerical model using fourth order spatial differencing may therefore be defined as

$$R_{A4} = \left|\frac{\vartheta}{\vartheta_T}\right| = \left|\left(\frac{D_{A4}}{im - 1/2H_0}\right)^{1/2}\right|. \tag{4.143}$$

Note that D_{A4} may be written as

$$D_{A4} = \frac{1}{12\Delta Z}\cos 2m\Delta Z\left(\exp^{\Delta Z/H_0} - \exp^{-\Delta Z/H_0}\right) +$$

$$\frac{2}{3\Delta Z}\cos m\Delta Z\left(\exp^{-\Delta Z/2H_0} - \exp^{\Delta Z/2H_0}\right) +$$

$$i\frac{1}{12\Delta Z}\sin 2m\Delta Z\left(-\exp^{\Delta Z/H_0} - \exp^{-\Delta Z/H_0}\right) +$$

$$i\frac{2}{3\Delta Z}\sin m\Delta Z\left(\exp^{-\Delta Z/2H_0} + \exp^{-\Delta Z/2H_0}\right). \tag{4.144}$$

The magnitude of the relative frequency R_{A4} for fourth order differencing is displayed in Fig. 4.4 for $\Delta Z = 100\,m$ and $0 < m\Delta Z/\pi \leq 1$ (green line). The improvement gained from fourth order differencing compared to second order differncing is the largest (about 10-20%) for short waves lengths (note that a normalized wave numer of 0.5 corresponds to the $4\Delta Z$ wave). The $2\Delta Z$ waves remain significantly retarded, howevever.

4.7.2.3 Sixth order vertical differencing

Using sixth order differencing to approximate the vertical derivative in term X of equation (4.131), the resulting dispersion relationship is:

$$m^2 = -\frac{1}{4H_0^2} + \left[\frac{N^2k^2}{\vartheta^2}\left(\frac{1}{im - 1/2H_0}\right) D_{A6} - k^2\right], \tag{4.145}$$

where

$$D_{A6} = \frac{1}{60}\left[\frac{\exp^{(im-1/2H_0)3\Delta Z} - \exp^{-(im-1/2H_0)3\Delta Z}}{\Delta Z}\right] +$$

$$\frac{3}{20}\left[\frac{\exp^{-(im-1/2H_0)2\Delta Z} - \exp^{(im-1/2H_0)2\Delta Z}}{\Delta Z}\right] +$$

$$\frac{3}{4}\left[\frac{\exp^{(im-1/2H_0)\Delta Z} - \exp^{-(im-1/2H_0)\Delta Z}}{\Delta Z}\right]. \tag{4.146}$$

The form of (4.145) is identical to that of the analytic dispersion (3.140) for the true frequency ϑ_T of the quasi-elastic equations, with the substitution:

$$\frac{1}{\vartheta_T^2} = \frac{1}{\vartheta^2}\left(\frac{1}{im - 1/2H_0}\right) D_{A6}. \tag{4.147}$$

The frequencies of gravity wave oscillations in the numerical model with sixth order spatial differencing are therefore related to the analytical ones via the relation

$$\vartheta^2 = \vartheta_T^2\left(\frac{1}{im - 1/2H_0}\right) D_{A6}. \tag{4.148}$$

The magnitude of the relative frequency of oscillations in the numerical model using sixth order spatial differencing may therefore be defined as

$$R_{A6} = \left|\frac{\vartheta}{\vartheta_T}\right| = \left|\left(\frac{D_{A4}}{im - 1/2H_0}\right)^{1/2}\right|. \tag{4.149}$$

Note that D_{A6} may be written as

$$D_{A6} = \frac{1}{60\Delta Z}\cos 3m\Delta Z\left(\exp^{-3\Delta Z/2H_0} - \exp^{3\Delta Z/2H_0}\right) +$$

$$\frac{3}{20\Delta Z}\cos 2m\Delta Z\left(\exp^{\Delta Z/H_0} - \exp^{-\Delta Z/H_0}\right) +$$

$$\frac{3}{4\Delta Z}\cos m\Delta Z\left(\exp^{-\Delta Z/2H_0} - \exp^{\Delta Z/2H_0}\right) +$$

$$i\frac{1}{60\Delta Z}\sin 3m\Delta Z\left(\exp^{-3\Delta Z/2H_0} + \exp^{3\Delta Z/2H_0}\right) +$$

$$i\frac{3}{20\Delta Z}\sin 2m\Delta Z\left(-\exp^{\Delta Z/H_0} - \exp^{-\Delta Z/H_0}\right) +$$

$$i\frac{3}{4\Delta Z}\sin m\Delta Z\left(\exp^{-\Delta Z/2H_0} + \exp^{\Delta Z/2H_0}\right). \qquad (4.150)$$

The magnitude of the relative frequency R_{A6} for sixth order differencing is displayed in Fig. 4.6 for $\Delta Z = 100\,m$ and $0 < m\Delta Z/\pi \leq 1$ (yellow line). Sixth order differencing results in an improvement of 15-25% in the representation of the frequency of short waves, compared to second order differencing. The $2\Delta Z$ wave remains significantly retarded.

More insight into the advantages of higher order differencing on the nonstaggered grid may be gained by considering Fig. 4.7. Here the relative frequencies corresponding to second (black), fourth (green line) and sixth (yellow line) order differencing are shown as a function of wavelength. $\Delta Z = 100\,m$, so that the shortest resolvable waves at this resolution have wave length $200\,m$. The red line in the figure represents the relative frequency obtained from using second order differencing with $\Delta Z = 50\,m$. It can be seen that from Fig. 4.7 that both fourth and sixth order differencing provide a significant improvement over second order differencing, particularly at short wave lengths. In fact, fourth and sixth order differencing provide more accurate results than second order differencing performed at double the resolution, for wave lengths longer than four grid lengths and three grid lengths respectively. At the shortest resolvable scales, the gravity waves are significantly retarded, for all the differencing schemes. However, it is useful to note that the two-grid-interval waves are not completely stationary as in the case of horizontal spatial differencing. Note that near the vertical boundaries of a numerical model the application of sixth or even fourth order differencing may be either impractical, or may require that artificial boundary conditions are specified.

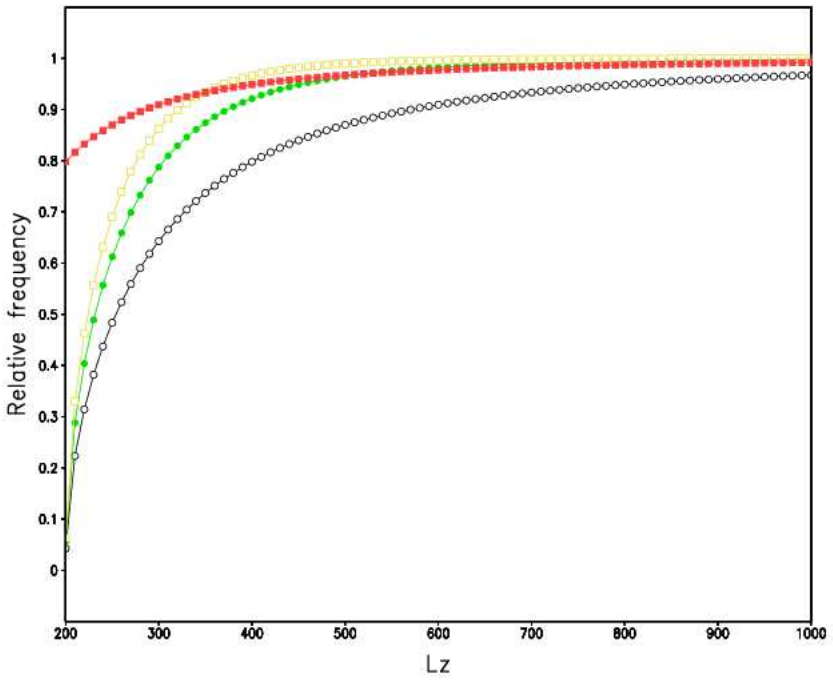

Figure 4.7: Relative frequency of the gravity waves described by the quasi-elastic equations, in response to centered finite diferencing in the vertical on the nonstaggered grid, as a function of the vertical wave length. The black, green and yellow lines represent second, fourth and sixth order differencing, respectively, with $\Delta Z = 100\,m$. The red line was obtained using second order differencing with $\Delta Z = 50\,m$.

4.8 Elliptic solvers for the diagnostic equation in the geopotential

As a final step in the adjustment procedure, the elliptic equations (3.81) and (3.86) need to be solved for three and two-dimensional applications respectively. Closely related elliptic equations are solved in the σ coordinate version of the MP equations (e.g. Xue, 1989; Xue and Thorpe, 1991) and in the anelastic σ coordinate NHAD model (Room et al., 2000). An efficient solution procedure to solve the elliptic eqution in the σ coordinate MP model was devised by Xue (1989). This method is based on the Fast Fourier Transform (FFT) technique. It involves the linerarization of certain terms in (3.81) and (3.86), and a careful consideration of the lower boundary conditions imposed on ϕ. Certain pre- and post-processing is necessary, in order to achieve maximum efficiency of the FFT subroutines (see Wilhelmson and Ericksen, 1976). A similar solution procedure was used by Room et al. (2001) to solve the elliptic equation implied by the anelastic σ coordinate equations. However, the FFT method of Xue (1989) is complicated and elaborate to code, and needs the implementation of some specific software. In the present study, where a completly new code for a new atmospheric model is developed, it was decided to rather develop an independently coded elliptic solver to solve equations (3.81) and (3.86). Successive Over-Relaxation (SOR) (see Burden and Faires, 1993), an iterative procedure, is used in the present study. This flexible technique is relatively easy to code and far more convenient to use during the development phase of a new model than the more complicated FFT techniques.

Unfortunately, the SOR method generally suffers from progressively slow convergence with the increase in model resolution, and the increase in the number of data points in the discretized elliptic operator (Xue, 1989). The efficiency of the SOR solution procedure developed in this section is discussed in Chapter 5, in the context of the numerical experiments performed in that Chapter. It is shown that the method is reasonably efficient for the tests performed, generally requiring only a few iterations per adjustment time step. Solving the elliptic equation represents a fundamental part of the computational costs of the model. It will be beneficial to implement a more efficient solution procedure, possibly based on the FFT method of Xue (1989), for the potential operational application of the model in the future. Still, it should be realized that the nature of the problem of solving the elliptic equation, namely that the solution at any point depends on all the conditions of the entire boundary, makes the numerical problem global. All the data points have to be in the core computer memory at the same instant. This will always make the solution of a three-dimensional elliptic equation expensive, even for the commercially available solvers based on transformation techniques or matrix inversion techniques based on tri-diagonalisation.

In what follows, the numerical discretization of the elliptic equation as used in the model will be discussed in two dimensions only, in order to keep the notation

simple. The extension of the solution procedure to three dimensons is obvious.

In section 4.6 equation (3.86) is linearized around an isothermal reference state of no motion to obtain (4.84). Equation (4.84) indicates that only the terms $\partial^2\phi/\partial x^2$and $\partial\left(s^2\partial\phi/\partial\sigma\right)/\partial\sigma$ are dominant in (3.86). The coefficients of the remaining terms on the left hand side of (3.86) are due to the variation of the surface pressure, and generally much smaller than those of the dominant terms (Xue, 1989). Following (Xue, 1989), the less important terms are moved to the right hand side and treated explicitly, in order to obtain a nearly standard Poison equation:

$$\left[\frac{\partial^2}{\partial x^2}+\frac{\partial}{\partial\sigma}\left(s^2\frac{\partial\phi}{\partial\sigma}\right)\right]\phi^{p+1}=L\left(\phi^p\right)+F_\phi. \tag{4.151}$$

Here 'p' denotes the p_{th} iteration,

$$L=-2\sigma\frac{\partial\ln p_s}{\partial x}\frac{\partial^2}{\partial x\partial\sigma}+\left(\frac{\partial\ln p_s}{\partial x}\right)^2\frac{\partial}{\partial\sigma}\left(\sigma^2\frac{\partial}{\partial\sigma}\right)-\frac{\sigma}{p_s}\left(\frac{\partial^2 p_s}{\partial x^2}\right)\frac{\partial}{\partial\sigma} \tag{4.152}$$

and

$$F_\phi=2\left[\frac{\partial u}{\partial x}\frac{\partial}{\partial\sigma}\left(\Omega\frac{p}{p_s}\right)-\frac{1}{p_s}\frac{\partial}{\partial x}\left(\Omega p\right)\frac{\partial u}{\partial\sigma}\right]-\frac{\partial}{\partial\sigma}\left[\left(sg\right)-\frac{1}{\gamma}\frac{p}{p_s}\Omega^2\right]. \tag{4.153}$$

Note that s in (4.153) is not linearized over x, as in the corresponding equation used by Xue (1989).

4.8.1 Spatial discretization

By discretizing the terms in (4.151) using the second order accurate differencing formulas (4.27) and (4.35), an iterative solution procedure of (4.151) based on SOR may be constructed (see Burden and Faires (1993) for a discussion of the SOR technique). This solution procedure will be referred to as the "second order solver" in the remainder of the text.

When the first derivatives in the adjustment step terms (section 4.5) are evaluated by using the fourth order spatial differencing operator (4.28), inconsistencies with the second order discretization of (4.151) leads to divergence of the SOR procedure (this was established while conducting the numerical experiments described in Chapter 5). Therefore, a "fourth order solver" was developed, where (4.151) is discretized using the fourth order accurate operators (4.28) and (4.36), and then solved iteratively using SOR. Because the spatial derivatives in the adjustment step and in the fourth order solver are evaluated consistently in this case, the SOR procedure in the fourth order solver was found to be convergent.

Similarly, a sixth-order discretization of the spatial derivatives in the adjustment step would be inconsistent with both the second and fourth order solvers, and divergence of the SOR procedure would occur. A sixth order solver needs to be constructed using the operatores (4.30) and (4.37), to obtain the convergence of iterations for the case of a sixth order discretization of the adjustment step terms. However, such a high-order solver is elaborate and cumbersome to code, and the SOR technique generally suffers from slower convergence if the number of data points in the discretized operator increases (Xue, 1989). Therefore, an elliptic solver beyond fourth order discretization was not constructed in this study.

4.8.2 Convergence of iterations

The criterion of convergence of iterations is

$$\frac{\sqrt{\Sigma_{i,j}\left(\phi^{p+1}-\phi^{p}\right)^{2}}}{\sqrt{\Sigma_{i,j}\left(\phi^{p+1}\right)^{2}}}<\epsilon$$

with $\epsilon = 10^{-6}$ being used in the model, except in the initialization step where $\epsilon = 10^{-6}/5$ is required for sufficient convergence of the solution. In the experiments described in Chapter 5, a relaxation coefficient $rl = 1.9$ (see Burden and Faires, 1993) was found to generally result in the fastest convergence. The efficiency of the elliptic solver and the convergence of iterations are discussed in more detail in Chapter 5.

4.9 Boundary conditions

In this section, lateral and vertical boundary conditions are formulated for the new model based on the split semi-Lagrange solution of the quasi-elastic equations. These boundary conditions are suitable for the series of numerical tests performed in Chapter 5. For more general, real-atmosphere applications of the model, the lateral boundary conditions in particular would need some modification (see the discussion in section 4.9.1). The boundary conditions are applied after each adjustment step in the solution procedure. The boundary conditions are stated for three-dimensional applications of the new model, the simplifications needed for two-dimensional applications are obvious.

4.9.1 Lateral boundary conditions

Unless stated otherwise for a specific experiment, the lateral boundary conditions used in the model in order to perform the numerical experiments described in Chapter 5 are:

$$\frac{\partial \ln p_s}{\partial x}=\frac{\partial \ln p_s}{\partial y}=0, \tag{4.154}$$

$$\frac{\partial T}{\partial x} = \frac{\partial T}{\partial y} = 0, \tag{4.155}$$

$$\frac{\partial \phi}{\partial x} = \frac{\partial \phi}{\partial y} = 0, \tag{4.156}$$

$$u = v = 0, \tag{4.157}$$

$$\frac{\partial \dot{\sigma}}{\partial x} = \frac{\partial \dot{\sigma}}{\partial y} = 0, \tag{4.158}$$

$$\frac{\partial \Omega}{\partial x} = \frac{\partial \Omega}{\partial y} = 0. \tag{4.159}$$

No-stress boundary conditions are imposed on the velocity field, which imply at the lateral boundaries that the horizontal derivatives of $\dot{\sigma}$ and the horizontal velocity field vanish (4.157 and 4.158). It is assumed that the horizontal derivatives of p_s, T and ϕ vanish at the lateral boundaries (4.154 to 4.156). From (4.154) and (4.158) it follows by the use of (3.69) that the horizontal derivatives of Ω will also vanish at the lateral boundaries (4.159).

At the lateral boundaries, the transformed surface pressure p_s and vertical velocity $\dot{\sigma}$ may alternatively be calculated from the continuity equation, similar to the approach followed by Xue and Thorpe (1991). The lateral boundary condition $u = v = 0$ is limiting in the sense that flow is not allowed through the lateral boundaries. For typical atmospheric flows in the westerly wind-regime, there is a zonal wind component that causes an inflow at the western boundary and an outflow at the eastern boundary. At the outflow boundary there is the possibility of developing numerical reflection, i.e. a numerical wave may unphysically interact with the boundary and energy in the numerical flow may travel backwards. An experiment with non-zero flow over the lateral boundaries is performed in section 5.6, however, the lateral boundaries are chosen to be far away from the flow features of interest in order to avoid potential boundary reflection problems. Careful consideration of the lateral boundary reflection problem will be required for real-atmosphere applications of the model. For such applications, lateral boundary conditions may be obtained from a forcing model that runs over a larger domain at lower resolution, that is, from a standard nesting procedure. An alternative suitable for some applications, would be to apply the radiative boundary condition (Orlanski, 1976) to the horizontal velocity field, the temperature T and transformed surface pressure p_s, following Xue and Thorpe (1991) and Miller and Thorpe (1981).

4.9.2 Lower and upper boundary conditions

The lower boundary of the model ($\sigma = 1$) is the ground surface. The model top ($\sigma = 0$) where $p = p_T = constant$ is a free surface, where external gravity waves are supported. The lower and upper boundary conditions for the various variables may be specified as follows:

4.9.2.1 Temperature field

At the top and bottom surfaces, a zero vertical gradient boundary condition is imposed on the potential temperature θ, that is, $\partial\theta/\partial\sigma = 0$. From this condition and the potential temperature definition

$$\theta = T\left(\frac{p_{STAN}}{p}\right)^{R/c_p}, \tag{4.160}$$

it follows that that in terms of the temperature field

$$T|_{\sigma=1} = T|_{\sigma=1-\Delta\sigma}\left[\frac{p_s + p_T}{(1-\Delta\sigma)\,p_s + p_T}\right]^{R/c_p} \tag{4.161}$$

and

$$T|_{\sigma=0} = T_{\sigma=\Delta\sigma}\left(\frac{p_T}{\Delta\sigma p_s + p_T}\right)^{R/c_p}, \tag{4.162}$$

for the lower and upper boundaries respectively. Note that p_s is the augmented surface pressure, whilst p_{STAN} denotes a standard reference pressure level. Equations (4.161) and (4.162) are applied as boundary conditions on the temperature field in the model.

It is worthwhile to note that, from the definition of potential temperature,

$$\frac{\partial\theta}{\partial\sigma} = 0 \Rightarrow \frac{\partial T}{\partial\sigma} = \frac{1}{c_p}\frac{p_s}{p}RT. \tag{4.163}$$

4.9.2.2 Geopotential field

The lower boundary condition imposed on ϕ is simply

$$\phi|_{\sigma=1} = h\,(x,\,y)\,g, \tag{4.164}$$

with $h(x, y)$ the actual terrain height and g is the gravitational acceleration defined earlier. Note that in the case of zero surface topography, condition (4.164) implies that $\phi|_{\sigma=1} = 0$.

Assuming hydrostatic balance and integrating over the top model layer gives:

$$\phi|_{\sigma=0} - \phi|_{\sigma=\Delta\sigma} = -R \int_{\sigma=\Delta\sigma}^{0} \frac{p_s}{p} T \, d\sigma \tag{4.165}$$

The assumption of hydrostatic balance over the top model layer is consistent with the linear analysis of the quasi-elastic equations discussed in Chapter 3. Integrating (4.163) over the top model layer, where $\partial\theta/\partial\sigma = 0$, gives:

$$T|_{\sigma=0} - T|_{\sigma=\Delta\sigma} = \frac{R}{c_p} \int_{\sigma=\Delta\sigma}^{0} \frac{p_s}{p} T \, d\sigma. \tag{4.166}$$

Combining (4.163) and (4.166) yields the upper boundary condition on ϕ that is used in the model:

$$\phi|_{\sigma=0} = \phi|_{\sigma=\Delta\sigma} - c_p \left(T|_{\sigma=0} - T|_{\sigma=\Delta\sigma} \right). \tag{4.167}$$

The vertical boundary conditions imposed on ϕ are much simpler than those used in σ coordinate numerical realizations of the MP and NHAD models, where the use of a reference geopotential profile induces a more complicated treatment (Xue and Thorpe, 1991; Room et al., 2001). The anelastic σ coordinate equations of Room et al. (2001) require additional careful treatment of the vertical boundary conditions imposed on ϕ, in order to ensure mass conservation in the model.

4.9.2.3 Velocity field

The no-stress boundary conditions imposed on the velocity field imply at the vertical boundaries ($\sigma = 1$ and $\sigma = 0$) that the vertical derivative of the horizontal wind is assumed to vanish. By definition, $\dot{\sigma} = 0$ at $\sigma = 1$ and $\sigma = 0$. In equation form, the vertical boundary conditions imposed on the velocity field are:

$$\dot{\sigma}|_{\sigma=1} = \dot{\sigma}|_{\sigma=0} = 0 \tag{4.168}$$

and

$$\frac{\partial u}{\partial \sigma}|_{\sigma=0} = \frac{\partial u}{\partial \sigma}|_{\sigma=1} = \frac{\partial v}{\partial \sigma}|_{\sigma=0} = \frac{\partial v}{\partial \sigma}|_{\sigma=1} = 0. \tag{4.169}$$

Vertical boundary conditions also need to be specified for variable $\Omega = \omega/p$. At the model top (a fixed pressure level),

$$\Omega|_{\sigma=0} = 0,$$

whilst the lower boundary condition on $\dot{\sigma}$ (4.168) implies that

$$\Omega|_{\sigma=1} = \left(\frac{p_s}{p_s + p_T} \frac{D \ln p_s}{Dt} \right),$$

by (3.69).

4.10 Comparison of the split semi-Lagrangian scheme to the numerics of the MP and NHAD models

It is useful to compare the properties of the split semi-Lagrangian procedure used to solve the quasi-elastic equations to those of the numerical methods used in the closely related σ coordinate MP and NHAD models:

- The split semi-Lagrangian scheme is formulated as a two time-level scheme, which implies that no computational modes are present, and there is no need for time-filtering. The explicit leap-frog scheme is applied in the σ coordinate numerical realizations of the MP and NHAD models (e.g. Xue and Thorpe, 1991; Miranda and James, 1992; Room et al., 2001). The leap-frog scheme is a three time-level scheme, and requires the use of a time filter in order to prevent decoupling of the numerical solution in time. The Robert-Asselin filtering technique (Robert, 1966; Asselin, 1972) is applied in the MP and NHAD models for this purpose (Xue and Thorpe, 1991; Miranda and James, 1992; Room et al., 2001).

- The MP and NHAD models employ a flux formulation of the relevant σ coordinate equations, whilst the advective formulation of the quasi-elastic equations is used for formulating the split semi-Lagrangian procedure.

- Eulerian procedures are used in the MP and NHAD models. This, in combination with the leapfrog-scheme for time integration, yields that the MP and NHAD models are stable under the CFL condition. This implies a restriction on the maximum size of time-step that may be used in these models. The split semi-Lagrangian procedure offers a computationally more efficient procedure. Courant numbers larger than unity (associated with relatively large time steps) may occur during the semi-Lagrangian advection step, without a compromise of numerical stability (see section 4.2 and Chapter 5). However, the presence of fast travelling gravity and Lamb waves limits the maximum size of the time-step that may be used in the adjustment step. It may be noted that the absence of Lamb waves in the NHAD model significantly alleviates the restrictions on the maximum size of time-step allowed in this model.

- The C-grid (e.g. Mesinger and Arakawa, 1976; Arakawa and Lamb, 1977) is used in the MP and NHAD models (Xue and Thorpe, 1991; Room et

al., 2001). The split semi-Lagrangian scheme is formulated on a grid that is nonstaggered in both the horizontal and vertical (the Arakawa A grid).

- The quasi-elastic σ coordinate equations are formulated independent of a thermodynamic reference profile (see Chapter 3), and the split semi-Lagrangian procedure is also formulated free of the use of a reference profile. In the MP and NHAD models, the temperature and geopotential fields are formulated as deviations of a thermodynamic reference profile. Since the reference profile depends on pressure that may be changing as a function of time on the σ levels, the reference profile needs to be updated at regular time intervals (see Xue and Thorpe, 1991). Additonally, the use of a reference geopotential profile complicates the solution of the elliptic equation for the geopotential deviation in the MP-models (Xue and Thorpe, 1991).

- In the numerical realizations of the σ coordinate MP-model, the vertical momentum equation is used explicitly for the calculation of the vertical motion field. In nonhydrostatic meso-scale circulation systems, the horizontal and vertical velocities are often of the same scale of magnitude. Under these circumstances, it may be advantageous to discretize the horizontal and vertical momentum equations in a similar fashion, by calculating both the horizontal and vertical motion fields directly from these equations. However, during the early development stage of the new numerical model developed in this study, it was attempted to use the vertical momentum equation explicitly to calculate the vertical motion field by means of an advection and adjustment step (silmilar to the approach presently used to calculate the horizontal wind). It was found that the calculation of the vertical motion field in this fashion, and the calculation of the surface pressure by means of the continuity equation, leads to an important inconsistency in the split semi-Lagrange procedure. Therefore, in the present version of the split semi-Lagrangian scheme, the vertical motion and surface pressure are calculated consistently from the continuity equation. The vertical momentum equation is not used explicitly, but is incorporated in the elliptic equation used to diagnose the geopotential. In the NHAD-model, the vertical motion field is also diagnosed from the continuity equation. However, in the latter model there is no prognostic eqution for the surface pressure (Room et al., 2001; also see Chapter 2). The approach in the split semi-Lagrangian scheme to obtain $\dot{\sigma}$ and p_s consistently from the continuity equation bears close resemblance to the solution procedure followed in hydrostatic σ coordinate models. This facilitates the development of a hydrostatic global or regional model to a nonhydrostatic model based on the quasi-elastic equations.

- In the σ coordinate MP and NHAD models, the elliptic equation for the geopotential is solved by an intricate procedure involving a Fast Fourier Transform method (Xue, 1989; Xue and Thorpe, 1991; Room et al., 1991; also see section 4.6). Some general software is required for this purpose

(Xue, 1989). During the development phase of the new model in the present study, it was thought best to have an independently coded elliptic solver available. A SOR procedure was therefore developed to solve the elliptic eqution in the geopotential, in two or three spatial dimensions (see section 4.6). This procedure is reasonably efficient (see Chapter 5), but it may be advantageous to implement a FFT method in the model for more efficient solution of the elliptic equation in the future.

4.11 Discussion

Chapter 4 reports on the development of a novel split semi-Lagrangian scheme formulated to solve the quasi-elastic σ coordinate equations on a nonstaggered grid. The main features of the new dynamic kernel are:

- nonhydrostatic, quasi-elastic formulation using a terrain-following coordinate based on the full pressure field;
- two time-level, time-split time integration scheme involving an advection, adjustment, spatial filtering and spatial smoothing step;
- spatial discretization on a horizontally and vertically nonstaggered grid;
- semi-Lagrangian advection for the horizontal wind, surface pressure and temperature, using McGregor's method for the calculation of departure points and bicubic spatial interpolation;
- high-order accurate centered differencing on the nonstaggered grid;
- high-order, highly scale-dependent Shapiro spatial filtering;
- option of explicit diffusion available;
- consistent evaluation of the surface pressure and vertical motion field by using the continuity equation;
- semi-implicit treatment of the Coriolis terms;
- three-dimensional iterative solution of a variable-coefficient, non-linear elliptic equation for the geopotential at each adjustment time-step, using SOR.

A distinguishing feature of the split semi-Lagrangian scheme, is its formulation on a nonstaggered grid. This set-up is very attracive from a computational point of view, since only one set of departure points needs to be calculated at each advection step of the model. However, it is well-known that the nonstaggered grid has poor gravity wave dispersion properties (see sections 4.3 and 4.8). These may be improved by the use of high-order spatial differencing on the nonstaggered grid (sections 4.3 and 4.8). However, the presence of stationary two-grid-interval waves remain problematic. These waves are filtered with

a high-order spatial Shapiro filter (see sections 4.4 and 4.5.3). This filter has a negligible damping effect at longer wave lengths, but completely removes the two-grid-interval waves. The explicit diffusion step (section 4.5.4) is not required for numerical stability considerations, but may be needed in order to obtain a grid-converged solution (see section 4.5.4 and Chapter 5).

A traditional stability analysis (see Mesinger and Arakawa, 1976) of the adjustment step of the split semi-Lagrangian scheme has not been presented in this Chapter. There appears to be no straight forward way to find an analytic result in this regard, because of the complicated nature of the σ coordinate quasi-elastic equations. However, for the case of linear advection, the semi-Lagrangian procedure used in the advection step is known to be unconditionally stable (see section 4.2). The frequency response of the adjustment step equations to the forward-backward scheme (see section 4.7) also provides some indication of how the gravity waves function to limit the maximum size of time step that may be used in the adjustment step. In Chapter 5 the stability properties of the full scheme are examined by means of numerical experiments. It is shown that the split semi-Lagrangian scheme is stable at large Courant numbers during the advection step. Fast travelling gravity and Lamb waves limit the size of the time-step that can be used in the adjustment procedure. The large time-steps allowed during the advection step, represent the main computational advantage of the split semi-Lagrangian scheme over the explicit procedures used in the MP and NHAD models. In fact, the split semi-Lagrangian approach may even in some cases offer computational advantages over the widely used, highly efficient, semi-implicit time differencing schemes.

In recent years, semi-implicit time integration schemes (e.g. Robert, 1969; Tapp and White, 1976) have become very popular for use in NWP and climate simulation models (e.g. Cullen, 1990; Tanguay et al., 1990; McGregor and Dix, 2001; Davies et al., 2005). This popularity is to a large extent linked to the development of models based on the fully-elastic, non-hydrostatic equations. These models contain acoustic waves as part of their solution set (see Chapter 1). The semi-implicit schemes neutralize the computational disadvantage caused by the presence of acoustic waves in the fully-elastic equations, without compromising the treatment of motion at spatial scales relevant to current NWP and climate simulation (Tapp and White, 1976; Tanguay et al., 1990, Davies et al., 2005). However, the stability of semi-implicit schemes at long time steps is achieved by spuriously retarding the fast-propagating acoustic and gravity waves responsible for the time step limitations of explicit schemes (e.g. Davies et al., 2003). For high-resolution, meso-scale applications of a nonhydrostatic model, the fast propagating gravity waves may be important in their own right, and the time-step used in a given semi-implicit scheme may have to be shortened in order to represent the dynamics and physics of the motion properly (e.g. Davies et al., 2003). Thus, the time-step advantage offered by semi-implicit schemes over explicit schemes would be lost. It is for cases such as

these where split semi-Lagrangian formulations may provide the most appealing choice of time integration scheme, from the perspective of computational efficiency. Even for situations where the fast moving gravity waves carry a non-negligible amount of the energy, the split semi-Lagrangian approach allows the use of relatively large time steps for the simulation of the much slower advection process. The fast moving gravity and sound waves may be accurately treated during the adjustment procedure involving a much smaller time-step. However, the explicit schemes and semi-implict schemes would be limited to the use of small time-steps, because of stability and accuracy considerations respectively.

At larger spatial scales, where the fast moving gravity waves are not important in their own right and may be parameterized (for orographic gravity waves, in the case of numerical weather prediction and climate simulation), semi-implicit time integration offers computational advantages over the split semi-Lagrangian approach. In the latter case, the adjustment step would be limited to relatively small values because of the presence of the fast moving gravity and sound waves. However, the semi-implicit schemes will be stable at much larger time steps because of the spurious retardation of the fast-moving waves by these schemes. Thus, the potential computational advantages of the split semi-Lagrangian approach are limited to high-resolution micro and meso-scale studies where the accurate representation of fast-moving gravity waves is important.

The split semi-Lagrangian scheme may also offer a computational advantage over traditional split-explicit procedures where Eulerian discretization is used for the advection terms. Janjic (2001) stated that the advection step in (Eulerian) time-split solutions of the atmospheric equations used in numerical weather prediction is limited by the CFL condition to values of about three times the adjustment time-step. This is beacuse the wind speed can exceed $100\,ms^{-1}$, compared to the speeds of up to $300\,ms^{-1}$and $350\,ms^{-1}$for gravity and sound waves respectively. However, the statement of Janjic does not hold when a split semi-Lagrangian method is used to solve the advection terms in the governing equations. The linear analysis in section 4.2 (following McDonald, 1984) indicates that the semi-Lagrangian scheme applied in the present study is unconditionally stable for the case of linear advection. The numerical results shown in Chapter 5 for highly non-linear flow illustrate that when the time-split method employs a semi-Lagrangian approach to solve the advection terms, advection time-steps at Courant numbers larger than unity may be used, without comprimising the numerical stability of the scheme. This yields a computational advantage over Eulerian split-explict schemes.

Chapter 5

Numerical experiments with the split semi-Lagrangian formulation of the quasi-elastic equations

5.1 Introduction

In the previous two Chapters a dynamic kernel for a new, nonhydrostatic meso-scale model was developed. The kernel consists of a split semi-Lagrangian formulation of the quasi-elastic σ coordinate equations on a nonstaggered grid. In this Chapter, numerical simulations of highly nonhydrostatic flow are performed with the new kernel. These are in the form of micro- to meso-scale buoyancy driven flows, in two and three spatial dimensions. There are two main objectives with the numerical tests presented here:

- to demonstrate that important nonhydrostatic processes are described by split semi-Lagrangian formulation of the quasi-elastic σ coordinate equations. However, the study of the nonhydrostatic processes themselves fall beyond the scope of the present study. Still, some interesting flow features are indicated and described, with the view on the future application of the new model to the study of nonhydrostatic circulation systems;

- to investigate the accuracy, stability and efficiency characteristics of the split semi-Lagrangian scheme.

It has become standard procedure to test nonhydrostatic models by performing the so called "bubble convection" and "mountain wave" experiments. In the typical bubble convection tests, an elliptically shaped disturbance in the

potential temperature is introduced to an isentropic, hydrostatic and dry atmosphere. The buoyant bubble initiates the formation of a density current, and highly nonhydrostatic and nonlinear flow results. Being of no relevance to the study of bubble convection, the Coriolis effect is neglected in these tests. The present chapter commences by reporting on a large set of two-dimensional bubble convection experiments performed with the split semi-Lagrangian scheme (sections 5.2 and 5.3). The experiments may be devided into cold bubble tests (e.g. Droegemeier and Wilhelmson, 1987; Straka et al., 1993) and warm bubble tests (e.g. Droegemeier, 1985; Mendez-Nunez and Carroll, 1994; Gallus and Rancic, 1996), depending on the nature of the initial potential temperature disturbance. The nonhydrostatic processes simulated in convective bubble experiments require the use of model resolutions as fine as 100 m, in both the horizontal and vertical. Typically, thousands or tens of thousands of time steps are required to complete the simulations. Experiments such as these have therefore traditionally been performed in two spatial dimensions, because of the high computational costs involved. Another advantage of working in two dimensions, is that present-day computers have enough speed and memory so that grid-converged numerical solutions for nonlinear two-dimensional problems can be obtained (see Straka et al., 1993). This facilitates the comparison of results obtained with different equation sets and numerical methods when applied to the same flow problem.

After satisfactory performance of the scheme in two spatial dimensions has been illustrated, three-dimensional bubble convection experiments are performed to illustrate that the three-dimensional version of the scheme also performs well (sections 5.4 and 5.6). However, because of the huge computational costs of three-dimensional simulations, these experiments were performed at lower spatial resolutions. The three-dimensional simulations may be compared to the corresponding two-dimensional tests. No grid-converged solutions of the three-dimensionals flow problems are available in literature, however. In fact, there appear to be no reports in literature on three-dimensional simulations of bubble convection. It may be noted that an interesting new bubble convection experiment was designed to test the performance of the new kernel in three spatial dimensions (see section 5.6). In this experiment, a warm bubble is inserted into an isentropic environment with strong vertical wind-shear. The results obtained show close correspondence to the linear theory of storm-splitting, confirming the suitability of using the split semi-Lagrangian formulation of the quasi-elastic equations to simulate highly nonhydrostatic flow in three spatial dimensions.

The numerical experiments performed are also used to investigate the accuracy, stability and efficiency properties of the split semi-Lagrangian scheme. It is shown that the scheme allows the use of large time-steps (implying large Courant numbers) during the advection step of the solution procedure. This implies a computational advantage over explicit solution procedures applied to the quasi-elastic (or fully-elastic) equations. At high spatial resolution, where small time-

steps are needed to accurately represent the gravity-wave processes, a relatively large advection time-step may still be used without compromising the overall accuracy of the scheme. This implies a computational advantage over semi-implicit formulations, where the small time-step needed to accurately represent the gravity-wave processes is also used for the advection step. An important part of the overall computational efficiency of the split semi-Lagrangian procedure, involves solving the elliptic equation (3.81 or 3.86) at each advection time-step. It is shown by a series of numerical tests that the SOR procedure described in Chapter 4 is reasonably efficient to use for this purpose.

The experiments in this section were performed using an Intel Pentim IV 3000 MHz personal computer with 512 Mram, or on even smaller computers. Although quite suitable for two-dimensional tests, the available computing power and memory limited the three-dimensional tests in the present study to relatively low spatial resolutions. For the typical size of domain needed for the three-dimensional bubble convection and mountain wave tests, the best spatial resolution that could be afforded was about 500 m in the horizontal, and about 100 m in the vertical.

5.2 Cold bubble experiments in two spatial dimensions

5.2.1 Design of the cold bubble tests

The experiments in this section are patterned after the two-dimensional cold bubble downburst problem described by Droegemeier and Wilhelmson (1987) and Straka et al. (1993). In an initially dry, at rest and isentropic atmosphere with potential temperature 300 K, an elliptically-shaped initial disturbance is introduced for the temperature:

$$\Delta T_0(x,z) = -15\cos^2(\frac{\pi}{2}r), \tag{5.1}$$

for $r \leq 1$, where, $r^2 = [(x-x_c)/x_t]^2 + [(z-z_c)/z_t]^2$, $x_c = 0$ m, $z_c = 3000$ m, $x_t = 4000$ m and $z_t = 2000$ m.

The integration domain extends over $-20000\,m \leq x \leq 20000\,m$ in the horizontal. The top of the model domain is chosen to be 442 hPa (about 6400 m). The center of the initial disturbance is in the middle of the domain in the x direction, that is, 20 km away from the lateral boundaries. Unless where stated differently, the horizontal resolution used in the following experiments is 100 m, and 65 equally spaced σ levels are used to give a vertical resolution of about 100 m on the average. Cold bubble experiments have been widely used to test the performance of z coordinate nonhydrostatic models (e.g. Straka et al., 1993; Wicker and Skamarock, 2002). Fairly recently, similar experiments were

performed using terrain-following pressure-based coordinate models (Gallus and Rancic, 1996; Janjic et al., 2001).

5.2.2 Initialization procedure

For all the bubble convection experiments discussed in this chapter, the initial environment is dry, isentropic and in hydrostatic balance. For such an environment the temperature lapse rate is dry adiabatic, and the temperature T_{env} is specified as a function of geometric height by

$$T_{env} = T_{surf\_env} - \frac{g}{c_p} z. \tag{5.2}$$

Here $T_{surf\_env} = 300\,K$ is the surface temperature of the environment. For model initialization, the environmental temperature and geopotential height are needed at each σ level of the model. The potential temperature of the isentropic environment is defined by

$$\theta_{env} = T_{surf\_env} = T_{env} \left(\frac{p_{surf\_env}}{\sigma p_{s\_env} + p_T} \right)^{R/c_p}. \tag{5.3}$$

Substituting for T_{env} in (5.2) by using (5.3) it may be shown that geometric height of each σ level may be calculated from

$$z = \frac{c_p}{g} T_{surf\_env} \left[1 - \left(\frac{\sigma p_{s\_env} + p_T}{p_{surf\_env}} \right)^{R/c_p} \right]. \tag{5.4}$$

Here $p_{surf\_env} = 1000\,hPa$ is the surface pressure of the hydrostatic environment and $p_{s\_env} = p_{surf\_env} - p_T$. Once z is known from (5.4) at each σ level, the corresponding environmental temperature field may be calculated from (5.2). The initial geopotential distribution is given by $\phi = gz$.

To provide positive or negative buoyancy and initiate a density current, a temperature perturbation ΔT, as specified for each particular set of bubble convection experiments, is added to the temperature field. In some experiments the perturbation is specified in terms of the potential temperature, from which ΔT may be evaluated.

In bubble convection experiments performed in z coordinates with the fully compressible equations, the pressure and density fields need to be adjusted towards the perturbed temperature field to obtain an initial state that avoids the generation of strong shock waves in the first time-steps (Droegemeier, 1985; Mendez-Nunez and Carroll, 1994). This may be achieved by a procedure that involves integrating the hydrostatic equation in the vertical at each grid point, to obtain an initial state that is in perfect hydrostatic balance (see Carroll et al.,

1987). For the σ coordinate equations solved in the present paper, a different procedure is followed. Here the natural choice to obtain a balanced initial state is to adjust the geopotential field towards the perturbed temperature field. This is achieved by solving (3.86), or (3.81) for the bubble convection experiments in three spatial dimensions, iteratively for the geopotential ϕ. The right-hand side of (3.81) or (3.86) is determined by the initial state of all the variables, for general applications of this initialization procedure. In the case of the bubble convection experiments, however, the perturbed temperature field is the only initial field with a non-zero forcing effect on the right-hand side of (3.81) or (3.86). Equation (5.4) is used to obtain an initial guess for ϕ in the form $\phi = gz$. This type of initialization procedure, where the geopotential distribution on σ levels is adjusted towards the (observed) initial values of variables on σ levels, is perhaps the most natural choice of initialization for a pressure-based atmospheric model. As an alternative to using (3.86) or (3.81) in order to obtain an balanced initial state, it would be possible to integrate the σ coordinate form of the hydrostatic equation in the vertical, in order to obtain a balanced state in perfect hydrostatic balance. However, since the vertical momentum equation is not used explicitly in the split semi-Lagrangian solution procedure, it seems to be more natural to use (3.86) and (3.81) for the purpose of initialization.

The main effect of the initialization procedure when applied to the convective bubble tests, is that the geopotential field reacts to the temperature profile of a given column of air. For the cold bubble experiments the free surface at the model top $\sigma = 0$, above the center of the bubble after initialization, is lower than the value implied by (5.4), with the opposite being true for the warm bubble experiments. In this way, the constant surface pressure is physically consistent with the temperature and geopotential fields, with the less dense (warmer) columns of air occupying larger volumes than the relatively more dense (colder) columns. Another consequence of the initialization procedure is that the geometric height of the bubble after initialization is slightly different to the value specified originally for a particular temperature perturbation ΔT. The initialization procedure is illustrated in Fig. 5.1. The figure shows the geopotential perturbation from the initial state implied by (5.3), obtained iteratively from the SOR procedure (see Chapter 4), using as criterion of convergence $\epsilon = 10^{-5}$ (Panel a), $\epsilon = 10^{-6}$ (Panel b), $\epsilon = 10^{-6}/5$ (Panel c) and $\epsilon = 10^{-7}$ (Panel d). Clearly, the solution is converged for for $\epsilon = 10^{-6}/5$, but not sufficiently converged for $\epsilon = 10^{-6}$ or smaller. A relaxation factor of $rl = 1.9$ was used in the SOR procedure. With this relaxation factor, 562 iterations are needed to satisfy a convergence criterion of $\epsilon = 10^{-6}/5$. The convergence criterion 10^{-7} is not met, even after 15 000 iterations. By trial and error it was established that for values of rl less than 1.9, more iterations are needed before the convergence criterion $10^{-6}/5$ is met. After the initialization step, a convergence criterion of 10^{-6} was found to be sufficient for convergence during the time-integration of the model. A relatively small amount of iterations are then needed to solve (3.81) or (3.86) during each adjustment step of the split semi-Lagrangian solu-

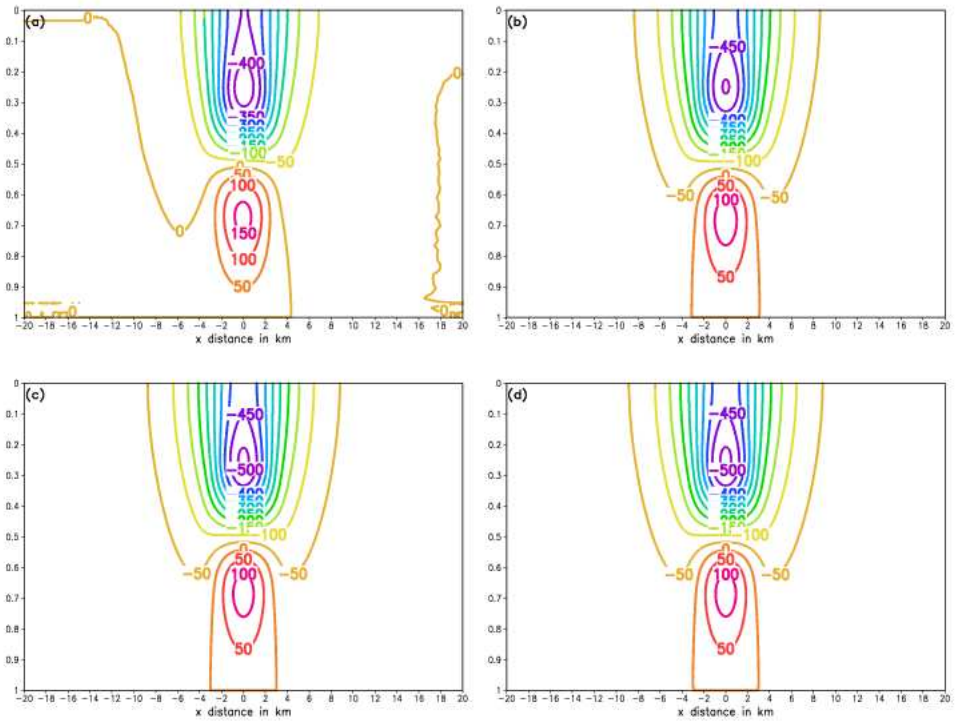

Figure 5.1: Initialization procedure for the two-dimensional cold bubble test. Perturbation from the geopotential distribution corresponding to the hydrostatic, isentropopic environmental state, for $0 \leq \sigma \leq 1$: using as condition of convergence (a) $\epsilon = 10^{-5}$; (b) $\epsilon = 10^{-6}$; (c) $\epsilon = 10^{-6}/5$; (d) 10^{-7}. The contour interval is 50 gpm.

tion procedure (see section 5.2.10).

It should finally be noted that in the practical application of the model to bubble convection experiments, there is no need for an explicit initialization step. The initialization procedure may effectively be carried out at the end of the first adjustment step, when (3.81) or (3.86) is solved for the first time. Since the interpolations involved in the advection step are performed in σ space, there is no need to have the initialized ϕ distribution available in the solution procedure before integrating the horizontal momentum equation(s) during the first adjustment step. Finding the horizontal wind in the first adjustment step from using ϕ as specified by (5.4), instead of using the initialized ϕ distribution, has a negligible effect on the simulations. However, this approach is strictly speaking unphysical, since the geopotential distribution implied by (5.4) belongs to an isentropic, hydrostatic atmosphere, and not to the true initial state that contains the buoyant bubble. Still, this unphysical situation is quickly brought into physical balance, when (3.81) or (3.86) is solved for the first time. In all the experiments reported in this chapter, however, an explicit initialization step was used. This is strictly speaking the correct procedure to apply, since all the fields are in physical balance after initialization. This approach is preferable for more general, real atmosphere applications of the model, for example to initial states that may contain heterogeneous wind fields. In all the experiments performed, the initialization procedure was found to work well, and no strong shock waves are observed to be generated during the first few time-steps of the model.

5.2.3 A reference solution for the cold bubble test

In the reference cold bubble simulation presented here, the D_3 scheme with two-dimensional $(x-\sigma)$ bicubic spatial interpolation is used in the semi-Lagrangian advection step. The spatial derivatives required in the calculation formula for the departure points (x^*, σ^*) (see Chapter 4) are evaluated using centered second order differencing. Centered second order differencing is also used to calculate the quantity $A^*_{p_s}$ and to discretize the spatial derivatives in the adjustment step equations. The advection time-step used is $\Delta t_s = 1\,s$ and the adjustment time-step $\Delta t_a = 0.1\,s$. The Shapiro filter is not used. The values of the diffusion coefficients used in the explicit diffusion step, for diffusion along the x axis, are $K_s = 75\,m^2 s^{-1}$ and $K_{Ts} = 75\,m^2 s^{-1}$. Diffusion of similar magnitude is applied along the σ axis for u. This is achieved by choosing $K_\sigma = K_s\left(\Delta\sigma^2/\Delta x^2\right)$, so that the non-dimensional quantity $K\Delta t_s/\Delta n^2$ defined in Chapter 4 has the same magnitude along both the x and σ axis (see Janjic et al., 2001). Diffusion of about double the magnitude of that used along the x axis is applied along the σ axis for T, by choosing $K_{T\sigma} = 2K_{Ts}\left(\Delta\sigma^2/\Delta x^2\right)$. These choices of diffusion coefficients were made empirically in order to qualitatively reproduce some quantitative aspects of the reference cold bubble simulation of Straka et al. (1993) (see the discussion later in this section). The diffusion coefficients chosen has an important influence on the time-evolution of the flow (see section

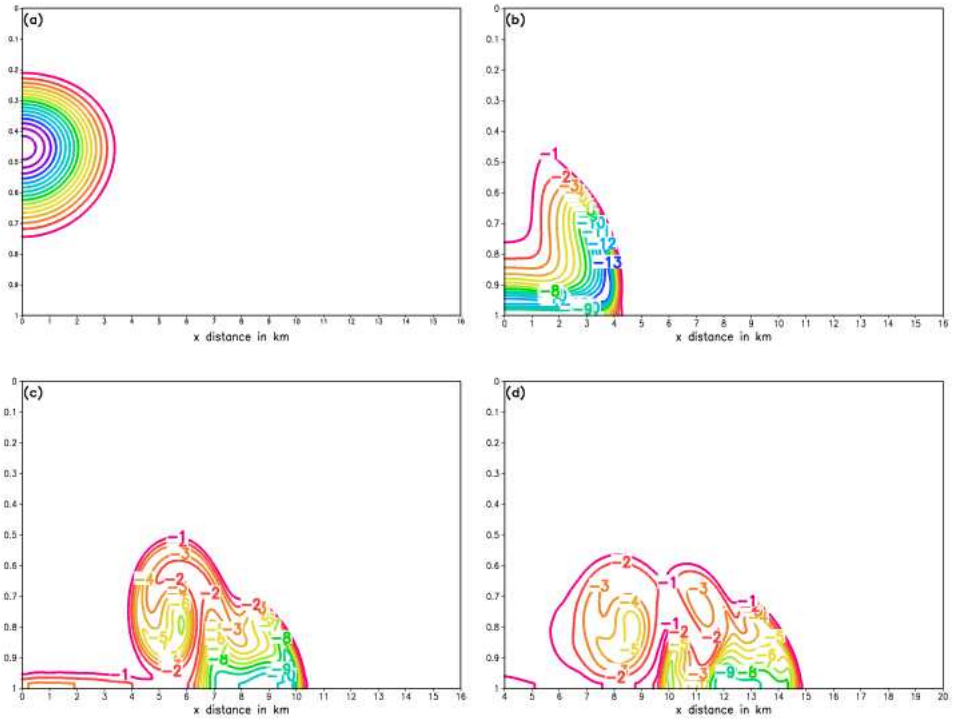

Figure 5.2: Reference solution for the cold bubble test. Potential temperature perturbation in the right-hand part of the integration domain for $0 \leq \sigma \leq 1$: (a) at 0 s; (b) after 300 s; (c) after 600 s; (d) after 900 s. The contour interval is 1 K. Note the displacement of the horizontal scale in (d).

5.2.4). The elliptic equation is solved with SOR, using $rl = 1.9$ as relaxation factor and $\epsilon = 10^{-6}$ as criterion of convergence.

The potential temperature deviations θ' from the isentropic background state for t = 0, 300, 600 and 900 s are shown in Fig. 5.2, for a simulation with $\Delta t_s = 1\,s$ and $\Delta t_a = 0.1\,s$. The contour interval is 1K. The u component of the wind (upper panel) and the $\hat{w}$ component of the wind (lower panel) after 900 s are shown in Fig. 5.3. The contour interval is 2 ms^{-1}. Recall from Chapter 3 that in the quasi-elastic σ coordinate equations, the relationship $\hat{w} = -\omega RT/gp$ defines the vertical wind. The minimum and maximum of θ', u and $\hat{w}$ atained for the reference solution (REFC) at t = 900 s are listed in Table 5.1.

In Fig. 5.2 it can be seen that the cold bubble is simulated to descend to the ground. This occurs in conjunction with a downdraft that develops and accelerates, in response to the negative buoyancy associated with the presence

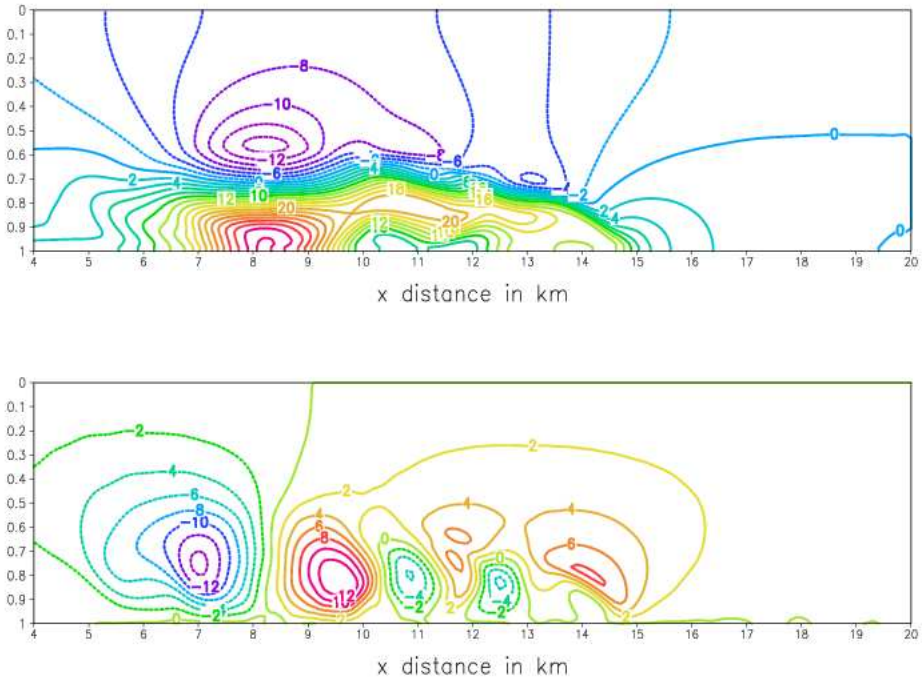

Figure 5.3: Reference solution for the cold bubble test. The u component of the wind (top panel) and the $\hat{w}$ component of the wind (bottom panel) after 900 s in the right-hand part of the integration domain, for $0 \leq \sigma \leq 1$. The contour interval is 2 ms^{-1}.

Table 5.1: Comparison of minimum and maximum values of θ', u and $\hat{w}$ for the reference solution REFC, and simulations obtained using different values of explicit diffusion (see section 5.2.4). The values of the diffusion coefficients used are $K_s = 75\,m^2s^{-1}$ (REFC and FA), $K_s = 50\,m^2s^{-1}$ (FB), $K_s = 25\,m^2s^{-1}$ (FC) and $K_s = 0\,m^2s^{-1}$ (FD), for diffusion of the u field along the x axis. The diffusion applied along the σ axis, and the T field diffusion, is as specified in the text. Note that diffusion of double the magnitude is applied along the σaxis for T in solution REFC, compared to solution FA.

Variable	REFC	FA	FB	FC	FD
θ'_{min}	-9.75	-10.70	-11.19	-11.86	-12.89
θ'_{max}	0.00	0.06	0.10	0.34	1.31
u_{min}	-14.87	-15.73	-17.13	-19.38	-22.24
u_{max}	34.79	31.31	31.64	30.56	31.49
w_{min}	-14.58	-15.58	-16.79	-18.01	-24.32
w_{max}	13.89	17.60	21.51	24.71	29.00

of the cold bubble in the warmer environment. On reaching the surface, the cold air spreads laterally to form a gust front (Panel b). Along the top part of the leading edge of the front, Kelvin Helmholtz shear-instability rotors are formed (Panel c). Three rotors have developed by t = 900 s, and the gust front has progressed to a distance of about 15 km from $x = 0$ (Panel d). The rotors have caused two cold pools to become separated from the main front by t = 900 s (Panel d). Three downdrafts and updrafts exists at t = 900 s in association with the rotors (Fig. 5.3, lower pannel). By this time, the magnitudes of horizontal wind and vertical speed are simulated to peak at 35 ms^{-1} and 15 ms^{-1} respectively (see Table 5.1). The maximum values attained by the horizontal and vertical advection Courant numbers (see Chapter 4) during the full 900 s period are 0.41 and 0.25 respectively. This corresponds to maximum values of 41 ms^{-1} and 23 ms^{-1} attained over the full 900 s period for the magnitudes of u and $\hat{w}$ respectively. Note that equally spaced σ levels are not equally spaced in geometric space, and that this is taken into account during the calculation of the vertical advection Courant number.

The simulation depicted in Figs. 5.2 and 5.3 qualitatively agrees closely with the 25 m resolution grid-converged solution of Straka et al. (1993), and with the (on average) 100 m resolution solutions obtained with three pressure-based models: the fully-elastic nonhydrostatic ETA model (Gallus and Rancic, 1996), the MP-model in σ coordinates (see Gallus and Rancic, 1996), and the fully elastic nonhydrostatic model developed by Janjic et al. (2001). All these models show the the development of three rotors (and therefore the same amount of updrafts and downdrafts) by t = 900 s. The advection time-step $\Delta t_s = 1\,s$ used to obtain

the reference solution, is considerably longer than the time steps applied in the previously mentioned studies by other authors, in which Eulerian procedures are used for the advection terms (see section 5.10).

There are only small quantitative differences between the t = 900 s extreme values listed in Table 5.1 for the reference cold bubble solution, and results obtained by other authors using different equation sets and numerical procedures. For example, the maximum horizontal wind speeds at t = 900 s are 36 ms^{-1}, 38 ms^{-1} and 35 ms^{-1} in reference solution of Straka et al. (1993), the nonhydrostatic ETA model and the σ coordinate MP model (Gallus and Rancic, 1996) cold bubble simulations respectively . In the present experiments a value of 35 ms^{-1} is attained (Table 5.1). The minimum vertical wind speeds are respectively about -15ms^{-1}, -14 ms^{-1} and -16 ms^{-1} for the solutions of Straka et al. (1993), and the ETA and MP models respectively, compared to the -15 ms^{-1} obtained in the reference solution (see Table 5.1). Straka et al. (1993) report a minimum potential temperature deviation of -9.77 K for their 25 m resolution simulation, which is in close agreement with the -9.75 K of the reference solution described here. It is shown in section 5.2.4 that the differences in the various simulations may be explained by the different magnitudes of explicit diffusion applied in the various experiments (see also Gallus and Rancic, 1996). In fact, the diffusion coefficients used in the reference solution presented here were empirically selected in order to obtain extreme values of $\theta^{'}$, u, and w at t = 900 s similar to those stated for the reference solution of Straka et al. (1993). It may also be noted that since the cold bubble downburst problem involves dry adiabatic motion, the maximum potential temperature perturbation of 15 K should be conserved during the time-evolution of the flow field. The smaller value that is obtained for $\theta^{'}_{max}$ at t = 900 s, is largely the result of the explicit diffusion and bicubic interpolation applied during the numerical solution procedure.

The gust front in the ETA model simulations progresses to more than 16 km in the x direction in 900 s, compared to 15 km in the present experiment, and about 15.5 km in the test with the σ coordinate MP-model (Gallus and Rancic, 1996) and the 25 m resolution reference solution of Straka et al (1993). Straka et al. report on a large set of cold bubble experiments, performed with different numerical models employing different equation sets and numerical procedures. In these experiments the displacement of the gust front after 900 s in the x direction varies from 14.5 to 17 km. They found that for monotonic schemes the flow features are underdeveloped and move too slowly due to the damping characteristics of these schemes. In the split semi-Lagrangian solution, the phase retardation of short wave- length waves (at advection Courant numbers less than 0.5) by the bicubic interpolation scheme (see Chapter 4) may be responsible for the relatively slightly slower progress of the gust front.

In totality, it may be said that the split semi-Lagrangian scheme with second order differencing gives a quite satisfactory solution of the cold bubble downburst

problem. A significant aspect of this result, is that it was obtained without the use of the Shapiro filter. Clearly, the stationary two-grid-interval waves and the generally retarded short wave-length waves on the nonstaggered grid (see Chapter 4) are not having a significant impact on the simulations. This is probably due to the explicit diffusion (smoothing) applied, as well as the strong damping of short wave-lengths during each advection step by the bicubic interpolation scheme (see Chapter 4). Indeed, the reference solution potential temperature deviation field (and wind field) is somewhat diffused in comparison to the results obtained by Straka et al. (1993), Gallus and Rancic (1996) and Janjic et al. (2001). The third rotor is not as strongly developed by 900 s as in the simulations by these authors. In the remaining sections, it is shown how high order spatial differencing and smaller values of the explicit diffusion coefficients, in combination with the Shapiro filter, may be used to improve on the reference solution described in this section.

5.2.4 The effect of explicit diffusion

Different choices of diffusion coefficients may explain the differences in quantitative results obtained by different authors for the cold bubble test (see Gallus and Rancic, 1996). In the experiments in this section, it is illustrated that the choice of diffusion coefficient applied in the cold bubble test indeed has a significant impact on the time evolution and amplitudes of the simulated fields. It may be noted that in the split semi-Lagrangian solution procedure presented in Chapter 4, explicit diffusion is applied (in a split manner) only to the horizontal wind and temperature fields. Since the vertical momentum equation is not used explicitly, diffusion is only applied indirectly to the vertical velocity field $\dot{\sigma}$, when the diffused horizontal wind field is used in the vertical integration of the continuity equation (see Chapter 4).

In order to quantify in some way the effects of explicit diffusion on the simulations, a series of experiments employing different values of the diffusion coefficients were performed. In the four experiments described here, diffusion of the same magnitude is applied to the u and T fields. That is, $K_s = K_{Ts}$, and the diffusion coefficients applied were chosen to be of similar impact along both the x and σ axis. This is achieved by choosing $K_\sigma = K_s\left(\Delta\sigma^2/\Delta x^2\right)$ and $K_{T\sigma} = K_{Ts}\left(\Delta\sigma^2/\Delta x^2\right)$, so that the non-dimensional quantity $K\Delta t_s/\Delta n^2$ defined in Chapter 4 has the same magnitude along both the x and σ axis. Except for the diffferent values of the diffusion coefficients used, the settings of the experiments described in this section are exactly as for the reference simulation described in section 5.2.3. The extreme values at t = 900 s obtained for $\theta^{'}$, u and $\hat{w}$ are listed in Table 5.1 for the different choices of diffusion coefficients $K_s = 75\,m^2s^{-1}$ (FA), $K_s = 50\,m^2s^{-1}$ (FB), $K_s = 25\,m^2s^{-1}$ (FC) and $K_s = 0\,m^2s^{-1}$ (FD) respectively. Fig. 5.4 shows $\theta^{'}$ after 900 s for $K_s = 75\,ms^{-2}$ (Panel a), $K_s = 50\,ms^{-2}$ (Panel b), $K_s = 25\,ms^{-2}$ (Panel c), and $K_s = 0\,ms^{-2}$ (Panel d). The corresponponding $\hat{w}$ fields are shown in Fig. 5.5.

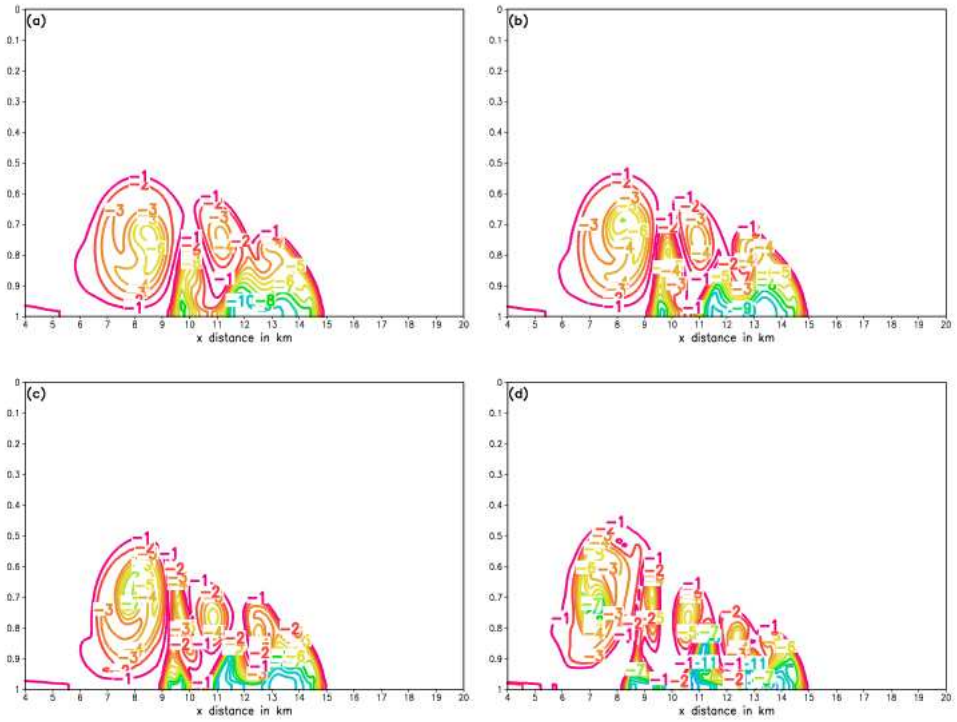

Figure 5.4: The potential temperature deviation after 900 s for the cold bubble test, in the right-hand part of the integration domain, for $0 \leq \sigma \leq 1$: (a) $K_s = 75\,ms^{-2}$; (b) $K_s = 50\,ms^{-2}$; (c) $K_s = 25\,ms^{-2}$; (d) $K_s = 0\,ms^{-2}$. The contour interval is 1K.

The downdraft of the third rotor depicted in Panel a of Fig. 5.3 (obtained with $K_s = 75\,m^2s^{-1}$), is more intense than in the reference solution (Fig. 5.3, lower panel). The corresponding potential temperature field (Panel a in Fig. 5.4) has reacted to the stronger downdraft , showing the presence of the third rotor more clearly than in the reference solution. In fact, the time evolution of the potential temperature deviation pattern depicted in Panel a of Fig. 5.4, is in very close agreement to the solutions presented by Straka et al. (1993), Gallus and Rancic (1996) and Janjic and Gerrity (2001). In the simulation with $K_s = 50\,m^2s^{-1}$, the initial stage of the development of a fourth rotor can be seen (note the formation of a fourth updraft in Panel b of Fig. 5.5). In all the experiments with smaller diffusion coefficients, a fourth rotor is well developed by t = 900 s (Panels c and d of Fig. 5.5). The $\theta^{'}$ fields in Panels c and d of Fig. 5.4 show that the third rotor has caused a third cold pool to separate from the main front, with the fourth rotor impacting on the evolution of the $\theta^{'}$ field at the leading edge of the gust front. Another noteworthy feature of the simulations with $K_s = 25\,m^2s^{-1}$ and $K_s = 0\,m^2s^{-1}$, is how the first rotor to develop starts to impact on the trailing edge of the gust front. Some of the cold air in this region gets caught in the updraft of the first rotor and is advected upwards (Panels c and d in Fig. 5.4).

Clearly, relatively larger values of the diffusion coefficients slow down the time-evolution of the main flow features. In simulations carried out with $K_s = 75\,m^2s^{-1}$, $K_s = 50\,m^2s^{-1}$, and for the reference solution settings, a small perturbation in the potential temperature can be seen at the leading edge of the gust front by t = 900 s. This perturbation is indicative of the initial stages of the development of the fourth rotor, that becomes fully developed after t = 900 s. Straka et al. (1993) report similar behaviour for their 25 m resolution reference solution.

All the simulations, even the one with zero diffusion, remained stable during the 900 s integration period. However, the $\hat{w}$ fields for $K_s = 25\,m^2s^{-1}$, and in particular for $K_s = 0\,m^2s^{-1}$, are noisy (Panels c and d of Fig. 5.5). More negative aspects of the simulations with relatively small diffusion coefficients are apparent from Table 5.1. Noting that potential temperature is conserved in an adiabatic atmosphere, the large positive values of $\theta^{'}_{max}$ for small values of the diffusion coefficients (see columns FC and FD in Table 5.1) are indicative of numerical inaccuracy. The errors in $\theta^{'}_{max}$ are diffused when higher values for the diffusion coefficients are used (see columns FA and FB in Table 5.1).

When comparing the extreme values of $\theta^{'}$, u and $\hat{w}$ listed in Table 5.1 for the simulations with various diffusion coefficients, it should be kept in mind that the time-evolution of the various simulations are different. This, and the reduced damping effect of explicit diffusion at smaller diffusion coefficients, may explain the larger extreme values of the vertical wind obtained for smaller diffusion coefficients (Table 5.1). However, the exceptionally large values of $\hat{w}$ obtained

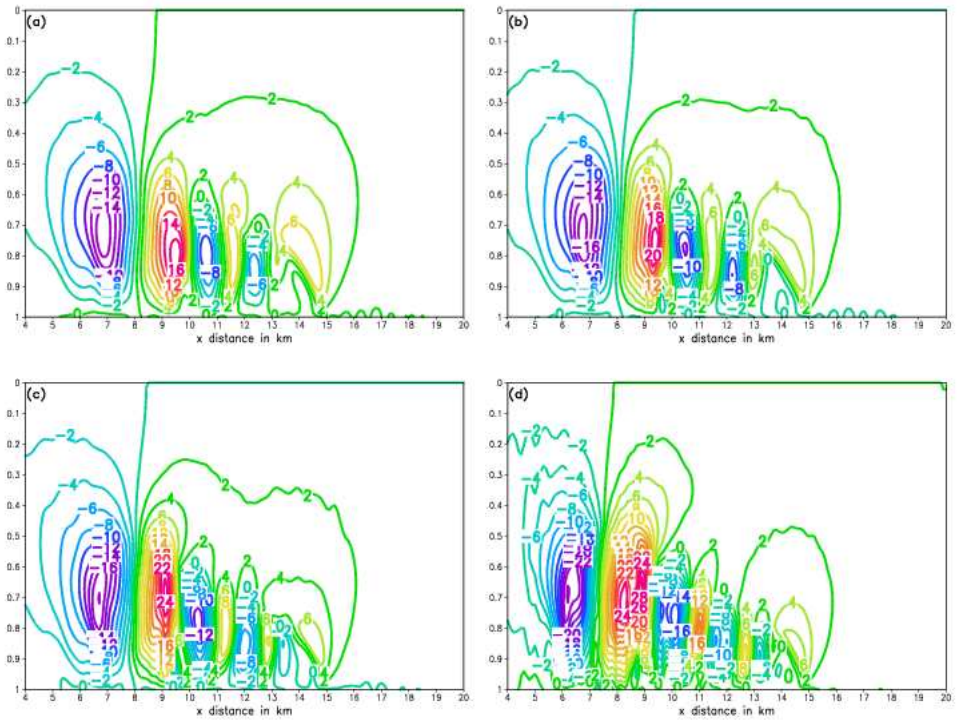

Figure 5.5: The $\hat{w}$ component of the wind for the cold bubble test after 900 s, in the right-hand part of the integration domain, for $0 \leq \sigma \leq 1$: (a) $K_s = 75\,ms^{-2}$; (b) $K_s = 50\,ms^{-2}$; (c) $K_s = 25\,ms^{-2}$; (d) $K_s = 0\,ms^{-2}$. The contour interval is 2 ms^{-1}.

for the case of zero diffusion is somewhat of a concern, since it may indicate the development of nonlinear instability in the simulations. Indeed, simulations with fourth order spatial differencing becomes unstable for $K_s = 0\,m^2s^{-1}$, unless a spatial filter is applied to some of the variables.

5.2.5 The effect of the Shapiro spatial filter

It has long been known that the A-grid used in the present study has poor gravity wave dispersion properties (see Chapter 4). An analysis of the linearized quasi-elastic equations in Chapter 4 has indicated that horizontal centered differencing on the nonstaggered grid results in the frequency (and phase speed) of short wave length gravity waves being significantly retarded, and the two-grid-interval waves are stationary. Higher order differencing leads to significant improvements in representing the true gravity wave properties at wave lengths as short as four grid-intervals, but the two-grid-interval waves remain stationary and problematic. For the linearized quasi-elastic equations, the effect of vertical centered differencing on gravity wave dispersion on the nonstaggered grid is similar to that of horizontal differencing. The vertical two-grid-interval waves are not stationary, however, only significantly retarded. In Chapter 4 the use of a high order Shapiro filter was suggested, to completely remove the two-grid-interval waves from the grid. This filter, when applied at high order, has a negligible effect on the amplitude of the longer wave length waves (see Chapter 4). In this section, the effect of Shapiro filter on the cold bubble simulations is investigated.

The settings of the experiments presented in this section correspond to those of the reference simulation. The only differences are the various values of the diffusion coefficients that are applied, and the fact that the spatial filtering is used. The Shapiro (1975) filter is applied only during the $\mathrm{N^{th}}$ time step of each adjustment phase of N time steps. The filter is first applied in the x direction for a specific field, whereafter the horizontally filtered field is filtered along the σ axis by a second application of the filter. The filter is applied to the fields u, $\ln p_s$, $\dot{\sigma}$ and ϕ only (see Chapter 4). The filter with p = 4 is applied, at grid points with stencils that allow this degree of filtering. Near the vertical boundaries, where grid points allow an order of filtering of 3 or less, lower order vertical filtering is performed. Similarly, horizontal filtering with p = 3 or less is performed near the lateral boundaries.

Fig. 5.6 shows the potential temperature perturbation θ' after t = 900 s, obtained with the settings of the Shapiro filter as described in the previous paragraph. The settings chosen for explicit diffusion used in the tests described here, are the same as for the explicit diffusion tests described in the previous section. That is, diffusion coefficients of $K_s = 75\,m^2s^{-1}$, $K_s = 50\,m^2s^{-1}$, $K_s = 25\,m^2s^{-1}$ and $K_s = 0\,m^2s^{-1}$ were used to obtain the simulations in Panels a to d of Fig. 5.6 respectively. Fig. 5.7 shows the corresponding $\hat{w}$ fields

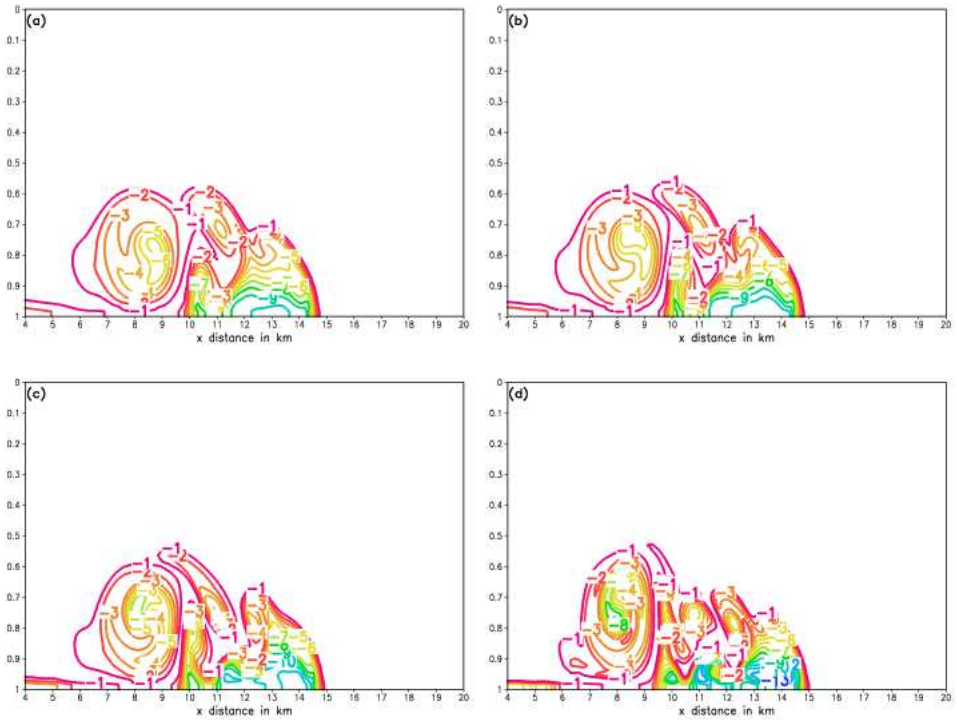

Figure 5.6: The potential temperature deviation after 900 s for the cold bubble test, in the right-hand part of the integration domain, for $0 \leq \sigma \leq 1$: (a) $K_s = 75\,ms^{-2}$; (b) $K_s = 50\,ms^{-2}$; (c) $K_s = 25\,ms^{-2}$; (d) $K_s = 0\,ms^{-2}$. The Shapiro filter is applied with $p = 4$. The contour interval is 1K.

obtained. The extreme values obtained for θ', u and $\hat{w}$ at t = 900 s are listed in Table 5.2.

The most striking effect of the Shapiro filter, is that simulated $\hat{w}$ fields are much smoother than the corresponding simulations obtained without the use of the filter (compare Fig. 5.7 to Fig. 5.5) . This suggests that the filter has succeeded in removing, at least to a large extent, the effects of stationary two-grid-interval waves on the simulations. However, there is still slight noise present in the $\hat{w}$ fields obtained for the case of zero diffusion (Panel d of Fig. 5.7). It is possible that retarded gravity waves, with wave-lengths near the shortest resolvable scales, contribute to the numerical noise still present in this simulation (e.g. Purser, 1987). However, application of the filter seems to keep the noise to acceptable levels. This is confirmed by the extreme values listed for $\hat{w}$ for the case of zero diffusion (simulation SD in Table 5.2). These extreme values are significantly smaller in magnitude than the values of $\hat{w}$ obtained for the case of zero diffusion without the application of the Shapiro filter (simulation FD in Table 5.1).

By comparing the potential temperature perturbation fields in Figs. 5.4 and 5.6, it may be seen that for a particular choice of diffusion coefficient, application of the Shapiro filter causes some retardation to occur in the time-evolution of the flow field. The same number of rotors are simulated by t = 900 s for all the corresponding cases. However, the time-evolution of the third rotor is slightly slower in the simulations where the Shapiro filtered is applied, compared to the corresponding simulations obtained without application of the filter. The relative positions of the first and second third rotors are different in the simulations obtained with application of the Shapiro filter compared to the simulations obtained without the use of the filter. The trailing edge of the gust front progresses further in the simulations where the Shapiro filter is applied compared to the nonfiltered simulations. However, the leading edge of the gust front has progressed slightly less in the simulations obtained with relatively large diffusion coefficients where the filter is applied (Panels a and b of Fig. 5.6), compared to the corresponding simulations obtained without application of the filter (Panels a and b of Fig. 5.4). For relatively large values of explicit diffusion, the extreme values obtained for θ', u and $\hat{w}$ with application of the filter, are similar to the values obtained without application of the filter (Compare FA and FB in Table 5.1 to SA and SB in Table 5.2).

From these and other experiments with the Shapiro filter, the following additional conclusions may be drawn:

- applying the spatial filter during each adjustment time-step, slows down the time-evolution of the flow field. For example, for the case $K_s = 50\, m^2 s^{-1}$ the gust front progresses to about 14.3 km in 900 s, instead of about 14.8 km as in the present case (Panel b of Fig. 5.6). Here the filter

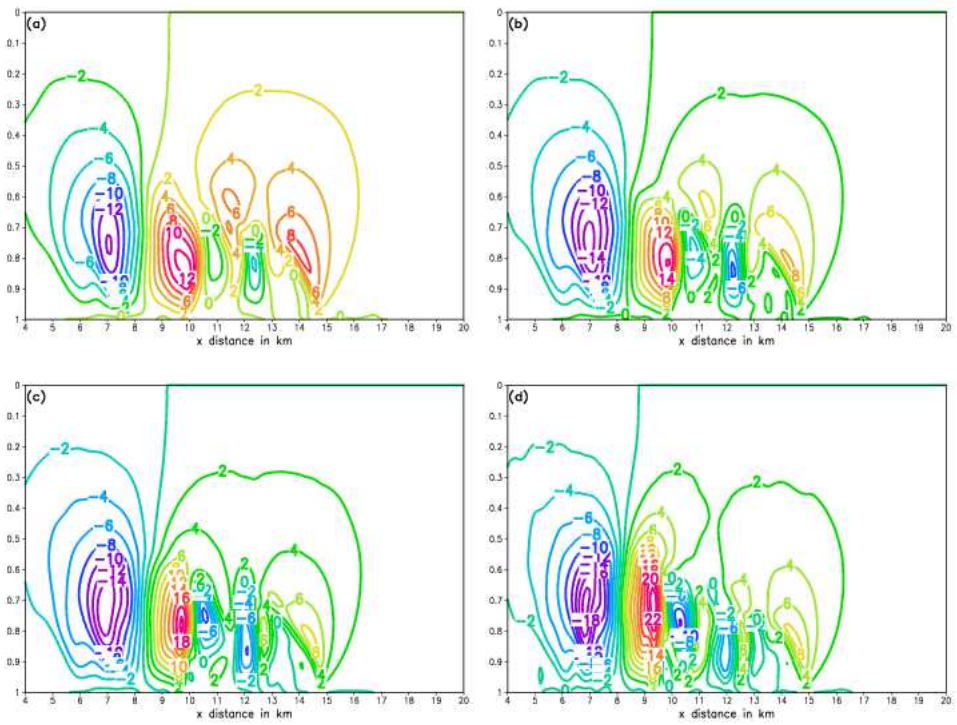

Figure 5.7: The $\hat{w}$ component of the wind for the cold bubble test after 900 s, in the right-hand part of the integration domain, for $0 \leq \sigma \leq 1$: (a) $K_s = 75\,ms^{-2}$; (b) $K_s = 50\,ms^{-2}$; (c) $K_s = 25\,ms^{-2}$; (d) $K_s = 0\,ms^{-2}$. The Shapiro filter is applied with p = 4. The contour interval is 2 ms^{-1}.

is applied only during the N^{th} adjustment time-step. The development of the third rotor is also somewhat retarded if the filter is applied during each adjustment time-step. The progress of the leading edge of the gust front in the present set of experiments is in close agreement to the experiments performed in the previous section where the Shapiro filter was not applied at all (compare Figs. 5.6 and 5.4), especially at relatively low values of explicit diffusion. The time evolution of the two rotors in the two sets of experiments is also similar, except for the case of zero diffusion. Clearly, a balance is needed between applying the filter too often (which somewhat slows down the time evolution of the flow) and applying the filter too infrequently (which leads to the development of two-grid-interval noise - see section 5.2.4). This aspect is investigated further in section 5.2.8;

- applying the Shapiro filter of order p = 4, during the N^{th} adjustment time-step only, produces satisfactory results. The noise originating from the two-grid-interval waves is sufficiently controlled, whilst no significant damping effects are visible at longer wave lengths. There seems to be no advantage in spending extra calculations, by filtering at values of p larger than 4, at grid points with stencils that do allow this order of filtering;

- filtering near the vertical boundaries is somewhat problematic. In the present set of experiments, it was found necessary to perform horizontal filtering with p = 2 at the row of grid points directly above the lower boundary, at grid points with stencils that do allow a higher order of filtering. Two-grid-interval noise originates near the lower boundary if higher order filtering (or no filtering) is performed along this row of grid points. Similarly, horizontal filtering with p = 2 is performed along the row of grid points adjacent to the upper boundary. However, filtering at higher values of p along this row was not found to have a significant impact on the simulations. Vertical filtering with p = 0, 1, 2 or 3 is performed near the lower and vertical boundaries, depending on on the order of filtering allowed by the stencils of grid points. It was found that this relatively low order of filtering has only a slight damping effect on the important flow features that are present near the lower boundary.

- filtering near the lateral boundaries, in the region where the stencils around the grid points allow filtering of degree p = 3 or less, was found to have a negligible effect on the simulations. This is probably due to the fact that by t = 900 s (the end of the integration time), the important flow features are still relatively far away from the lateral boundaries. However, if important flow features are present near the lateral boundaries, filtering in this region by applying the Shapiro filter at relatively low values of p may be problematic. For example, in the case where dynamic (time-dependent) lateral boundary conditions are used, the damping induced by low order filtering may have negative effects on the simulation.

Table 5.2: Comparison of minimum and maximum values of $\theta^{'}$, u and $\hat{w}$ obtained for the various values of explicit diffusion. The values of the diffusion coefficients used are $K_s = 75\,m^2s^{-1}$ (FA), $K_s = 50\,m^2s^{-1}$ (FB), $K_s = 25\,m^2s^{-1}$ (FC) and $K_s = 0\,m^2s^{-1}$ (FD). The Shapiro filter is applied, with p = 4.

$Variable$	SA	SB	SC	SD
$\theta^{'}_{min}$	-10.32	-10.92	-11.80	-13.56
$\theta^{'}_{max}$	0.07	0.09	0.13	1.45
u_{min}	-14.58	-15.46	-16.80	-19.44
u_{max}	34.81	35.87	36.47	35.68
w_{min}	-14.19	-14.79	-15.95	-18.64
w_{max}	12.68	16.12	20.59	23.39

5.2.6 Advantages to be gained from fourth order spatial differencing

In the experiments presented in the previous sections, all spatial derivatives present in the adjustment step equations were discretized using second order differencing. Stationary two-grid-interval waves, and a significant retardation of the frequency (and phase speed) of gravity waves near the shortest resolvable scales, may therefore be expected to be present in the discretized equations (see Chapter 4). In the previous two sections, it has been shown that the problems arising from these poor gravity wave dispersion properties of the A-grid, such as two-grid-interval noise, may to a large extent be controlled by the use of explicit diffusion and the highly scale-dependent Shapiro filter. The linear analysis presented in Chapter 4 indicates that additional improvements in the numerical representation of gravity wave frequencies near the shortest resolvable scales may be expected from the use of higher order (fourth and sixth order) spatial differencing on the nonstaggered grid. In this section, a fourth order discretization of the adjustment step equations is presented. The advantages to be gained from this higher order discretization (compared to the second order discretization used in the previous sections) are illustrated by means of a series of numerical tests.

In order to obtain a full fourth order discretization of the spatial derivatives in the the adjustment step equations, not only the first derivatives present in these equations, but also the second derivatives that appear in the elliptic equation (3.86) are discretized using fourth order differencing (see Chapter 4 for the appropriate fourth order differencing formulas). Second order vertical differencing needs to be applied at the grid points adjacent to the lower and upper boundaries, since the stencils of these grid points do not allow a higher degree of differencing (unless artifical computational boundaries are introduced). Similarly,

second order horizontal differencing needs to be applied at grid points adjacent to the lateral boundaries. Note that for most grid points adjacent to the lateral boundaries, fourth order differencing is used for the vertical derivatives, whilst second order difeerencing needs to be used to discetize the horizontal derivatives. The converse is true for grid points adjacent to the vertical boundaries. It has been found crucial to consistently apply the same order of differencing at each grid point in the domain, for each of the adjustment step equations, for horizontal and vertical differencing respectively. The coding of the fourth order elliptic solver, with mixed second-fourth order differencing applied at grid points adjacent to the vertical and lateral boundaries, was found to be a rather cumbersome exercise.

Fourth-order differencing also implies that more grid points are used in the discretized operator. For example, fourth order discretization of the second derivatives in the elliptic equation (3.86) involves the use 25 grid points. whilst only 9 grid points are needed in the corresponding second order discretization. It is known that the SOR procedure is associated with progressively slower convergence as the number of grid points in the discretized operator increases (Xue, 1989). The efficiency of the fourth order elliptic solver is compared to that of the second order solver in section 5.2.10.

Figure 5.8 shows the potential perturbation at t = 900 s, obtained with the fourth order differencing scheme, for various magnitudes of explicit diffusion as specified in section 5.2.4. That is, diffusion coefficients of $K_s = 75\,m^2s^{-1}$, $K_s = 50\,m^2s^{-1}$, $K_s = 25\,m^2s^{-1}$ and $K_s = 0\,m^2s^{-1}$ were used to obtain the simulations in Panels a to d of Fig. 5.8 respectively. The Shapiro filter with $p = 4$ was applied, with filtering of lower order used near the vertical boundaries as described in the previous section. Figure 5.9 shows the corresponding results obtained for the $\hat{w}$ field.

The simulations presented in this section are directly comparable to those of the previous section, where the Shapiro filter with $p = 4$ was also applied, but second order differencing was used to discretize the spatial derivatives in the adjustment step equations. For fourth order differencing, the flow features are further evolved than for second order differencing, for each value of the diffusion coefficient used (compare Panels a to d in Fig. 5.8 to the corresponding panels in Fig. 5.6). This significant result may be explained by the fact that for second order differencing, the phase speed of short wave-length gravity waves is significantly retarded. With fourth order differencing, the representation of the analytic gravity wave phase speed is more accurate (see Chapter 4), which leads to the faster evolution of flow features displayed in Fig. 5.8. In the fourth order simulation with zero diffusion, the fourth rotor is better developed than in any of the previously performed simulations, as can be seen clearly from the potential temperature perturbation field in Panel d of Fig. 5.8. The trailing edge of the gust front has broken off from the main pool of cold air travelling

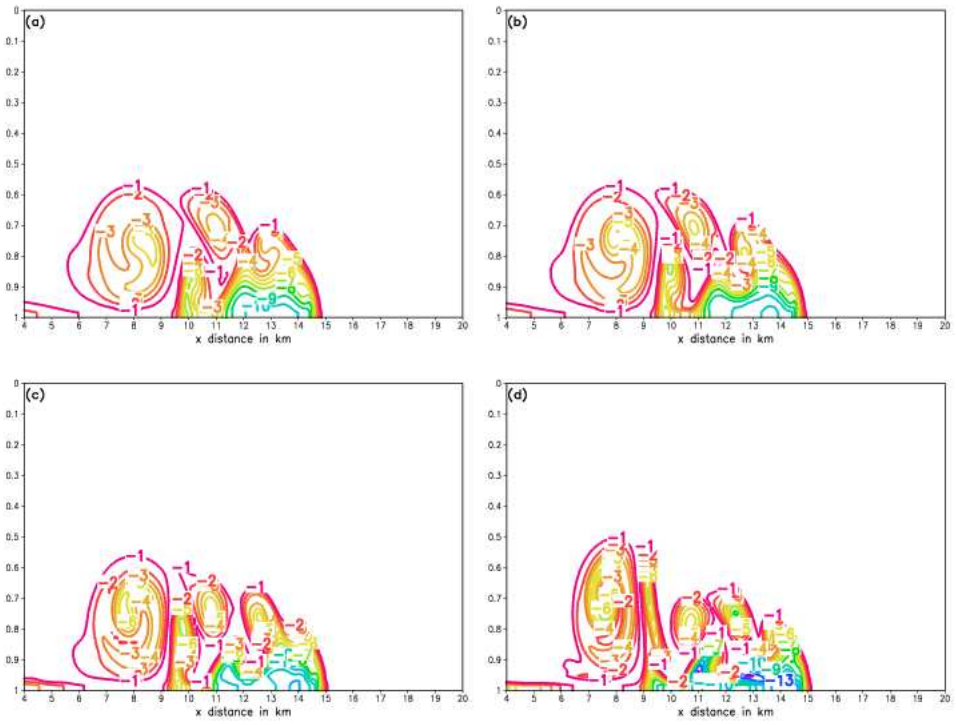

Figure 5.8: The potential temperature deviation after 900 s for the cold bubble test, in the right-hand part of the integration domain, for $0 \leq \sigma \leq 1$: (a) $K_s = 75\,ms^{-2}$; (b) $K_s = 50\,ms^{-2}$; (c) $K_s = 25\,ms^{-2}$; (d) $K_s = 0\,ms^{-2}$. The fourth order discretization of spatial derivatives in the adjustment step equations and the Shapiro filter with $p = 4$ were used. The contour interval is 1K.

Table 5.3: Comparison of minimum and maximum values of $\theta^{'}$, u and $\hat{w}$ obtained when fourth order discretization of spatial derivatives is applied. The Shapiro filter with $p = 4$ is used. The values of the diffusion coefficients used are $K_s = 75\,m^2s^{-1}$ (FA), $K_s = 50\,m^2s^{-1}$ (FB), $K_s = 25\,m^2s^{-1}$ (FC) and $K_s = 0\,m^2s^{-1}$ (FD).

$Variable$	FA	FB	FC	FD
$\theta^{'}_{min}$	-10.55	-11.19	-12.18	-14.15
$\theta^{'}_{max}$	0.07	0.10	0.19	1.50
u_{min}	-14.79	-15.81	-17.77	-19.64
u_{max}	34.29	35.24	35.00	32.04
w_{min}	-14.87	-15.52	-16.64	-18.36
w_{max}	13.69	17.44	21.15	26.89

in the horizontal near the surface, and has been flung into the vertical by the first rotor's updraft. This feature is also present in the corresponding simulation obtained with second order differencing, however.

As in the case of second order differencing with application of the Shapiro filter, the $\hat{w}$ fields in Fig. 5.9, are much less noisy than the fields obtained with second order differencing without the use of the Shapiro filter (compare in particular Panels c to d of Fig. 5.9 to the corresponding panels of Fig. 5.5). There is also no excessive growth in the amplitudes of the $\theta^{'}$, u, and $\hat{w}$ fields obtained for the case zero diffusion (see Table 5.3). Thus, it seems as if the Shapiro filter controls the noise originating from the nonstaggered grid, also for the case of the fourth order spatial differencing. A comparison of the extreme values listed in Table 5.3 (fourth order differencing) to those in Table 5.2 (second order differencing) shows very close agreement, even for the case of zero diffusion. The slightly larger differences in the zero diffusion case may be attributed to the further evolved flow field obtained for the case of fourth order differencing at t = 900 s, compared to the field obtained with second order differencing.

It may be said that the Shapiro filter with p = 4 effectively removes two-grid-interval waves on the nonstaggered grid, for both the cases of second and fourth order spatial differencing. In the case of second order differencing with application of the Shapiro filter, the time-evolution of the flow features is somewhat retarded compared to the corresponding nonfiltered solutions. In this regard, the fourth order simulations with application of the Shapiro filter offers an improvement over second order differencing. In the former case, the improved representation of the gravity wave phase speed leads to more accurate and further evolved flow fields at t = 900 s, for each particular design of explicit diffusion used.

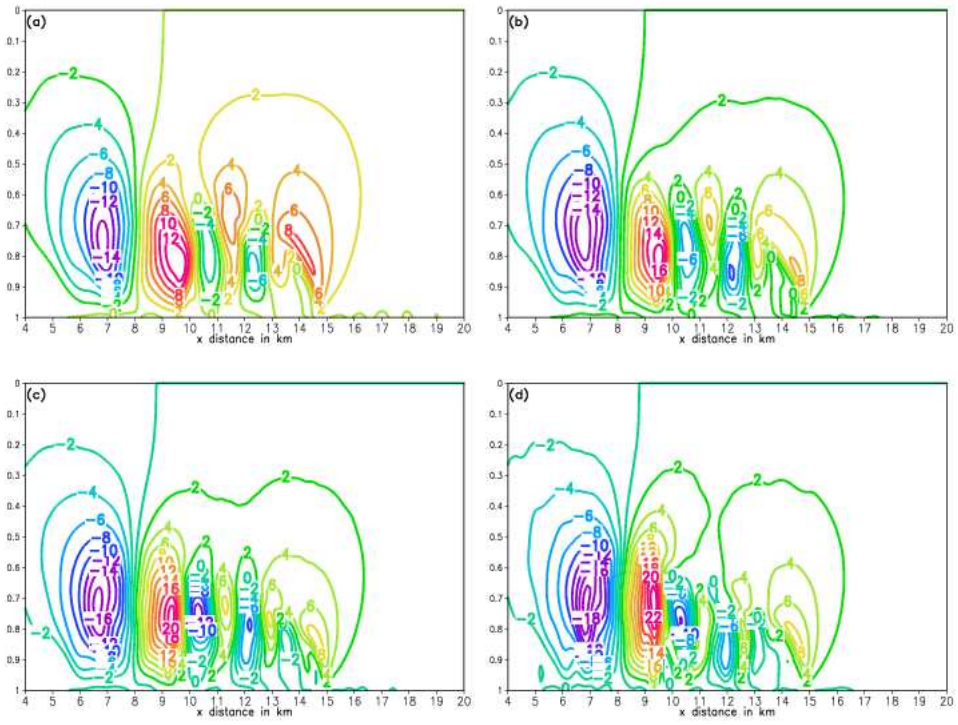

Figure 5.9: The $\hat{w}$ component of the wind for the cold bubble test after 900 s, in the right-hand part of the integration domain, for $0 \leq \sigma \leq 1$: (a) $K_s = 75\,ms^{-2}$; (b) $K_s = 50\,ms^{-2}$; (c) $K_s = 25\,ms^{-2}$; (d) $K_s = 0\,ms^{-2}$. The fourth order discretization of spatial derivatives in the adjustment step equations and the Shapiro filter with $p = 4$ were used. The contour interval is 2 ms^{-1}.

5.2.7 The effect of the choice of D_N scheme

The most simple way of calculating the departure points at time level τ in a semi-Lagrangian discretization of the two-dimensional atmospheric equations, is by using the formula

$$\begin{bmatrix} x^* \\ \sigma^* \end{bmatrix} = \begin{bmatrix} x \\ \sigma \end{bmatrix} - \Delta t \begin{bmatrix} u^\tau \\ \dot{\sigma}^\tau \end{bmatrix}. \tag{5.5}$$

Here $\left(u^\tau, \dot{\sigma^\tau}\right)$is the time level τ wind field, which is assumed to remain constant over the time interval $(\tau, \tau + \Delta t)$. This way of calculating the departure points will be referred to as the D_0 scheme. It is interesting to investigate the advantages that can be gained over the D_0 scheme in the cold bubble simulations, by using the D_N schemes of McGregor (1993). In the D_N schemes the approximated velocity at time level $\tau + \Delta t/2$ (and its approximated total time derivatives of various order for the higher order D_N schemes) are used to calculate the departure points (see Chapter 4). In all the experiments described in the previous sections, the D_3 scheme was used. The spatial derivatives that occur in the two-dimensional form of the calculation formula (4.8) for the D_3 scheme and the term $A^*_{p_s}$ (see Chapter 4), were evaluated using second order differencing. In combination with the question of most suitable choice of D_N scheme, the question arises whether more accurate results can be expected by using fourth order spatial differencing in the calculation of the term $A^*_{p_s}$ and the departure point formulas (4.7) and (4.8) of the D_2 and D_3 schemes.

The resolution and general design of the experiments performed in this section are as described for the reference solution (see section 5.2.3). The settings of explicit diffusion along the x and σ axis are as described in section 5.2.4, with $K_s = 25\, m^2 s^{-1}$. The Shapiro filter is used, with the settings as described in section 5.2.5. Fourth order spatial differencing is used in the adjustment step, as described in section 5.2.6. Fig. 5.10 shows the potential temperature perturbation at t = 900 s obtained using respectively the D_0 scheme (Panel a), D_1 scheme (Panel b) and D_2 scheme (Panel c). Here second order differencing was applied to the spatial derivatives in the departure point formulas and the term $A^*_{p_s}$. The D_3 scheme with fourth order spatial differencing applied to the departure point formulas and the term $A^*_{p_s}$ was used to obtain the simulation depicted in Panel d of Fig. 5.10. The corresponding $\hat{w}$ fields are displayed in Fig. 5.11. These results may be compared to the corresponding solution obtained using the D_3 scheme with second order spatial differencing applied to the departure point formula and the term $A^*_{p_s}$ (Panels c of Figs. 5.8 and 5.9). The extreme values obtained for $\theta^{'}$, u and $\hat{w}$ are listed in Table 5.4 for the D_0, D_1 and D_2 schemes. The D_3 scheme with fourth order spatial differencing applied to the departure point formula and the term $A^*_{p_s}$is denoted by D_{3F} in the Table 5.4. Note that corresponding results obtained with the D_3 scheme, but with second order differencing applied to the departure point formula and the term A_{p_s}, are displayed in column FC of Table 5.3.

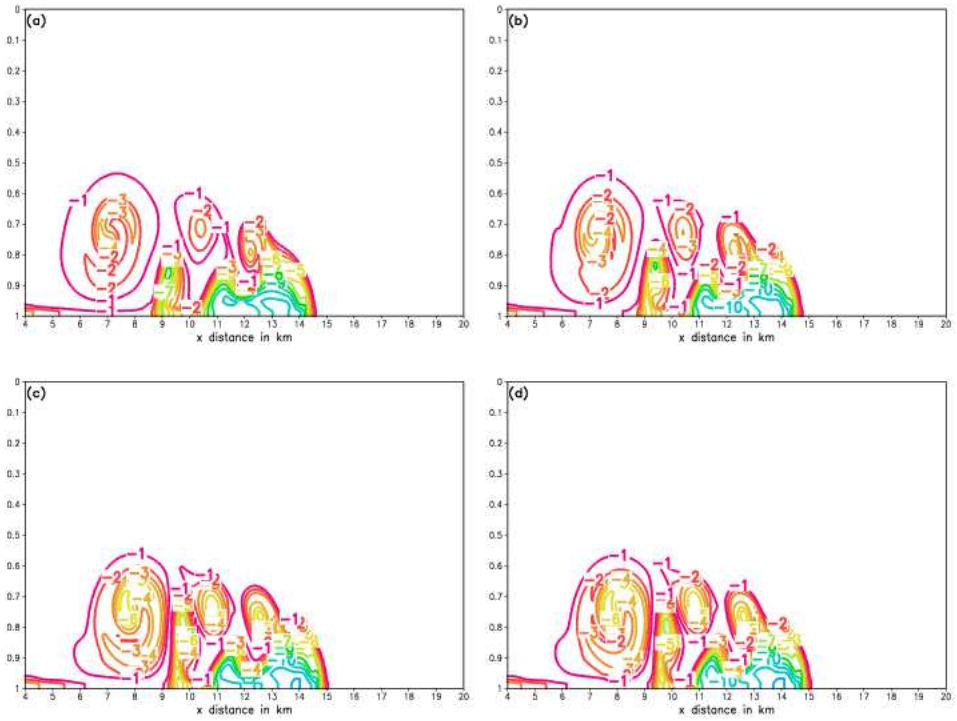

Figure 5.10: The potential temperature deviation after 900 s for the cold bubble test, in the right-hand part of the integration domain, for $0 \leq \sigma \leq 1$: (a) D_0 scheme; (b) D_1 scheme; (c) D_2 scheme; (d) D_3 scheme with fourth order differencing applied to the departure point formula and the term $A^*_{p_s}$. The fourth order discretization of spatial derivatives in the adjustment step equations and the Shapiro filter with $p = 4$ are used. $K_s = 25\, m^2 s^{-1}$. The contour interval is 1K.

There are mainly three conclusions that can be drawn from the experiments presented in this section:

- the results obtained from using respectively the D_2 and D_3 schemes to calculate the departure points are almost indistinguishable (Compare Panels c of Figs. 5.10 and 5.11 to Panels c of Figs. 5.8 and 5.9). Even the relevant extreme values listed in Tables 5.4 and 5.3 (columns D_2 and FC respectively) show very close correspondence. Thus, at least in the present of set experiments, there seems to be no advantage in going beyond the $\mathrm{D_2}$ scheme to calculate the departure points in the split semi-Lagrangian procedure.

- The differences are negligible between the results obtained when the D_3 scheme is used with second order differencing applied to the spatial derivatives in the departure point formula and term $A^*_{p_s}$, compared to when the D_3 scheme is used with fourth order differencing applied to the relevant derivatives (compare Panels c of Figs. 5.8 and 5.9 to Panels d of Figs. 5.10 and 5.11). Even the relevant extreme values listed in Tables 5.3 and 5.4 (columns FC and $\mathrm{D_{3F}}$ respectively) show very close correspondence. Clearly, there seems to be no advantage in going beyond second order spatial differencing when calculating the spatial derivatives in the departure point formula and term $A^*_{p_s}$.

- the D_0 and D_1 schemes (Panels a and b of Figs. 5.10 and 5.11) produce reasonable results, but there are some important differences with the corresponding D_2 and D_3 simulations (Panels c of Figs. 5.10 and 5.11 and Panels c of Figs 5.8 and 5.9). For example, the gust front in the D_0 and D_1 simulations progresses slightly slower than in the corresponding D_2 and D_3 simulations, and the maximum amplitude of the updraft of the first rotor is weaker in the D_0 and D_1 simulations than in the D_2 and D_3 simulations. Most important perhaps, is the much steeper gradient in the potential temperature perturbation field present in the D_2 and D_3 simulations, compared to the corresponding D_0 and D_1 fields. It may be said that the D_0 and D_1 schemes produce excessive smoothing of the potential temperature perturbation field, compared to the D_2 and D_3 schemes. Thus, stronger amplitude damping and phase retardation (with respect to the advection process) seems to be caused by the D_0 and D_1 schemes, compared to the D_2 and D_3 schemes.

It may be noted that in the experiments of McGregor (1993) it was found sufficient to use the D_3 scheme with second order spatial differencing applied to the spatial derivatives in the departure point formula. In these experiments, and in the regional climate model DARLAM and variable resolution global model C-CAM, the D_3 scheme is used only for the simulation of horizontal advection (see McGregor, 1993, 1996; McGregor and Dix, 2001). Huang (1994) applied the D_2 scheme for horizontal advection in a series of numerical tests that investigated the use of various interpolation methods in semi-Lagrangian advection schemes.

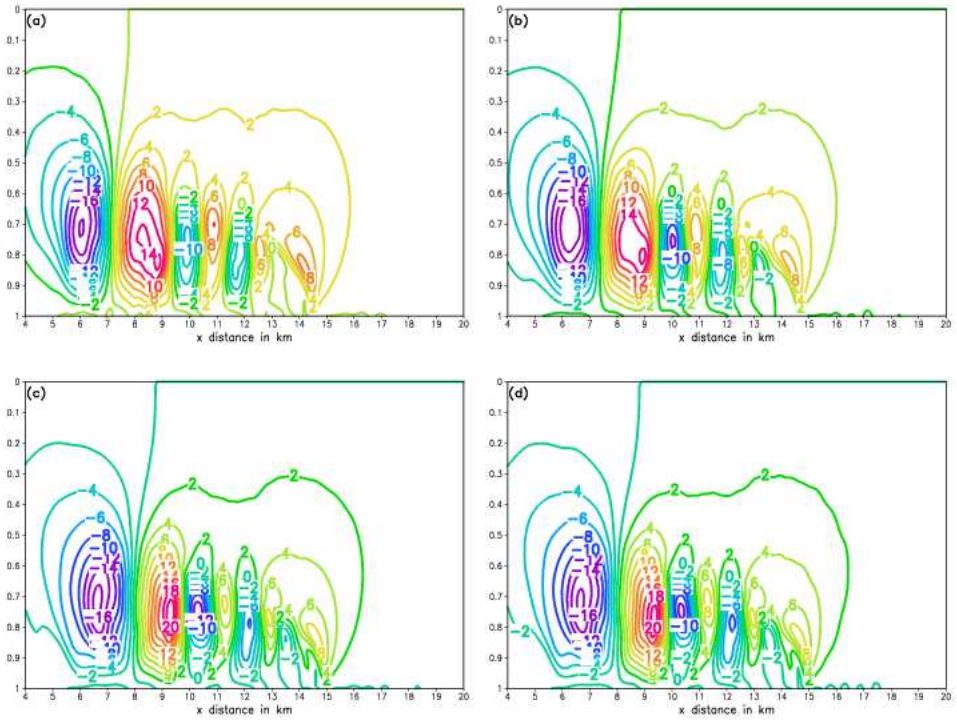

Figure 5.11: The $\hat{w}$ component of the wind after 900 s for the cold bubble test, in the right-hand part of the integration domain, for $0 \leq \sigma \leq 1$: (a) D_0 scheme; (b) D_1 scheme; (c) D_2 scheme (d) D_3 scheme with fourth order differencing applied to the departure point formula and the term $A^*_{p_s}$. The fourth order discretization of spatial derivatives in the adjustment step equations and the Shapiro filter with $p = 4$ are used. $K_s = 25\, m^2 s^{-1}$. The contour interval is 2 ms^{-1}.

Table 5.4: Comparison of minimum and maximum values of $\theta^{'}$, u and $\hat{w}$ obtained for the various departure point schemes. The fourth order discretization of spatial derivatives in the adjustment step equations and the Shapiro filter with $p = 4$ are used. $K_s = 25\, m^2 s^{-1}$.

$Variable$	D_0	D_1	D_2	D_{3F}
$\theta^{'}_{min}$	-11.50	-11.79	-12.14	-12.21
$\theta^{'}_{max}$	0.35	0.19	0.17	0.17
u_{min}	-17.41	-17.78	-17.85	-17.56
u_{max}	32.26	33.31	34.79	35.69
w_{min}	-18.19	-17.95	-16.66	-16.42
w_{max}	14.49	16.53	21.70	21.10

5.2.8 Marginally and poorly resolved flow

Operational weather prediction beyond the hydrostatic limit (horizontal resolutions finer than about 15 km) has become a reality at meteorological institutions all over the world. However, even at the largest meteorological centers, it would not in the foreseeable future be possible to integrate global nonhydrostatic models at resolutions where convection can be fully resolved (horizontal and vertical resolutions of a few hundred meters or finer). Even for the case of regional-scale NWP and climate simulation, horizontal resolution of a few kilometers at best is likely to be the only practical choice for many years to come (see the discussion in Chapter 1). Thus, nonhydrostatic regional models will most probably be integrated at resolutions where convection can only be poorly, or at best marginally, resolved. Conversely, hydrostatic models have traditionally been used at low spatial resolutions where convection is not resolved at all. Most of the parameterization schemes used in these models to represent the effects of convection on the atmosphere have therefore been developed to function well at relatively low spatial resolutions, where convection is not explicitly resolved. However, with the advent of nonhydrostatic models and the increase in model resolution, convection schemes are now required to function well in a model atmosphere where convection is marginally resolved. This is likely to become an increasingly important new focus area in numerical weather simulation in the near future (see Chapter 1). Even more fundamental, is the ability of the numerical solution procedure used in the model to perform well in the case of marginally or poorly resolved convection. In the present section, the performance of the split semi-Lagrangian scheme in the cold bubble downburst problem is investigated, for the cases of marginally and poorly resolved flow.

In all the experiments performed in this section, the D_3 scheme of McGregor (1993) with bicubic spatial interpolation is applied in the advection step. Second

order differencing is used to discretize the spatial derivatives in the departure point formula and the term $A^*_{p_s}$. The Shapiro filter with p = 4 is used, with lower order filtering performed near the boundaries as described in section 5.2.5. The explicit diffusion applied along both the x and σ axis is as described in section 5.2.4, with $K_s = 50\, m^2 s^{-1}$.

In order to simulate the basic flow structures of the diffusion limited cold bubble downburst problem, Straka et al. (1993) found that the grid spacing should be at least 133.3 m (in both the horizontal and vertical). At coarser resolutions, the basic flow features (that is, the development of the three rotors) are not fully captured. They found that at 200 m grid spacing the flow is marginally resolved, and poorly resolved at 400 m grid spacing. The first two experiments performed in this section employ a horizontal grid spacing of 200 m; 33 σ levels are used to give an average grid spacing of 200 m in the vertical. The advection time-step is $\Delta t_s = 2\, s$ and the adjustment time-step is $\Delta t_a = 0.2\, s$. Thus, the ratios $\Delta t_s / \Delta x$ and $\Delta t_a / \Delta x$ used in the previous sections are kept constant. The potential temperature perturbation after t = 900 s obtained with these settings, for second and fourth order spatial differencing applied to the adjustment step equations respectively, are shown in Panels a and b of Fig. 5.12. The corresponding $\hat{w}$ fields are shown in Panels a and b of Fig. 5.13 respectively.

In the third experiment performed, the horizontal grid spacing used is 400 m, and 17 σ levels are used to give an average grid spacing of 400 m in the vertical. Here the advection time-step is $\Delta t_s = 4\, s$ and the adjustment time-step is $\Delta t_a = 0.4\, s$. The potential temperature perturbation after t = 900 s for the 400 m simulation is shown in Panel c of Fig. 5.12. Fourth order spatial differencing is applied to the adjustment step equations. The corresponding $\hat{w}$ field is shown in Panel c of Fig. 5.13. In the final experiment performed in this section, the horizontal grid spacing used is 500 m and 65 σ levels are used as in the previous sections, in order to give a vertical grid spacing of about 100 m. Fourth order spatial differencing is applied to the adjustment step equations. This test will be useful for later comparison to three-dimensional cold bubble simulations. The fourth experiment also corresponds to the current situation in operational NWP and climate simulation, where computational constraints generally determine that models are integrated at relatively low horizontal resolutions, compared to the vertical resolution. The solutions obtained in this section may be compared to the corresponding 100 m solutions that were obtained using second order differencing (Panel b of Fig. 5.8) and fourth order differencing (Panel b of Fig. 5.8).

Two rotors have developed by t = 900 s in the 200 m solution obtained with second order differencing applied to the adjustment step equations (Panel a of Fig. 5.13). In the corresponding 200 m solution obtained with fourth order differencing applied to the adjustment step equations, a third rotor has almost fully developed by t = 900 s (Panel b of Fig. 5.13). The presence of two well de-

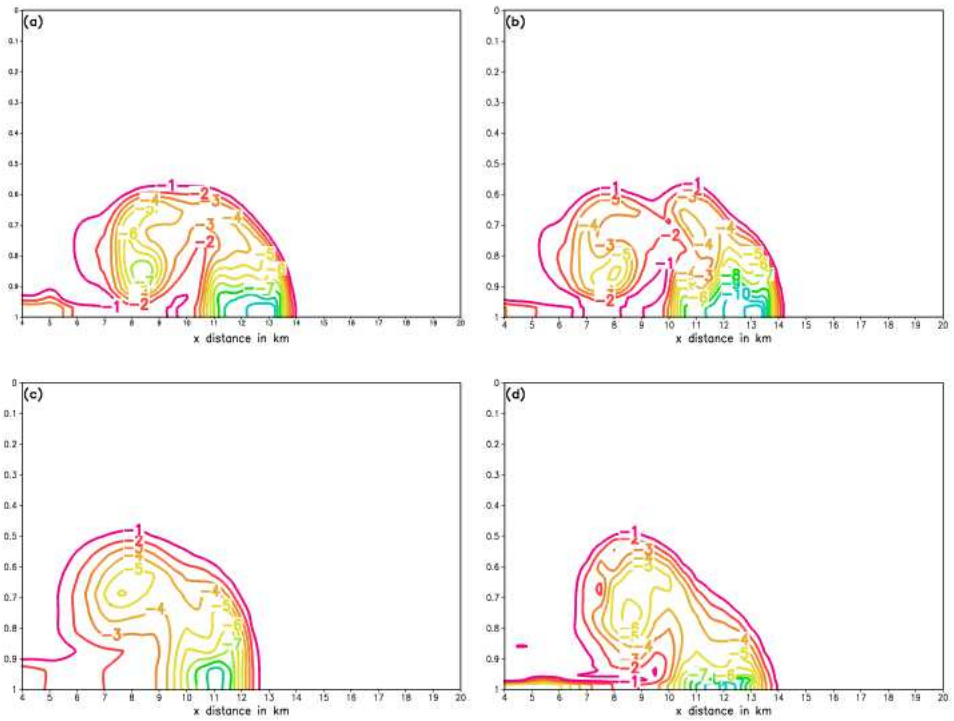

Figure 5.12: Marginally and poorly resolved flow in the cold bubble test. The potential temperature deviation after 900 s in the right-hand part of the integration domain, for $0 \leq \sigma \leq 1$: (a) $\Delta z \approx \Delta x = 200\,m$ with second order differencing; (b) $\Delta z \approx \Delta x = 200\,m$ with fourth order differencing; (c) $\Delta z \approx \Delta x = 400\,m$ with fourth order differencing; (d) $\Delta z \approx 100\,m$, $\Delta x = 500\,m$ with fourth order differencing. The D_3 scheme with second order discretization of spatial derivatives was used in the advection step. The Shapiro filter with $p = 4$ was used. $K_s = 50\,m^2 s^{-1}$. The contour interval is 1 K.

veloped rotors in the case of fourth order differencing can be seen in the relevant potential temperature perturbation (Panel b of Fig. 5.4). In the corresponding second order solution (Panel a of Fig. 5.12), the second rotor is only starting to impact on the potential temperature field. The further evolved flow field in the case of fourth order differencing shows that fourth order differencing offers a significant advantage over second order differencing in these relatively low resolution simulations.

By comparing the flow features displayed in Panel b of Fig. 5.12 to Panel b of Fig. 5.8 (obtained at 100 m resolution), it may be said that in the 200 m simulation the flow features are marginally resolved. The flow pattern is coherent and quite similar to the 100 m solution. However, only two fully developed rotors are simulated in the 200 m solution, in comparison to the three fully developed rotors present in the 100 m solution. The gust front has progressed more slowly in the 200 m solution, to a distance of about 14 km from the center of the x axis, in stead of 15 km as in the 100 m solution. The 200 m solution is dissipative compared to the 100 m solution, as is evident from comparing the 200 m resolution extreme values of $\theta^{'}$, u and $\hat{w}$ listed in Table 5.5 (column M-4) to the corresponding 100 m resolution extreme values (column FB in Table 5.3). The 400 m solution is even more dissipative (see Panel c of Fig. 5.12 and column P of Table 5.5). The gust front progresses even more slowly in the 400 m resolution solution, to a distance of 13 km away from the center x axis. The presence of one rotor in the 400 m resolution solution at t = 900 s can be deduced from the relevant potential temperature perturbation field (Panel c of Fig. 5.12). The corresponding $\hat{w}$ field shows that a second rotor is developing , with only a weak downdraft present at t = 900 s. The solution obtained with 500 m horizontal and on average 100 m vertical resolution (Panels d of Figs. 5.12 and 5.13) is similar to the 400 m solution. Only one fully developed rotor is present at t = 900 s, with a second rotor starting to impact on the leading edge of the gust front. The propagation speed of the gust front corresponds more closely with the 200 m solution than with the 400 m solution, however. The extreme values that correspond to the 500 m horizontal - 100 m vertical simulations (column PM in Table 5.5) correspond more closely to the 200 m solutions than to the 400 m solutions (columns M-4 and P of Table 5.5 respectively).

The main reason for the dissipativeness of the 200 m and 400 m solutions, is the strong damping at high wave numbers that results from the bicubic interpolations used in the semi-Lagrangian advection step (see Chapter 4). At 200 and 400 m grid spacing, the shortest resolvable wave-length waves (that are damped most) carry a more important part of the energy of the system than the shortest resolvable waves in the 100 m grid spacing simulations. The delayed development of flow features in the 200 and 400 m simulations may be attributed to the phase speed damping of the shortest resolvable gravity waves (with the highest wave numbers) on the nonstaggered grid. Once again, the highest wave numbers in the case of the 200 and 400 m simulations represent

longer wave length waves that carry more energy than the highest wave number waves in the 100 m simulation. The slower progress of the gust front in the lower resolution simulations compared to the 100 m simulation, is probably the result of the relatively more important phase damping of the high wave number gravity waves and phase damping of the advected fields by the bicubic interpolation scheme. Both the 200 and 400 m solutions at t = 900 s are smooth and without any signs of numerical noise.

A variety of numerical solution procedures have been tested by Straka et al. (1993) for the cases of poorly, marginally and adequately resolved flow. They found that models with damped advection schemes produce smooth flow structures for the case of poorly resolved flow (similar to the results obtained with the split semi-Lagrangian scheme). However, high-order finite difference models produced noisy or unstable results, whilst the results obtained with local spectral and spectral models were essentially unusable. For the case of marginally resolved flow, it was found that the schemes with damped advection schemes produced only two Kelvin-Helmholtz rotors, similar to the results obtained here with the split semi-Lagrangian scheme. They found that high order finite difference and spectral models correctly simulate three rotors at t = 900 s for the case of marginally resolved flow, but the simulations are noisy. The local spectral model performed best, but had problems with energy accumulation at the highest wave numbers. For the case of adequately resolved flow, the high order finite difference, spectral and local spectral methods performed well. For the models with damped advection schemes the flow features were underdeveloped and moved too slow. The split semi-Lagrangian scheme is different in this respect from the models with damped advection schemes studied by Straka et al. (1993), since although also employing a damped advection scheme, three Kelvin-Helmholtz rotors are fully developed at t = 900 s. This corresponds to the 100 m resolution simulations obtained by Straka et al. (1993) using high-order finite difference and spectral models.

It appears as if the split semi-Lagrangian scheme presented here is unique in the sense that it produces acceptable results for all the cases of adequately, margianally and poorly resolved flow. For adequately resolved flow (100 m grid spacing) the flow features are fully developed in comparison to the grid-converged solutions of Straka et al. (1993) and the solutions of Gallus and Rancic (1994) and Janjic et al. (2003). At coarser resolutions, the results are dissipative, but usable, smooth and without any signs of numerical noise.

5.2.9 Time-step experiments and stability tests

In all the experiments performed so far, the maximum values attained by the horizontal and vertical advection Courant numbers (see Chapter 4) during the 900 s integration period are about 0.45 and 0.25 respectively (see section 5.2.3). It may be noted that the advection time-step $\Delta t_s = 1\,s$ employed in these

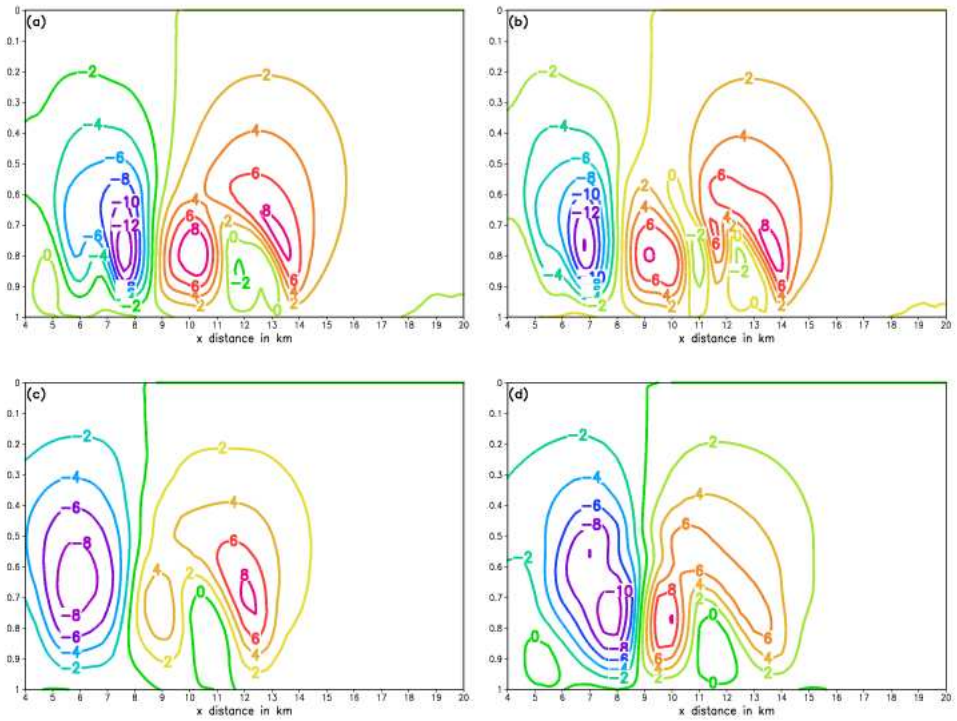

Figure 5.13: Marginally and poorly resolved flow in the cold bubble test. The $\hat{w}$ component of the wind after 900 s in the right-hand part of the integration domain, for $0 \leq \sigma \leq 1$: (a) $\Delta z \approx \Delta x = 200\,m$ with second order differencing; (b) $\Delta z \approx \Delta x = 200\,m$ with fourth order differencing; (c) $\Delta z \approx \Delta x = 400\,m$ with fourth order differencing; (d) $\Delta z \approx 100\,m$, $\Delta x = 500\,m$ with fourth order differencing. The D_3 scheme with second order discretization of spatial derivatives was used in the advection step. The Shapiro filter with $p = 4$ was used. $K_s = 50\,m^2 s^{-1}$. The contour interval is 2 ms^{-1}.

Table 5.5: Comparison of minimum and maximum values of θ', u and $\hat{w}$ for the cases of marginally and poorly resolved flow. The spatial resolutions corresponding to the listed values are $\Delta z \approx \Delta x = 200\,m$ (M-2 and M-4), $\Delta z \approx \Delta x = 400\,m$ (P) and $\Delta z \approx 100\,m$, $\Delta x = 500\,m$ (PM). Fourth order differencing was used to discretize the adjustment step equations, except for simulation M-2, where second order differencing was used.

Variable	M-2	M-4	P	PM
θ'_{min}	-10.94	-11.60	-9.35	-11.21
θ'_{max}	0.32	0.34	0.65	1.03
u_{min}	-14.37	-13.80	-12.48	-14.82
u_{max}	34.38	33.91	21.18	29.18
w_{min}	-13.56	14.03	-8.84	-11.28
w_{max}	9.70	9.07	8.56	10.05

experiments is considerably larger than the size of the advection time-steps used in the cold bubble solutions shown by Gallus and Rancic (1996) and Janjic et al. (2001). In both these studies, split-explicit techniques are used to solve the fully-elastic equations cast in vertical coordinates based on the hydrostatic pressure field, with Eulerian procedures employed for the advection terms. Janjic et al. (2001) used a time-step of 0.3 s, whilst Gallus and Rancic (1996) used "an advection time-step twice the sound wave time-step". Gallus and Rancic state that they obtained similar results using an advection time-step as large as 16 times the sound wave time-step, provided diffusion or filtering is increased. They found that this results in small damping of the meteorologically significant features. However, for general atmospheric applications, fully-elastic models employing split-explicit techniques with Eulerian procedures for the advection would be limited to ratios of about 4:1 between the advection and sound wave time steps (Janjic et al., 2001; also see Chapter 4).

In a series of mountain wave experiments using explicit techniques, Room et al. (2001) found the σ coordinate MP model stable at advection Courant numbers varying between 0.005 and 0.024, whilst the NHAD model was stable at advection Courant numbers varying between 0.025 and 0.3. Thus, the values of Courant numbers in the experiments performed so far in the present study, associated with the time-step $\Delta t_s = 1\,s$, are relatively large. It is interesting to investigate the performance of the split semi-Lagrangian scheme at even larger advection time-steps and Courant numbers, in order to quantify the advantages to be gained from the semi-Lagrangian approach used for the advection terms. It is also useful to investigate the performance of the scheme at larger adjustment time-steps. Since the quasi-elastic equations are filtered of vertically propagating acoustic modes, it may be expected that larger adjustment time-steps can

Table 5.6: Stability experiments $\Delta t_s = \Delta t_a$ for various simulations as described in the text.

Differencing and Filtering		TA	TB	TC	TD
SO	Δt_{s_max}	1.6	1.5	1.5	Unstable
	HC	0.69	0.64	0.65	-
	VC	0.54	0.53	0.58	-
SH	Δt_{max}	1.7	1.7	1.7	1.6
	HC	0.75	0.76	0.77	0.91
	VC	0.53	0.58	0.63	0.79
FH	Δt_{max}	1.2	1.2	1.2	1.2
	HC	0.48	0.48	0.50	0.52
	VC	0.36	0.38	0.41	0.45

be used compared to what would be allowed in similar discretizations of the fully-elastic equations. The maximum size of the adjustment time-step used in the split semi-Lagrangian formulation may be expected to be determined by the fast propagating Lamb and gravity waves described by the quasi-elastic equations.

The ratio $\Delta t_s/\Delta t_a$ was 10 in all the previously performed experiments. In addition to the stability tests performed in this section, it is interesting to investigate the performance of the split semi-Lagrangian scheme for different ratios of $\Delta t_s/\Delta_a$.

The resolution and general design of the experiments described in this section are as for the reference solution (see section 5.2.3). In the first set of experiments performed, $\Delta t_s = \Delta t_a$. Working in increments of 0.1 s, a large number of experiments with increasingly larger time-steps was performed, until numerical stability was destroyed within the 900 s integration period. These experiments were performed for the different choices of diffusion coefficients described in section 5.2.4, applied separately to the cases of second order differencing without application of the Shapiro filter (simulations SO), second order differencing with application of the Shapiro filter after each time-step (simulations SH), and fourth order differencing with application of the Shapiro filter after each time-step (simulations FH). The maximum allowable time-steps for the various numerical configurations are displayed in Table 5.6. The associated maximum horizontal and vertical advection Courant numbers attained during the 900 s integration period are also listed in the table. Columns TA, TB, TC and TD in the Table represent respectively diffusion coefficients of $K_s = 75\,m^2s^{-1}$, $K_s = 50\,m^2s^{-1}$, $K_s = 25\,m^2s^{-1}$ and $K_s = 0\,m^2s^{-1}$.

A few conclusions may be drawn from Table 5.6:

- a comparison between the SO and SH results reveals that application of the Shapiro filter results in only a slight increase in the maximum allowable time-step $\Delta t_s = \Delta t_a$, in simulations where explicit diffusion is applied (columns TA to TC). Clearly, the use of explicit diffusion effectively suppresses the nonlinear stability that may develop in association with two-grid interval noise. If no explicit diffusion is used, the SO simulation is unstable, whilst the SH simulation is stable with a maximum allowable time-step similar to the SH and SO cases where explicit diffusion is applied. This points to an efficient removal of two-grid-interval waves by the Shapiro filter in the case of zero explicit diffusion;

- in the stable SO, SH and FH simulations, the maximum advection Courant numbers generally decrease only slightly with an increase in the magnitude of explicit diffusion used (an exception is the SH simulation obtained with zero explicit diffusion and $t_s = t_a = 1.6\,s$, which is on the verge of becoming unstable at t = 900 s). Thus, the explicit diffusion used has only a small damping effect on the extreme values reached by the horizontal and vertical winds. This conclusion is related to the results in sections 5.2.4, 5.2.5 and 5.2.6, where the displacement of the gust front at t = 900 s became only slightly smaller with an increase in the explicit diffusion used. It may be said that the explicit diffusion has only a small damping effect on the wind field and the advection process. However, it was illustrated in sections 5.2.4 to 5.2.6 that the use of explicit diffusion may considerably retard the gravity wave phase speed and the time evolution of the Kelvin-Helmholtz intability rotors;

- the FH scheme becomes unstable at smaller time-steps $\Delta t_s = \Delta t_a$ than the SO and SH schemes. This may be due to the more accurate representation of the gravity wave phase speed when fourth order differencing is used, compared to the more retarded gravity wave phase speed asscociated with the second order discretizations (see Chapter 4).

Figure 5.14 shows the potential temperature perturbation at t = 900 s for some of the time-step experiments performed. The fields in Panels a to c were obtained using second order differencing with time-steps of respectively $\Delta t_s = \Delta t_a = 0.5\,s$, $\Delta t_s = \Delta t_a = 1\,s$ and $\Delta t_s = \Delta t_a = 1.5\,s$. The field in Panel d was obtained using fourth order differencing, with $\Delta t_s = \Delta t_a = 1\,s$. In all the simulations the Shapiro filter with $p = 4$ was applied after each time-step (see section 5.2.5). $K_s = 50\,m^2 s^{-1}$.

A few conclusions may be drawn from considering the results depicted in Figure 5.14, and the corresponding simulations obtained with time steps $\Delta t_s = 1\,s$, $\Delta t_a = 0.1\,s$ (Panel b of Fig. 5.6 for second order differencing and Panel b of Fig. 5.8 for fourth order differencing):

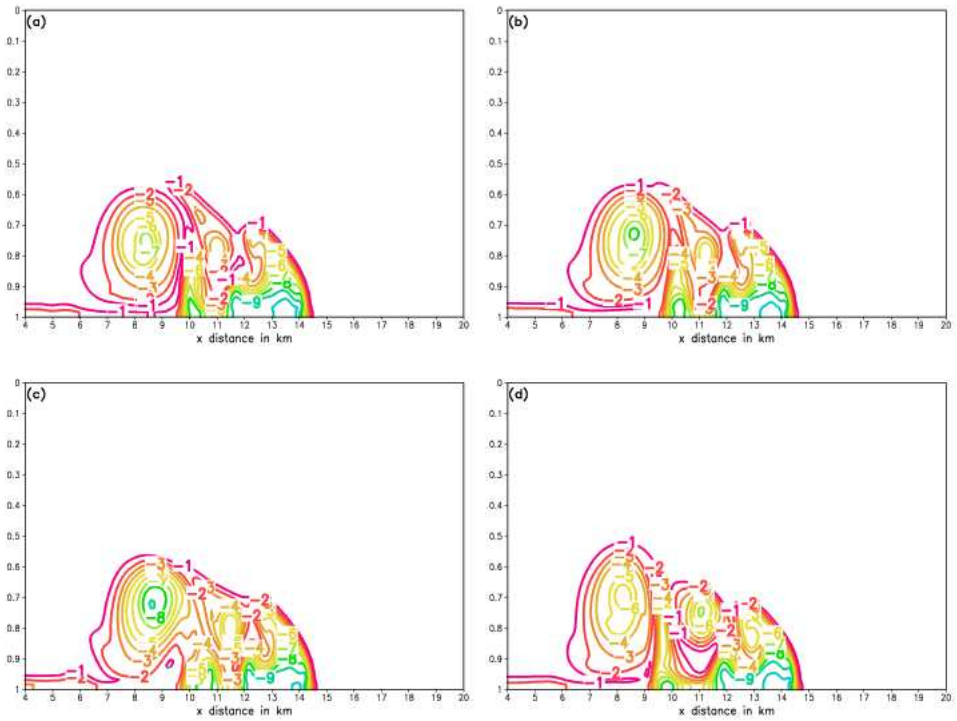

Figure 5.14: The potential temperature deviation after 900 s for the cold bubble test, in the right-hand part of the integration domain, for $0 \leq \sigma \leq 1$: (a) SH simulation with $\Delta t_s = \Delta t_a = 0.5\,s$; (b) SH simulation with $\Delta t_s = \Delta t_a = 1\,s$; (c) SH simulation with $\Delta t_s = \Delta t_a = 1.5\,s$; (d) FH simulation with $\Delta t_s = \Delta t_a = 1\,s$. The Shapiro filter with $p = 4$ was used, with $K_s = 50\,m^2 s^{-1}$. The contour interval is 1K.

- the progress of the gust front in all the simulations with $\Delta t_s = \Delta t_a$ is somewhat slower by t = 900 s than in the corresponding simulations with $\Delta t_s = 1\,s$ and $\Delta t_a = 0.1\,s$. Simulations with $\Delta t_s = \Delta t_a$ where the Shapiro filter is applied less frequently, or not at all, show similar behaviour. Thus, the slower progress of the gust front in the $t_a = t_s$ simulations is likely to be the result of the damping at high wave numbers exerted by the bicubic spatial interpolations used in the semi-Lagrangian advection step (see Chapter 4). The effect of the damping nature of the advection scheme appears to be less if an adjustment time-step smaller than the advection time-step is used (see Panels b of Figs. 5.6 and 5.8). In such a case, flow features may develop more unhindered (by damping) during the adjustment process.

- Three rotors are simulated at t = 900 s in all the experiments performed with $\Delta t_s = \Delta t_a = 1\,s$ (Fig. 5.14), in correspondence to the simulations obtained with $\Delta t_s = 1\,s$, $\Delta t_a = 0.1\,s$ (Panels b of Figs. 5.6 and 5.8). However, for the case of second order differencing (Panels a to c of Fig. 5.14), the first rotor to develop in the $\Delta t_s = \Delta t_a$ simulations is more intense and the second rotor somewhat underdeveloped at t = 900 s compared to the coresponding simulations with $\Delta t_s = 1\,s$, $\Delta t_a = 0.1\,s$ (Panel b of Fig. 5.6).

- The third rotor in the t = 900 s solution obtained with fourth order differencing and $\Delta t_s = \Delta t_a = 1\,s$ (Panel d of Fig. 5.14) is better developed than in the corresponding solution obtained with second order differencing (Panel b of Fig. 5.14). In fact, the time-evolution of the three rotors depicted in Fig. 5.14 Panel d, obtained with the fourth order discretization, is very similar to the corresponding simulation obtained with $\Delta t_s = 1\,s$, $\Delta t_a = 0.1\,s$ (Panel b of Fig. 5.8). This illlustrates that the fourth order differencing scheme provides more accurate results than second order differencing at large time-steps (in simulations with second order differencing at relatively large time-steps the time evolution of the three rotors are somewhat different compared to the corresponding simulations performed with smaller adjustment time-steps).

- It may be said that the split semi-Lagrangian scheme, for both second and fourth order differencing applied in the adjustment step, produces very reasonable results at large adjustment time-steps $\Delta t_a = \Delta t_s$. The adjustment time-steps used here are considerably larger than the "sound wave time-steps" used in the corresponding cold bubble solutions shown by Gallus and Rancic (1996), Janjic et al. (2001) and Straka et al. (1993).

In order to investigate the maximum time-steps allowed during the semi-Lagrangian advection step, a second set of experiments was performed. In these experiments the adjustment time-step was kept fixed at $\Delta t_a = 0.5\,s$, but the advection time-step Δt_s was increased in increments of 0.5 until the numerical stability was

Table 5.7: Advection time-step stability experiments, with $\Delta t_a = 0.5$, for various simulations as described in the text.

Differencing and Filtering		TA	TB	TC	TD
SO	Δt_{smax}	1.5	1.5	1.5	Unstable
	HC	0.62	0.62	0.63	-
	VC	0.40	0.43	0.48	-
SH	Δt_{smax}	3.0	3.0	3.0	2.5
	HC	1.20	1.21	1.21	1.03
	VC	0.74	0.77	0.82	0.74
FH	Δt_{smax}	2.0	2.0	2.0	1.5
	HC	0.79	0.79	0.80	0.81
	VC	0.51	0.53	0.56	0.65

destroyed within the 900 s integration period. The maxiumum advection time-step for which numerical stability is maintained is denoted by Δt_{smax}. The experimental settings and notation in Table 5.7 are as described for Table 5.6. In the SH and FH simulations, the Shapiro filter was applied after each adjustment time-step.

A few conclusions can be made from considering the stability experiments presented in Table 5.7:

- the split semi-Lagrangian scheme employing second order differencing in the adjustment step, but without application of the Shapiro filter (simulations SO), is unstable when no explicit diffusion is applied. It is stable at advection Courant numbers as large as about 0.62, for the cases where explicit diffusion is used;

- the split semi-Lagrangian scheme employing second order differencing in the adjustment step, with application of the Shapiro filter after each adjustment time-step (simulations SH) is stable at advection Courant numbers as large as 1.2, provided that explicit diffusion is used. Even for the case of zero diffusion, the scheme is stable at Courant numbers slightly larger than unity. Application of the Shapiro filter, and the associated removal of two-grid-interval waves and noise from the grid, clearly allows the use of significantly larger advection time-steps compared to the SO simulations;

- the split semi-Lagrangian scheme employing fourth order differencing in the adjustment step, with application of the Shapiro filter after each adjustment time-step (simulations SH), is stable for Courant numbers as large as about 0.8. The semi-Lagrangian advection procedure is unconditionally stable for the case of linear advection (see Chapter 4). For fourth

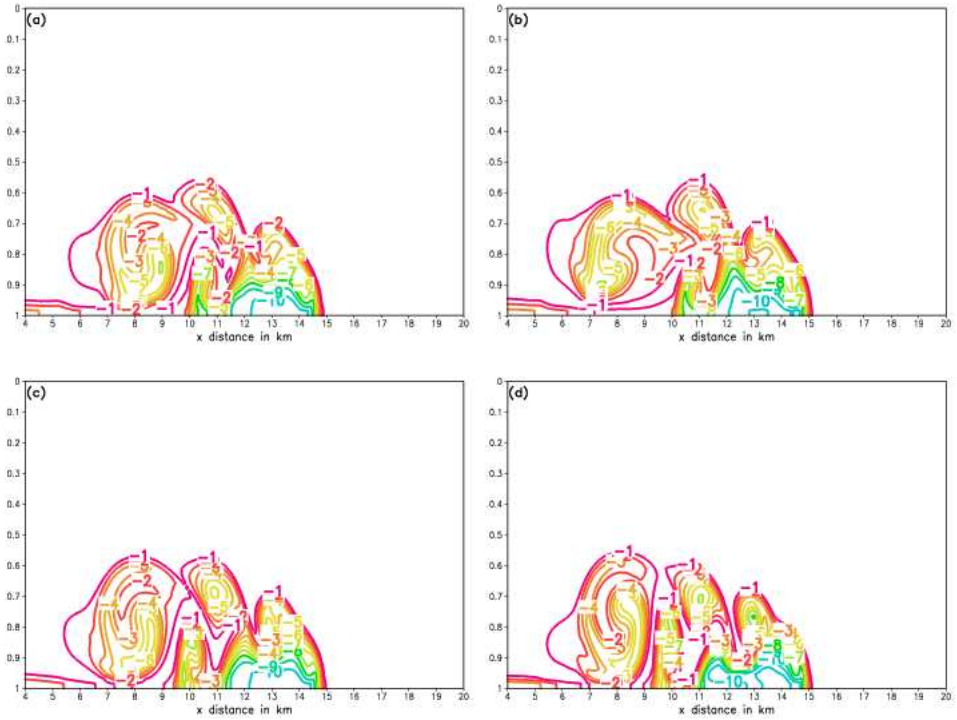

Figure 5.15: The potential temperature deviation after 900 s for the cold bubble test, in the right-hand part of the integration domain, for $0 \leq \sigma \leq 1$: (a) SH simulation with $\Delta t_s = 2\,s$, $\Delta t_a = 0.5\,s$ and $K_s = 50\,m^2 s^{-1}$; (b) SH simulation with $\Delta t_s = 3\,s$, $\Delta t_a = 0.5\,s$ and $K_s = 50\,m^2 s^{-1}$; (c) FH simulation with $\Delta t_s = 2\,s$, $\Delta t_a = 0.5\,s$ and $K_s = 50\,m^2 s^{-1}$; (d) FH simulation with $\Delta t_s = 2\,s$, $\Delta t_a = 0.5\,s$ and $K_s = 25\,m^2 s^{-1}$. The Shapiro filter with $p = 4$ was used . The contour interval is 1K.

> order differencing the gravity wave phase speed is simulated more accurately with less retardation than in the case of second order differencing. Thus, the instabilities observed at relatively large advection Courant numbers may possibly be attributed to nonlinear instability that develops in association with these relatively fast moving gravity waves that are not sufficiently controlled by the Shapiro filter at the shortest resolvable scales.

Some of the t = 900 s solutions obtained using large advection time-steps are displayed in Fig. 5.15. Panels a and b show the potential temperature perturbation obtained using second order spatial diferencing, with application of the Shapiro filter at each adjustment time-step (numerical design SH), for advection time-steps of $\Delta t_s = 2\,s$ and $\Delta t_s = 3\,s$ respectively. $K_s = 50\,m^2 s^{-1}$ for these simulations. Panel c and d show solutions obtained using fourth order

spatial differencing (numerical design FH) with $\Delta t_s = 2\,s$. The diffusion coefficients used to obtain the simulations in Panels c and d are $K_s = 50\,m^2 s^{-1}$ and $K_s = 25\,m^2 s^{-1}$ respectively.

A few conclusions may be drawn from considering the results displayed in Fig. 5.15:

- even at advection time-steps as large as 2.5 s, the solutions contain the basic flow features, namely the development of three rotors by t = 900 s.
- The gust front has progressed a distance of about 15 km by t = 900 s in all the simulations, which is in close agreement with the simulations obtained using $\Delta t_s = 1\,s$ and $\Delta t_a = 0.1\,s$ (see sections 5.2.5 and 5.2.6). This result confirms that the somewhat slower progress of the gust front in the simulations with $\Delta t_s = \Delta t_a$ (see Fig. 5.14) is caused by the damping induced by the bicubic interpolation scheme during each time-step of the model, and not by the size of the time-steps. In the present simulations (Fig. 5.7), the gravity waves are less damped by the relatively infrequent application of the bicubic interpolation procedure. Thus, a ratio of $\Delta t_s/\Delta t_a$ larger than unity is recommended for application of the split semi-Lagrangian procedure.
- In the simulations where fourth order differencing is used (Panels c and d of Fig. 5.7), the third rotor is better developed than in the second order solutions (Panels a and b of Fig. 5.7). The potential temperature perturbation field for the case $K_s = 25\,m^2 s^{-1}$ and mixed second-fourth order differencing, even shows signs of a fourth rotor starting to impact on the leading edge of the gust front.

Overall, it may be said that the split semi-Lagrangian solution procedure is stable and quite accurate at large adjustment and advection time-steps (that is, at large Courant numbers). The good stability properties of the split semi-Lagrangian solution procedure stem from the semi-Lagrangian approach used for the advection terms, and the quasi-elastic nature of the equations.

5.2.10 Efficiency of the elliptic solver

Solving the elliptic equation at the end of each adjustment time-step, represents a fundamental contribution to the number of computations performed in the split semi-Lagrangian solution procedure. In this section, the efficiency of the second and fourth order elliptic solvers described in sections 4.6 and 5.2.6 are quantified for the case of the cold bubble test. Table 5.8 shows the number of iterations required per second of integration time, for various of the experiments conducted in previous sections. Rows SO, SH and FH represent respectively simulations obtained by using second order differencing without application of the Shapiro filter, second order differencing with application of the Shapiro filter after the N_{th} adjustment time-step, and fourth order differencing with application

Table 5.8: Efficiency of the second and fourth order elliptic solvers, giving the amount of iterations required for convergence per second of integration time, for various simulations as described in the text.

Simulation	EA	EB	EC	ED	ET1	ET2	ER1	ER2
SO	93.6	101.2	114.1	165.7	32.1	53.3	117.2	81.6
SH	91.3	98.6	110.3	129.2	31.4	57.9	104.4	88.4
FH	92.2	98.3	108.8	123.0	31.9	59.2	105.4	97.2

of the Shapiro filter after the N_{th} adjustment time-step. The explicit diffusion applied along the x and σ axis is as described in section 5.2.4. Columns EA to ED represent simulations obtained with diffusion coefficients of respectively $K_s = 75\,m^2s^{-1}$, $K_s = 50\,m^2s^{-1}$, $K_s = 25\,m^2s^{-1}$ and $K_s = 0\,m^2s^{-1}$. These experiments were performed at 100 m resolution with time-steps $\Delta t_s = 1\,s$ and $\Delta t_a = 0.1\,s$, and are described in sections 5.2.4 (SO), 5.2.5 (SH) and 5.2.6 (FH). The simulations represented by columns ET1 and ET2 were also perfomed at 100 m resolution, but with $\Delta t_s = \Delta t_s = 1\,s$ (ET1) and $\Delta t_s = 1.5\,s$, $\Delta t_a = 0.5\,s$ (ET2). $K_s = 50\,m^2s^{-1}$ for these experiments (which are described in section 5.2.8). The last two columns in Table 5.8, are from the low resolution experiments described in section 5.2.7. Column ER1 represents the 200 m simulations performed with time-steps $\Delta t_s = 2\,s$, $\Delta t_s = 0.2\,s$, whilst column ER2 represents the 400 m simulations obtained with time-steps $\Delta t_s = 4\,s$, $\Delta t_a = 0.4\,s$. $K_s = 50\,m^2s^{-1}$, and fourth order differencing was used to discretize the spatial derivatives in the adjustment step equations for the low resolution experiments discussed here.

From the results shown in Table 5.8, the following conclusions may be drawn:

- The number of iterations required for convergence increases as the magnitude of explicit diffusion decreases (compare columns EA to ED for each of the numerical designs SO, SH and FH). This is to be expected, since finer scale structures are described by the simulations that use relatively small magnitudes of explicit diffusion (see sections 5.2.4, 5.2.5 and 5.2.6).

- Comparing the SO and SH simulations for fixed diffusion coefficients, shows that application of the Shapiro filter generally leads to faster convergence of the SOR procedure. This may be attributed to an effective removal of two-grid interval waves and associated noise by the filter. The slow convergence in the case of zero diffusion without application of the Shapiro filter (simulation SO column ED) indicates, in particular, the negative effect of two-grid-interval waves on the eficiency of the elliptic solver. For the relatively large advection time-step simulations (column ET2) and relatively low spatial resolution simulations (column ER2), convergence is

somewhat slower when the filter is applied (compared to the corresponding SO simulations).

- The number of iterations required for the solutions obtained with fourth order differencing (row FH in Table 5.8) is quite similar to the number required in the corresponding solutions obtained with second order differencing (row SH of Table 5.8). In fact, for most of the solutions obtained with $\Delta t_s = 1\,s$, $\Delta t_a = 0.1\,s$ at 100 m resolution, less iterations are required for by fourth order solver than by the second order solver per second of integration time. Thus, the larger amount of grid points used by the fourth order solver compared to the second order solver do not lead to slower convergence iteration wise. Of course, more calculations are performed when the fourth order solver is used (since it makes use of 25 surrounding points for the geopotential calculation at each grid point away from the boundaries, compared to the 9 points needed by the second order solver). In this way, the use of the fourth order solver does slow down the numerical integration process.

- The 200 m grid spacing simulations require slightly more iterations per second of integration time than the corresponding 100 m grid spacing simulations (compare columns EB and ER1). The 400 m solutions require less iterations per second of integration time than the corresponding 200 m and 100 m simulations.

- The simulations employing the time-steps $\Delta t_s = \Delta t_a = 1\,s$ and $t_s = \Delta 1.5\,s$, $\Delta t_a = 0.5\,s$ require significantly less iterations per second of integration time than the corresponding simulations with $\Delta t_s = 1\,s$ and $\Delta t_a = 0.1\,s$ (compare columns ET1, ET2 and EB). Clearly, significant advantages are to be gained in computation time with an increase of particularly the adjustment time-step used in the simulations.

Xue (1989) has developed a FFT procedure to solve the closely related elliptic equation used in the σ coordinate MP model (see section 4.6). It is not clear to what extent this procedure offers computational advantages over the SOR procedure aplied in this study. The procedure of Xue (1989) combines the use of a double Fourier transform, a Gaussian elimination procedure and an iterative technique to solve the ellipctic equation (Xue, 1989; Xue and Thorpe, 1991, also see section 4.6). They found that only "a few" iterations are needed per time-step. However, the time-steps applied in the studies by Xue (1989) and Xue and Thorpe are comparativley smaller to the "1 s of the integration time" over which the iterations are counted in this study . They also do not state explicitly how the number of iterations required depends on the size of the time-step used, however, their explicit solutions were generally performed at Courant numbers much smaller than in the experiments described in the present study (see section 4.2.9). It should also be kept in mind that in addition to the iterative process used in the method of Xue (1989), more calculations are needed for the double Fourier transform and Gaussian elimination that are applied. Still, potential

computational advantages of the approach followed by Xue (1989) over the present SOR procedure is worth to be explored (see section 4.6).

5.3 Warm bubble experiments in two spatial dimensions

5.3.1 Design of the warm bubble tests

The warm bubble simulations presented in this section closely follow the experimental design of the two-dimensional simulations performed by Janjic et al. (2001). Similar experiments were performed by Droegemeier (1985), Mendez-Nunez and Carroll (1994) and Gallus and Rancic (1996). In an initially dry, at rest and isentropic atmosphere with potential temperature 300 K, a circularly-shaped initial disturbance is introduced for the potential temperature:

$$\Delta\theta_0(x,z) = 6.6\cos^2(\frac{\pi}{2}r), \tag{5.6}$$

for $r \leq 1$, where $r^2 = \left[(x-x_c)/x_t\right]^2 + \left[(z-z_c)/z_t\right]^2$, $x_c = 0$ m, $z_c = 2750$ m, $x_t = 2500$ m and $z_t = 2500$ m.

The integration domain extends over $-10000\,m \leq x \leq 10000\,m$ in the horizontal. The top of the model domain is chosen to be 135 hPa (about 13500 m). The center of the initial disturbance is in the middle of the domain in the x direction, that is, 10 km away from the lateral boundaries. Unless where stated differently, the horizontal resolution in the following experiments is 100 m, and 135 equally spaced σ levels are used to give a vertical resolution of about 100 m on the average. The bubble simulations of Gallus and Rancic (1996) and Janjic (2001) were performed at similar spatial resolutions, and also employed terrain-following pressure-based coordinates. Mendez-Nunez and Carroll performed corresponding experiments at 500 m resolution, using the fully-elastic z coordinate equations. It may be noted that a different class of warm bubble experiments have been performed at even higher resolutions (10 - 20 m) over much smaller domains using a smaller temperature perturbation (Robert, 1993; Mendez-Nunez and Carroll, 1994; Hsu and Sun, 2001).

5.3.2 A reference solution obtained with fourth order spatial differencing

The numerical settings of the split semi-Lagrangian scheme that were found to give superior results in the cold bubble tests, are used to obtain the reference warm bubble simulation of the present section. In the semi-Lagrangian advection step, the D_3 scheme of McGregor (1993) is used for the calculation of departure points (see Chapter 4 and section 5.2.7). The spatial derivatives in the departure point formula and the term $A^*_{p_s}$ are evaluated using second order spatial differencing. All spatial derivatives in the adjustment step equations are

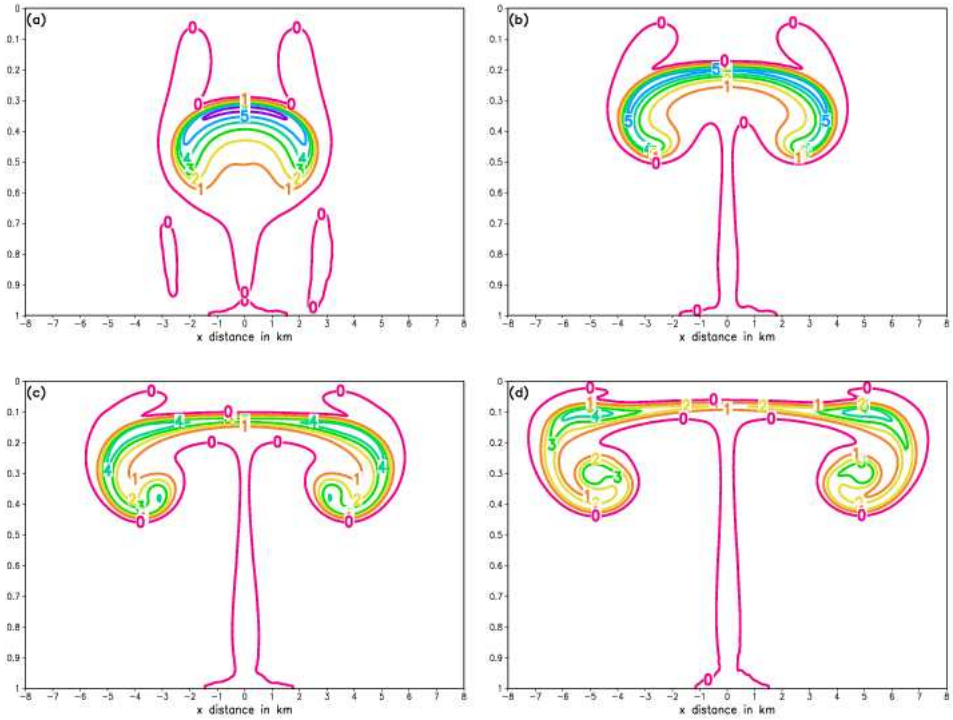

Figure 5.16: Reference solution for the warm bubble test. Potential temperature perturbation for $-8000\,m \leq x \leq 8000\,m$ and $0 \leq \sigma \leq 1$: (a) after 360 s; (b) after 520 s; (c) after 720 s; (d) after 900 s. The contour interval is 1 K.

discretized using fourth order differencing (see Chapter 4 and section 5.2.6). The Shapiro filter is applied with p = 4, with lower order filtering performed near the lateral and vertical boundaries (see Chapter 4 and section 5.2.5).

The values of the diffusion coefficients used in the explicit diffusion step, for diffusion along the x axis, are $K_s = 300\,m^2 s^{-1}$ and $K_{Ts} = 50\,m^2 s^{-1}$. Similar magnitudes of explicit diffusion are applied along the σ axis, for u and T respectively. That is, $K_\sigma = K_s\left(\Delta\sigma^2/\Delta x^2\right)$ and $K_{T\sigma} = K_{Ts}\left(\Delta\sigma^2/\Delta x^2\right)$, so that the non-dimensional quantity $K\Delta t_s/\Delta n^2$ defined in Chapter 4 has the same magnitude along the x and σ axis, for u and T respectively (see Janjic et al., 2001). The magnitude of explicit diffusion applied to the u field is fairly large, compared to the corresponding magnitudes of explicit diffusion used in the cold bubble tests. The choice of explicit diffusion coefficients used here follows the experimental design of Janjic et al. (2001). In fact, in order to reproduce the basic time evolution of the warm bubble, as discussed in the experiments of Gallus and Rancic (1996) and Janjic et al. (2001), the relatively large diffusion of the u field is necessary. If smaller magnitudes of explicit diffusion are used,

finer scale structures of the flow field may be resolved (see the next section). The elliptic equation is solved with SOR, using $rl = 1.6$ as relaxation factor. The solution was found to be sufficiently converged using $\epsilon = 10^{-6}$ as criterion of convergence. On average 16.13 iterations are required per second of integration time over the 900 s integration period, that is, less than 2 iterations per adjustment time-step $t_a = 0.1\,s$ (see row WREF of Table 5.9). The potential temperature deviation θ' from the isentropic background state after 360, 540, 720 and 900 s is shown in Fig. 5.16. The contour interval is 1 K. The corresponding vertical velocity fields $\hat{w}$ are shown in Fig. 5.17, with contour interval 2ms^{-1}.

In Fig. 5.16 it can be seen that that warm bubble is simulated to ascend in the isentropic environment. This occurs in conjunction with an updraft that develops in response to the positive buoyancy associated with the presence of the warm bubble in the colder environment (Fig. 5.17). Since the updraft is the strongest at the center of the bubble, it rises the fastest, causing the potential temperature gradient to steepen in the upper part of the bubble (Fig. 5.16 Panels a and b). By mass conservation, the updraft induces convergence below the vertical velocity maximum, and divergence occurs above the vertical velocity maxiumum. The convergence-divergence pattern results in the formation of two vortices, one on each side of the symmetry axis. As noted in the lower resolution experiments of Mendez-Nunez and Carroll (1994), relatively cooler air from the environment is entrained into the lower part of the bubble by the two rotors (Note the intrusion of the 0 K contour into the lower part of the bubble in Panels b, c and d of Fig. 5.16). The divergent flow associated with the rotors at the uper part of the bubble causes the potential temperature maximum to move away from the center axis. The splitting that occurs in the potential temperature field is visible in the t = 540 s potential temperature deviation field (Panel b of Fig. 5.16), and is well developed in the t = 720 and 900 s fields (Panels c and d of Fig. 5.16). Thus, two potential temperature maxima evolve, one on each side of the symmetry axis.The positive buoyancy associated with these potential temperature maxima, leads to the development of two secondary updrafts (and eventually two secondary rotors) on both sides of the symmetry axis (Panels c and d of Fig. 5.17). A portion of the high potential temperature air is drawn into each main rotor, causing two sub-maxima to be present by t = 900 s on each side of the symmetry axis, within each of the main rotors.

The rate of ascent and the intensity of the disturbance shown in Fig. 5.16 agree with those reported by Gallus and Rancic (1996) and Janjic (2001) (Note that the present results are displayed in a $x - \sigma$ coordinate system, whilst the mentioned autors display their results in an $x - z$ coordinate system). The time-evolution of the main flow features (the development of the rotors and the formation of a potential temperature maximum on each side of the symmetry axis) are also similar for the various simulations.

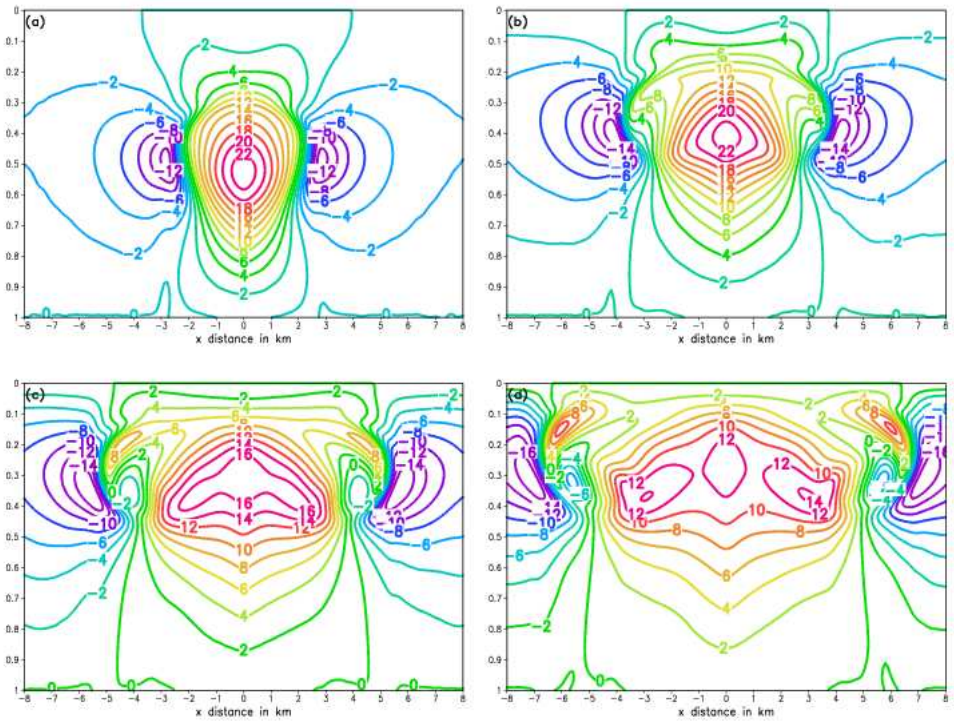

Figure 5.17: Reference solution for the warm bubble test. Vertical velocity $\hat{w}$ for $-8000\,m \leq x \leq 8000\,m$ and $0 \leq \sigma \leq 1$: (a) after 360 s; (b) after 520 s; (c) after 720 s; (d) after 900 s. The contour interval is 2 ms^{-1}.

The horizontal and vertical velocities u and $\hat{w}$ attains maximum values of $u_{max} = 16.37$ and $w_{max} = 24.20\,ms^{-1}$during the 900 s integration period, respectively. The corresponding maximum values of the horizontal and vertical advection Courant numbers attained (see Chapter 4) are 0.16 and 0.29, respectively (see row WREF of Table 5.9). The simulations by Gallus and Rancic (1994) were performed using a sound wave time-step of less than 0.09 s, and an advection time-step of double the sound-wave time-step. The experiments by Janjic et al. (2001) were performed using a time-step of 0.3 s. Thus, the advection time-step $\Delta t_s = 1\,s$ used in the present study is considerably larger than the time-steps used in the studies by the mentioned authors. The simulations depicted in Figs. 5.16 and 5.17 are smooth and without any signs of two-grid-interval noise. This indicates the application of the Shapiro filter, and the additional damping that result from the bicubic interpolation and explicit diffusion, effectively removes the two-grid-interval waves from the nonstaggered grid. In fact, the split semi-Lagrangian scheme produces stable and smooth warm bubble solutions at much larger time-steps $\Delta t_s$and Δt_a, with larger associated Courant numbers (see section 5.3.4).

5.3.3 Marginally and poorly resolved flow

In this section, lower resolution warm bubble experiments are performed, in order to investigate the performance of the split semi-Lagrangian scheme for the case of flow that is marginally or poorly resolved. Corresponding cold bubble tests were carried out in section 5.2.8. As mentioned earlier, operational constaints are likely to limit the application of nonhydrostatic models to NWP and climate simulation to resolutions where the flow is only marginally or even poorly resolved (see Chapter 1 and section 5.2.8).

The experiments performed in the present section closely follow the experimental design used to obtain the reference solution. The only differences are with respect to the time-steps, spatial resolutions and explicit diffusion coefficients that are used. Some details of the simulations are listed in Table 5.9. In the first two experiments performed, the horizontal resolution is 200 m, and 68 equally spaced σ levels are used to give a vertical resolution of about 200 m on the average. The time-steps used are $\Delta t_s = 2\,s$, $\Delta t_a = 0.2\,s$. In the first experiment (see row WM of Table 5.9), $K_s = 300\,m^2s^{-1}$ and $K_{Ts} = 50\,m^2s^{-1}$. Diffusion of similar magnitudes is applied along the σ axis, for u and T respectively (see the previous section). Thus, the explicit diffusion coefficients used in this experiment are exactly the same as for the reference warm buble experiment, however, the nondimensional quantity $K\Delta t_s/\Delta n^2$ (see Chapter 4) is two times smaller with respect to the value it assumes in the reference solution. The 200 m simulation may be therefore be expected to be less diffused than the reference simulation. In the second 200 m simulation performed (row WMD of Table 5.9), the diffusion coefficients used are $K_s = 600\,m^2s^{-1}$ and $K_{Ts} = 100\,m^2s^{-1}$. Diffusion of similar magnitudes is applied along the σaxis, for u and T respectively. Thus, for this simulation the non-dimensional quantity $K\Delta t_s/\Delta n^2$ has the same value

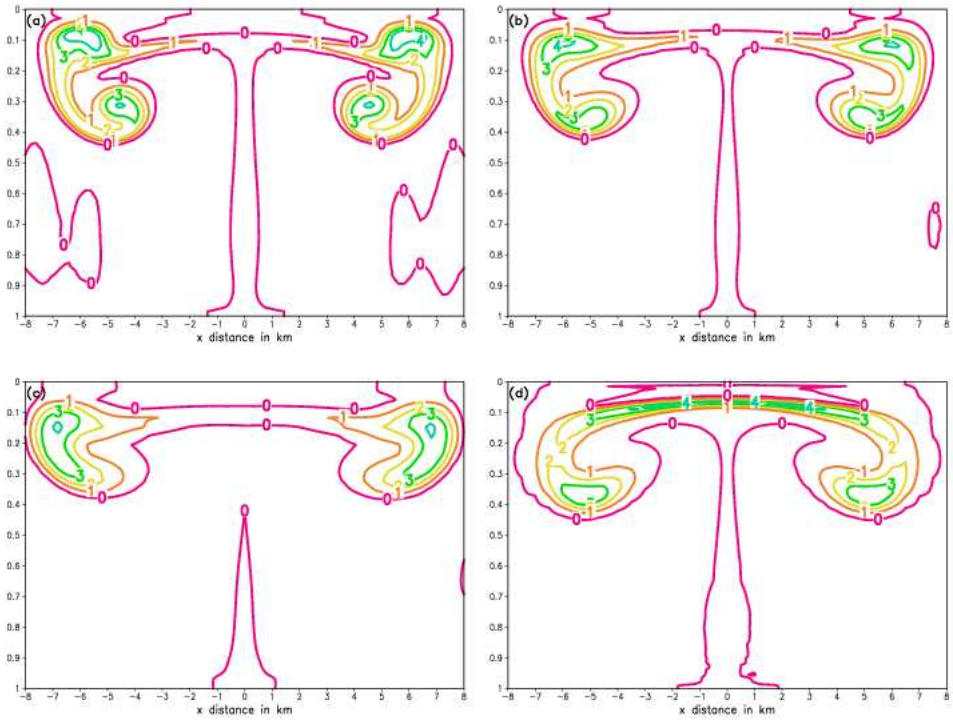

Figure 5.18: Marginally and poorly resolved flow in the warm bubble test. The potential temperature deviation after 900 s, for $-8000\,m \leq x \leq 8000\,m$ and $0 \leq \sigma \leq 1$: (a) $\Delta z \approx \Delta x = 200\,m$ with $K_s = 300\,m^2s^{-1}$ and $K_{Ts} = 50\,m^2s^{-1}$;(b) $\Delta z \approx \Delta x = 200\,m$ with $K_s = 600\,m^2s^{-1}$ and $K_{Ts} = 100\,m^2s^{-1}$; (c) $\Delta z \approx \Delta x = 400\,m$ with $K_s = 1200\,m^2s^{-1}$ and $K_{Ts} = 200\,m^2s^{-1}$; (d) $\Delta z \approx 100\,m$, $\Delta x = 500\,m$ with $K_s = 300\,m^2s^{-1}$ and $K_{Ts} = 50\,m^2s^{-1}$. The contour interval is 1 K.

as for the reference simulation, and it may be expected to be similarly diffused. The third simulation is performed using a horizontal resolution of 400 m, and 35 equally spaced σlevels are used to give a resolution of about 400 m in the vertical, on the average (see row WP of Table 5.9). The time-steps used are $\Delta t_s = 4\,s$, $\Delta t_a = 0.4\,s$. The diffusion coefficients used are $K_s = 1200\,m^2 s^{-1}$ and $K_{Ts} = 200\,m^2 s^{-1}$, with diffusion of similar magnitudes applied along the σ axis, for u and T respectively. In the final experiment performed in this section, the horizontal resolution is 500 m, and 135 σ levels are used as in the reference simulation (row WPM of Table 5.9). The time-steps Δt_s and Δt_a and the explicit diffusion used are as specified for the reference simulation. The potential temperature deviation $\theta^{'}$ fields obtained for the various experiments, at t = 900 s, are shown in Fig. 5.18. The corresponding vertical velocity $\hat{w}$ fields are shown in Fig. 5.19.

A few remarks can be made with regard to the various t = 900 s solutions displayed in Figs. 5.18 and 5.19.

- The 200 m solution obtained with with $K_s = 300\,m^2 s^{-1}$ and $K_{Ts} = 50\,m^2 s^{-1}$ (Panels a of Figs. 5.18 and 5.13) is less diffused than the corresponding 100 m solution (Panels d of Figs. 5.16 and 5.17) and the 200 m solution obtained with $K_s = 600\,m^2 s^{-1}$ and $K_{Ts} = 100\,m^2 s^{-1}$ (Panels b of Figs. 5.12 and 5.19). This is most evident from the evolution of the potential temperature pattern by t = 900 s, as shown in Panel a of Fig. 5.18). For the relatively less diffused solution, the buoyancy of the potential temperature maxima on both sides of the symmetry axis has overcome the horizontal momentum provided by the rotors. In stead of moving largely sideways as in the more diffused simulations, the maxima shows a clear vertical displacement by t = 900 s. This vertical displacement is related to the development of two intense secondary updrafts, one on each side of the symmetry axis (Panel a of Fig. 5.19). These secondary updrafts are also present in the more diffused simulations, but are less intense (Panel d of Fig. 5.17 and Panel b of Fig. 5.19). The vertical displacement of the potential temperature maxima are also present in in 100 m solutions (not shown) obtained with diffusion coefficients having half the magnitude (or smaller) of those used to obtain the reference solution.

- For the relatively less diffused 200 m simulation, the a convergence criterion $\epsilon = 10^{-6}/2$ needs to be used to obtain a sufficiently converged solution. This is to be expected, since the relatively less diffused solution contains some finer scale and more intense structures than in the more diffused cases.

- The 400 m solution shown for t = 900 s (Panels c of Figs. 5.18 and 5.13) was obtained using explicit diffusion comparable to that used to obtain the reference solution. It shows the development of the main flow features, namely one rotor on each side of the symmetry axis. Potential temperature maxima are simulated to be present on both sides of the symmetry axis,

although the detail of two separated submaxima within the rotors (as in the higher resolution simulations) are not present. The development of two secondary updrafts are present in the 400 m solution for t = 900 s, although the two secondary rotors are not fully developed by this time.

- The evolution of the potential temperature perturbation field by t = 900 s obtained with $\Delta x = 500\,m$, $\Delta z \approx 100\,m$ (5.18) is similar to that of the reference solution. Potential temperature sub-maxima occur within each of the two main rotors. The main potential temperature maxima on either sides of the symmetry axis are not well developed, however. This is related to the fact that the secondary updrafts are only starting to evolve by t = 900 s (Panle d of Fig. 5.19).
- All the θ' and $\hat{w}$ fields shown are smooth and without any signs of numerical noise. It may be said that as in the corresponding cold bubble tests (section 5.2.8), the split semi-Lagrangian scheme functions well for the cases of marginally and poorly resolved flow.

5.3.4 Time-step experiments and stability

In this section, time-step and stability tests are performed, similar to those described in section 5.2.9 for the cold bubble tests. The resolution and general design of the experiments described in this section are as for the reference solution (see section 5.3.2). The only differences are with respect to the size of the time-steps, the criterion of convergence ϵ used and the frequency of application of the Shapiro filter. In the first set of experiments, $\Delta t_s = \Delta t_a$. The split semi-Lagrangian scheme is stable over the 900 s integration period for time-steps as large as 1.5 s (with application of the Shapiro filter after each adjustment time-step). However, for the solution to be fully converged using time-steps $\Delta t_s = \Delta t_a$ this large, a criterion of convergence $\epsilon = 10^{-6}/3$ needs to be used. In the second set of experiments performed, the adjustment time-step was kept fixed as $\Delta t_a = 0.5\,s$, and the Shapiro filter was applied after each adjustment step. Here it was found that the semi-Lagrangian scheme is unconditionally stable, and only accuracy requirements place a limit on the maximum time-step Δt_s to be used. The criterion of convergence $\epsilon = 2.10^{-6}/3\,s$ is sufficient for convergence of the $\Delta t_a = 0.5\,s$ tests.

Some of the t = 900 s solutions obtained using large time-steps are displayed in Figs. 5.20 (potential temperature perturbation θ') and 5.21 (vertical velocity $\hat{w}$). Panels a to d of Figs. 5.20 and 5.21 represent solutions obtained with time-steps $\Delta t_s = \Delta t_a = 0.5\,s$, $\Delta t_s = \Delta t_a = 1.5\,s$, $\Delta t_s = 2.5\,s$, $\Delta t_a = 0.5\,s$ and $\Delta t_s = 5\,s$, $\Delta t_a = 0.5\,s$, respectively. Some details of the simulations may be found in Table 5.9.

A few remarks can be made with regard to the various t = 900 s solutions displayed in Figs. 5.20 and 5.21.

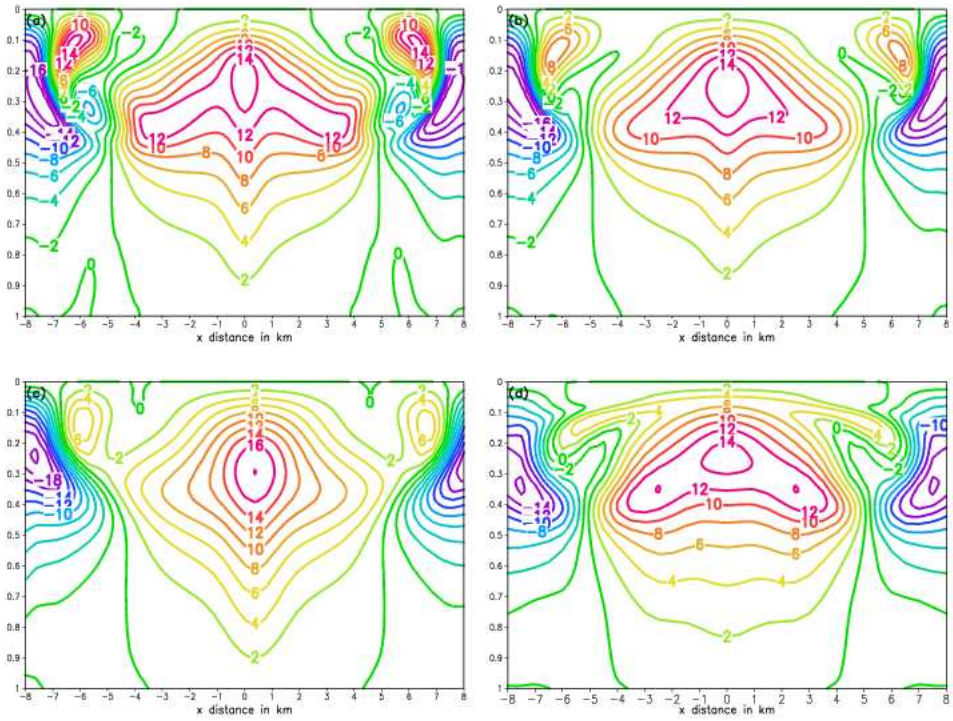

Figure 5.19: Marginally and poorly resolved flow in the warm bubble test. The $\hat{w}$ component of the wind after 900 s, for $-8000\,m \leq x \leq 8000\,m$ and $0 \leq \sigma \leq 1$: (a) $\Delta z \approx \Delta x = 200\,m$ with $K_s = 300\,m^2s^{-1}$ and $K_{Ts} = 50\,m^2s^{-1}$;(b) $\Delta z \approx \Delta x = 200\,m$ with $K_s = 600\,m^2s^{-1}$ and $K_{Ts} = 100\,m^2s^{-1}$; (c) $\Delta z \approx \Delta x = 400\,m$ with $K_s = 1200\,m^2s^{-1}$ and $K_{Ts} = 200\,m^2s^{-1}$; (d) $\Delta z \approx 100\,m$, $\Delta x = 500\,m$ with $K_s = 300\,m^2s^{-1}$ and $K_{Ts} = 50\,m^2s^{-1}$. The contour interval is 2ms^{-1}.

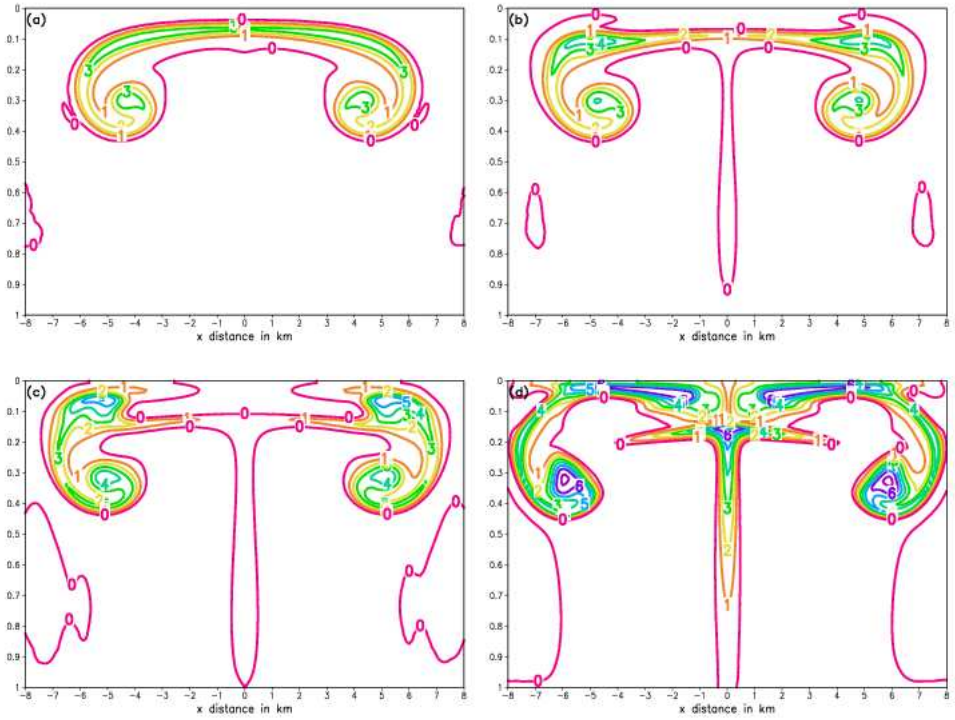

Figure 5.20: The potential temperature deviation after 900 s for the warm bubble test, for $-8000\,m \leq x \leq 8000\,m$ and $0 \leq \sigma \leq 1$: (a) $\Delta t_s = \Delta t_a = 1.5\,s$; (b) $\Delta t_s = 1.5\,s$, $\Delta t_a = 0.5\,s$(c) $\Delta t_s = 2.5\,s$, $\Delta t_a = 0.5\,s$; (d) $\Delta t_s = 5\,s$, $\Delta t_a = 0.5\,s$. The contour interval is 1K.

- For the simulation obtained with $\Delta t_s = \Delta t_a = 1.5\,s$, the evolution of the main flow features and the rate of ascent of the bubble correspond to that of the reference solution (Fig. 5.16). However, the t = 900 s solution is slightly diffused compared to the refence solution, and the splitting of the potential temperature field into maxima on both sides of the symmetry axis is not as well defined (compare Panel a of Fig. 5.20 to Panel d of Fig. 5.16). This latter is related to the relatively less well developed secondary updrafts simulated for the $\Delta t_s = \Delta t_a = 1.5\,s$ solution (Panel a of Fig. 5.17).

- The diffused nature of the $\Delta t_s = \Delta t_a = 0.5\,s$ solutions may be attributed to the damping that results from the bicubic interpolations performed during each time-step. For simulations where the adjustment time-step is less than the advection time-step, flow features can develop more unhindered by the damping of the semi-Lagrangian advection scheme. This is confirmed when the t = 900 s solution obtained with $\Delta t_s = 1.5\,s$, $\Delta t_a = 0.5\,s$ is considered (Panels b of Figs. 5.20 and 5.21) This solution resembles the reference solution very closely. Two well developed potential temperature maxima are present, one of each side of the symmetry axis (Panel b of Fig. 5.20). These have resulted in the formation of two well developed secondary updrafts (5.21). The latter are starting to impact on the flow field, resulting in a slight vertical displacement of the potential temperature maxima by t = 900 s. Similar results have been obtained in the cold bubble tests with regard to the damping effect of the bicubic interpolations.

- For the t = 900 s solution obtained with $\Delta t_s = 2.5\,s$, $\Delta t_a = 0.5\,s$, the two potential temperature maxima are displaced further in the vertical than in the reference solution (compare Panel c of Fig. 5.20 to Panel d of Fig. 5.16). With the more infrequent application of bicubic interpolation and explicit diffusion in this simulation, the flow features are less damped. The positive buoyancy associated with the relatively intense potential temperature maxima (compared to the reference solution), has resulted in the formation of two intense secondary updrafts (Panel c of Fig. 5.21). These, in return, are responsible for the stronger vertical displacement of the potential temperature maxima. The maximum horizontal and vertical Courant numbers attained in the simulation with $\Delta t_s = 2.5\,s$ are 0.43 and 0.72, respectively (see Table 5.9).

- The split semi-Lagrangian scheme is stable at even larger advection time-steps. The t = 900 s solution shown in Panels d of Figs. 5.20 and 5.21 was obtained with time-steps $\Delta t_s = 5\,s$, $t_a = 0.5\,s$. The maximum horizontal and vertical advection Courant numbers attained are 1.19 and 1.51, respectively (see Table 5.9). However, although stable, the t = 900 solution for the vertical velocity $\hat{w}$ is noisy (Panel d of Fig. 5.21). The secondary updrafts are very intense and have displaced the potential temperature maxima to the top of the model atmosphere (Panel d of Fig. 5.20).

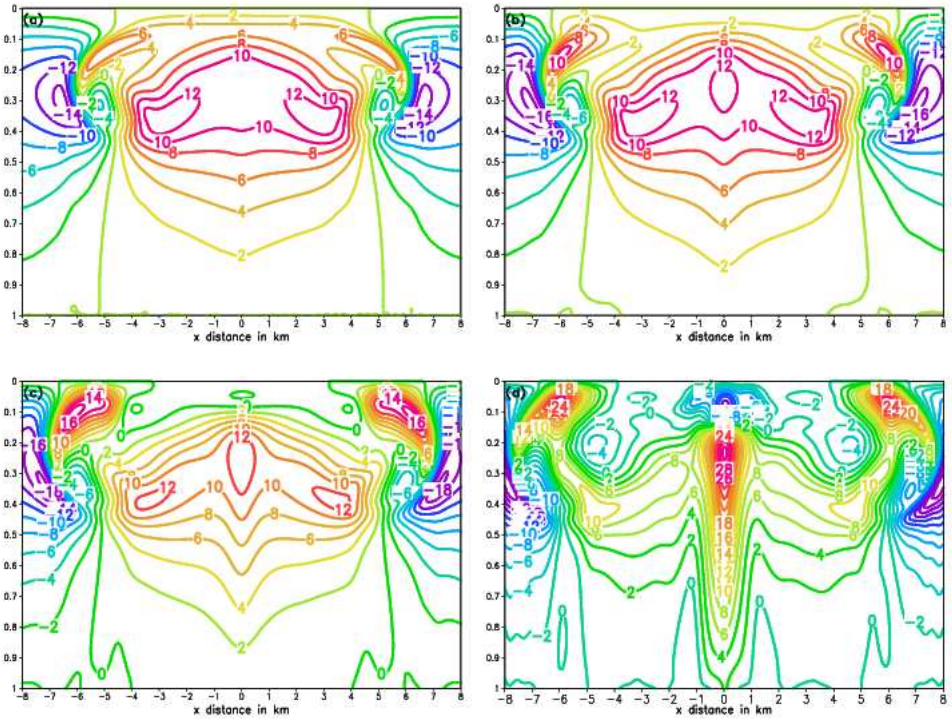

Figure 5.21: The vertical component of the velocity field $\hat{w}$ after 900 s for the warm bubble test, for $-8000\,m \leq x \leq 8000\,m$ and $0 \leq \sigma \leq 1$: (a) $\Delta t_s = \Delta t_a = 1.5\,s$; (b) $\Delta t_s = 1.5\,s$, $\Delta t_a = 0.5\,s$(c) $\Delta t_s = 2.5\,s$, $\Delta t_a = 0.5\,s$; (d) $\Delta t_s = 5\,s$, $\Delta t_a = 0.5\,s$. The contour interval is 2ms^{-1}.

- The t = 900 s solutions shown in Figs. have been obtained using advection and adjustment time-steps much larger than in the corresponding solutions shown by Gallus and Rancic (1994) and Janjic et al. (2001). In fact, for the warm bubble test the size of the advection time-step used is solely determined by accuracy considerations, since the split semi-Lagrangian scheme was found to be unconditionally stable. In the case of the cold bubble tests, the split semi-Lagrangian scheme became unstable at Courant numbers larger than about 0.8. This suggests than the non-linear instability has a more important effect in the cold bubble test, where more intense and finer scale features are present than in the warm bubble simulations described here.

5.3.5 Efficiency of the elliptic solver

The number of iterations required per second of integration time, for each of the various simulations discussed in the previous sections, is listed in Table 5.9. For

the simulations which are less diffused, either because of the smallness of the nondimensional quantity $K\Delta t_s/\Delta n^2$ or because of the infrequent application of explicit diffusion and bicubic interpolations, a criterion of convergence $\epsilon < 10^{-6}$ is required for the solution to be sufficiently converged (see Table 5.9). The following conclusions may be drawn based on the results in Table 5.9.

- For sufficient convergence of the reference solution, less than 20 iterations are required per second of integration time, that is, less than 2 iterations per adjustment time-step of 0.1 s (row WREF).
- The simulations that are similarly diffused (damped) as the reference solution generally require about 20 iterations per second of integration time (rows WMD, WPM and WT1).
- Simulations that are less diffused than the reference solution contain finer scale structures and more iterations per second of integration time for sufficient convergence. There are mainly three effects (possibly working in combination) that result in simulations to be less diffused:

1. Smallness of the non-dimensional quantity $K\Delta t_s/\Delta n^2$ (row WM).
2. The infrequent application of the bicubic interpolation scheme when large advection time-steps are used (rows WP, WT3 and WT4).
3. The use of relatively large advection time-steps in combination with smaller adjustment time-steps (rows WT2, WT3 and WT4).

- The relaxation factor $w_s = 1.6$ was found to lead to the fastest convergence of the SOR procedure in the warm bubble tests performed. In the cold bubble tests, $w_s = 1.9$ is the optimum value.
- The warm bubble tests generally require significantly fewer iterations per second of integration time than the cold bubble tests. This is due to the finer scale structures that are present in the less diffused cold bubble tests.
- Recalling the discussion on the efficiency of the elliptic solver for the cold bubble test and the comparative efficiency of the method of Xue (1989), it may be said that the SOR procedure provides efficient solutions for the case of the warm bubble test.

5.4 A cold bubble experiment in three spatial dimensions

5.4.1 Design of the three-dimensional cold bubble test

The experiment described in this section is an extension to three spatial dimensions of the two-dimensional cold bubble downburst problem described in

Table 5.9: Experimental design, maximum horizontal (HC) and vertical (VC) advection Courant numbers, criterion of convergence ϵ and average number of iterations per second of integration time, for various of the simulations as described in the text.

Simulation	Δx	$\Delta z \approx$	Δt_s	Δt_s	HC	VC	ϵ	Iterations
WREF	100	100	1	0.1	0.16	0.29	10^{-6}	16.13
WM	200	200	2	0.2	0.18	0.29	10^{-6} /2	54.99
WMD	200	200	2	0.2	0.15	0.28	10^{-6}	22.59
WP	400	400	4	0.4	0.16	0.25	10^{-6}	43.81
WPM	500	100	1	0.1	0.03	0.27	10^{-6}	19.25
WT1	100	100	1.5	1.5	0.22	0.41	$10^{-6}/3$	17.92
WT2	100	100	1.5	0.5	0.23	0.42	$2.10^{-3}/3$	26.15
WT3	100	100	2.5	0.5	0.43	0.72	$2.10^{-6}/3$	26.98
WT4	100	100	5	0.5	1.19	1.51	$2.10^{-6}/$ 3	36.65

section 5.2.1. In an initially dry, at rest and isentropic atmosphere with potential temperature 300 K, an ellipsoidally-shaped initial disturbance is introduced for the temperature:

$$\Delta T_0(x,z) = -15\cos^2(\frac{\pi}{2}r), \tag{5.7}$$

for $r \leq 1$, where, $r^2 = [(x-x_c)/x_t]^2 + [(y-y_c)/y_t]^2 + [(z-z_c)/z_t]^2$, $x_c = y_c =$ 0 m, $z_c = 3000$ m, $x_t = y_t = 4000$ m and $z_t = 2000$ m.

The integration domain extends over $-20000\,m \leq x \leq 20000\,m$ and $-20000\,m \leq y \leq 20000\,m$ in the horizontal. The top of the model domain is chosen to be 442 hPa (about 6400 m). The center of the initial disturbance is in the middle of the horizontal domain, that is, 20 km away from any of the lateral boundaries. The horizontal resolution used in the present experiment is 500 m, and 65 equally spaced σ levels are used to give a vertical resolution of about 100 m on the average. The experiment corresponds to the two-dimensional cold bubble experiment PM described in section 5.2.8, which was performed at the same horizontal and vertical resolutions.

5.4.2 A three-dimensional cold bubble simulation obtained with fourth order differencing

The numerical settings of the split semi-Lagrangian scheme that were found to give optimum results in the two-dimensional convective bubble tests are used to perform the three-dimensional cold bubble simulation. In the semi-Lagrangian

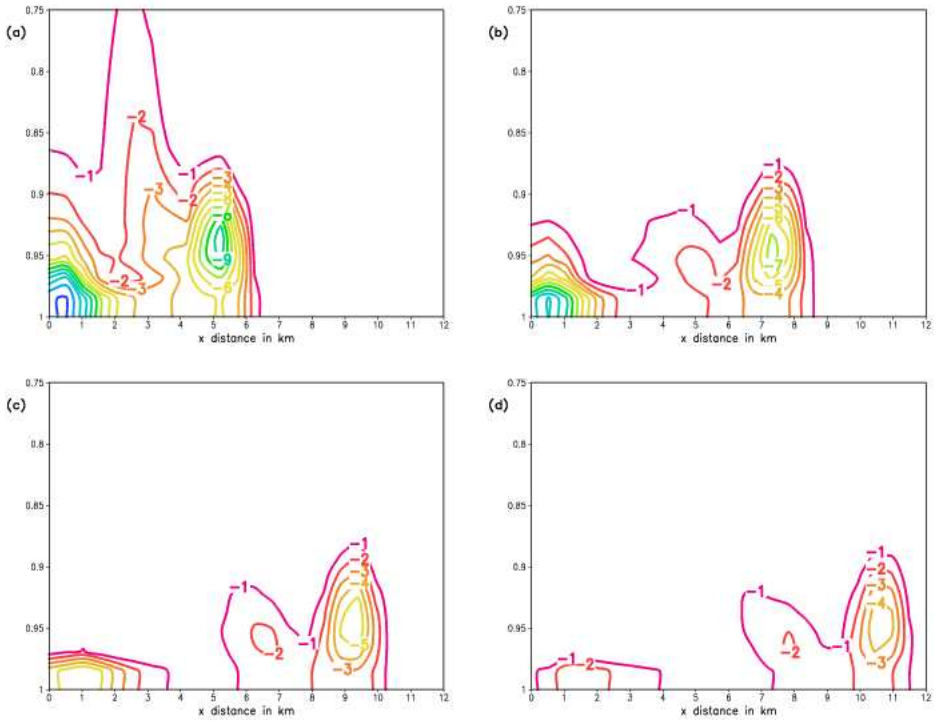

Figure 5.22: The three-dimensional cold bubble test. Vertical cross section of the potential temperature perturbation at $y = 0$, for $0\,m \leq x \leq 12\,000\,m$ and $0.75 \leq \sigma \leq 1$: (a) after 360 s; (b) after 520 s; (c) after 720 s; (d) after 900 s. The contour interval is 1 K.

advection step, the D_3 scheme of McGregor (1993) is used for the calculation of departure points (see Chapter 4). Note that the departure points are calculated in three spatial dimensions, and that tri-cubic spatial interpolation is used to evaluate the values of variables at the departure points. The spatial derivatives in the departure point formula and the term $A^*_{p_s}$ are evaluated using second order spatial differencing. All spatial derivatives in the adjustment step equations are discretized using fourth order differencing (see Chapter 4). Thus, fourth order differencing is used to discretize all partial derivatives in the three-dimensional elliptic equation **(3.81)**. The Shapiro filter is applied with p = 4, with lower order filtering performed near the lateral and vertical boundaries (see Chapter 4 and section 5.2.5). For each variable, the filter is applied consecutively along the x, y and σ axis (see Chapter 4). The values of the diffusion coefficients used in the explicit diffusion step, for diffusion along the x and y axis, are $K_s = K_{Ts} = 50\,m^2 s^{-1}$. Diffusion of similar magnitude is applied along the σ axis (see section 5.2.4). The advection and adjustment time-steps used are $\Delta t_s = 1.2\,s$ and $\Delta t_a = 0.3\,s$. The elliptic equation is solved with SOR, using $rl = 1.9$ as relaxation factor and $\epsilon = 10^{-6}$ as criterion of convergence. About four iterations were required per adjustment time-step for the criterion of convergence to be met. The potential temperature perturbation θ' fields from the isentropic background state after 360, 540, 720 and 900 s are shown in Fig. 5.22, for a vertical cross section along $y = 0$. The contour interval is 1 K. The corresponding vertical velocity fields $\hat{w}$ are shown in Fig. 5.24, with the contour interval 2 ms^{-1}. Note the displacement of the vertical scale in Fig. 5.22 relative to Fig. 5.24. The θ' field at $\sigma = 1$ is displayed in Fig. 5.23, for t = 360, 540, 720 and 900 s.

Some remarks can be made from considering the results displayed in Figs. 5.22 to 5.24:

- the intensity of the potential temperature disturbance in the three-dimensional simulation is considerably less than in the two-dimensional simulations (compare Panel d of Fig. 5.22 to Panel d of Fig. 5.12). This may be related to the fact that there are physical differences between the two and three-dimensional cold bubble downburst problems. In the three-dimensional problem, the gust front spreads out into a three-dimensional environment after reaching the surface. This is probably the most important reason for the relatively less intene disturbance in the three-dimensional environment;

- the damping of the tri-cubic spatial interpolation scheme may also contribute to the relatively smaller amplitude of the disturbance in the three-dimensional simulation;

- after the cold bubble reaches the surface in the three-dimensional simulation, it spreads out radially as a gust front (Fig. 5.23). The gust front progresses more slowly away from the center of the domain than in the corresponding two-dimensional simulation. By t = 900 s, the leading edge

of the gust front is about 11 km away from its orgin in the plane $\sigma = 0$, compared to the about 14 km it travels in the two dimensional simulations (compare Panels d of Figs. 5.22 and 5.12). The relatively slower progress of the gust front in the three-dimensional simulation may be related to the lower intensity of the disturbance, that loses its momentum more rapidly as it spreads out into the three-dimensional environment;

- one Kelvin-Helmholtz instability rotor is simulated to develop along the leading edge of the gust front as it spreads out radially (Fig. 5.26). The corresponding two-dimensional simulation is similar in this respect, showing a second rotor that is starting to develop at t = 900 s (Panel d of Fig. 5.13) . The intensity of the rotor is less in the three-dimensional case, however;
- the three-dimensional simulations are smooth and without any signs of numerical noise;
- It may be said that the split semi-Lagrangian scheme provides a satisfactorily solution of the three-dimensional cold bubble downburst problem.

5.5 A warm bubble experiment in three spatial dimensions

5.5.1 Design of the three-dimensional warm bubble test

The experiment described in this section is an extension of the two-dimensional warm bubble test described in section 5.3.1 to three spatial dimensions. In an initially dry, at rest and isentropic atmosphere with potential temperature 300 K, a circularly-shaped initial disturbance is introduced for the potential temperature:

$$\Delta\theta_0(x,z) = 6.6\cos^2(\frac{\pi}{2}r), \tag{5.8}$$

for $r \leq 1$, where $r^2 = [(x-x_c)/x_t]^2 + [(y-y_c)/y]^2 + [(z-z_c)/z_t]^2$, $x_c = y_c = 0$ m, $z_c = 2750$ m, $x_t = y_t = 2500$ m and $z_t = 2500$ m.

The integration domain extends over $-10000\,m \leq x \leq 10000\,m$ and $-10000\,m \leq y \leq 10000\,m$ in the horizontal. The top of the model domain is chosen to be 135 hPa (about 13500 m). The center of the initial disturbance is in the middle of the horizontal domain, that is, 10 km away from any of the lateral boundaries. The horizontal resolution used is 500 m and 135 equally spaced σ levels are used to give a vertical resolution of about 100 m on the average. The experiment corresponds to the two-dimensional warm bubble experiment WPM described in section 5.3.3, that was performed at similar horizontal and vertical resolutions.

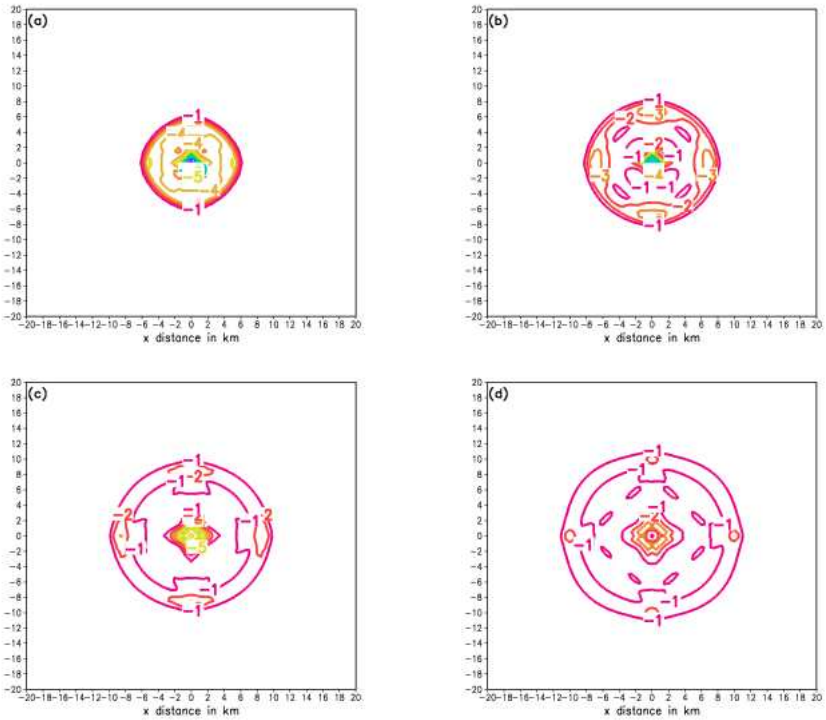

Figure 5.23: The three-dimensional cold bubble test. Horizontal cross section of the potential temperature perturbation at $\sigma = 0$, for : (a) after 360 s; (b) after 520 s; (c) after 720 s; (d) after 900 s. The full horizontal domain $-20000\,m \leq x \leq 20000\,m$, $-20000\,m \leq y \leq 20000\,m$ is shown. The contour interval is 1 K.

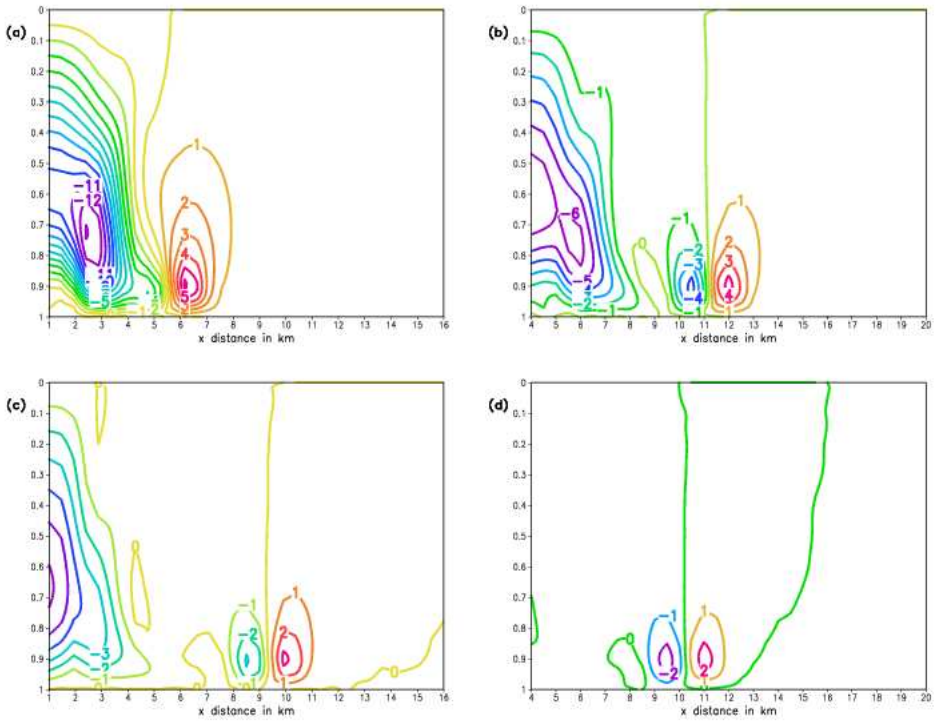

Figure 5.24: The three-dimensional cold bubble test. Vertical cross section of the vertical velocity $\hat{w}$ field at $y = 0$, for $0 \leq \sigma \leq 1$: (a) after 360 s; (b) after 520 s; (c) after 720 s; (d) after 900 s. The contour interval is 1 ms^{-1}. Note the displacement of the horizontal scale in (d).

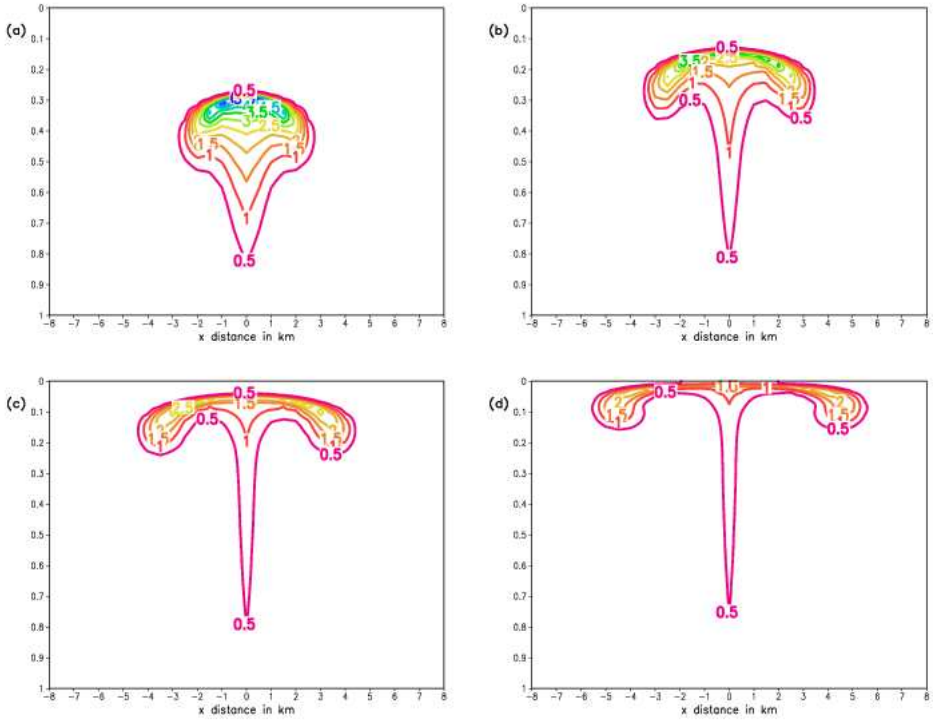

Figure 5.25: The warm bubble test in three spatial dimensions. Vertical cross section of the potential temperature perturbation at $y = 0$, for $-8000\,m \leq x \leq 8000\,m$ and $0 \leq \sigma \leq 1$: (a) after 360 s; (b) after 520 s; (c) after 720 s; (d) after 900 s. The contour interval is 0.5 K.

5.5.2 A three-dimensional warm bubble simulation obtained with fourth order differencing

The numerical settings used to obtain the three-dimensional warm bubble simulation in the present section, are as described for the three dimensional cold bubble test (see section 5.4.2). The only difference are with respect to the values of diffusion coefficients used. The same settings of explicit diffusion were used to obtain the corresponding two-dimensional warm bubble simulation WPM described in section 5.3.3. That is, $K_s = 300\,m^2s^{-1}$ and $K_{Ts} = 50\,m^2s^{-1}$, with diffusion of similar magnitudes applied along the σ axis, for u and T respectively. The elliptic equation is solved with SOR, using $rl = 1.6$ as relaxation factor and $\epsilon = 10^{-6}$ as criterion of convergence. On average only one iteration was required per adjustment time-step for the criterion of convergence to be met. The potential temperature deviation θ' from the isentropic background state after 360, 540, 720 and 900 s is shown in Fig. 5.25, for a vertical cross section along $y = 0\,m$. The contour interval is 0.5 K. The corresponding vertical

velocity fields $\hat{w}$ are shown in Fig. 5.26, with contour interval 2ms^{-1}.

A few remarks can be made with regard to the simulation displayed in Figs. 5.25 and 5.26:

- generally, the time evolution of the flow features in the three-dimensional simulation are very similar to that of the two-dimensional reference solution (see section 5.3.2). In particular, the development of the rotors on both sides of the symmetry axis are simulated (Fig. 5.26). The rotors entrain relatively cooler air from the environment into the lower part of the bubble (note the intrusion of the 0 K contour into the lower part of the bubble in Panels b to c of Fig. 5.25), whilst divergent motion caused by the rotors result in the formation of potential temperature maxima on both sides of the center axis (Panels b to c of Fig. 5.25);

- the rate of ascent of the three-dimensional warm bubble corresponds closely to that of the two-dimensional bubble in the reference solution (compare Fig. 5.25 to Fig. 5.16);

- however, the lateral displacement of the disturbance by t = 900 s (Panel d of Fig. 5.25) is somewhat less than that of the two-dimensional reference solution (Panel d of Fig. 5.16) and the two-dimensional simulation WPM (Panel d of Fig. 5.18) performed at similar resolutions than the present experiment. A similar result was obtained with regard to the displacement of the gust front in the three-dimensional cold bubble test (see the previous section);

- the potential temperature perturbation in the three-dimensional simulation is less intense than the reference two-dimensional simulation at t = 900 s ($\theta'_{max} = 2.15\,K$ for the three-dimensional simulation compared to $\theta'_{max} = 4.24\,K$ for the two-dimensional case). The relative stronger damping of the three- dimensional solution may be related to the explicit diffusion that takes place as the bubble spreads out into the three-dimensional environment. The damping of the tri-cubic interpolation scheme may also contribute to the relatively smaller amplitude of the θ' (and $\hat{w}$) field of the three-dimensional solution;

- the vertical velocity field at t = 900 s (Panel) is similar to that of the corresponding two-dimensional simulation (Panel d of). However, the downdrafts in particular are less intense in the case of the three-dimensional solution. Two secondary updrafts are starting to develop in the three-dimensional solution at t = 900 s;

- in totality, it may be said that the split semi-Lagrangian scheme gives a satisfactorily solution of the warm bubble test in three spatial dimensions.

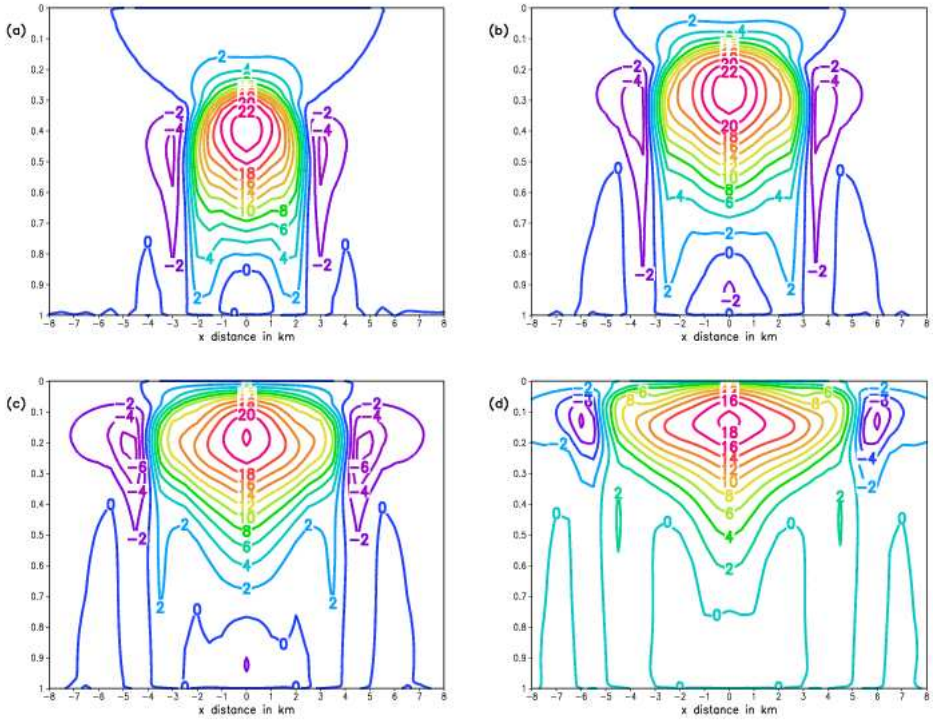

Figure 5.26: The warm bubble test in three spatial dimensions. Vertical cross section of the vertical velocity $\hat{w}$ at $y = 0$, for $-8000\,m \leq x \leq 8000\,m$ and $0 \leq \sigma \leq 1$: (a) after 360 s; (b) after 520 s; (c) after 720 s; (d) after 900 s. The contour interval is 2 ms^{-1}.

5.6 A three-dimensional warm bubble in an environment with strong unidirectional wind shear

5.6.1 Design of the experiment

In this experiment a warm bubble is introduced to an atmosphere with strong unidirectional vertical wind shear. The initial environment is dry and isentropic, and in hydrostatic balance. The x component of the initial horizontal wind has vertical shear of

$$\frac{d\tilde{u}}{dz} = 0.005\, s^{-1}, \tag{5.9}$$

that is, the x component of the horizontal wind increases with $20\, ms^{-1}$ over each interval of $4000\, m$ in the vertical. The initial y component of the horizontal wind and the vertical motion field are zero.

The integration domain is larger than in the previous experiment, and extends over $0\, m \leq x \leq 50\,000\, m$ and $0\, m \leq y \leq 50\,000\, m$ in the horizontal. The top of the model domain is chosen to be 135 hPa (about 13500 m) as before. The shape and intensity of the initial disturbance in the potential temperature is given by (5.8), with $x_c = 10\,000\, m$, $y_c = 25\,000\, m$, $z_c = 2750\, m$ and $x_t = y_t = z_t = 2500\, m$. In its initial position, the center of the bubble is located $10\,000\, m$ away from the upstream boundary $x = 0\, m$. The horizontal resolution used is $1000\, m$, and 135 equally spaced σ levels are used to give a vertical resolution of about $100\, m$ on the average.

The model was initialized following the procedure described in section 5.2.2. The boundary conditions are as described in section 4.9, with the exception of the lateral boundary conditions that are imposed on u. During the integration, the latter is kept constant at its initial vertical profile determined by (5.9) at all the lateral boundaries. The numerical settings of the split semi-Lagrangian scheme are as in section 5.5. The advection and adjustment time-steps used are $\Delta t_s = 1.2\, s$, $\Delta t_a = 0.3\, s$ and the integration period is $900\, s$. One average only one iteration of the SOR procedure was needed per adjustment time-step for the criterion of convergence to be met.

5.6.2 Horizontal splitting of the disturbance in the environment with vertical wind shear

The potential temperature perturbation θ' from the isentropic background state after 360, 540, 720 and $900\, s$ are shown in Fig. 5.27, for a vertical cross section along $y = 25\,000\, m$. The contour interval is $0.5\, K$. The corresponding vertical velocity fields $\hat{w}$ are shown in Fig. 5.28, with the contour interval $1\, ms^{-1}$. Horizontal cross sections of θ' at levels of constant σ are shown in in Fig. 5.29, for $t = 360$, 540, 720 and $900\, s$. The contour interval is $0.5\, K$. The constant

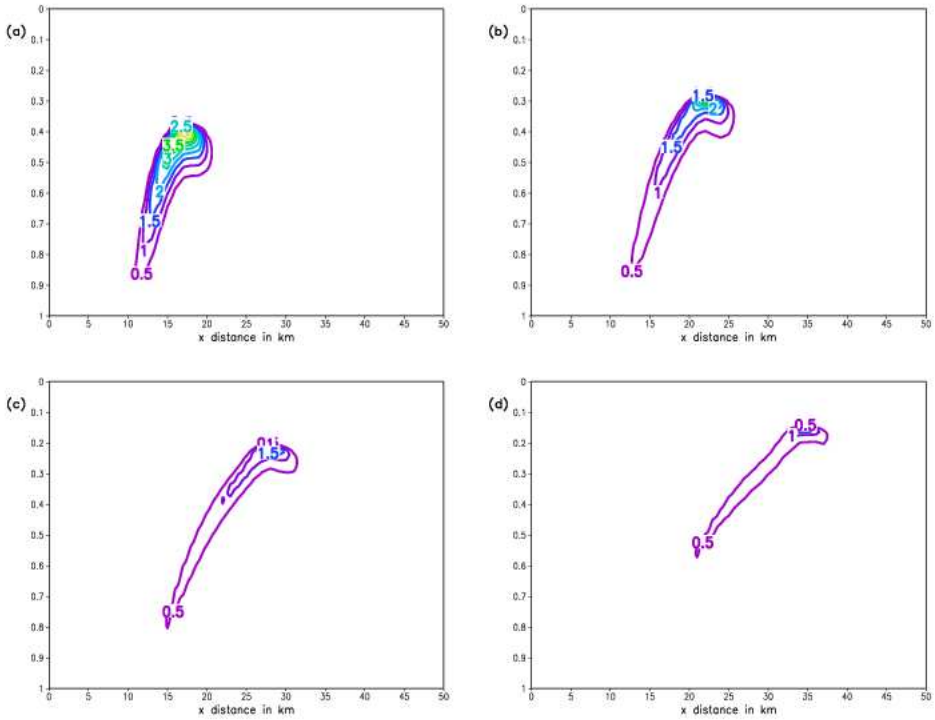

Figure 5.27: The three-dimensional warm bubble in an environment with strong unidirectional vertical wind shear. Vertical cross section of the potential temperature perturbation at $y = 25\,000\,m$ and $0 \leq \sigma \leq 1$: (a) after $360\,s$; (b) after $540\,s$; (c) after $720\,s$; (d) after $900\,s$. The contour interval is $0.5\,K$.

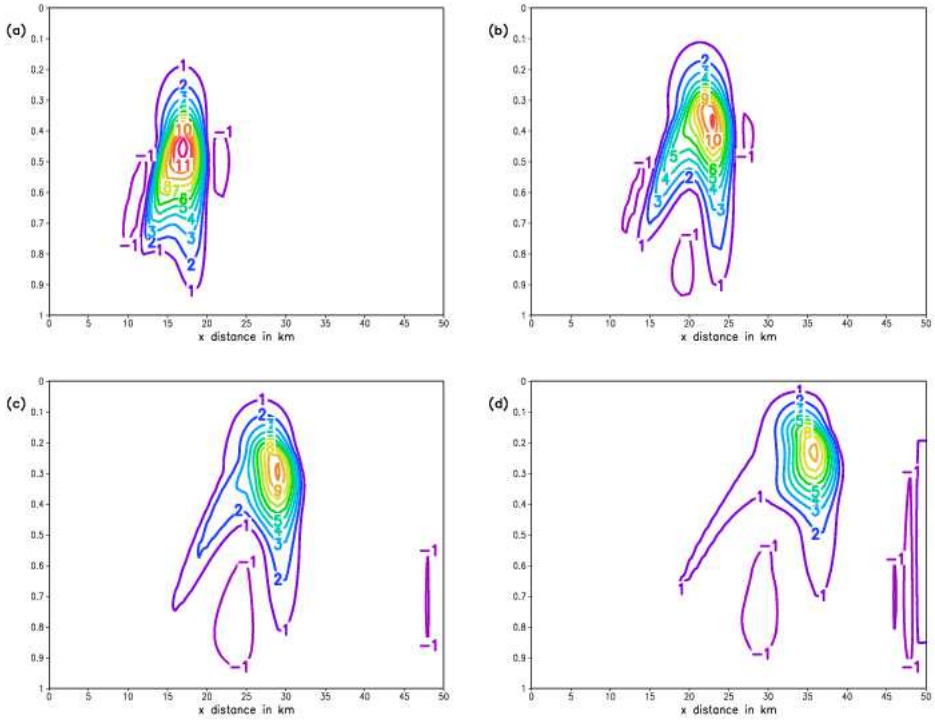

Figure 5.28: The three-dimensional warm bubble in an environment with strong unidirectional vertical wind shear. Vertical cross section of the vertical component of the wind $\hat{w}$ at $y = 25\,000\,m$ and $0 \leq \sigma \leq 1$: (a) after $360\,s$; (b) after $540\,s$; (c) after $720\,s$; (d) after $900\,s$. The contour interval is $1\,ms^{-1}$.

sigma levels are 0.44, 0.37, 0.29 and 0.22 for Panels a to d, respectively. For each of the time-levels, the σ level used corresponds to the height at which the vertical velocity attains a maximum along $y = 25\,000\,m$. Note the displacement of the horizontal scale in Panels a to d of Fig. 5.29.

In Fig. 5.27 it can be seen how the warm bubble rises in the environment with strong vertical wind shear, while being advected in the positive x direction by the u component of the wind. Because of the increase in the magnitude of u with height, the horizontal displacement of the upper part of the bubble is the fastest. Initially, the updraft induced by the positive buoyancy of the bubble is tilted slightly in the positive x direction by the horizontal wind field (Panel a of Fig. 5.28). Rotors develop along the outermost edges of the bubble (note the downdrafts in Panels a and b of Fig. 5.28). These rotors are even better developed along the flanks of the bubble that are perpendicular to the advecting wind u (not shown). As time goes by, the orientation of the core of the updraft gradually changes its orientation and eventually it is tilted in the negative x

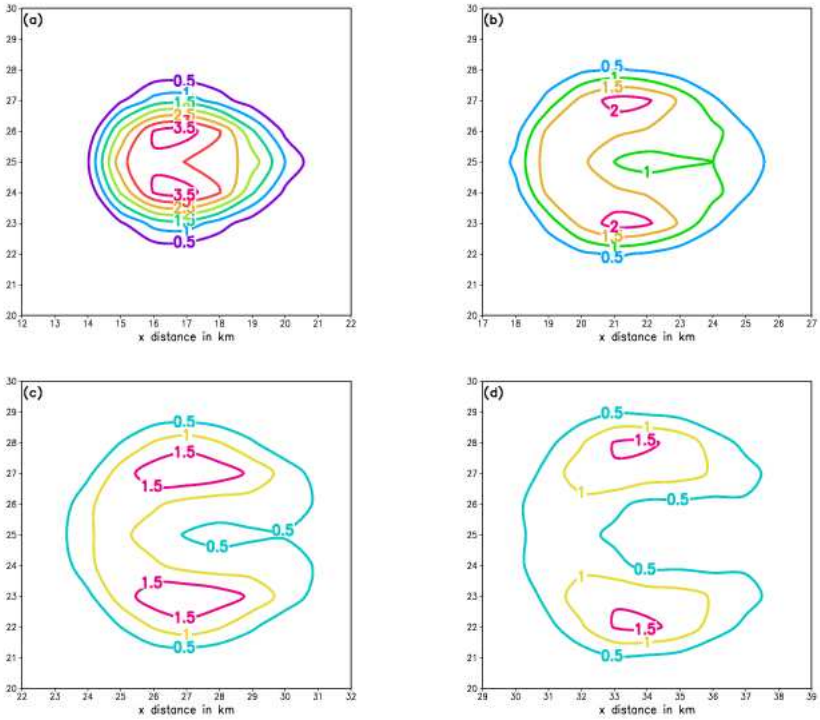

Figure 5.29: The three-dimensional warm bubble in an environment with strong unidirectional vertical wind shear. Horizontal cross section of the potential temperature perturbation for: (a) after $360\,s$ at $\sigma = 0.44$; (b) after $540\,s$ at $\sigma = 0.37$; (c) after $720\,s$ at $\sigma = 0.29$; (d) after $900\,s$ at $\sigma = 0.22$. The contour interval is $0.5\,K$. The σ level used for each time-step correspond to the height of maximum vertical velocity along $y = 25\,000\,m$. Note that $20\,000\,m \leq y \leq 30\,000\,m$, with a displacement of the x direction scale in the Panels.

direction (Fig. 5.28 Panels c and d).

Figure 5.29 shows how the potential temperature perturbation maximum on the σ level that corresponds to the height of maximum vertical velocity, splits around the vertical center axis of the bubble during its displacement in the positive x direction by the horizontal wind. Two potential temperature maxima, one on each side of the vertical center axis, are well developed by $t = 900\,s$. The "horizontal splitting" of the potential temperature disturbance is indicative of a feature that is well-known from the linear theory of rotating thunderstorms, namely "storm splitting" (e.g. Klemp, 1987; Holton, 1992). In an environment characterized by strong unidirectional vertical wind shear, low pressure areas develop on both the left and right flanks of the original updraft (Klemp, 1987). These tend to be the strongest at the middle levels of the atmosphere. The

associated pressure forcing may be sufficient to cause the updraft to split into two separate updrafts moving to the right and left of the environmental wind. The left- and right-moving updrafts rotate clockwise and anticlockwise, respectively. The rotation that develops is the result of the tilting of horizontal shear vorticity into the vertical by the original updraft (e.g. Rotunnu, 1981; Davies-Jones, 1983; Holton, 1992). Storm splitting has indeed been observed for cases where strong unidirectional wind shear has been observed in the real atmosphere (Fujita and Grandoso, 1968).

Figure 5.30 shows the vertical velocity $\hat{w}$ (shaded) and the vertical component of the vorticity $\zeta = \partial v/\partial x - \partial u/\partial y$ (contours) at $t = 900\,s$, for a portion of the horizontal domain at $\sigma = 0.48$. Indeed, negative vorticity (indicating clockwise rotation) and positive vorticity (indicating anticlockwise rotation) are present to the left and right of the center axis $y = 25\,000\,m$, respectively. The development of the potential temperature maxima on each side of this center axis (Fig. 5.29) may be attributed to advection that results from the two counterrotating vortices. Two well established updrafts can also be seen at $t = 900\,s$ (Fig. 5.30), moving to the left and right of the environmental wind. It is interesting to note that the splitting of the original updraft into the two separate updrafts is best developed well below the region of maximum vertical velocity at $\sigma = 0.22$ (Panel d of Fig. 5.28), where a single updraft still exists by $t = 900\,s$.

The results described in this section correspond very well to the linear theory of storm splitting and the development of rotation in thunderstorms. Clearly, the new model kernel based on a split semi-Lagrangian formulation of the quasi-elastic equations can be used to adequately describe highly nonlinear and non-hydrostatic flow. A detailed study of the dynamics relevant to the present experiment falls beyond the scope of the thesis, but the experiment illustrates the potential of the new model to be used in the study of nonhydrostatic circulation systems.

5.7 Discussion

In this chapter the split semi-Lagrange formulation of the quasi-elastic equations has been applied to simulate bubble convection in two and three spatial dimensions. For the two-dimensional tests the available computing power allowed high-resolution simulations, where the flow is adequately resolved, to be performed. For the three-dimensional tests, the flow features are marginally resolved. The three-dimensional convective bubbble experiments performed appear to be of the first to be described in literature. A new test where a warm bubble ascends in an environment with strong unidirectional wind shear was devised. Overall, the results obtained in this section confirms that the both the two- and three-dimensional split semi-Lagrangian formulations of the quasi-elastic equations are robust, and may be used to describe highly nonlinear and nonhydrostatic flow.

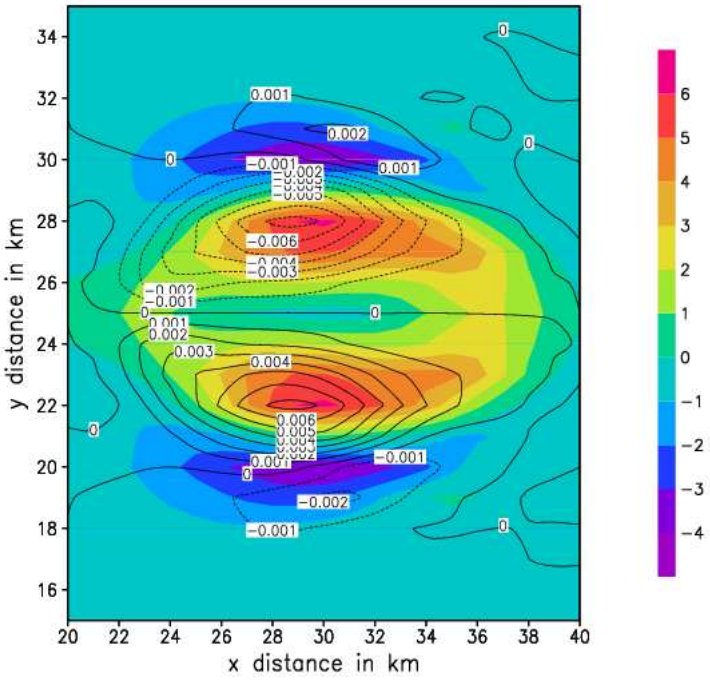

Figure 5.30: The vertical component of the wind $\hat{w}$ (shaded, ms^{-1}) and the vertical component of the vorticity ζ (contours, s^{-1}) at $\sigma = 0.48$ and $t = 900\,s$.

With regard to the properties and performance of the split semi-Lagrangian scheme, the most important results may be summarized as follows:

- no advantage was found in going beyond the D_2 scheme of McGregor (1993) for the calculation of departure points;
- fourth order differencing of the adjustment step equations provides superior results compared to second order differencing. In particular, the gravity wave phase speed is less retarded when fourth order differencing is used, which results in more accurate simulations of the time-evolution of the main flow features;
- explicit diffusion and the damping applied by the bicubic interpolation scheme at the shortest resolvable scales are often sufficient to control the development of two-grid interval noise on the nonstaggered grid, in particular when the flow is marginally resolved (as in the three-dimensional tests);
- however, for high-resolution tests where the flow is adequately resolved, it is essential that the Shapiro spatial filter is applied. The filter effectively removes the two-grid-interval waves, and two-grid-interval noise, from the nonstaggered grid. The filter suppresses the development of nonlinear instability at the shortest resolvable scales, allowing in particular a larger advection time-step to be used in the simulations;
- for adequately resolved flow, the split semi-Lagrangian scheme produces accurate results that are comparable to those obtained with high order finite element and fine difference models;
- for marginally resolved flow (in two and three spatial dimensions), the solutions obtained are damped, but smooth, stable and useable;
- a unique property of the split semi-Lagrangian scheme is that it performs well for both the cases of adequately and marginally resolved flow. Damped advection schemes generally perform well when the flow is marginally resolved, but spuriosly retard the time-evolution of flow features when the flow is adequatly resolved. High order finite element and finite difference models generally gives accurate results when the flow is adequately resolved, but produce noisy solutions for marginally resolved flow. The reason for the satisfactorily solutions produced by the split semi-Lagrangian scheme for both the cases of adequately and marginally resolved flow is to be found in its dual nature: the advection process may be treated during the advection step, whilst the fast travelling gravity waves may be treated accurately by using a smaller adjustment time-step.
- At high spatial resolutions, both the semi-implicit and explicit schemes require the use of small time-steps, for accuracy and stability reasons, respectively. Here the split semi-Lagrangian scheme may offer a computational advantage over other schemes, since it may be applied with a

relatively large advection time-step. The fast travelling waves may still be treated accurately by using a small adjustment time-step.

- The SOR procedure provides reasonably efficient solutions of the elliptic equation, in both two and three spatial dimensions.

It is appealing from a computational perspective to use a nonstaggered grid when using a semi-Lagrangian approach for the simulation of advection, since only one set of trajectories needs to be calculated. On the other hand, the damping at the shortest resolvable scales by the bicubic interpolation scheme used in the semi-Lagrangian scheme described here contributes to control the two-grid interval noise that may develop on the nonstaggered grid. It may therefore be said that when discretizing the atmospheric equations on a nonstaggered grid, it is appealing to use a semi-Lagrangian approach, rather than an Eulerian procedure, to discretize the advection terms.

It may be noted that all the bubble convection tests performed in this Chapter are carried out in an isentropic environment, that is, the environment is neutrally stratified. This effectively filters out internal gravity waves, which develop in a stably stratified environment, from the numerical solutions. The experiments may be extended to stably stratified environments, in order to investigate the performance of the split semi-Lagrangian scheme under these conditions. However, since the fastest travelling waves in the equation system are the Lamb waves (Miller and White, 1984; also see Chapter 3), internal gravity waves are not likely to have a dominant effect on the maximum size of the adjustment time step allowed. Preliminary tests of airflow over a three-dimensional bell-shaped mountain in a stably stratified environment (not shown) have been performed with the split semi-Lagrangian scheme, at a horizontal resolution of 500 m and a vertical resolution of about 100 m. The scheme was found to be stable at large advection Courant numbers, and at adjustment time-steps of size similar to those used in the convective bubble tests.

The emphasis in this Chapter is on the simulation of micro- and meso-scale buoyance driven flows, where the Coriolis effect is of negligible importance. The dynamic kernel has not been tested at the synoptic-scale, where the geostrophic adjustment process occurs. Of particular interest would be how the semi-implicit treatment of the Coriolis terms (see section 4.5.2) impact on numerical stability during the adjustment phase of the solution procedure. Purser and Leslie (1988) have shown that for the system of gravity-inertia wave equations (e.g. Mesinger and Arakawa, 1976), geostrophic adjustment on the nonstaggered grid may be treated accurately using high order spatial differencing and filtering. They've extended this approach to a hydrostatic primitive equation model (Leslie and Purser, 1991). These results provide some confidence that the split semi-Lagrangian formulation of the quasi-elastic equations will perform well, at least from a numerical perspective, at spatial scales larger than the meso-scale.

All the simulations in this chapter were performed on a personal computer (PC). Computational constraints prevented the three-dimensional simulations to be performed at spatial resolutions where the flow is adequately resolved. Recently, a PC cluster was obtained by the Faculty of Science at the University of Pretoria. This makes possible more extensive testing of the performance of the scheme in three spatial dimensions in the future.

Chapter 6

Conclusions and recommendations

6.1 Recent developments in nonhydrostatic atmospheric modelling

Nonhydrostatic models have been developed and used for research purposes since the early days of numerical atmospheric modelling (e.g. Ogura and Charney, 1962; Ogura and Phillips, 1962; Dutton and Fichtl, 1969; Furukawa, 1973; Miller, 1974; Miller and Pearce, 1974). However, with the advent of ever faster computers, the era of operational nonhydrostatic atmospheric models has dawned. That is, NWP and climate simulation models may be applied at resolutions beyond the hydrostatic limit, where convection can at least be partially resolved. This has lead to a renewed worldwide research effort into the development of nonhydrostatic atmospheric models (e.g. Laprise, 1992; Dudhia, 1993; Bubnova et al., 1995; Gallus and Rancic, 1996; Janjic et al., 2001; Smolarkiewicz et al., 2001; Dudhia and Bresch, 2002; Davies et al., 2005). A primary aspect of this international research effort, is the quest to find a "universal model" that may be applied at any spatial resolution, globally or over a limited area, and for time-scales ranging from the typical life-time of mesoscale systems to the extensive periods required for climate simulation. The need for a universal model stems partially from the labour involved in maintaining and developing different model codes sutable for application at different spatial scales. Many believe that the fully-elastic (unapproximated) equations provide the only option for the development of a universal model (Laprise, 1992; Caya and Laprise, 1999; Davies et al., 2003; White et al., 2005). However, these equations contain fast moving acoustic waves as part of their solution set, which may imply computational penalties when the equations are solved numerically (e.g. Room et al., 1998; Davies et al., 2003). Apart from the fully-elastic models, two other main classes of nonhydrostatic models have evolved, namely anelas-

tic (e.g. Ogura and Charney, 1962; Dutton and Fichtl, 1969; Furukawa, 1973; Miller, 1974; Mahrt, 1986; Tritton, 1988, White, 1989; Room et al., 2001, Smolarkiewicz et al., 2001) and quasi-elastic models (e.g. Ogura and Phillips, 1962; Wilhelmson and Ogura, 1972; Clark and Peltier, 1977; Miller and White, 1984; Durran, 1989). The anelastic equations are completely filtered of sound waves (whilst the quasi-elastic equations are partially filtered), and therefore offer computational advantages over the fully-elastic equations (e.g. Room et al., 1998). However, at least for the anelastic and quasi-elastic equations in height-based vertical coordinates, the property of universal applicability is lost (Davies et al., 2003). These equation sets result when approximations are introduced to the fully-elastic equations, with the aim of eliminating the terms responsible for the generation of sound waves. Unfortunately, the approximations may also effect the gravity and Rossby waves of the resulting equation sets, causing the properties of these waves to be different from those of the fully-elastic equations and the true atmosphere at the synoptic scale and larger (Davies et al., 2003). Indeed, traditionally the anelastic and quasi-elastic equation sets have been used for the study of meso-scale circulation systems for relatively short integration periods (e.g. Ogura and Charney, 1962; Miller and Pearce, 1974; Miranda and James, 1992; Dudhia, 1993; Gallus and Rancic, 1996). They remain important today to be used for this purpose (Davies et al., 2003), just as the hydrostatic equations remain important for the study of synoptic and large scale circulation. The different classes of nonhydrostatic models are reviewd in Chapter 1 of the thesis.

Another aspect that has received much attention in recent research effort into nonhydrostatic models, is the choice of vertical coordinate system to be used. Most of the early nonhydrostatic models developed for research purposes employed height-based coordinates (e.g. Ogura and Charney, 1962; Furukawa, 1973), whilst the highly evolved operational hydrostatic models developed over the last four decades are all cast in pressure-based vertical coordinates. The most convenient way to obtain a nonhydrostatic model suitable for operational use, is to convert an existing operational hydrostatic model to a nonhydrostatic model (Janjic et al., 2001). This can be most conveniently achieved if the pressure-based vertical coordinate system of the hydrostatic model is still used for the nonhydrostatic model. In fact, until fairly recently, it was believed that nohydrostic models formulated in terms of a vertical coordinate based on the hydrostatic pressure (Laprise, 1992; Bubnova et al., 1995) would offer the only practical option for the development of a fully-elastic nonhydrostatic model suitable for universal application (Caya and Laprise, 1999). However, research efforts at the UKMO over the last few years have led to the development of a fully-elastic model employing a height-based vertical coordinate system (Davies et al., 2005).

The first nonhydrostatic model employing a pressure-based vertical coordinate was developed by Miller (1974) and Miller and Pearce (1974). The MP model

differs from the recently developed fully-elastic models based on the hydrostatic pressure field, in the sense that it is anelastic and employs the full pressure field as vertical coordinate. A σ coordinate form of the MP model was developed by Miller and White (1984). The latter model is filtered of vertically propagating acoustic waves, but contains Lamb waves as part of its solution set. Its quasi-elastic nature still offers significant computational advantages over the fully-elastic equations (Miller and White, 1984; Gallus and Rancic, 1996; Room et al., 2001). A closely related anelastic σ coordinate model (the NHAD model) was developed by Room et al. (2001). Numerical models have been developed based on the MP equations, in both pressure and σ coordinates, and have been used for the study of convection (e.g. Miller and Pearce, 1974) and gravity waves (Miranda and James, 1994; Miranda and Valente, 1997). The MP model has never been applied at larger spatial scales, mainly because it is formulated in terms of a reference thermodynamic profile that limits its application to cases where the temperature distribution on pressure surfaces is fairly uniform (e.g. White, 1989; Caya and Laprise, 1999). For example, the MP equations are probably not applicable to frontal zones, or at large spatial scales where significant variations in temperature from the reference state are possible. The NHAD model is subject to the same limitation. The different types of pressure-based nonhydrostatic models are reviewed in Chapter 2 of the thesis.

With the limitations of the MP model in mind, White (1989) produced a closely related equation set that still employs the full pressure field as vertical coordinate, but is formulated independently of a thermodynamic reference profile. In Chapter 3 of this study, the σ coordinate equivalent of the equation set of White (1989) is derived, by means of a coordinate transformation of the pressure coordinate equations of White (1989) into a σ coordinate based on the full pressure field. The σ coordinate equation set is shown to be quasi-elastic, with the speed of the Lamb waves depending on the choice of model top p_T. The frequency equation for the gravity wave equations in the quasi-elastic equations is similar to the corresponding equation of the fully-elastic equations, whilst the energy equation of the fully-elastic equations is similar to that of the hydrostatic equations (see Chapter 3). These results, and the fact that the equations are formulated independent of a reference profile, suggests that the quasi-elastic σ coordinate equations based on the full pressure field may be used at spatial scales larger than the meso-scale.

6.2 A novel dynamic kernel based the split semi-Lagrangian formulation of the quasi-elastic equations

A novel dynamic kernel based on this set of quasi-elastic σ coordinate equations is formulated in Chapter 4 of the thesis. The new numerical model is the first realization of White's (1989) idea of a nonhydrostatic model based on

the full pressure field, that may be applied at spatial scales larger than the meso-scale. The numerical solution procedure applied to solve the quasi-elastic equations is closely linked to that used to solve the hydrostatic equations, in the sense that both the surface pressure tendency and vertical motion fields are calculated from the continuity equation (see Chapter 4). In most nonhydrostatic models, including the numerical realizations of the MP model (e.g. Xue, 1989; Xue and Thorpe 1991), the vertical motion field is calculated from the vertical momentum equation. Because the present approach is in harmony with the solution procedure typically used in hydrostatic models, it facilitates the convenient transformation of an existing hydrostatic model to a nonhydrostatic model based on the quasi-elastic equations. The numerical procedure used to solve the quasi-elastic equations involves the use of an elliptic equation in the geopotential (derived in Chapter 3), which is solved with SOR. Similar equations are solved in the MP and NHAD models (Xue, 1989; Xue and Thorpe, 1991; Room et al., 2001).

The most distinguishing feature of the numerical solution procedure developed, is that it uses a split semi-Lagrangian scheme to solve the quasi-elastic equations on a nonstaggered grid (see Chapter 4). The numerical realizations of the MP and NHAD models employ explicit solution procedures on staggered grids (e.g. Xue, 1989; Xue and Thorpe, 1991; Room et al., 2001). The use of the semi-Lagrangian technique to solve the advection process in the newly developed model offers a significant computational advantage over explicit procedures. The model remains stable at large Courant numbers, whereas the advection time-step in explicit solution procedures is always limited by a CFL-type stability condition. The fast propagating gravity and Lamb waves in the quasi-elastic equations can be treated accurately during an adjustment procedure, which may employ a smaller time-step than that used in the advection step.

It is advantageous from a computational perspective to use a nonstaggered grid when a semi-Lagrangian scheme is used for the advection process, since only one set of trajectories needs to be calculated. Semi-Lagrangian procedures applied on staggered grids require the calculation of more than one set of trajectories (for the staggered and nonstaggered positions), which implies that more than one set of spatial interpolations needs to performed to evaluate the values of variables at the different sets of departure points. Unfortunately, the nonstaggered grid (or Arakawa A-grid) is known to have poor gravity wave dispersion properties (e.g. Winninghoff 1968; Mesinger and Arakawa 1976; Arakawa and Lamb, 1977; Schoenstadt, 1978), which renders its use during the adjustment step of the present procedure problematic. If second order differencing is used to calculate the spatial derivatives that occur in the adjustment step equations, the phase speed of the gravity waves in the quasi-elastic equations are retarded considerably near the shortest resolvable scales. In fact, for the horizontal spatial discretization the two-grid-interval waves are stationary. However, it is shown in the thesis that fourth order discretization may be used to significantly

improve the gravity wave dispersion properties of the quasi-elastic equations on the nonstaggered grid. Stationary two-grid-interval waves, and numerical noise that originate near the shortest resolvable scales, may be sufficiently controlled by the use of explicit diffusion and the highly scale-dependent Shapiro (1975) spatial filter. The successful and economical implementation of the split semi-Lagrangian procedure to solve the set of nonhydrostatic quasi-elastic equations on a nonstaggered grid, is one of the main aspects of the research that is novel. However, note that high order spatial differencing and filtering have been used in semi-implicit semi-Lagrangian discretizations of the hydrostatic equations (Purser and Leslie, 1988; Leslie and Purser, 1991). McGregor (2005) has recently developed an alternative approach for application in the hydrostatic variable resolution model C-CAM, where a semi-Lagrangian procedure is used on a nonstaggered grid. By transforming the wind components via a reversible interpolation scheme, the geostrophic adjustment process may then be carried out on a staggered grid.

The new split semi-Lagrangian kernel was tested by a series of numerical experiments described in Chapter 5. All the simulations in the thesis were performed on a single processor personal computer, so that high-resolution simulations where the flow is adequately resolved, were limited to two spatial dimensions by computational constraints. When working in two spatial dimensions, there is the additional advantage that the available computing power allowed grid-converged solutions to be obtained for diffusion-limited problems. This facilitated a comparsion of the solutions obtained to the results obtained in similar studies performed with different equation sets and numerical solution procedures. Cold and warm bubble experiments were performed, in two and three spatial dimensions. These numerical experiments have shown that the split semi-Lagrangian formulation of the quasi-elastic equations is robust, and may be used to accurately describe highly nonlinear and nonhydrostatic flow. The solutions obtained correspond well to the two-dimensional results obtained using Eulerian formulations of the fully-elastic equations (Straka et al., 1993; Gallus and Rancic, 1996; Janjic and Gerrity, 2001). An interesting new three-dimensional numerical experiment was devised, where a warm bubble rises in an environment with vertical wind shear. The results obtained in this test correspond to the linear theory of storm splitting. A three dimensional experiment of air flow over a bell shaped mountain was performed, illustrating that the split semi-Lagrangian formulation performs well for the case of nonzero topography.

With regard to the optimum choice of numerical settings to be used in the split semi-Lagrangian scheme, the experiments indicated that there is little or no advantage in going beyond the D_2 scheme of McGregor (1993) for the calculation of advection departure points. Fourth order spatial differencing of the adjustment step equations provides a significantly improved gravity wave phase speed representation compared to second order spatial differencing. For the

high-resolution experiments performed at small values of explicit diffusion, two-grid-interval noise develops unless the Shapiro spatial filter is applied. For these high-resolution tests the Shapiro filter effectively removes the two-grid interval waves from the nonstaggered grid, whilst having a negligible damping effect at longer wave lengths. The use of the filter prevents the development of nonlinear instability, allowing the use of significantly larger advection time-steps than is allowed in nonfiltered simulations. The combined use of explicit diffusion and the Shapiro filter on the nonstaggered grid generally allow solutions that are smooth and free of any signs of numerical noise. However, when relatively small adjustment time-steps are used, the filter should be applied only every few adjustment time-steps to prevent the solution from becoming excessively damped. Similarly, for the three-dimensional tests performed at relatively low spatial resolutions, where wavelengths near the shortest resolvable scales carry an important part of the energy of the motion, application of the filter may lead to excessively damped solutions. Fortunately, it was found that explicit diffusion sufficiently controls the two-grid-interval noise for these relatively low resolution simulations on the nonstaggered grid. Finally, the SOR procedure used to solve the elliptic equation provides reasonably efficient solutions for application of the model in both two and three spatial dimensions, generally requiring only a few iterations per adjustment time-step. However, potential computational advantages of a solution procedure based on the FFT technique (e.g. Xue, 1989) over the present SOR procedure is an aspect that requires further investigation.

The fully elastic equations are nowadays mostly solved with semi-implicit techniques, that slow down not only the sound waves, but also the gravity waves (e.g. Tanguay et al., 1990; Davies et al., 2003). With a split semi-Lagrangian approach, with explicit spatial filtering, selective damping of only the smallest resolvable waves is achieved. The remaining fast travelling waves are handled during the adjustment step that employs a (necessarily small) time step. However, the semi-Lagrangian procedure still allows a large time step to be used during the advection step. When the fast travelling gravity waves are important for their own sake, for example when they carry an important part of the energy of the dynamic system studied, the split semi-Lagrangian approach allows them to be handled accurately during the adjustment step. However, they may be artificially damped by a semi-implicit procedure employing a large time-step. In order to treat the gravity waves accurately, a small time step will have to be used in the semi-implicit solution procedure. In this way, the economical efficiency of the procedure is lost as it will now become equivalent in time step to a purely explicit solution procedure. However, in the split semi-Lagrangian approach, the advection time step may still be large, making the method more economical than a semi-implicit approach for cases where damping of the gravity wave phase speed is not desirable.

6.3 Ongoing research

6.3.1 Marginally resolved flow

The operational use of atmospheric models beyond the hydrostatic limit has opened up numerous unexplored areas of research. For example, the performance of models at spatial resolutions where convection is marginally resolved will be of practical importance for many years to come. Although it is the advent of faster computers that has made the operational use of atmospheric models beyond the hydrostatic limit possible, computational constraints are still limiting the resolution of operational regional and global nonhydrostatic models to a few kilometers (in the horizontal) at best. At these resolutions, convection can only be marginally resolved. Conversely, hydrostatic models are applied at resolutions where convection is not explicitly resolved. In these models, convection parameterization schemes are used to represent the effects of convection on the atmosphere. Thus, an important new focus area in numerical atmospheric modelling, is the development of numerical solution procedures (including parameterisation schemes) for nonhydrostatic models, that functions well at spatial resolutions where convection is marginally resolved.

The development of a truly "universal model" is still far from being a practical reality. It is unlikely that a numerical scheme will be found that performs best from an accuracy and computational perspective at all spatial resolutions. More likely is that certain schemes will offer computational advantages and produce more accurate results at specific spatial scales. There is also no guarantee that the convection schemes used in hydrostatic models will function well at resolutions where convection is marginally resolved. In fact, a necessary condition for development of a universal model, is the development of a parameterization scheme that may be applied at all spatial scales. The present research effort facilitates the participation of scientists in South Africa into the current international research effort into the development of nonhydrostatic models.

6.3.2 A quasi-elastic universal model?

It should also be asked if a set of anelastic or quasi-elastic equations exist that is suitable for universal application. The recent normal mode analysis performed for various approximated height-based equation sets has shown that none of these sets has the property of universal applicability (Davies et al., 2003). The question arises if a universally applicable filtered equation set based on the hydrostatic or full pressure field may be constructed. The formulation independent of a reference thermodynamic profile of the set of quasi-elastic equations derived in the thesis allow their application at scales larger than the meso-scale. It remains to be investigated how the approximations introduced to formulate these equations affect the representation of Rossby waves in the equation set. There also seems to have been no attempt to formulate filtered nonhydrostatic equations based on the hydrostatic pressure field. A normal mode analysis of

such filtered equations, and the equation sets based on the full pressure field described in the thesis, may provide more clarity on their potential application at large spatial scales. A Hamiltonian approach may provide a useful way of formulating such equation sets (e.g. Salmon and Smith, 1994). These research aspects fall beyond the scope of the present study, which is primarily about the formulation of a split semi-Lagrangian scheme to solve the quasi-elastic equations on a nonstaggered grid, and applications at the micro and meso-scales.

6.3.3 The study of nonhydrostatic circulation systems and continued model development

The dynamics of many interesting nonhydrostatic circulation systems occurring over South Africa has never been studied in detail. Examples include the frequent occurrence of mountain waves over Lesotho and the south-western Cape (De Villiers, 1998, 2001), and the development of severe thunderstorms over the Highveld and eastern escarpment areas (e.g. De Coning and Adam, 2000; De Coning et al., 2000). The newly developed model may be used to study the dynamics of these systems, possibly in combination with the high resolution MSG satellite pictures that recently became available in the country. More generally, the new model may be used to gain deeper insight into convective storm-splitting, interaction of updrafts with vertical shear of the horizontal wind, the development of mesocyclones in supercell storms, the merging of two cumulus cells, cold pools in two-dimensional squall lines, roll convection, airflow over mountains, etc.

Already, the new kernel has been tested for applications over regions of nonzero topography, by a series of experiments involving airflow over a three-dimensional bell-shaped mountain. The split semi-Lagrangian procedure performed well in these preliminary tests, giving typical results of three-dimensional splitting flow or breaking gravity waves, depending on the size of Froude number used. The simple lower boundary condition for the geopotential stated in Chapter 4 was applied succcessfully in these experiments. The SOR procedure required a similar number of iterations for convergence, per second of integration time, compared to the number of iterations required for convergence in the three-dimensional bubble convection tests (see Chapter 5). Thus, at least in these preliminary tests, nonzero topography didn't cause the SOR procedure to be computationally more expensive.

All the numerical experiments in the thesis have been performed on a single PC (see Chapter 5). Having a numerical code that runs on a PC is an advantage, in the sense that the researcher involved have total control over the numerical experiments to be performed. There is no dependency on external factors such as available computer time on a super computer, or on other researchers to assist with the design and set-up of numerical experiments (as may be the case at some of the large computing centers of the world). This provides the

freedom of improving the model code, by adding variables such as water vapor and cloud water, improving the lateral boundary conditions, adding a frictional boundary layer into the model, etc. Still, some recent advances in computational capacity at research institutions in South Africa may facilitate the potential real-atmosphere and three-dimensional applications of the new model. At UP, a PC cluster was obtained in 2005 for general use of scientists in the Faculties of Natural and Agricultural Sciences and Engineering. Unfortunately, the software needed for parallel computing possibilities and human capacity to maintain the system are still lacking. At a national level, the Center for High Performance Computing (CHPC) was established in 2005. The center strives to make super computing facilities (in the form of a powerful PC cluster) more accessible to South African researchers. The present model code will need to be modified for its potential future implementation on a PC cluster.

6.3.4 Implementation of the quasi-elastic equations in C-CAM

The nonhydrostatic equation set developed was introduced to C-CAM during a visit of the author to CSIRO Marine and Atmospheric Research in January and February 2004. In C-CAM the quasi-elastic equation set is solved with a modified version of the semi-implicit semi-Lagrangian method used previously in the model to solve the hydrostatic equations in σ- coordinates. The new nonhydrostatic dynamical kernel of C-CAM was used sucessfully to perform a cold bubble simulation in the conformal cubic grid (Rautenbach et al., 2005). This illustrated the suitability of the developed quasi-elastic equation set for use in nonhydrostatic modelling, and that the equations may be introduced to an existing hydrostatic model with relative ease.

6.4 The new Nonhydrostatic Sigma coordinate Model (NSM)

In summary, a new nonhydrostatic model based on the quasi-elastic equations has been developed. The equation set cast in a terrain-following coordinate based on the full pressure field has not been applied before in atmospheric modelling. The equations are formulated independent of a reference profile, making them suitable for application at spatial scales larger than the meso-scale. However, in the present study the model is applied only to simulate highly nonhydrostatic and nonlinear flow at the micro - and meso-scales. The split semi-Lagrangian procedure provides accurate solutions for the case of adequately resolved flow and is stable at large Courant numbers. For the case of marginally resolved flow, the solutions obtained are damped, but smooth, stable and useable. The main advantage of the split semi-Lagrangian solution procedure may be at high spatial resolutions, where the accurate representation of gravity waves requires the use of small adjustment time steps. At these

resolutions, both explicit and semi-implicit procedures require the use of small time steps. Although requiring a similarly small adjustment time step, the split semi-Lagrangian procedure may still be applied at large advection time steps, in this way offering a computational advantage over other methods. The newly developed model has the potential of being used for the study of nonhydrostatic circulation systems, and for research into the improvement of numerical techniques and parameterization schemes used in nonhydrostatic models. The name "Nonhydrostatic Sigma coordinate Model (NSM)" is proposed for the model developed in the thesis. It is concluded that the new model is worth developing further.

Appendix A

Derivation of the elliptic equation directly from the σ coordinate quasi-elastic equations

In this appendix, the elliptic equation (3.81) is derived directly from the σ coordinate equations (3.64) to (3.68). Multiplying (3.66) by s gives:

$$s\frac{R}{g}\frac{D}{Dt}(\frac{\omega T}{p}) + gs + s^2\frac{\partial \phi}{\partial \sigma} = 0. \tag{A.1}$$

Taking $(\partial/\partial x)$ of (3.64), $(\partial/\partial y)$ of (3.65) and $(\partial/\partial \sigma)$ of (A.1), and adding the three resulting equations gives:

$$\frac{\partial^2 \phi}{\partial x^2} + \frac{\partial^2 \phi}{\partial y^2} + \frac{\partial}{\partial \sigma}\left(s^2\frac{\partial \phi}{\partial \sigma}\right) - \sigma\frac{\partial \phi}{\partial \sigma}\left(\frac{\partial^2 \ln p_s}{\partial x^2} + \frac{\partial^2 \ln p_s}{\partial y^2}\right)$$

$$-\sigma\left[\frac{\partial \ln p_s}{\partial x}\left(\frac{\partial^2 \phi}{\partial x \partial \sigma}\right) + \frac{\partial \ln p_s}{\partial y}\left(\frac{\partial^2 \phi}{\partial y \partial \sigma}\right)\right] = -\frac{\partial}{\partial x}\left(\frac{Du}{Dt}\right) - \frac{\partial}{\partial y}\left(\frac{Dv}{Dt}\right)$$

$$-\frac{\partial}{\partial \sigma}\left[\frac{p}{p_s T}\frac{D}{Dt}\left(\frac{\omega T}{p}\right)\right] + f\left(\frac{\partial v}{\partial x} - \frac{\partial u}{\partial y}\right) - u\frac{df}{dy} - \frac{\partial}{\partial \sigma}(sg). \tag{A.2}$$

In order to simplify (A.2), it is necessary to expand the terms $-\partial\left(Du/Dt\right)/\partial x$, $-\partial\left(Dv/Dt\right)/\partial y$ and $-\partial\left[\left(p/p_s T\right)D\left(\omega T/p\right)/Dt\right]\partial\sigma$. First note that from expanding the total derivatives of the two components of the horizontal wind, it follows that:

$$-\frac{\partial}{\partial x}\left(\frac{Du}{Dt}\right) = -\frac{D}{Dt}\left(\frac{\partial u}{\partial x}\right) - \left(\frac{\partial u}{\partial x}\frac{\partial u}{\partial x} + \frac{\partial v}{\partial x}\frac{\partial u}{\partial y} + \frac{\partial \dot{\sigma}}{\partial x}\frac{\partial u}{\partial \sigma}\right) \tag{A.3}$$

and

$$-\frac{\partial}{\partial y}\left(\frac{Dv}{Dt}\right)=-\frac{D}{Dt}\left(\frac{\partial v}{\partial y}\right)-\left(\frac{\partial u}{\partial y}\frac{\partial v}{\partial x}+\frac{\partial v}{\partial y}\frac{\partial v}{\partial y}+\frac{\partial \dot{\sigma}}{\partial y}\frac{\partial v}{\partial \sigma}\right). \tag{A.4}$$

Finding an appropriate expansion for $-\partial\left[\left(p/p_sT\right)D\left(\omega T/p\right)/Dt\right]\partial\sigma$ requires a more extensive procedure. From the use of relationship (3.69), it follows that

$$\frac{p}{p_sT}\frac{D}{Dt}(\frac{\omega T}{p})=\frac{p}{p_sT}\frac{D}{Dt}\left[\frac{Tp_s}{p}\left(\sigma\frac{D\ln p_s}{Dt}+\dot{\sigma}\right)\right]$$

$$=\frac{p}{p_sT}\left[\frac{D}{Dt}\left(\frac{Tp_s\sigma}{p}\frac{D\ln p_s}{Dt}\right)+\frac{D}{Dt}\left(\frac{Tp_s}{p}\dot{\sigma}\right)\right]$$

$$=\underbrace{\sigma\frac{D^2\ln p_s}{Dt^2}}_{A}+\underbrace{(\frac{p}{p_sT})\frac{D}{Dt}(\frac{Tp_s\sigma}{p})\frac{D\ln p_s}{Dt}}_{B}+\underbrace{(\frac{p}{p_sT})\frac{D}{Dt}(\frac{Tp_s}{p}\dot{\sigma}).}_{C} \tag{A.5}$$

Noting that

$$B=\left[\dot{\sigma}+\frac{\sigma p}{p_sT}\frac{D}{Dt}\left(\frac{Tp_s}{p}\right)\right]\frac{D\ln p_s}{Dt} \tag{A.6}$$

and

$$C=\frac{D\dot{\sigma}}{Dt}+\dot{\sigma}\left(\frac{p}{p_sT}\right)\frac{D}{Dt}\left(\frac{Tp_s}{p}\right) \tag{A.7}$$

it follows that

$$\frac{\partial A}{\partial\sigma}=\frac{D^2\ln p_s}{Dt^2}+\sigma\frac{\partial}{\partial\sigma}\left(\frac{D^2\ln p_s}{Dt^2}\right), \tag{A.8}$$

$$\frac{\partial B}{\partial\sigma}=\frac{\partial}{\partial\sigma}\left\{\left[\dot{\sigma}+\frac{\sigma p}{p_sT}\frac{D}{Dt}\left(\frac{Tp_s}{p}\right)\right]\frac{D\ln p_s}{Dt}\right\} \tag{A.9}$$

and

$$\frac{\partial C}{\partial\sigma}=\frac{D}{Dt}\left(\frac{\partial\dot{\sigma}}{\partial\sigma}\right)+\left[\frac{\partial u}{\partial\sigma}\frac{\partial\dot{\sigma}}{\partial x}+\frac{\partial v}{\partial\sigma}\frac{\partial\dot{\sigma}}{\partial y}+\frac{\partial\dot{\sigma}}{\partial\sigma}\frac{\partial\dot{\sigma}}{\partial\sigma}\right]$$
$$+\frac{\partial}{\partial\sigma}\left[\dot{\sigma}\left(\frac{p}{p_sT}\right)\frac{D}{Dt}\left(\frac{Tp_s}{p}\right)\right]. \tag{A.10}$$

Equation (A.10) is derived from expanding the total derivative of $\dot{\sigma}$ in (A.7). From combining (A.8) to (A.10) it is obtained that:

$$-\frac{\partial}{\partial\sigma}\left[\frac{p}{p_sT}\left(\frac{D}{Dt}(\frac{\omega T}{p})\right)\right]=-\frac{D}{Dt}\left(\frac{\partial\dot{\sigma}}{\partial\sigma}\right)-\left[\frac{\partial u}{\partial\sigma}\frac{\partial\dot{\sigma}}{\partial x}+\frac{\partial v}{\partial\sigma}\frac{\partial\dot{\sigma}}{\partial y}+\frac{\partial\dot{\sigma}}{\partial\sigma}\frac{\partial\dot{\sigma}}{\partial\sigma}\right]$$

$$-\frac{\partial}{\partial\sigma}\left[\dot{\sigma}\left(\frac{p}{p_sT}\right)\frac{D}{Dt}\left(\frac{Tp_s}{p}\right)\right]-\frac{D}{Dt}\left(\frac{D\ln p_s}{Dt}\right)-\sigma\frac{\partial}{\partial\sigma}\left(\frac{D^2\ln p_s}{Dt^2}\right)$$

$$-\frac{\partial}{\partial\sigma}\left\{\left[\dot{\sigma}+\frac{\sigma p}{p_sT}\frac{D}{Dt}\left(\frac{Tp_s}{p}\right)\right]\frac{D\ln p_s}{Dt}\right\}. \tag{A.11}$$

From substituting (A.3), (A.4) and (A.11) into (A.2), and applying the continuity equation (3.67), it follows that:

$$\frac{\partial^2\phi}{\partial x^2}+\frac{\partial^2\phi}{\partial y^2}+\frac{\partial}{\partial\sigma}(s^2\frac{\partial\phi}{\partial\sigma})-\sigma\frac{\partial\phi}{\partial\sigma}\left(\frac{\partial^2\ln p_s}{\partial x^2}+\frac{\partial^2\ln p_s}{\partial y^2}\right)$$

$$-\sigma\left[\frac{\partial\ln p_s}{\partial x}\left(\frac{\partial^2\phi}{\partial x\partial\sigma}\right)+\frac{\partial\ln p_s}{\partial y}\left(\frac{\partial^2\phi}{\partial y\partial\sigma}\right)\right]=$$

$$+\left(\underbrace{-\frac{\partial u}{\partial x}\frac{\partial u}{\partial x}}_{B_{2a}}-\frac{\partial v}{\partial x}\frac{\partial u}{\partial y}\underbrace{-\frac{\partial\dot{\sigma}}{\partial x}\frac{\partial u}{\partial\sigma}}_{B_{4a}}\right)+\left(-\frac{\partial u}{\partial y}\frac{\partial v}{\partial x}\underbrace{-\frac{\partial v}{\partial y}\frac{\partial v}{\partial y}}_{B_{2b}}\underbrace{-\frac{\partial\dot{\sigma}}{\partial y}\frac{\partial v}{\partial\sigma}}_{B_{4b}}\right)$$

$$+\left[\underbrace{-\frac{\partial u}{\partial\sigma}\frac{\partial\dot{\sigma}}{\partial x}}_{B_{4c}}\underbrace{-\frac{\partial v}{\partial\sigma}\frac{\partial\dot{\sigma}}{\partial y}}_{B_{4d}}\underbrace{-\frac{\partial\dot{\sigma}}{\partial\sigma}\frac{\partial\dot{\sigma}}{\partial\sigma}}_{B_3}\right]-\frac{\partial}{\partial\sigma}\left[\dot{\sigma}\left(\frac{p}{p_sT}\right)\frac{D}{Dt}\left(\frac{Tp_s}{p}\right)\right]\underbrace{-\sigma\frac{\partial}{\partial\sigma}\left(\frac{D^2\ln p_s}{Dt^2}\right)}_{B_1}$$

$$-\frac{\partial}{\partial\sigma}\left\{\left[\dot{\sigma}+\frac{\sigma p}{p_sT}\frac{D}{Dt}\left(\frac{Tp_s}{p}\right)\right]\frac{D\ln p_s}{Dt}\right\}+f\left(\frac{\partial v}{\partial x}-\frac{\partial u}{\partial y}\right)-u\frac{df}{dy}-\frac{\partial}{\partial\sigma}(sg). \tag{A.12}$$

In order to simplify (A.12), the labeled terms need to be written in alternative form. Firstly, note that

$$B_1=-\sigma\frac{\partial}{\partial\sigma}\left(\frac{D^2\ln p_s}{Dt^2}\right)=-\sigma\left[\frac{\partial\ln p_s}{\partial x}\frac{\partial}{\partial\sigma}\left(\frac{Du}{Dt}\right)+\frac{\partial\ln p_s}{\partial y}\frac{\partial}{\partial\sigma}\left(\frac{Dv}{Dt}\right)\right]$$

$$-2\sigma\left[\frac{\partial u}{\partial\sigma}\frac{D}{Dt}\left(\frac{\partial\ln p_s}{\partial x}\right)+\frac{\partial v}{\partial\sigma}\frac{D}{Dt}\left(\frac{\partial\ln p_s}{\partial y}\right)\right]. \tag{A.13}$$

By expanding the total derivatives of u and v in (A.13), it is obtained that:

$$B_1 = -\sigma\frac{\partial}{\partial\sigma}(\frac{D^2\ln p_s}{Dt^2}) = \sigma f\left(\frac{\partial u}{\partial\sigma}\frac{\partial\ln p_s}{\partial y} - \frac{\partial v}{\partial\sigma}\frac{\partial\ln p_s}{\partial x}\right)$$

$$+\sigma\left(\frac{\partial^2\phi}{\partial x\partial\phi}\frac{\partial\ln p_s}{\partial x} + \frac{\partial^2\phi}{\partial y\partial\phi}\frac{\partial\ln p_s}{\partial y}\right) - \sigma\frac{\partial}{\partial\sigma}\left(\sigma\frac{\partial\phi}{\partial\sigma}\right)\left[\left(\frac{\partial\ln p_s}{\partial x}\right)^2 + \left(\frac{\partial\ln p_s}{\partial y}\right)^2\right]$$

$$-2\sigma\left[\frac{\partial u}{\partial\sigma}\frac{D}{Dt}\left(\frac{\partial\ln p_s}{\partial x}\right) + \frac{\partial v}{\partial\sigma}\frac{D}{Dt}\left(\frac{\partial\ln p_s}{\partial y}\right)\right]. \qquad (A.14)$$

From making use of the continuity equation (3.67) it follows that:

$$B_{2a} + B_{2b} = 2\frac{\partial u}{\partial x}\frac{\partial v}{\partial y} + \left(\frac{\partial u}{\partial x} + \frac{\partial v}{\partial y}\right)\left(\frac{D\ln p_s}{Dt} + \frac{\partial\dot\sigma}{\partial\sigma}\right) \qquad (A.15)$$

From differentiating relationship (3.69) with respect to σ it follows that

$$\frac{\partial\dot\sigma}{\partial\sigma} = \frac{\partial}{\partial\sigma}\left(\frac{p}{p_s}\Omega\right) - \frac{D\ln p_s}{Dt} - \sigma\left(\frac{\partial u}{\partial\sigma}\frac{\partial\ln p_s}{\partial x} + \frac{\partial v}{\partial\sigma}\frac{\partial\ln p_s}{\partial y}\right). \qquad (A.16)$$

It follows, from applying the continuity equation, that

$$B_3 = -\left(\frac{\partial\dot\sigma}{\partial\sigma}\right)^2 = \left(\frac{\partial u}{\partial x} + \frac{\partial v}{\partial y}\right)\frac{\partial\dot\sigma}{\partial\sigma} + \frac{D\ln p_s}{Dt}\frac{\partial\dot\sigma}{\partial\sigma}. \qquad (A.17)$$

Making use of (3.69) to write $\dot\sigma$ in terms of ω and $D\ln p_s/Dt$ implies that

$$B_{4a}+B_{4b}+B_{4c}+B_{4d} = -2\left(\frac{\partial u}{\partial\sigma}\frac{\partial\dot\sigma}{\partial x} + \frac{\partial v}{\partial\sigma}\frac{\partial\dot\sigma}{\partial y}\right) = -2\left[\frac{\partial u}{\partial\sigma}\frac{\partial}{\partial x}\left(\frac{p}{p_s}\Omega\right) + \frac{\partial v}{\partial\sigma}\frac{\partial}{\partial y}\left(\frac{p}{p_s}\Omega\right)\right]$$

$$+2\sigma\left[\frac{\partial u}{\partial\sigma}\frac{D}{Dt}\left(\frac{\partial\ln p_s}{\partial x}\right) + \frac{\partial v}{\partial\sigma}\frac{D}{Dt}\left(\frac{\partial\ln p_s}{\partial y}\right)\right]$$

$$+2\sigma\frac{\partial u}{\partial\sigma}\left(\frac{\partial u}{\partial x}\frac{\partial\ln p_s}{\partial x} + \frac{\partial v}{\partial x}\frac{\partial\ln p_s}{\partial y}\right) + 2\sigma\frac{\partial v}{\partial\sigma}\left(\frac{\partial u}{\partial y}\frac{\partial\ln p_s}{\partial x} + \frac{\partial v}{\partial y}\frac{\partial\ln p_s}{\partial y}\right). \qquad (A.18)$$

By substituting (A.14), (A.15), (A.17) and (A.18) into (A.12), it follows, after some cancellations between terms, that:

$$\frac{\partial^2\phi}{\partial x^2}+\frac{\partial^2\phi}{\partial y^2}+\frac{\partial}{\partial\sigma}(s^2\frac{\partial\phi}{\partial\sigma})-\sigma\frac{\partial\phi}{\partial\sigma}\left(\frac{\partial^2\ln p_s}{\partial x^2}+\frac{\partial^2\ln p_s}{\partial y^2}\right)$$

$$+\sigma\frac{\partial}{\partial\sigma}\left[\left(\frac{\partial\ln p_s}{\partial x}\right)^2+\left(\frac{\partial\ln p_s}{\partial y}\right)^2\right]-2\sigma\left[\frac{\partial\ln p_s}{\partial x}\left(\frac{\partial^2\phi}{\partial x\partial\sigma}\right)+\frac{\partial\ln p_s}{\partial y}\left(\frac{\partial^2\phi}{\partial y\partial\sigma}\right)\right]=$$

$$2\left(\frac{\partial u}{\partial x}\frac{\partial v}{\partial u}-\frac{\partial v}{\partial x}\frac{\partial u}{\partial y}\right)\underbrace{+2\left(\frac{\partial u}{\partial x}+\frac{\partial v}{\partial y}\right)\left(\frac{\partial\dot\sigma}{\partial\sigma}\right)+\frac{D\ln p_s}{Dt}\frac{\partial\dot\sigma}{\partial\sigma}+\left(\frac{\partial u}{\partial x}+\frac{\partial v}{\partial y}\right)\left(\frac{D\ln p_s}{Dt}\right)}_{C_2}$$

$$\underbrace{-2\left[\frac{\partial u}{\partial\sigma}\frac{\partial}{\partial x}\left(\frac{p\omega}{p_s}\right)+\frac{\partial v}{\partial\sigma}\frac{\partial}{\partial y}\left(\frac{p\omega}{p_s}\right)\right]}_{C_1}$$

$$+2\sigma\frac{\partial u}{\partial\sigma}\left(\frac{\partial u}{\partial x}\frac{\partial\ln p_s}{\partial x}+\frac{\partial v}{\partial x}\frac{\partial\ln p_s}{\partial y}\right)+2\sigma\frac{\partial v}{\partial\sigma}\left(\frac{\partial u}{\partial y}\frac{\partial\ln p_s}{\partial x}+\frac{\partial v}{\partial y}\frac{\partial\ln p_s}{\partial y}\right)$$

$$\sigma f\left[\frac{\partial u}{\partial\sigma}\frac{\partial\ln p_s}{\partial y}-\frac{\partial v}{\partial\sigma}\frac{\partial\ln p_s}{\partial x}\right]+f\left(\frac{\partial v}{\partial x}-\frac{\partial u}{\partial y}\right)-u\frac{df}{dy}-\partial(sg)$$

$$\underbrace{-\frac{\partial}{\partial\sigma}\left[\dot\sigma\left(\frac{p}{p_sT}\right)\frac{D}{Dt}\left(\frac{Tp_s}{p}\right)\right]}_{C_3}\underbrace{-\frac{\partial}{\partial\sigma}\left\{\left[\dot\sigma+\frac{\sigma p}{p_sT}\frac{D}{Dt}\left(\frac{Tp_s}{p}\right)\right]\frac{D\ln p_s}{Dt}\right\}}_{C_4}. \quad \text{(A.19)}$$

It may finally be noted that

$$C_1=-\frac{2}{p_s}\left[\frac{\partial u}{\partial\sigma}\frac{\partial}{\partial x}(p\Omega)+\frac{\partial v}{\partial\sigma}\frac{\partial}{\partial y}(p\Omega)\right]+\frac{2p\omega}{p_s}\left(\frac{\partial\ln p_s}{\partial x}\frac{\partial u}{\partial\sigma}+\frac{\partial\ln p_s}{\partial y}\frac{\partial v}{\partial\sigma}\right), \quad \text{(A.20)}$$

$$C_2=2\left(\frac{\partial u}{\partial x}+\frac{\partial v}{\partial y}\right)\left(\frac{\partial\dot\sigma}{\partial\sigma}\right)+\frac{D\ln p_s}{Dt}\frac{\partial\dot\sigma}{\partial\sigma}+\left(-\frac{\partial\dot\sigma}{\partial\sigma}-\frac{D\ln p_s}{Dt}\right)\left(\frac{D\ln p_s}{Dt}\right)$$

$$=2\left(\frac{\partial u}{\partial x}+\frac{\partial v}{\partial y}\right)\left(\frac{\partial\dot\sigma}{\partial\sigma}\right)-\left(\frac{D\ln p_s}{Dt}\right)^2=2\frac{D\ln p_s}{Dt}\frac{\partial\dot\sigma}{\partial\sigma}+\left(\frac{D\ln p_s}{Dt}\right)^2 \quad \text{(A.21)}$$

and

$$C_3 + C_4 = -\frac{\partial}{\partial\sigma}\left(\dot{\sigma}\frac{D\ln p_s}{Dt}\right) - \frac{\partial}{\partial\sigma}\left[\left(\frac{p}{p_s T}\right)\frac{D}{Dt}\left(\frac{Tp_s}{p}\right)\frac{p\omega}{p_s}\right]$$

$$= -\frac{\partial}{\partial\sigma}\left(\dot{\sigma}\frac{D\ln p_s}{Dt}\right) + \frac{1}{\gamma}\left[\frac{p\omega}{p_s}\frac{\partial\omega}{\partial\sigma} + \frac{\partial(p\omega)}{\partial\sigma}\frac{\omega}{p_s}\right] - \frac{p\omega}{p_s}\frac{\partial}{\partial\sigma}\left(\frac{D\ln p_s}{Dt}\right)$$

$$-\frac{\partial}{\partial\sigma}(p\Omega)\frac{1}{p_s}\frac{D\ln p_s}{Dt}$$

$$= -2\frac{\partial\dot{\sigma}}{\partial\sigma}\frac{D\ln p_s}{Dt} - 2\frac{p\omega}{p_s}\left(\frac{\partial u}{\partial\sigma}\frac{\partial\ln p_s}{\partial x} + \frac{\partial v}{\partial\sigma}\frac{\partial\ln p_s}{\partial y}\right) - \left(\frac{D\ln p_s}{Dt}\right)^2$$

$$+\frac{1}{\gamma}\left[\frac{p\omega}{p_s}\frac{\partial\omega}{\partial\sigma} + \frac{\partial(p\omega)}{\partial\sigma}\frac{\omega}{p_s}\right]. \qquad \text{(A.22)}$$

Equations (A.19) to (A.22) may now be substituted in (A.18). After some cancellations and reorganization of the terms, the elliptic equation (3.81) is obtained.

Appendix B

Alternative derivation of the linearized elliptic equation

Linearizing equation (3.81) gives

$$\frac{\partial^2\phi}{\partial x^2}+\frac{\partial}{\partial\sigma}\left(s_0^2\frac{\partial\phi}{\partial\sigma}\right)+\frac{\partial}{\partial\sigma}\left(s_0\frac{T^{'}}{T_0}g\right)=0. \tag{B.1}$$

Substituting wave-like solutions of the form (3.106) into (B.1) leads to

$$\frac{d}{d\sigma}\left(\frac{\sigma p_0+p_T}{p_0}\right)^2\frac{d\hat{\phi}^{'}}{d\sigma}-H_0^2k^2\hat{\phi}^{'}+H_0^2\frac{d}{d\sigma}\left(s_0\frac{\hat{T}^{'}}{T_0}g\right)=0. \tag{B.2}$$

Here

$$H_0^2\frac{d}{d\sigma}\left(s_0\frac{\hat{T}^{'}}{T_0}g\right)=\frac{H_0^2g}{T_0}\left(s_0\frac{d\hat{T}^{'}}{d\sigma}+\frac{T^{'}}{H_0}\right). \tag{B.3}$$

From (3.110) it follows that

$$\frac{dT^{'}}{d\sigma}=-\kappa\left[\left(\frac{p_0}{\sigma p_0+p_T}\right)\left(\frac{1}{ikc}\right)(\frac{d\hat{\sigma}}{d\sigma}-ikc\hat{\pi})\right]T_0+$$

$$\kappa\left[\left(\frac{p_0}{\sigma p_0+p_T}\right)^2\left(\frac{1}{ikc}\right)\left(\hat{\sigma}-ikc\sigma\hat{\pi}\right)\right]T_0=0. \tag{B.4}$$

Making use of (3.110) and (B.4) to substitute for $\hat{T}^{'}$ and $d\hat{T}^{'}/d\sigma$ in (B.3) gives:

$$H_0^2\frac{d}{d\sigma}\left(s_0\frac{\hat{T}^{'}}{T_0}g\right)=-H_0g\kappa\left(\frac{1}{ikc}\right)\left(\frac{d\hat{\sigma}}{d\sigma}-ikc\hat{\pi}\right). \tag{B.5}$$

Substituting from (3.107) and (3.109) gives

$$H_0^2 \frac{d}{d\sigma}\left(s_0 \frac{\hat{T}'}{T_0} g\right) = \frac{H_0 g \kappa}{c^2}\hat{\phi}' = H_0^2 \frac{N^2}{c^2}\hat{\phi}' . \tag{B.6}$$

From substituting (B.6) in (B.2) equation (3.113) is obtained.

Appendix C

The linearized elliptic equation under transformations Z and F

The transformation relationship (3.114) implies that for any function $G = G(\sigma)$, it holds that

$$\frac{dG}{d\sigma} = \frac{dG}{dZ}\frac{dZ}{d\sigma} = \left(-H_0 \frac{p_0}{\sigma p_0 + p_T}\right)\frac{dG}{dZ}. \tag{C.1}$$

From (3.114) it may also be noted that

$$\frac{d\sigma}{dZ} = -\frac{1}{H_0}\left(\frac{\sigma p_0 + p_T}{p_0}\right). \tag{C.2}$$

Equation (3.113) may written alternatively as:

$$2\left(\frac{\sigma p_0 + p_T}{p_0}\right)\frac{d\hat{\phi}'}{d\sigma} + \left(\frac{\sigma p_0 + p_T}{p_0}\right)^2 \frac{d^2\hat{\phi}'}{d\sigma^2} + H_0^2\left(\frac{N^2}{c^2} - k^2\right)\hat{\phi}' = 0. \tag{C.3}$$

From applying (C.1), (C.3) transforms to:

$$-2H_0\frac{d\hat{\phi}'}{dZ} - H_0\left(\frac{\sigma p_0 + p_T}{p_0}\right)\frac{d}{dZ}\left[-H_0\left(\frac{p_0}{\sigma p_0 + p_T}\right)\frac{d\hat{\phi}'}{dZ}\right] + H_0^2\left(\frac{N^2}{c^2} - k^2\right)\hat{\phi}' = 0. \tag{C.4}$$

Applying transformation relationship (3.115) to (C.4) leads to:

$$-2H_0\frac{dF}{dZ}\exp^{z/2H_0} - F\exp^{z/2H_0} + H_0^2\left(\frac{1}{4H_0^2}F + \frac{1}{H_0}\frac{dF}{dZ} + \frac{d^2F}{dZ^2}\right)\exp^{z/2H_0}$$

$$+H_0\frac{dF}{dZ}\exp^{z/2H_0}+\frac{1}{2}F\exp^{z/2H_0}+H_0^2\left(\frac{N^2}{c^2}-k^2\right)F\exp^{z/2H_0}=0, \qquad \text{(C.5)}$$

which reduces to the required relationship (3.116).

Appendix D

Alternative derivation of the Lamb wave frequency equation

Relationship (3.118) may also be consistently obtained from considering the boundary conditions that apply to $\dot{\sigma}$, $\hat{\phi}'$ and $d\hat{\phi}'/d\sigma$. The details are as follows.

At the lower boundary, where $\sigma = 1$ and $\dot{\sigma} = 0$ by definition, it follows from substituting (3.112) and (3.126) in (3.127) that:

$$c^2 H_0^2 \left(k^2 - \frac{N^2}{c^2}\right)\hat{\pi} = AH_0\left(\mu - \frac{1}{2H_0}\right)\left(\frac{p_0 + p_T}{p_0}\right)^{H_0(\mu+\frac{1}{2H_0})} + BH_0\left(-\mu - \frac{1}{2H_0}\right)\left(\frac{p_0 + p_T}{p_0}\right)^{H_0(-\mu+\frac{1}{2H_0})}. \tag{D.1}$$

Substituting (3.126) into (D.1), and applying (3.129) gives:

$$\left(\mu^2 - \frac{1}{4H_0^2}\right)\left[\left(\frac{p_0 + p_T}{p_0}\right)^{H_0(\mu+\frac{1}{2H_0})} - \left(\frac{p_T}{p_0}\right)^{2H_0\mu}\left(\frac{p_0 + p_T}{p_0}\right)^{H_0(-\mu+\frac{1}{2H_0})}\right] =$$

$$\left(k^2 - \frac{N^2}{c^2}\right)\left\{\left[\left(\frac{p_0 + p_T}{p_0}\right)^{H_0(\mu+\frac{1}{2H_0})} - (\left(\frac{p_T}{p_0}\right)^{2H_0\mu}\left(\frac{p_0 + p_T}{p_0}\right)^{H_0(-\mu+\frac{1}{2H_0})}\right] + \left[\left(\frac{p_T}{p_0}\right)^{2H_0\mu}\left(\frac{p_T}{p_0}\right)^{H_0(-\mu+\frac{1}{2H_0})} - \left(\frac{p_T}{p_0}\right)^{H_0(\mu+\frac{1}{2H_0})}\right]\right\}. \tag{D.2}$$

Noting that the last two terms in (D.2) cancel, it follows that:

$$\left[\left(\mu^2 - \frac{1}{4H_0^2}\right) - \left(k^2 - \frac{N^2}{c^2}\right)\right]\left[\left(\frac{p_0 + p_T}{p_0}\right)^{H_0(\mu+\frac{1}{2H_0})} - \left(\frac{p_T}{p_0}\right)^{2H_0\mu}\left(\frac{p_0 + p_T}{p_0}\right)^{H_0(-\mu+\frac{1}{2H_0})}\right] = 0 \tag{D.3}$$

which implies (3.118).

Appendix E

Applying the continuity equation for the case of solutions with sinusoidal variation in height

Substituting (3.143) in (3.117) gives:

$$\hat{\pi} = \frac{1}{c^2}\left(A\int_0^1 \exp^{imH_0 \ln X} X^{-1/2} d\sigma + B\int_0^1 \exp^{-imH_0 \ln X} X^{-1/2} d\sigma\right). \quad \text{(E.1)}$$

Both integrals appearing in (E.1) have the form $\int_0^1 \exp^{ia \ln X} X^{-1/2} d\sigma$, with a a real number and $X = (\sigma p_0 + p_T)/p_0$, and

$$\int_0^1 \exp^{ia \ln X} X^{-1/2} d\sigma = \int_0^1 \cos(a \ln X) X^{-1/2} d\sigma + i\int_0^1 \sin(a \ln X) X^{-1/2} d\sigma. \quad \text{(E.2)}$$

The two integrals implied by (E.2) may both be evaluated by using integration by parts, which gives:

$$(1+4a^2)\int_0^1 \cos(a \ln X) X^{-1/2} d\sigma = \left[2X^{1/2}\cos(a \ln X)\right]_{\sigma=0}^{\sigma=1} + \left[4aX^{1/2}\sin(a \ln X)\right]_{\sigma=0}^{\sigma=1}$$

$$= 2\left\{\left(\frac{p_0+p_T}{p_0}\right)^{1/2}\cos\left[a\ln\frac{p_0+p_T}{p_0}\right] - \left(\frac{p_T}{p_0}\right)^{1/2}\cos\left[a\ln\frac{p_T}{p_0}\right]\right\} +$$

$$4a\left\{\left(\frac{p_0+p_T}{p_0}\right)^{1/2}\sin\left[a\ln\frac{p_0+p_T}{p_0}\right] - \left(\frac{p_T}{p_0}\right)^{1/2}\sin\left[a\ln\frac{p_T}{p_0}\right]\right\} \quad \text{(E.3)}$$

and

$$\left(1+4a^2\right)\int_0^1 \sin\left(a\ln X\right)X^{-1/2}d\sigma = \left[2X^{1/2}\sin\left(a\ln X\right)\right]_{\sigma=0}^{\sigma=1} - \left[4aX^{1/2}\cos\left(a\ln X\right)\right]_{\sigma=0}^{\sigma=1}$$

$$= 2\left\{\left(\frac{p_0+p_T}{p_0}\right)^{1/2}\sin\left[a\ln\frac{p_0+p_T}{p_0}\right] - \left(\frac{p_T}{p_0}\right)^{1/2}\sin\left[a\ln\frac{p_T}{p_0}\right]\right\} -$$

$$4a\left\{\left(\frac{p_0+p_T}{p_0}\right)^{1/2}\cos\left[a\ln\frac{p_0+p_T}{p_0}\right] - \left(\frac{p_T}{p_0}\right)^{1/2}\cos\left[a\ln\frac{p_T}{p_0}\right]\right\}. \qquad \text{(E.4)}$$

Substituting results (E.3) and (E.4) in (E.2) leads to:

$$\int_0^1 \exp^{ia\ln X}X^{-1/2}d\sigma = \frac{1}{c^2\left(1+4a^2\right)}\left[(2-4ai)\left(\frac{p_0+p_T}{p_0}\right)^{1/2}\exp^{ia\ln[(p_0+p_T)/p_0]}\right.$$

$$\left. +(-2+4ai)\left(\frac{p_T}{p_0}\right)^{1/2}\exp^{ia\ln(p_T/p_0)}\right] \qquad \text{(E.5)}$$

Applying result (E.5) in (E.1) gives the required equation (3.145).

Bibliography

[1] Admirat P, Goyer GG, Wojtiw L, Carte EA, Roos D and Lozowki EP (1985) A comparitive study of hailstorms in Switzerland, Canada and South Africa. *J. of Climatol.* **5** 35-51.

[2] Arakawa A and Lamb VR (1977) Computational design of the basic dynamical processes of the UCLA general circulation model. *Methods of Computational Physics,* Vol. 17, Academic Press, 174-265, 337 pp.

[3] Asselin R (1972) Frequency filter for time integration. *Mon. Wea. Rev.* **100** 487-490.

[4] Bates JR (1984) An efficient semi-Lagrangian and alternating direction implicit method for integrating the shallow water equations. *Mon. Wea. Rev.* **112** 2033-2047.

[5] Bates JR and McDonald A (1982) Multiply upstream, semi-Lagrangian advective schemes: analysis and application to a multi-level primitive equation model. *Mon. Wea. Rev.* **110** 1831-1842.

[6] Bates JR, Li Y, Brandt SF, McCormick SF and Ruge J (1995) A global shallow-water numerical model based on the semi-Lagrangian advection of potential vorticity. *Quart. J. Roy. Meteor. Soc.* **121** 1981-2005.

[7] Benoit R, Desgagne M, Pellerin P, Desjardins S and Chartier Y (1997) The Canadian MC2: A semi-Lagrangian, semi-implicit wide-band atmospheric model suited for fine-scale process studies and simulation. *Mon. Wea. Rev.* **125** 2382-2415.

[8] Burden RL and Faires JD (1993) *Numerical analysis.* PWS Publishing company, Boston. 768 pp.

[9] Brugge R and Moncrieff MW (1985) The effect of physical processes on numerical simulations of two-dimensional cellular convection. *Beitr. Phys. Atmos.* **58** 417-440.

[10] Burger AP (1991) The potential vorticity equation: from planetary to small scale. Tellus **43A**, 191-197.

[11] Burger AP and Riphagen HA (1978) *Analysis of energy-consistency of simple weather prediction models.* CSIR Special Report, SWISK 1, 55 p.

[12] Burger AP and Riphagen HA (1979) The lower boundary condition and energy consistency in primitive and filtered models. *J. Atmos. Sci.* **36** 1436-1449.

[13] Burger AP and Riphagen HA (1981) Available potential energy and simplifications to the adiabatic equation. *Tellus* **33** 505-508.

[14] Burger AP and Riphagen HA (1990) The basic equations in meteorological dynamics - a reexamination of unsimplified forms for a general vertical coordinate. *Beitr. Phys. Atmosph.* **63** 151-164.

[15] Burger AP and Riphagen HA (1999) Energy conservation for a general vertical coordinate - a reexamination of unsimplified forms. *Beitr. Phys. Atmosph.* **72** 25-50.

[16] Carpenter KM (1979) An experimental forecast using a nonhydrostatic mesoscale model. *Quart. J. Roy. Meteor. Soc.* **105** 629-655.

[17] Carte AE and Held G (1978) Variability of hailstorms on the South African Plateau. *J. Appl. Meteorol.* **17** 365-373.

[18] Caya D and Laprise R (1999) A semi-implicit semi-Lagrangian climate model: the Canadian RCM.

[19] Clark TL and Peltier W (1997) On the evolution and stability of finite-amplitude mountain waves. *J. Atmos. Sci.* **34** 1715-1730.

[20] Crimp SJ, Lutjeharms JRE and Mason SJ (1998) Sensitivity of a tropical-temperate trough to sea-surface temperature anomalies in the Agulhas retroflection region. *Water SA* **24** 93-100.

[21] Clark TL and Peltier W (1977) On the evolution and stability of finite-amplitude mountain waves. *J. Atmos. Sci.* **34** 1715-1730.

[22] Cullen MJP (1990) A test of a semi-implicit integration technique for a fully-compressible non-hydrostatic model. *Quart. J. Roy. Meteor. Soc.* **116** 1253-1258.

[23] Daley R (1988) The normal modes of the spherical non-hydrostatic equations with the application to the fitering of acoustic modes. *Tellus* **40A**, 96-106.

[24] Davies T, Staniforth A, Wood N and Thuburn J (2003) Validity of the anelastic and other equation sets as inferred from normal-mode analysis. *Quart. J. Roy. Meteor. Soc.* **129** 2761-2775.

[25] Davies T, Cullen MJP, Malcolm AJ, Mawson MH, Staniforth A, White AA and Wood N (2005) A new dynamical core for the Met Office's global and regional modelling of the atmosphere. *Quart. J. Roy. Meteor. Soc.* **131** 1759-1782.

[26] Davies-Jones RP (1983) The onset of rotation in thunderstorms. Preprints, 13th Conference of Severe Local Storms, Tulsa, Okla., American Meteorological Society, Boston, 215-218.

[27] De Coning E and Adam BF (2000) The tornadic thunderstorm events during the 1998-1999 South African Summer. *Water SA* **26** 361-376.

[28] De Coning E, Adam BF and Banitz L (2000) A severe weather event on 29 December 1997: Synoptic and mesoscale perspectives. *Water SA* **26** 137-146.

[29] De Villiers MP (1998) *Clear air turbulence over the republic of South Africa.* MSc-thesis, University of Pretoria, 136 p.

[30] De Villiers MP (2001) Clear air turbulence over South Africa. *Meteorol. Appl.* **8** 119-126.

[31] Doswell III CA (1991) A review for forecasters on the application of hodographs to forecasting severe thunderstorms. *NWA Digest* **16** 2-16.

[32] Droegemeier KK (1985) *The numerical simulation of thunderstorm outflow dynamics.* Ph.D. dissertation, University of Illinois at Urbana-Champaign, 695 pp.

[33] Droegemeier KK and Wilhemson (1987) Numerical simulations of thunderstorm outflow dynamics. Part I: Outflow sensitivity experiments and turbulent dynamics. *J. Atmos. Sci.* **44** 1180-1210.

[34] Dudhia J (1993) A nonhydrostatic version of the Penn-State-NCAR mesoscale model: Validation tests and simulation of an Atlantic cyclone and cold front. *Mon. Weather. Rev.* **121** 1493-1513.

[35] Dudhia J and Bresch JF (2002) A global version of the PSU-NCAR mesoscale model. *Mon. Wea. Rev.* **130** 2989-3007.

[36] Durran DR (1989) Improving the anelastic approximation. *J. Atmos. Sci.* **46** 1453-1461.

[37] Dutton JA and Fichtl GH (1969) Approximate equations of motion for gases and liquids. *J. Atmos. Sci.* **26** 241-254.

[38] Eckart C (1960) The hydrodynamics of oceans and atmospheres. Pergamon Press, Oxford.

[39] Eliassen A (1949) The quasi-static equation of motion with pressure as independent variable. *Geophs. Publ.* **17** 1-44.

[40] Engelbrecht FA (2000) Nested climate modelling over southern Africa with a semi-Lagrangian limited area model. MSc-thesis, University of Pretoria, 134 pp.

[41] Engelbrecht FA (2005) Simulations of climate and climate change over southern and tropical Africa with the conformal-cubic atmospheric model. In *Potential Impacts and Vulnerabilities of Climate Change on Hydrological Responses in southern Africa,* ed. R.E. Schulze, chap. 4. WRC Report **1430/1/05**. Water Research Commission, Pretoria.

[42] Engelbrecht FA and Rautenbach CJ deW (2000) Perspective for nested climate modelling over southern Africa. *SA Tydskrif vir Natuurwetenskap en Tegnologie* **19** 47-51.

[43] Engelbrecht FA, Rautenbach CJ deW, McGregor JL and Katzfey JJ (2002) January and July climate simulations over the SADC region using the limited-area model DARLAM. *Water SA,* **28**, 361-374.

[44] Fischer G. (1965). On a finite difference scheme for solving the non-linear primitive equations for a barotropic fluid with application to the boundary current problem. *Tellus* **4** 405-412.

[45] Fujita TT (1973a) Experimental classification of tornadoes in FPP scale. *SMRP Research paper* No **98** University of Chicago, Illinois.

[46] Fujita TT (1973b) Tornadoes around the world. *Weatherwise* **26** 56-83.

[47] Fujita T and Grandoso H (1968) Split of a thunderstorm into anticyclonic and cyclonic storms and their motion as determined from numerical model experiments. *J. Atmos. Sci.* **35** 1070-1096.

[48] Gal-Chen T and Somerville RCJ (1975) On the use of a coordinate transformation for the solution of the Navier-Stokes equations. *ibid.* **17** 209-228.

[49] Gallus WA Jr and Rancic M (1996) A nonhydrostatic version of NMC's regional Eta model. *Quart. J. Roy. Meteor. Soc.* **122** 495-513.

[50] Garstang M, Kelbe BE, Emmitt GD and London WB (1987) Generation of convective storms over the escarpment of northeastern South Africa. *Mon. Wea. Rev.* **115** 429-443.

[51] Goliger AM, Milford RV, Adam BF and Edwards M (1997) *Inkanyamba - Tornadoes in South Africa.* United Litho, ISBN 0-7988-5417-0.

[52] Haltiner GJ (1971) *Numerical Weather Prediction.* New York, Wiley.

[53] Haltiner GJ and Williams RT (1980) *Numerical prediction and Dynamic Meteorology (2nd edition).* John Wiley and sons. 477 p.

[54] Harrison MSJ (1984) A generalized classification of South African summer rain-bearing synoptic systems. *J. Climatol.* **4** 547-560.

[55] Harrison MSJ (1986) *A synoptic climatology of South African rainfall variations.* Ph.D. thesis. University of the Witwatersrand.

[56] Held G (1978) The probability of hail in relation to radar echo heights on the South African Highveld. *J. Appl. Meteorol.* **17** 755-762.

[57] Held G (1982) Comparison of radar observations of a devastating hailstorm and a cloudburst at Jan Smuts airport. In: Agee EM and Asai T (eds.) *Cloud Dynamics.* D Reidel Publishing Company, Hamburg, Germany. 273-284.

[58] Hewitson B, Tadross M and Jack C (2005) Scenarios from the University of Cape Town. In *Potential Impacts and Vulnerabilities of Climate Change on Hydrological Responses in southern Africa,* ed. R.E. Schulze, chap. 3. WRC Report **1430/1/05**. Water Research Commission, Pretoria.

[59] Holton JR (1992) *An Introduction to Dynamic Meteorology (3rd edition).* Academic press limited. 511 pp.

[60] Hoskins BJ and Pearce RP (1983) *Large-scale dynamical processes in the atmosphere.* London Academic Press.

[61] Hsu W-R and Sun W-Y (2001) A time-split forward-backward numerical model for solving a nonhydrostatic and compressible system of equations. *Tellus* **53A** 279-299.

[62] Janjic ZI, Gerrity JP Jr and Nickovic S (2001) An alternative approach to nonhydrostatic modeling. *Mon. Wea. Rev.* **129** 1164-1178.

[63] Janjic Z.I. and Wiin-Nielsen A (1977) On geostrophic adjustment and numerical procedures in a rotating fluid. *J. Atmos. Sci.* **34** 297-310.

[64] Johnson M (1978) *The structure of vorticity in cumulonimbus convection: a numerical study.* Ph.D. thesis, University of London.

[65] Joubert AM, Katzfey JJ, McGregor JL and Nguyen KC (1999) Simulating mid-summer climate over southern Africa using a nested regional climate model. *J. Geophys. Res.* **104** 19015-19025.

[66] Juang H.-M. H. (1992) A spectral fully compressible nonhydrostatic model in hydrostatic sigma coordinates: Formulation and preliminary results. *Meteorol. Atmos. Phys.* **50** 75-88.

[67] Jury MR, Pathack B, Rautenbach CJ deW and Van Heerden J (1996) Drought over South Africa and Indian Ocean SST: Statistical and GCM results. *The Global Atmosphere and Ocean System* **4** 47-63.

[68] Jury MR, Mulenga H and Rautenbach CJ deW (2000) Tropical Atlantic variability and Indo-Pacific ENSO: Statistical analysis and numerical simulation. *The Global Atmosphere and Ocean System* **7** 107-124.

[69] Kalnay-Rivas E and Hoitsma D (1979) Documentation of the fourth-order GLAS model. *NASA Tech. Memo* **80608**, 126 pp.

[70] Kaplan ML, Zack JW, Wang VC and Tuccillo JJ (1982) Initial results from a mesoscale atmospheric simulation system and comparisons with the AVE-SESAME I dataset. *Mon. Wea. Rev.* **110** 1564-1590.

[71] Kasahara A (1974) Various vertical coordinate systems used for numerical weather prediction. *Mon. Wea. Rev.* **102** 504-522.

[72] Klemp JB (1987) Dynamics of tornadic thunderstorms. *Annu. Rev. Fluid Mech.* **19** 369-402.

[73] Laprise R (1992) The Euler equations of motion with hydrostatic pressure as an independent variable. *Mon. Weather Rev.* **122** 3-26.

[74] Laprise R, Caya D, Bergeron G and Giguere M (1997) The formulation of Andre Robert MC2 (Mesoscale compressible Community) model. *The Andre J. Robert Memorial Volume (C Lin, R Laprise and H Ritchie, Eds.), companion volume to Atmos.-Ocean*, **35** 195-220.

[75] Laprise R (1998) Semi-implicit semi-Lagrangian fully elastic nonhydrostatic model formulation. *ECMWF Seminar 1998.*

[76] Leslie LM and Purser RJ (1991) High-order numerics in an unstaggered three-dimensional time-split semi-Lagrangian forecast model. *Mon. Weather Rev.* **119** 1612-1623.

[77] Lipps FB and Hemler RS (1982) A scale analysis of deep moist convection and some related numerical calculations. *J. Atmos. Sci.* **51** 3549-3565.

[78] Mahrt L (1986) On the shallow motion approximations. *J. Atmos. Sci.* **43** 1036-1044.

[79] McDonald A (1984) Accuracy of multiply-upstream, semi-Lagrangian advection schemes. *Mon. Wea. Rev.* **112** 1267-1275.

[80] McDonald A (1986) A semi-Lagrangian and semi-implicit two time-level integration scheme. *Mon. Wea. Rev.* **114** 824-830.

[81] McGregor (1987) Accuracy and initialization of a two-time level split semi-Lagrangian model. *Short- and Medium-Range Numerical Weather Prediction,* T. Matsuno, Ed., Special Volume of the J. Meteor. Soc. Japan, 233-246.

[82] McGregor JL (1993) Economical determination of departure points for semi-Lagrangian Models. *Mon. Wea. Rev.* **121** 221-230.

[83] McGregor JL (1996) Semi-Lagrangian advection on conformal-cubic grids. *Mon. Wea. Rev.* **124** 1311-1322.

[84] McGregor JL and Dix MR (2001) The CSIRO conformal-cubic atmospheric GCM. *IUTAM Symposium on Advances in Mathematical Modelling of Atmosphere and Ocean Dynamics,* P.F. Hodnett, Ed., Kluwer, 197-202.

[85] McGregor JL, Nguyen KC and Katzfey JJ (2002) Regional climate simulations using a stretched-grid global model. *Research activities in Atmospheric and Oceanic Modelling* Rep. **32**, WMO Tech Doc. 1105, 2 pp.

[86] McGregor JL (2005) Geostrophic adjustment for reversibly staggered grids. *Mon. Wea. Rev.* **133** 1119-1128.

[87] Mendez-Nunez LR and Carroll JJ (1994) Application of the MacCormack scheme to atmospheric nonhydrostatic models. *Mon. Wea. Rev.* **122** 984-1000.

[88] Mesinger F and Arakawa A (1976) *Numerical Methods used in Atmospheric Models.* Volume 1. GARP Publications Series No. 17 64 pp.

[89] Miller MJ (1974) On the use of pressure as vertical coordinate in modelling convection. *Quart. J. Roy. Meteor. Soc.* **100** 155-162.

[90] Miller MJ and Bets AK (1977) Travelling convective storms over Venezuela. *Mon. Weather Review.* **105** 833-848.

[91] Miller MJ and Pearce RP (1974) A three-dimensional primitive equation model of cumulonimbus convection. *Quart. J. Roy. Meteor. Soc.* **100** 133-154.

[92] Miller MJ and Thorpe AJ (1981) Radiation conditions for the lateral boundaries of limited-area numerical models. *Quart. J. Roy. Meteor. Soc.* **107** 615-628.

[93] Miller MJ and White AA (1984) On the nonhydrostatic equations in pressure and sigma coordinates. *Quart. J. Roy. Meteor. Soc.* **110** 515-533.

[94] Miranda PMA and James IN (1992) Nonlinear three-dimensional effects on gravity-wave drag: Splitting flow and breaking waves. *Quart. J. Roy. Meteor. Soc.* **118** 1057-1081.

[95] Miranda PMA and Valente MA (1997) Critical level resonance in three-dimensional flow past isolated mountains. *J. Atmos. Sci.* **54** 1574-1588.

[96] Moncrieff MW and Miller MJ (1976) The dynamics and simulation of tropical cumulonimbus and squall lines. *Ibid.* **102** 373-394.

[97] Ogura Y and Charney JC (1962) A numerical model of thermal convection in the atmosphere. *Proc. Int. Symp. Numerical Weather Prediction,* Tokyo, Japan, Meteor. Society of Japan, 431-451.

[98] Ogura Y and Phillips NA (1962) Scale analysis of deep and shallow convection in the atmosphere. *J. Atmos. Sci.* **19** 173-179.

[99] Orlanski I (1976) A simple boundary condition for unbounded hyperbolic flows. *J. Comput. Phys.* **21** 251-269.

[100] Phillips NA (1957) A coordinate system having some special advantages for numerical forecasting. *J. Meteor.* **14** 184-185.

[101] Pielke RA (1984) *Mesoscale Meteorological Modeling.* Academic Press, San Diego, USA.

[102] Pudykiewicz J and Staniforth A (1984) Some properties and comparitive performance of the semi-Lagrangian method of Robert in the solution of the advection-diffusion equation. *Atmos.-Ocean,* **22**, 283-308.

[103] Purnell DK (1976) Solution of the advective equation by upstream interpolation with a cubic spline. *Mon. Wea. Rev.* **104** 42-48.

[104] Purser RJ (1987) The filtering of meteorological fields. *J. Climate Appl. Meteor.* **26** 1764-1769.

[105] Purser RJ and Leslie LM (1988) A semi-implicit semi-Lagrangian finite-difference scheme using high-order spatial differencing on a nonstaggered grid. *Mon. Wea. Rev.* **116** 2069-2080.

[106] Rautenbach CJ deW (1999) *Introduction of a hybrid vertical co-ordinate to an atmospheric general circulation model.* PhD-thesis, University of Pretoria, 149 pp.

[107] Rautenbach CJ deW (2003) Seasonal climate predictions with a coupled atmosphere-ocean general circulation model. *Water Research Commission Report,* No **904/1/03** 82 pp.

[108] Rautenbach CJ deW, Engelbrecht FA, Engelbrecht CJ, Ndarandana T and McGregor JL (2005) *Regional model development for simulating atmospheric behavior and rainfall over southern Africa.* Water Research Commission, Pretoria, RSA, Report 1261/1/05.

[109] Richtmyer RD and Morton KW (1967) *Difference methods for initial value problems.* Wiley-Interscience.

[110] Riishogaard LP, Cohn SE, Li Y and Menard R (1998) The use of spline interpolation in semi-Lagrangian transport models. *Mon. Wea. Rev.* **126** 2008-2016.

[111] Riphagen HA (1984) *The implementation of a split explicit weather prediction model for the Southern Hemisphere.* MSc dissertation, University of Pretoria, South Africa, November 1984, 164 p.

[112] Riphagen HA (1989) High latitude filtering for the global prediction model. *In: Proc. Sixth Annual Conference of the S.A. Society for Atmospheric Sciences,* Pretoria, 26-27 October, p 14.

[113] Riphagen HA (1993) Meteorological modelling in South Africa. *In: Proc. Tenth Annual conference of the S.A. Society for Atmospheric Sciences,* Midrand, 13-14 October, p 18.

[114] Riphagen HA (1999) The Eta model in South Africa. *International ETA Model Newsletter,* no. 2, February 1999.

[115] Riphagen HA and Burger AP (1978) *A non-integrated, adiabatic three-level filtered weather prediction model.* CSIR Special Report, SWISK 7, 26 p.

[116] Riphagen HA and Burger AP (1986) Comments on the computational stability of Gadd's adjustment and advection schemes for a split explicit model. *Quart. J. Roy. Met. Soc.* **112** 276-282.

[117] Riphagen HA, Bruyere CL, Jordaan W, Poolman ER and Gertenbach JD (2002) Experiments with the NCEP regional ETA model at the South African Weather Bureau, with emphasis on terrain presentation and its effect on precipitation predictions. *Mon. Wea. Rev.* **130** 1246-1263.

[118] Ritchie H (1987) Semi-Lagrangian advection on a Gaussian grid. *Mon. Wea. Rev.* **115** 608-619.

[119] Robert A (1966) The integration of a low order spectral form of the primitive meteorological equations. *J. Meteorol. Soc. Jpn.* **44** 237-245.

[120] Robert A (1969) The integration of a spectral model of the atmosphere by the implicit method. Pp. VII-19-VII-24 in Proceedings WMO/IUGG Symposium on Numerical Weather Prediction. Japan Meteorol. Agency.

[121] Robert A (1981) A stable numerical integration scheme for the primitive meteorological equations. *Atmos.-Ocean* **19** 35-46.

[122] Robert A (1982) A semi-Lagrangian and semi-implicit numerical integration scheme for the primitive meteorological equations. *J. Meteor. Soc. Japan* **60** 319-325.

[123] Robert A (1993) Bubble convection experiments with a semi-implicit formulation of the Euler equations. *J. Atmos. Sci.* **50** 1865-1873.

[124] Room R (1989) The general form of dynamical equations of the atmosphere in the isobaric coordinate space. Pp. 368-371 *in Proceedings of the Estonian Academy Sci. Phys. Math* **38**

[125] Room R (1990) General form of the equations of atmospheric dynamics in isobaric coordinates. *Izvestiya, Atmospheric and Ocean Physics* **26** 9-14.

[126] Room R (1998) Acoustic filtering in nonhydrostatic pressure coordinate dynamics: A variational approach. *J. Atmos. Sci.* **46** 1154-1164.

[127] Room R, Miranda PMA and Thorpe AJ (2001) Filtered non-hydrostatic models in pressure-related coordinates. *Quart. J. Roy. Meteor. Soc.* **127** 1277-1292.

[128] Rotunno R (1981) On the evolution of thunderstorm rotation. *Mon. Wea. Rev.* **109** 171-180.

[129] Salmon R and Smith LM (1994) Hamiltonian derivation of the nonhydrostatic pressure-coordinate model. *Q. J. R. Meteor. Soc.* **120** 1409-1413.

[130] Schoenstadt AL (1978) A tranfer function analysis of numerical schemes used to simulate geostrophic adjustment. *NPS Rept.* NP.-53-79-001, Naval Postgraduate School, Monterey. CA, 93943, 44 pp.

[131] Shapiro R (1975) Linear filtering. *Math. Comp.* **29** 1094-1097.

[132] Shutts GJ and Gray MEB (1994) A numerical modelling study of the geostrophic adjustment process following deep convection. *Q. J. R. Meteorol. Soc.* **120** 1145 1178.

[133] Skamarock WC, Klemp JB, Dudhia J, Gill DO, Barker DM, Wang W and Powers JG (2005) A description of the Advanced Research WRF Version 2. *NCAR Technical Note,* TN-468+STR, 88 pp.

[134] Smolarkiewicz PK, Margolin LG and Wyszgrodzki AA (2001) A class of nonhydrostatic global models. *J. Atmos. Sci.* **58** 349-364.

[135] Straka JM, Wilhelmson RB, Wicker LJ, Anderson JR and Droegemeier KK (1993) Numerical solutions of a nonlinear density current: A benchmark solution and comparisons. *Int. J. Num. Methods Fluids* **17** 1-22.

[136] Tanguay MA, Robert A and Laprise R (1990) A semi-implicit semi-Lagrangian fully compressible regional forecast model. *Mon. Wea. Rev.* **118** 1970-1980.

[137] Tapp MC and White PW (1976) A nonhydrostatic mesoscale model. *Quart. J. Roy. Meteor. Soc.* **102** 277-296.

[138] Tennant WJ, Riphagen HA, Gertenbach JD, De Villiers MP and Rae KJ (1997). The effect of radiosonde and buoy reduction on numerical prediction products at the South African Weather Bureau. *Proceedings of CGC/WMO Workshop on the Impact of Various Observing Systems on Numerical Weather Prediction,* Geneva, 7-9 April, World Weather Watch Technical Report No. 18, WMO/TD No. 686, 165-183.

[139] Thorpe AJ and Miller MJ (1978) Numerical simulations showing the role of the downdraught in cumulonimbus motion and splitting. *Quart. J. Roy. Meteor. Soc.* **104** 873-893.

[140] Thorpe AJ, Miller MJ and Moncrieff MW (1982) Two-dimensional convection in non-constant shear: a model of mid-latitude squall lines. *Ibid.* **108** 739-762.

[141] Thuburn J, Wood N and Staniforth A (2002a) Normal modes of deep atmospheres. I: Spherical geometry. *Quart. J. Roy. Meteor. Soc.* **128** 1771-1792.

[142] Thuburn J, Wood N and Staniforth A (2002b) Normal modes of deep atmospheres. II: f-F plane geometry. *Quart. J. Roy. Meteor. Soc.* **128** 1793-1806.

[143] Tritton DJ (1988) *Physical fluid dynamics,* 2nd edn. Oxford University Press, Oxford, UK.

[144] Van Heerden J, Rautenbach CJ deW and Truter MM (1995) Techniques for seasonal and longer term rainfall prediction in South Africa. *Water Research Commission Report* No **373/1/92**, 1-51.

[145] Visser PJM (2000) The storm-structure-severity method for the identification of convective storm characteristics with conventional radar. *Meteorol. Appl.*

[146] Weismann ML and Klemp JB (1982) The dependence of numerically simulated convective storms on vertical wind shear and buoyancy. *Mon. Wea. Rev.* **110** 504-520.

[147] White AA (1989) An extended version of a nonhydrostatic, pressure coordinate model. *Quart. J. Roy. Meteor. Soc.* **115** 1243-1251.

[148] White AA and Bromley RA (1995) Dynamically consistent, quasi-hydrostatic equations for global models with a complete representation of the Coriolis force. *Quart. J. Roy. Meteor. Soc.* **121** 399-418.

[149] White AA, Hoskins BJ, Roulstone I and Staniforth A (2005) Consistent approximate models of the global atmosphere: shallow, deep, hydrostatic, quasi-hydrostatic and nonhydrostatic. *Quart. J. Roy. Meteor. Soc.* **131** 2081 2107.

[150] Wicker LJ and Skamarock WC (2002) Time-splitting methods for elastic models using forward time schemes. *Mon. Wea. Rev.* **130** 2088-2097.

[151] Wilhelmson RB and Ericksen JH (1977) Direct solutions for Poisson's equation in three dimensions. *J. Comput. Phys.* **25** 319-331.

[152] Wilhelmson R and Ogura Y (1972) The pressure perturbation and the numerical modelling of a cloud. *J. Atmos. Sci.* **29** 1295-1307.

[153] Winninghoff FJ (1968) On the adjustment toward a geostrophic balance in a simple primitive equation model with apllication to the problems of initialization and objective analysis. Ph.D. thesis, University of California, Los Angeles, 161 pp.

[154] Wood N and Staniforth A (2003) The deep-atmosphere Euler equations with a mass-based vertical coordinate. *Q. J. R. Meteorol. Soc.* **129** 1289-1300.

[155] Xue M (1989) *A Nonhydrostatic Numerical Model in Sigma-coordinates and Simulations of Mesoscale Phenomena.* PhD Thesis, Reading University, 258 pp.

[156] Xue M and Thorpe AJ (1991) A mesoscale numerical model using the nonhydrostatic pressure-based sigma-coordinate equations: Model experiments with dry mountain flows. *Mon. Wea. Rev.* **119** 1168-1185.